Contributions to the characterization of grating-based x-ray phase-contrast imaging

Dissertation

zur Erlangung des akademischen Grades

Doctor rerum naturalium
(Dr. rer. nat.)

vorgelegt

der Fakultät Mathematik und Naturwissenschaften
der Technischen Universität Dresden

von
Dipl.-Phys. Michael Chabior

geboren am 28.11.1981 in Peiskretscham

Eingereicht am 09.09.2011

Die Dissertation wurde in der Zeit vom September 2008 bis
August 2011 bei Siemens CT München angefertigt

meinen Eltern gewidmet

Abstract

In this work, a characterization and optimization of the grating-based x-ray imaging technique is presented. The investigations are introduced by analytical considerations, are underpinned with numerical simulations and validated using exemplary experiments.

A detailed examination of the image formation in a grating interferometer is given, highlighting the dependence of the measured signal on the profile of the gratings. Subsequently, it is shown analytically and in experiments that grating-based imaging can be performed using three basic grating arrangements, which differ in their requirements on grating fabrication and experimental implementation. By a characterization of the measurement signal for each arrangement, a dependence of the signal strength on the sample position within the interferometer is identified. The consecutive evaluation of the impact of this position dependence on radiographic and tomographic data leads to the derivation of optimized reconstruction algorithms and to a correction of resulting image artifacts. Additionally, it is shown that the simultaneous measurement of attenuation and phase images allows the determination of the atomic number of the sample, opening new possibilities for material discrimination.

Apart from these investigations on the contrast formation, various imperfections of the technique are investigated: The properties of the image noise are examined in a detailed statistical analysis, yielding a fundamental understanding of the signal-to-noise behavior of the three available contrast channels. Additionally, beam-hardening artifacts at polychromatic x-ray sources are investigated and their correction by a linearization approach is presented. By a subsequent analysis of the influence of various different grating imperfections on the image quality, tolerance limits for grating fabrication are specified. Furthermore, analytical considerations show that gratings with a duty cycle of 1/3 are advantageous with respect to the signal-to-noise ratio in comparison to common gratings with a duty cycle of 1/2.

In conclusion, the results, concepts and methods developed in this work broaden the understanding of grating-based x-ray imaging and constitute a step forward towards the practical implementations of the technique in imaging applications.

Kurzfassung

Die vorliegende Arbeit befasst sich mit der Charakterisierung und Optimierung der gitterbasierten Röntgen-Phasenkontrasttechnik. Die Untersuchungen gliedern sich in einführende analytische Überlegungen, vertiefende numerische Simulationen und exemplarische Testmessungen.

Ausgehend von einer einleitenden analytischen Beschreibung der Kontrasterzeugung in der gitterbasierten Röntgenbildgebung wird der Einfluss der Gitterprofile auf das Messsignal evaluiert. Darauf aufbauend wird experimentell als auch analytisch gezeigt, dass ein Gitterinterferometer in drei grundlegenden Anordnungen der Gitter realisiert werden kann, welche sich in ihren Anforderungen an die Gitterherstellung und an das Interferometerdesign unterscheiden. Für die verschiedenen Anordnungen führt die Charakterisierung des Messsignals zur Identifikation einer Abhängigkeit der Signalstärke von der Position des Objekts innerhalb des Interferometers. Die anschließende Untersuchung des Einflusses dieser Positionsabhängigkeit auf Radiographien und Tomographien ermöglicht die Herleitung optimierter Rekonstruktionsalgorithmen sowie eine Korrektur der aus der Positionsabhängigkeit resultierenden Artefakte. Des Weiteren wird gezeigt, dass die simultane Messung des Absorptions- und Brechungsdekrements die Berechnung der Kernladungszahl der betrachteten Probe erlaubt, wodurch in der Phasenkontrastbildgebung neue Wege bei der Materialunterscheidung eröffnet werden.

Neben diesen Studien zur Kontrasterzeugung wird der Einfluss verschiedener Imperfektionen der Messapparatur auf die Bildgebung untersucht: Das Bildrauschen in der gitterbasierten Röntgenbildgebung wird einer detaillierten statistischen Analyse unterzogen, wodurch ein grundlegendes Verständnis des Signal-zu-Rausch-Verhaltens in den drei verfügbaren Kontrasten ermöglicht wird. Die bei der Verwendung von polychromatischen Laborquellen auftretenden Strahlaufhärtungsartefakte werden charakterisiert und eine Linearisierungsmethode als Ansatz zu deren Korrektur erarbeitet. Ebenso werden Abweichungen der Gitter von ihrer Idealform untersucht und daraus resultierende Toleranzwerte für die Gitterherstellung definiert. Zusätzlich zur Untersuchung des Einflusses von Gitterimperfektionen wird in analytischen Betrachtungen gezeigt, dass Gitter mit einem Tastverhältnis von 1/3 im Vergleich zu Gittern mit einem Tastverhältnis von 1/2 Vorteile in der Bildgebung und im Interferometerdesign bieten. Insgesamt erweitern die erarbeiteten Resultate, Konzepte und Methoden das Verständnis der gitterbasierten Phasenkontrastbildgebung und liefern wertvolle Beiträge zur praktischen Umsetzung der Technik in der medizinischen Diagnostik und zerstörungsfreien Materialprüfung.

Acknowledgements

While there is always only a single author on the front cover of a Ph. D thesis, this work would not have been possible without the contribution, advice and guidance of a great many different people. Although it was of immeasurable value for me, I will at least try to honor their help with a few words of recognition to express my deepest thanks.

During this thesis, I had the opportunity not only to be part of the scientific community, but also to view scientific research from the perspectives of an corporation. By the collaboration of company and university, I had the advantage of having been guided by three different supervisors, Dr. Schuster, Prof. Schroer and Prof. Pfeiffer. First and biggest thanks are reserved for Manfred Schuster for his patient and tireless commitment. He was always willing to listen, even if pressed for time, with valuable and frequent advice enhanced by his vast experience in the field of x-ray science. I would like to thank Christian Schroer for his encouragement and continuous and always helpful counseling. His quick understanding of the problems that I presented to him on my regular visits always impressed me and his counsel helped me to find new solutions and new directions of thought. Great thanks are due to Franz Pfeiffer, who generously introduced me into his group and gave me the possibility to perform my research at his experimental facilities, providing guidance, advice and frequent help.

Working for Siemens during my Ph. D thesis gave me the exceptional opportunity to work in a corporate environment and to get an impression of the work-flow of a multinational company. From the various colleagues I have been working with at Siemens I would especially like to thank Matthias Goldammer, Joachim Baumann and Jürgen Stephan for their support and frequent help with the great many questions that I had. I would like to thank all other people I had the pleasure of becoming acquainted with spending my time at Siemens, especially Matthias Honal, Barbara Jobst and Fenna Bleyl. Additional thanks to Karsten Schörner and Konstantin Eisler for our constructive coffee breaks and after-work night outs.

The work in the scientific community in Garching has been a pleasant change from the surroundings of the corporate world at Siemens. I would like to cordially thank everyone in the Garching group that I came to work with during my time there: Klaus, Dieter (the Elder), Martin (the Elder), Julia, Guillaume, Pierre, Nellie, Hans, Brunhilde, Martin (the Younger), Björn, Michael, Dieter (the Younger), Andreas, Simone, Miljana, Michael, Arne, Astrid, Marian, Thomas and Marco: Thanks for the atmosphere, it has been always a pleasure and fun working with all you. Keep the cakes coming!

I have also been given the opportunity to do measurements at the Paul Scherrer Institut. A special thank to everyone at the whole institution, especially for Tilman Donath, for his help, assistance and company while sharing beamtime, and to Christian David, for his generous assistance and advice.

It has been a valuable experience to have been a part of the PHACT project, at the crossroads between scientific research and commercial application. I would like to thank Prof. Gisela Anton, Jürgen Mohr, Joachim Schulz, Georg Wittmann and Eckhard Hempel for their guidance and organization of the project. Furthermore, I would like to thank everyone involved in the project: Jürgen Durst, Peter Bartl, Thomas Weber, Florian Beyer, Andre Ritter, Wilhelm Haas and Thilo Michel from Erlangen, Rainer Raupach, Martin Hoheisel, Thomas Mertelmeier, Marcus Radicke from Siemens in Forchheim and Erlangen, and Thomas Grund from Karlsruhe. Special thanks to Johannes and Marco, with whom I had the pleasure to work with at least for a short while.

My final thanks go to Caro, all my friends and the people at the Villa, for bringing a little chaos into the order.

Contents

Abbreviations, symbols and conventions

This section summarizes common mathematical formulas and abbreviations that will be used in this work:

$a \approx b$	a is approximately b
$a \sim b$	a is proportional to b
$a \equiv b$	a is identical to b
$a \Rightarrow b$	from a follows b
$a \Leftrightarrow b$	a is equivalent to b, $a \Rightarrow b$ & $b \Rightarrow a$
$a := b$	a is defined by b
$\lvert z\rvert = \sqrt{\mathrm{Re}^2(z) + \mathrm{Im}^2(z)}$	magnitude of complex number z
$\arg z$	argument function/phase of complex number z
E	photon energy
λ	photon wavelength
$k = 2\pi/\lambda$	photon wave vector
$F(f,g) = \mathscr{F}\{f(x,y)\}$	$F(f,g)$ is Fourier transform of $f(x,y)$
$f(x,y) \xleftrightarrow{\mathscr{F}} F(f,g)$	f and F are Fourier pairs
$f(x) \otimes g(x)$	convolution of f and g
$f(x) * g(x)$	correlation of f and g
$\mathrm{rect}(x)$	normalized unit rectangle function
$\mathrm{sinc}(x) = \sin(\pi x)/\pi x$	normalized sinus cardinalis
$\Delta_p(x) = \sum_{m=-\infty}^{\infty} \delta\,(x - mp)$	Dirac comb function
$\partial_x f = \partial f/\partial x$	derivative of f along x
$\nabla = (\partial_x, \partial_y, \partial_z)$	nabla operator, gradient
$E(X)$	expectation value of X
$V(X) = E\left[(X - E(X))^2\right]$	variance of X
$\mathrm{Cov}(X,Y) = E\left[(X - E(X))(Y - E(Y))\right]$	covariance of X and Y

Throughout this work, the following coordinate system will be used:

$+z$	beam direction, towards detector, 'downstream'
$+x$	when looking in beam direction, to the right, 'horizontal','lateral'
$+y$	when looking in beam direction, upwards, 'vertical'
$\mathbf{r} = (x,y,z)$	position vector in 3D space
rotations	right-handed

1 Introduction

1.1 X-ray phase contrast as a research field

Since their discovery more than 100 years ago, the penetration capabilities of x-rays have been widely utilized for the investigation of the inner structure of objects opaque for visible light. Nowadays, important imaging applications include medical diagnostics, non-destructive testing, security inspections and scientific research. Conventional imaging techniques utilize the attenuation of x-rays along their path through the sample, neglecting the phase information of the x-ray wave in the measurement. While visible light microscopy gained a large impetus by the development of phase contrast imaging by Zernike [Zernike34] in the 1940s, the implementation of similar phase-contrast techniques in x-ray imaging turned out to be much more challenging, due to the small refraction angles involved and the difficulties in the fabrication of appropriate and efficient x-ray optics. While crystal-based interferometers were the first devices to deliver phase contrast, currently there are three imaging techniques being pursued for the application of phase contrast in medical imaging and other areas of interest: the diffraction-enhanced, the propagation-based and the grating-based imaging techniques. A brief introduction into all imaging techniques, together with their advantages and disadvantages, will be presented in the following.

1.1.1 Interferometric methods

X-ray phase-contrast imaging was pioneered by Bonse and Hart [Bonse65] in the 1960s. In their approach, an interferometer consisting of typically three crystals is used, as shown in Fig. 1 (a). The first crystal splits the collimated and monochromatic beam into two separate beams inclined by the Bragg angle. While the sample is positioned in the path of one of the beams, the other remains undisturbed and is used as a reference. After being deflected by a second crystal, the two beams are overlaid coherently at the plane of the third crystal, creating an interference pattern with a fringe period inversely proportional to the deflections caused by the sample. By an evaluation of the interference fringes, the phase shift imposed by the sample can be retrieved.

The crystal interferometer technique is generally considered to be the most sensitive phase-contrast technique. This advantage is also its biggest drawback, since in the presence of a strongly phase-shifting sample the interference fringes may become unresolvable. Thus, the method is most suitable for samples which do not exhibit strong jumps in the refractive index, as for example present at the tissue-air boundary. Additionally, the high sensitivity of the technique requires the alignment of the crystals to be stable at a length scale finer than the x-ray wavelength in use. This stringent stability requirement also limits the potential field-of-view to sizes insufficient for medical imaging. The requirement of a monochromatic and collimated beam, together with the stability requirements, essentially limits the use of this technique to highly brilliant x-ray sources like synchrotrons. Nevertheless, approaches for medical imaging have been demonstrated for example in [Momose03].

1.1.2 Diffraction enhanced imaging

Similar to the Bonse-Hart interferometer, in analyzer-based imaging, also known as diffraction-enhanced imaging, crystals are used for the analysis of phase variations. The method was pioneered separately at the National Synchrotron Light Source [Chapman97], at the

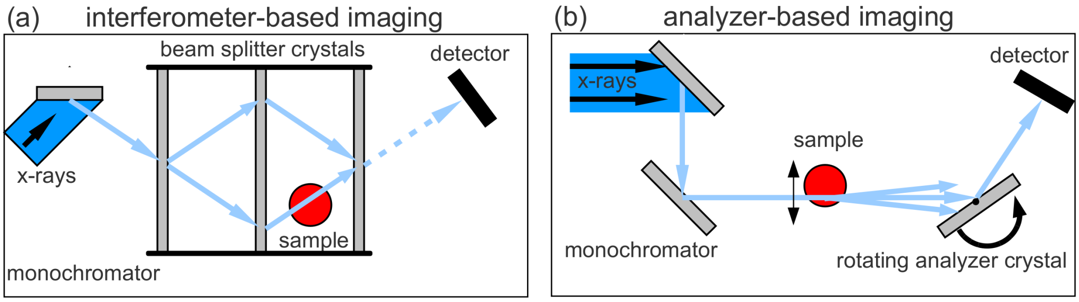

Fig. 1: *(a) Typical Bonse-Hart interferometer using the interference between two beams separated by a beam-splitter crystal optics. (b) In diffraction enhanced imaging, a rotating crystal is used for the angular selection of rays deflected by the sample.*

Commonwealth Scientific and Industrial Research Organisation (CSIRO) [Davis95] as well as in St. Petersburg [Ingal95]. Other related approaches were presented in Refs. [Keyriläinen02] and [Nesch09]. The central part of the imaging setup is the analyzer crystal, as shown in Fig. 1 (b): X-rays directed towards the crystal will be diffracted into the detector, if the incidence angle fulfills the angular acceptance of the crystal, given by the Bragg condition. The crystal acts as an angular selective device, allowing an analysis of the angular spectrum of the rays passing the sample. The intensity measured in each detector pixel as a function of the crystal tilt angle is called the rocking curve, with an approximately bell-shaped form. Different positions on the curve correspond to different refraction angles of the sample. Therefore, from the slope of the rocking curve, the angular deviation relative to a reference scan and thus the phase shift caused by the sample can be reconstructed. If the analyzer crystal is positioned to the peak of the rocking curve, an attenuation image is obtained, which is free of scattered photons. If compared to a reference attenuation image, this image gives rise to an extinction contrast unique to the DEI technique. Since the image quality depends on the coherence of the utilized radiation, the decoherence caused by diffuse multiple scattering within the sample can be used as a source of contrast, leading to an additional coherent scattering contrast.

While first developed for use with monochromatic and highly collimated radiation, it was also shown that the method remains feasible using a polychromatic source spectrum, with the rocking curve adapted to the K α_1 radiation of the target material [Muehlman10]. The method is being evaluated for the application in medical imaging, especially in cartilage and bone imaging [Coan10] and mammography [Keyriläinen08].

1.1.3 Propagation technique

The propagation technique, also called in-line phase contrast or in-line holography, utilizes the fact that the phase shift imposed by the sample can be reconstructed by the propagation of the disturbed x-ray wavefront. If the detector is positioned right behind the sample, a conventional attenuation image is obtained. In contrast, if the distance between sample and detector is increased, the attenuation image will be edge-enhanced by diffraction effects. By taking several images of the sample at different sample-detector distances, the propagation of the x-ray wavefront is sampled in spatial and frequency domain, allowing the separation of phase and attenuation contrast and a reconstruction of the second derivative of the phase of the wavefront. This principle is shown in Fig. 2 (a). This approach was developed separately at the European Synchrotron Radiation Facility (ESRF) [Snigirev95, Cloetens97] and at the CSIRO [Wilkins96].

In comparison to the interferometric technique, the propagation technique offers the advantage

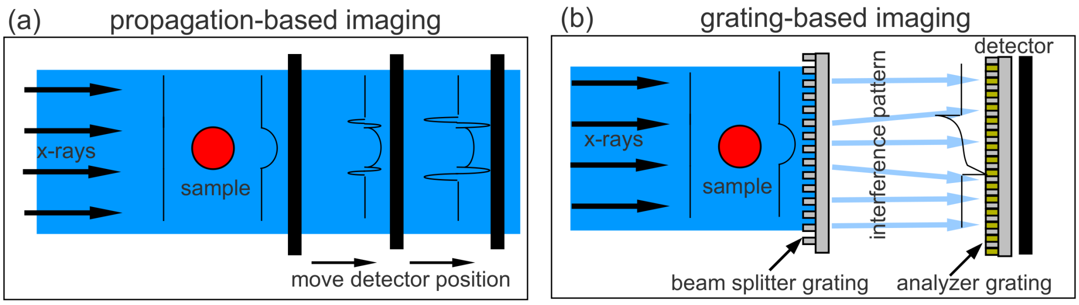

Fig. 2: *(a) In propagation-based phase contrast, several images of the propagating wavefield are taken at different sample-detector distances, (b) In grating-based phase contrast, the interference pattern created by a diffracting beam-splitter grating is utilized for the analysis of beam deflections.*

that it is capable of working with polychromatic radiation, thus reducing the requirements and restrictions for the imaging hardware. Additionally, the method is simple to implement and the requirements on the stability of the setup are comparatively small. Nevertheless, the method requires high spatial resolution and coherence, which narrows the possible polychromatic x-ray sources down to microfocus tubes with low power and thus low photon flux.

1.1.4 Grating-based phase contrast

Grating-based differential phase-contrast imaging (DPC) was pioneered at the ESRF [David02], Tokyo university [Momose02] and the Paul Scherrer Institut [Weitkamp05]. Independent investigations have been performed by Clauser et al. [Clauser98]. The technique uses the distortions of an interference pattern created by a diffracting beam-splitter grating for the evaluation of the gradient of the phase of the wavefront. Since the interference pattern cannot be resolved by most common digital detectors, an additional analyzer grating is introduced, creating Moiré fringes in the presence of a sample. The Moiré fringes can be either analyzed using a Fourier transform of a phase-stepping approach. A third attenuation grating placed in front of the others, splits the broad focus of a spatially incoherent x-ray tube into a series of line sources, each independently meeting the lateral coherence requirements of the technique [Pfeiffer06, Pfeiffer07].

Grating-based phase-contrast imaging offers the advantage over the other methods that it is not only feasible with polychromatic beams, but also with high-powered laboratory sources with broad foci. Beyond the attenuation- and phase-contrast channels, the method is capable of delivering a contrast which is related to the internal structure of the traversed object [Pfeiffer08]: Diffuse small-angle x-ray scattering within the sample leads to a coherence degradation of the wavefront, which can be used for contrast formation. In comparison to the propagation technique, which yields the second derivative of the phase, the DPC technique measures deflections and thus offers the first derivative of the wavefront, which makes the reconstruction of the phase less prone to noise in the image. Together with its compatibility with large fields of view, the technique remains the most promising technique for the application in medical diagnostics. The grating-based x-ray phase-contrast technique is the subject of this thesis and will be developed and analyzed in more detail in the following.

1.2 Outline

The purpose of this thesis is an in-depth analysis and characterization of the grating-based x-ray imaging technique. In the course of this text, the technique will be analyzed from a number of different perspectives and with different imaging parameters under consideration. The subjects and sections are organized by increasing complexity, where each new section requires the results and the understanding obtained in the previous sections. Each section will be introduced by a short outline and concluded by a summary of the obtained results. Extensive calculations are shifted to the appendix for the sake of readability. Important new concepts and ideas are given bold faced.

Following this introduction into x-ray phase-contrast imaging as a research field, the contrast generation in grating-based x-ray imaging will be analyzed in the successive sections. First, in section 2, the basic principles of the technique are investigated. The use of each grating is explained and data evaluation techniques are revised and/or developed. A thorough analysis of the grating arrangement using a graphical approach to interferometer design is presented in section 2.8, yielding the identification and realization of three fundamental interferometer geometries. In section 3, the differences in the formation of phase and dark-field contrast in comparison to the classical attenuation contrast are revised. A dependence of the measurement signal on the sample position within the interferometer is found and analyzed in terms of its influence on tomographic imaging using a grating interferometer. In section 4, it is shown that the dependence of the attenuation and refraction decrements on material properties allows the calculation of an additional atomic number contrast, whose origin and properties will be evaluated.

Following these discussions of the origin and strength of the measurement signal and the available contrasts, an evaluation of the influence of various imperfections of the measurement setup on the image quality in grating-based imaging is aspired. In section 5, the fundamental characteristics of the noise in the reconstructed images is analyzed. Based on a simple noise propagation approach, expectation values and noise variances will be given for all three contrast channels, with a highlight on the noise properties in the low signal-to-noise limit. Consecutively, in section 6, it will be investigated how the use of polychromatic x-ray sources influences the image quality for all three contrast channels, with an emphasis on the understanding and correction of beam-hardening effects and artifacts connected to the attenuation of low energy components of the source spectrum. In section 7, the results of the noise analysis and the interferometer's performance under polychromatic radiation are used for a quantification of the influence of various grating imperfections on the image quality.

In the final section 8, an analysis of imaging using gratings with a duty cycle different from 1/2 is presented. The imaging performance of the gratings is analyzed in terms of signal strength, noise properties, spectral sensitivity and error-proneness, thus providing a summary and application of the methods and results obtained in the previous sections. The thesis concludes in section 9 with a summary of the thesis and a discussion of the obtained results, highlighting open questions and unresolved problems.

1.3 Publication list

The results of this thesis have been published in the following journals:

Grating geometries and sensitivity (sections 2.8 and 3):
T. Donath, M. Chabior, F. Pfeiffer, O. Bunk, E. Reznikova, J. Mohr, E. Hempel, S. Popescu, M. Hoheisel, M. Schuster, J. Baumann, and C. David, "Inverse geometry for grating-based x-ray phase-contrast imaging," J. Appl. Phys. **106**, 054703 (2009).

Sensitivity and tomography (section 3):
M. Chabior, M. Schuster, C. Schroer, and F. Pfeiffer, "Grating-based phase-contrast computed tomography of thick samples," Phys. Med. Biol. submitted (08.2011).

Atomic number imaging (section 4):
M. Chabior and M. Schuster, "Abbildung der effektiven Kernladungszahl mittels gitterbasierter Radiographie bzw. Tomographie," Technik Up2date 2011 #3, Prior Art Publishing, p. 14 (2011).

Signal and noise analysis (section 5):
M. Chabior, T. Donath, C. David, M. Schuster, C. Schroer, and F. Pfeiffer, "Signal-to-noise in grating-based x-ray dark-field imaging," J. Appl. Phys. accepted (08.2011).

Polychromatic imaging and beam hardening (section 6):
M. Chabior, T. Donath, C. David, M. Schuster, C. Schroer, and F. Pfeiffer, "Beam-hardening effects in grating-based x-ray phase-contrast imaging," Med. Phys. **38**, 1189-1195 (2011).

Imaging with imperfect gratings (section 7):
M. Chabior, M. Schuster, C. Schroer, and F. Pfeiffer, "Analytical evaluation of grating-based x-ray imaging using imperfect gratings," in preparation (2011).

2 Basic principles of grating-based phase contrast

In this section, the fundamental principles of differential x-ray phase-contrast imaging using a grating interferometer will be developed. Beginning from a description of the interactions of x-rays with matter in section 2.1, the contrast mechanisms of differential phase-contrast imaging are highlighted in section 2.2. The basic interferometer design will be developed by consecutively applying restrictions to the available experimental hardware, leading to a description of each grating of a typical three-grating setup in sections 2.3 - 2.5. Contrast generation and data extraction are examined in sections 2.6 and 2.7 for the different contrast channels obtainable with the technique. On the basis of a graphical design scheme for a three-grating setup using a magnifying fan-beam source, three fundamental interferometer geometries are presented in section 2.8. The section closes with a guideline for interferometer design under given experimental restrictions.

2.1 Interactions of x-rays with matter

On their passage through matter, x-rays interact in a variety of ways with the traversed material. Microscopically, the interactions can be described in a semi-classical picture by the scattering of an x-ray wave by the charge distribution around the atoms. The number of scattered photons per solid angle Ω and thus the probability of an interaction is given by the differential cross-section $(d\sigma/d\Omega)$. If the incoming and outgoing electric field component is denoted $\mathscr{E}_{\text{in}}$ and $\mathscr{E}_{\text{out}}$, respectively, the scattered signal at distance R from the point of interaction can be written

$$\left(\frac{d\sigma}{d\Omega}\right) = \frac{|\mathscr{E}_{\text{out}}|^2}{|\mathscr{E}_{\text{in}}|^2} \cdot R^2. \tag{2.1}$$

The oscillating electromagnetic field of the incoming x-ray photon forces the shell electrons to perform harmonic oscillations. An oscillating electron acts as a point source, emitting an outgoing electrical field that has the form of a spherical wave $\mathscr{E}_{\text{out}} \sim e^{ikR}/R$. In this model, the ratio between the incoming and outgoing electric field components can be written

$$\frac{|\mathscr{E}_{\text{out}}|}{|\mathscr{E}_{\text{in}}|} = -r_e \cdot f(\mathbf{q},E) \cdot P \cdot \frac{e^{ikR}}{R}, \tag{2.2}$$

where r_e is the classical electron radius and P a factor accounting for the polarization of the radiation [Nielsen00]. The amplitude of the outgoing spherical wave $f(\mathbf{q},E)$ is called the atomic scattering factor (also atomic scattering length for low energies), which contains all information on the interaction of x-rays with the bound electrons in the material. Its parameters are the scattering vector $\mathbf{q} = \mathbf{k'} - \mathbf{k}$, with $\mathbf{k}$ and $\mathbf{k'}$ the wave vectors of the incoming and outgoing waves, and the energy E of the x-ray photon. The atomic scattering factor is the resonant scattering amplitude of x-rays scattered by atomic charges and is described in more detail in appendix B. The scattering factor is usually written

$$f(\mathbf{q},E) = f_0(\mathbf{q}) + f_1(E) + i \cdot f_2(E), \tag{2.3}$$

where f_0 is the form factor, and f_1 and f_2 are the so-called the dispersion corrections. Using this model, the differential scattering cross-section can be rewritten

$$\left(\frac{d\sigma}{d\Omega}\right) = r_e^2 \cdot |f(\mathbf{q},E)|^2 \cdot P^2. \tag{2.4}$$

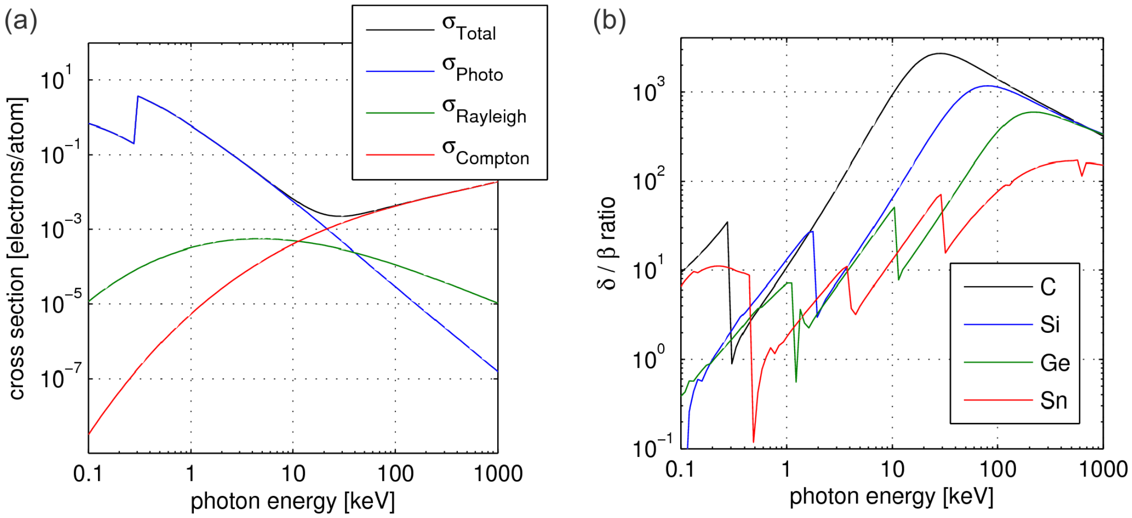

Fig. 3: *(a) The different interaction cross-sections for x-rays in carbon and (b) ratio of refraction and attenuation decrements δ/β as a function of photon energy for x-rays in carbon, silicon, germanium and tin.*

Integrating over the solid angle yields the scattering cross-section σ. The total cross-section σ_{Total} can be split into several distinct physical effects that contribute to the interaction of x-rays with matter

$$\sigma_{\text{Total}} = \sigma_{\text{Rayleigh}} + \sigma_{\text{Photo}} + \sigma_{\text{Compton}}, \tag{2.5}$$

where σ_{Rayleigh}, σ_{Photo} and σ_{Compton} are the Rayleigh-, the photoelectric- and the Compton cross-sections, respectively. Exemplarily, in Fig. 3 (a), the different cross-sections for the material carbon as a function of energy can be seen. While the Rayleigh and photoelectric cross-sections can be derived using the semi-classical picture given by Eq. (2.4), a thorough quantum-mechanical derivation is needed for the derivation of the Compton cross-section.
Rayleigh scattering is a coherent and elastic scattering. The photon is scattered elastically without change in its energy but with a phase shift relative to the incoming photon. This effect is the physical basis for phase-contrast imaging, while its contribution to the attenuation of x-rays is negligible. For the energies of interest, the photo effect is the main contribution to the attenuation of x-rays. The contribution of Compton scattering to the beam attenuation rises with increasing energy and atomic number. Above the K-edges, the cross-section for photoelectric absorption can be approximated by [Evans55]

$$\sigma_{\text{Photo}} \approx C_1 \cdot \frac{Z^{C_2}}{E^3}, \tag{2.6}$$

where C_1 only depends on natural constants and $C_2 \approx 4$. An in-depth analysis of the underlying physics reveals that the exponent C_2 is not constant, but a slowly varying function of the atomic number and the energy $C_2 = C_2(Z,E)$ [Evans55]. In the following, we will therefore keep the exponent as an undetermined variable. For photon energies below the K-edge of the material, the cross-section does not depend on the atomic number Z, but instead on the number of shell electrons with binding energies below the photon energy. The Compton cross-section can be written

$$\sigma_{\text{Compton}}(Z,E) = Z \cdot \sigma_{KN}(E), \tag{2.7}$$

where $\sigma_{KN}(E)$ is the relativistic Klein-Nishina cross-section for the scattering of a photon on a single free electron [Evans55]. By multiplying the Klein-Nishina cross-section with the number of electrons per atom interacting with the given x-ray photon, the Compton cross-section is obtained.

While microscopic interactions of x-ray photons with matter are best described in a particle picture, in optics, it is more common to use a semi-classical wave or ray formalism. The interaction and propagation of an x-ray wave can be described phenomenologically by the parameter of the complex **index of refraction** n. It is defined as the ratio of the wavenumber in the material relative to the wavenumber in vacuum. The complex index of refraction n can be related to the atomic scattering factor $f(0,\omega)$ in the forward scattering direction by [Booklet09]

$$n = \frac{k'}{k} = 1 - \frac{r_e}{2\pi} \cdot \lambda^2 \cdot \rho_N \cdot f(0,E), \tag{2.8}$$

where r_e is the classic electron radius, λ the wavelength, and ρ_N the particle number density. The number of atoms per unit volume ρ_N depends on the material under investigation and may be rewritten

$$\rho_N = \frac{\rho_M N_A}{M}, \tag{2.9}$$

where ρ_M is the mass density, N_A Avogadro's number and M the molar mass. By combining Eq. (2.8) with the definition of the scattering factor as given by Eq. (2.3), the index of refraction can be written

$$n(\mathbf{r}) = 1 - \delta(\mathbf{r}) + i\beta(\mathbf{r}), \tag{2.10}$$

where

$$\delta = \frac{r_e}{2\pi} \cdot \lambda^2 \cdot \rho_N \cdot (f_0 + f_1) \tag{2.11}$$

is the **refraction decrement** and

$$\beta = \frac{r_e}{2\pi} \cdot \lambda^2 \cdot \rho_N \cdot f_2 \tag{2.12}$$

the **attenuation decrement**. The real part of the refractive index is written as a decrement, since the refractive index at x-ray energies differs only slightly from unity. The decrement of refraction is by orders of magnitude bigger than the decrement of attenuation, as shown in Fig. 3 (b).

For objects which are thin, the propagation of x-rays within matter can be considered along straight lines. In that case the object can be projected onto a single plane. The propagation of a monochromatic plane wave $u(\mathbf{r}) = u_0(x,y) \cdot \exp(ik'z)$ propagating in z direction through a sample with an index of refraction n can in this approximation be written

$$\begin{aligned} u(\mathbf{r}) &= u_0 \cdot \exp\left(i \int k \cdot n(\mathbf{r}) \cdot dz\right) \\ &= u_0 \cdot \underbrace{\exp\left(ik \int dz\right)}_{\text{propagation}} \cdot \underbrace{\exp\left(-ik \int \delta(\mathbf{r}) dz\right)}_{\text{phase shift}} \cdot \underbrace{\exp\left(-k \int \beta(\mathbf{r}) dz\right)}_{\text{attenuation}}. \end{aligned} \tag{2.13}$$

Thus, the real part of the refractive index $1-\delta$ imposes a phase shift onto the wavefront, while the imaginary part leads to an exponential attenuation of the amplitude of the wave. This basic interaction principle is illustrated in Fig. 4. The total phase shift caused by the sample can be written

$$\Delta\Phi(x,y) = k \int_{-\infty}^{\infty} (1 - \delta(\mathbf{r}))\, dz = \Delta\Phi_0 - k \int_{-\infty}^{\infty} \delta(\mathbf{r}) dz, \tag{2.14}$$

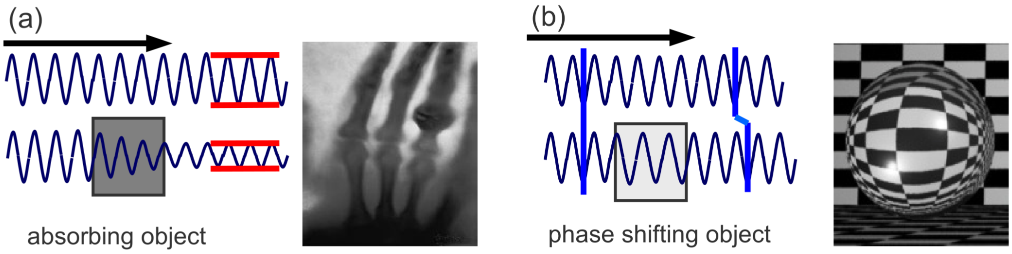

Fig. 4: *(a) An absorbing object reduces the amplitude of a wave, while (b) a refracting object shifts the phase of a wave traversing the sample. The images show the first X-ray radiography, made by W.C. Röntgen 1895 [Röntgen96], and a refracting sphere in visible light. While the attenuation itself creates an intensity modulation, a purely refracting object can be made visible using the distortion of a reference intensity pattern as given by the checkerboard in b).*

where $\Delta\Phi_0$ is the phase shift that would be observed in the absence of a sample due to propagation. Since the object was approximated as thin, the integration is performed along straight lines in z direction.

For the refraction and attenuation decrements as used in x-ray science, explicit dependencies on material composition and energy can be derived. The refraction decrement δ is equal to the real part of the index of refraction, and thus depends on the form factor f_0 and the dispersion correction f_1. The atomic form factor f_0 can be generally given by

$$f_0(\mathbf{q}) = \int_{-\infty}^{+\infty} \rho(\mathbf{r}) \cdot e^{i\mathbf{q}\mathbf{r}} d\mathbf{r}, \tag{2.15}$$

where $\rho(\mathbf{r})$ is the charge distribution around the atom. Scattering in the forward direction $(\mathbf{q} = 0)$ is dominant, so that the form factor approaches [Booklet09]

$$f_0(0) = \int_{-\infty}^{+\infty} \rho(\mathbf{r}) \cdot d\mathbf{r} \approx Z. \tag{2.16}$$

The dispersion correction f_1 is approximately zero, except near absorption edges, where it shows a resonant character. Therefore, for energies far above the K-edges of the material, the refraction decrement defined in Eq. (2.11) depends on the electron density $\rho_Z = \rho_N \cdot Z$ and the energy:

$$\delta = \frac{r_e}{2\pi} \cdot \lambda^2 \cdot \rho_Z. \tag{2.17}$$

In classical attenuation imaging, usually the **linear attenuation coefficient** $\mu(\mathbf{r})$ instead of the attenuation decrement $\beta(\mathbf{r})$ is used to characterize the attenuation of x-rays. Using Eq. (2.12), the linear attenuation coefficient as a function of the atomic scattering factor can thus be equivalently given by

$$\mu := 2 \cdot k \cdot \beta = 2 \cdot r_e \cdot \lambda \cdot \rho_N \cdot f_2. \tag{2.18}$$

Experimentally, the total interaction cross-section σ_{Total} per atom is more readily measurable than the atomic scattering factor. It is by definition connected to the linear attenuation coefficient by

$$\mu = \rho_N \cdot \sigma_{\text{Total}} = \frac{\rho_M N_A}{M} \cdot \sigma_{\text{Total}}. \tag{2.19}$$

Combining Eqs. (2.5), (2.6) and (2.7), the linear attenuation coefficient can be related to the sample material and the energy of the x-rays by

$$\mu = \rho_N \cdot \left(C_1 \cdot \frac{Z^{C_2}}{E^3} + Z \cdot \sigma_{KN} \right). \tag{2.20}$$

Usually, the materials under investigation are not pure elements, but are composites of different elements and compounds. In this case, measurements will yield an effective index of refraction, averaged over the composites of the material

$$n_{\text{eff}} = 1 - \frac{r_e}{2\pi} \lambda^2 \sum_i \rho_{N,i} f_i(0), \tag{2.21}$$

where $\rho_{N,i}$ is the atomic density of element i and $f_i(0)$ its scattering factor in forward direction. Following Eq. (2.10), the effective refraction and attenuation decrements can be calculated from its constituents by

$$\delta_{\text{eff}} = \frac{r_e}{2\pi} \cdot \lambda^2 \cdot \sum_i \rho_{N,i} \cdot Z_i, \tag{2.22}$$

and

$$\beta_{\text{eff}} = \frac{r_e}{2\pi} \cdot \lambda^2 \cdot \sum_i \rho_{N,i} \cdot f_{2,i}. \tag{2.23}$$

Following Eq. (2.19), the linear attenuation coefficient is usually used instead of the attenuation decrement

$$\mu_{\text{eff}} = \sum_i \rho_{N,i} \cdot \sigma_{\text{Total},i} = \rho_{\text{eff}} \cdot \sum_i w_i \left(\frac{\mu}{\rho} \right)_i, \tag{2.24}$$

where $\sigma_{\text{Total},i}$ is the total scattering cross-section, $(\mu/\rho)_i$ is the mass attenuation coefficient, w_i the mass fraction of material i and ρ_{eff} the density of the compound material.

In an experiment with a detector directly behind the sample, only the intensity and thus the squared magnitude of the wave function is measurable

$$\begin{aligned} I(x,y) &= |u_1(x,y)|^2 \\ &= u_0(x,y)^2 \cdot e^{-2k\int \beta(\mathbf{r})dz} \\ &= I_0(x,y) \cdot e^{-\int \mu(\mathbf{r})dz}. \end{aligned} \tag{2.25}$$

Eq. (2.25) is known as **Lambert-Beer's law** of attenuation. From the measured intensity relative to a reference intensity $I_0 = |u_0|^2$, the projected linear attenuation coefficient $\int \mu(\mathbf{r}) \cdot dz$ can be reconstructed. This is the basic principle of classical attenuation radiography. Nevertheless, in the measurement, all phase information is lost and not directly obtainable from raw intensity data. Over the time, various methods have been developed to reconstruct the phase information of the transmitted sample from a measured intensity modulation, as introduced in section 1.1. The grating-based differential phase-contrast imaging technique, which is evaluated in this thesis, depends on deflections of an x-ray and thus offers access to the gradient of the phase of the wavefront.

2.2 Differential phase-contrast imaging

In order to describe the basic principle of differential phase-contrast imaging, first, we will formulate the propagation of x-rays in terms of ray optics, following Ref. [Born99]. The transition from wave optics to ray optics can be described by the concept of the **eikonal**. The eikonal S, or optical path length, is defined by $S(\mathbf{r}) := 1/k \cdot \Phi(\mathbf{r})$. By solving the Helmholtz equation, the eikonal can be shown to satisfy the eikonal differential equation

$$(\nabla S(\mathbf{r}))^2 = n(\mathbf{r})^2, \tag{2.26}$$

where $n(\mathbf{r})$ is the complex refractive index. Rays can now be defined as the orthogonal trajectories to the geometrical wavefronts $S = \text{const}$. In isotropic media, the direction of such a ray can be shown to coincide with the direction of the energy flux of the wave, i.e. with the direction of the time-averaged Poynting vector. If $\mathbf{r}$ is the position vector of a point on a ray, the ray may be analytically described by a curve $\mathbf{r}(s)$, parametrized by its path length s from any given starting point $\mathbf{r}(s_0)$ on the ray. The direction of the ray, given by the unit tangent vector $\mathbf{t} := d\mathbf{r}/ds$, thus coincides with the normal of the wavefront

$$\frac{d\mathbf{r}}{ds} := \frac{\nabla S}{|\nabla S|}. \tag{2.27}$$

Differentiating Eq. (2.27) with respect to s yields a differential equation for the ray trajectory $\mathbf{r}(s)$ in terms of the refractive index distribution $n(\mathbf{r})$

$$\frac{d}{ds}\left(n(\mathbf{r})\frac{d\mathbf{r}}{ds}\right) = \nabla n(\mathbf{r}). \tag{2.28}$$

For a homogeneous material, i.e. $n = |\nabla S| = const.$, one obtains $d^2\mathbf{r}/ds^2 = d\mathbf{t}/ds = 0$, so that the rays are straight lines in this case. By applying Stokes' theorem to Eq. (2.28), Snell's law of refraction can be obtained

$$n_2(\mathbf{n}_{12} \times \mathbf{t}_2) = n_2(\mathbf{n}_{12} \times \mathbf{t}_1), \tag{2.29}$$

with n_1 and n_2 the refractive indices of two materials on both sides of the surface, $\mathbf{n}_{12}$ the normal to the surface, and $\mathbf{t}_1$ and $\mathbf{t}_2$ the directions of the incoming and outgoing rays, respectively. From Eqs. (2.27) and (2.29), we can see that a ray will be deflected by an angle α if a sample in the beam path causes a distortion of the wavefront. In the thin object approximation and using the definition of the eikonal, the deflection angle can be related to the phase of the wavefront Φ and thus the distribution of the refractive decrement $\delta(\mathbf{r})$ by

$$\begin{aligned} \sin(\alpha) &= \nabla\left(\frac{1}{k}\cdot\Phi\right) \\ &= \nabla\int_0^{L(\mathbf{x,y})} \delta(\mathbf{r})\cdot ds, \end{aligned} \tag{2.30}$$

where the integration is performed along the path of a ray and $L(\mathbf{x,y})$ is the sample thickness along that ray. The basic idea of differential x-ray phase-contrast imaging is to use the deflections of the x-rays for contrast generation, thus providing access to the gradient of the phase of the wavefront.

Applying the chain rule in Eq. (2.30), the differentiation can be split into two separate terms, first the lateral change of sample thickness ∇L, and second the change in material composition $\nabla\delta$

$$\sin(\alpha) = \delta\cdot\nabla L(x,y) + L(x,y)\cdot\int_{-\infty}^{\infty}\nabla\delta(\mathbf{r})\cdot dz. \tag{2.31}$$

Assuming a homogeneous sample with a thickness gradient equal to unity, i.e. $\nabla\delta = 0$ and $\nabla L = 1$, yields a deflection angle equal to $\sin(\alpha) \approx \delta$ rad. For x-ray photons in the energy range between $10-100$ keV, the refraction decrement is of the order $10^{-8} \leq \delta \leq 10^{-6}$ [NIST95]. We can thus conclude that the angular deflections will be small in most experimental situations. In this case, we may apply the **paraxial approximation**, greatly simplifying further analysis by the use of the linearizations

$$\sin\alpha \approx \alpha, \quad \tan\alpha \approx \alpha \quad \text{and} \quad \cos\alpha \approx 1. \tag{2.32}$$

To quantify the deflections caused by a sample, the deflected beam as obtained in a measurement has to be compared with an undeflected beam. For this purpose, a measure for referencing the deflections caused by the sample has to be introduced.

2.3 Spatial reference - the beam-splitter grating

In order to make the deflections of a purely refracting phase object visible, a reference intensity modulation is used. This principle is illustrated in Fig. 4 (b) by the distortion of a checkerboard intensity modulation created by a spherical phase object. The period of this reference pattern has to be at a similar length scale as lateral beam shifts caused by the sample, if the deflected reference pattern shall be discriminated from the undeflected pattern with acceptable accuracy. Assuming a deflection by an angle α, the reference pattern will be laterally displaced by

$$x_d = \alpha \cdot d \tag{2.33}$$

behind a propagation distance d. To give an example, an x-ray beam that is deflected by an angle of $\alpha = 10^{-6}$ rad will shift the reference pattern by only $x_d = 1$ μm at a propagation distance of $d = 1$ m. The period of the reference intensity modulation therefore has to be in the micron range.

The simplest way to create a periodic intensity modulation is by the use of optical gratings. The manufacturing of optical gratings at μm-length scale is challenging, yet feasible using state-of-the-art microfabrication techniques. Available approaches combine photolithography, anisotropic wet etching, deep silicon etching and/or galvanization [David07, Reznikova08]. The use of the grating as a beam-splitter can be based on the attenuation or the phase shift of the grating material. For attenuation gratings, high-Z metals like lead or gold are utilized, while phase-shifting gratings are made of various low-Z materials that exhibit low attenuation and high phase shifts, like silicon or nickel. Available grating structures can be classified into three groups: easiest in fabrication are **binary gratings**, consisting of rectangular bars with equal height. In the following, the ratio between the relative height of the structure and the period will be denoted the **aspect ratio**, while the ratio between the slit width between two bars and the period is named the **duty cycle** τ of the binary grating. Please note that by this definition, for ideal attenuation gratings, the numerical value of the duty cycle is also equal to the transmission of the grating. For **non-binary gratings**, a vast number of different gratings are conceivable. Non-binary gratings can be considered a multilayer superposition of binary gratings. Due to the difficulties in fabrication of micron- and sub-micron-sized structures, non-binary gratings have not found application so far. For a detailed account the reader is referred to Ref. [Zhou94]. Gratings using **non-rectangular grating** structures, like gratings with a sinusoidal, triangular, trapezoidal or parabolic profile, have not been widely used in x-ray phase-contrast imaging so far. In the following, the grating that creates the reference intensity modulation will be denoted the **beam-splitter grating $\mathbf{G}_1$**, with a grating period of p_1.

While two-dimensional gratings have recently been considered in Ref. [Zanette10, Wen08], usually and throughout this thesis only one-dimensional slit-gratings are considered in grating-based imaging. The orientation of the bars of a one-dimensional grating can be used for the definition of a coordinate system: In the following, without loss of generality, we will define the orientation of the grating structures to be parallel to the y-axis. As the deflections are measured relative to the intensity modulation caused by the grating structure, we have to apply the substitution $\nabla\Phi \rightarrow \partial\Phi/\partial x$, loosing the information of the gradient along the y-axis. It should be noted that in principle, the full gradient of the phase of the wavefront can be reconstructed by performing a separate, second measurement with the grating structures rotated by 90°, as implemented for example in Ref. [Kottler07]. This allows the reconstruction of the two-dimensional phase shift, yet at the cost of a doubled measuring effort.

For the creation of the reference pattern, usually, but not necessarily, the Talbot self-imaging effect is utilized [Talbot36, Winthorp65]: If a periodic structure with period p_1 is illuminated by light of wavelength λ, a perfect image of the grating will be visible at the Talbot-distance d_T downstream of the grating, given by

$$d_T = \frac{2p_1^2}{\lambda}. \tag{2.34}$$

This effect is derived from scalar diffraction theory in appendix C. The use of the Talbot effect offers the advantage of making a well defined intensity modulation available at the Talbot distance d_T. To give a numerical example, at 40 keV photon energy, for a grating with a period of $p_1 = 5\ \mu$m, the Talbot distance is equal to $d_T \approx 1.6$ m, while the distance is $d_T \approx 1600$ km for a grating with a macroscopic period of $p = 5$ mm. Thus, the grating period is restricted to a micron-sized length scale not only to maximize the signal strength, but due to limitations of the setup dimensions as well.

The first beam-splitter gratings that have been used were attenuation gratings. Nevertheless, since attenuation gratings inevitably reduce the number of available photons downstream of the grating, the use of phase gratings for the creation of an interference pattern was conceived [Guigay71, Lohmann88, Arrizon94, Suleski97]. The phase modulation imposed on a wavefront by certain phase gratings is transformed into an intensity modulation with a period p_T after a fraction of the Talbot distance, leading to the **fractional Talbot effect**. For different grating types, the **fractional Talbot distance** d_m downstream of the grating, i.e. the distance with maximum intensity modulation, can in general be written

$$d_m = mn \cdot d_T, \tag{2.35}$$

where $m = 0, 1, 2, ...$ is the **fractional Talbot order**, and $n \in [0, 1]$ depends on the type of the grating. The parameter n can be understood as the ratio between the lowest fractional Talbot order d_1 and the full Talbot length d_T. Exemplary interference patterns for an attenuation grating and two binary phase gratings with $\pi/2$ and π phase shift at the bars, respectively, can be seen in Fig. 5 (a)-(c). Each grating creates an intensity modulation downstream of the grating, only with maximum intensity modulation at different fractional Talbot distances d_m, in the examples $d_1 = d_T/2$ for the attenuation grating, $d_1 = d_T/4$ for the $\pi/2$-shifting phase grating and $d_1 = d_T/16$ for the π-shifting phase grating. For the phase gratings, maximum intensity modulation occurs at odd fractional Talbot orders, while at even orders, the phase profile of the grating is reconstructed and no intensity modulation is observed. For the π-shifting phase grating, the interference pattern additionally exhibits half the period of the grating. Phase-gratings with duty cycles of $1/3$ and $2/3$ will be discussed in section 8.

The differential phase shift of the wavefront caused by a sample in the beam path will create a lateral displacement of the reference intensity pattern. Suppose that one period of the intensity

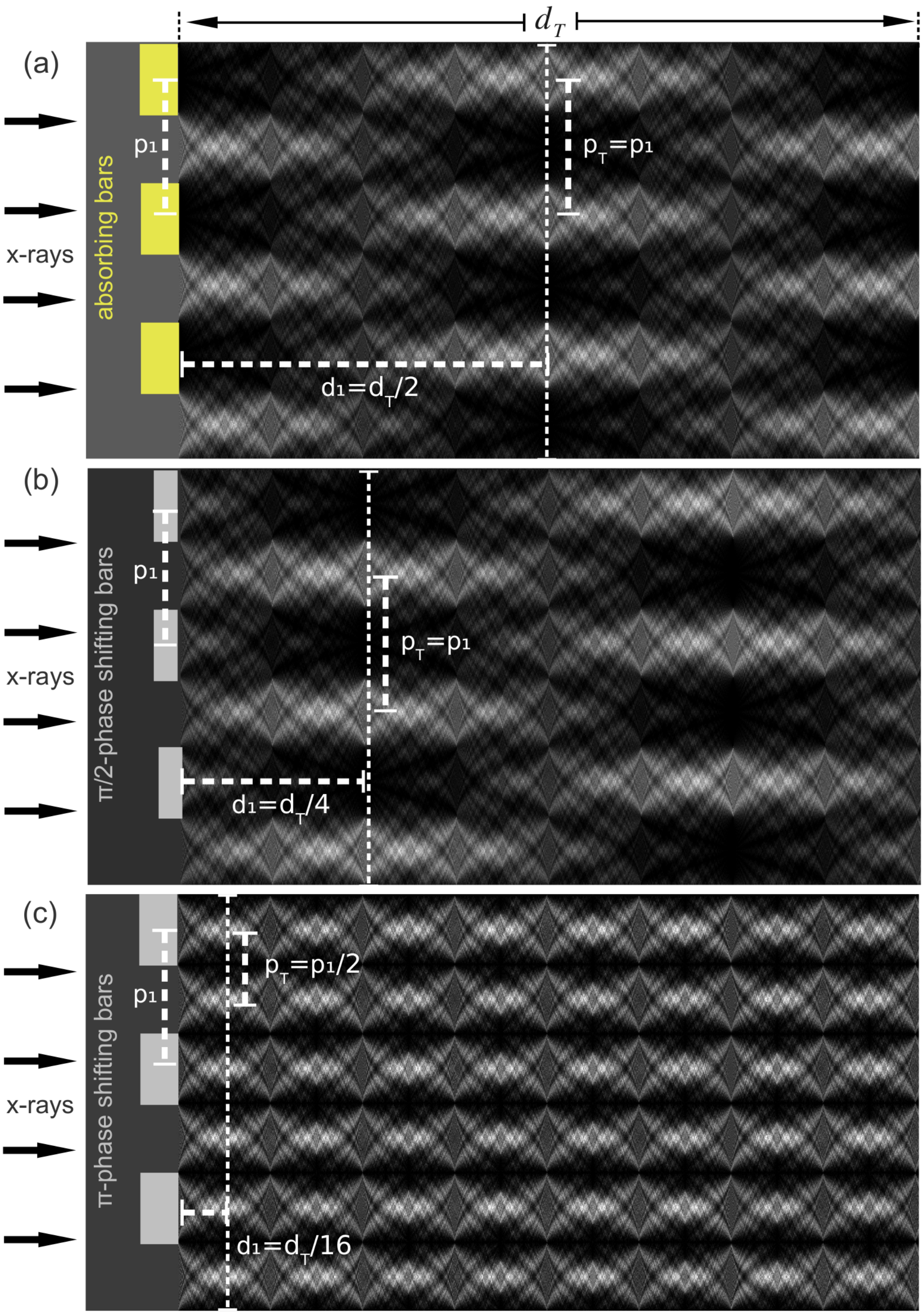

Fig. 5: *Monochromatic intensity patters downstream of (a) an attenuation grating, (b) a phase grating with* $\pi/2$ *phase shift at the bars and (c) a phase grating with* π *phase shift at the bars. The propagation distance shown in the figure corresponds to the full Talbot distance* d_T. *The first fractional Talbot distance* d_1 *and the period of the interference pattern* p_T *at that distance is marked for each grating (dashed white lines). For the phase gratings, maximum intensity modulation occurs at odd fractional Talbot orders, while at even orders, the phase profile of the grating is reconstructed and no intensity modulation is visible.*

modulation can be laterally described by a function $T_1(x)$. The shift of the intensity pattern by a distance of x_d can be expressed analytically by a convolution with a shifted Dirac comb

$$S(x) = T_1(x) \otimes \Delta_{p_T}(x - x_d), \tag{2.36}$$

where $S(x)$ is the lateral intensity signal in the detection plane and $\Delta_{p_T}(x) = \sum_{m=-\infty}^{\infty} \delta\left(x - mp_T\right)$ is a Dirac comb, describing an infinitely extended intensity pattern with period p_T

$$p_T = \frac{p_1}{\eta}, \tag{2.37}$$

where $\eta = 1$ for an attenuation and $\pi/2$-shifting phase grating and $\eta = 2$ for a π-shifting phase grating. A finite beam-splitter grating and intensity pattern can easily be accounted for by multiplying Eq. (2.36) with an appropriate window function. In Fourier domain, the convolution becomes a multiplication and the shifted intensity pattern can be described by

$$s(f) = t_1(f) \cdot \frac{1}{p_T} \cdot \Delta_{\frac{1}{p_T}}(f) \cdot \exp\left(2\pi i x_d f\right), \tag{2.38}$$

where $s(f)$ and $t_1(f)$ are the Fourier spectra of $S(x)$ and $T_1(x)$, respectively, $1/p_T \Delta_{1/p_T}(f) = \mathscr{F}\{\Delta_{p_T}(x)\}$ and $\exp\left(2\pi i x_d f\right)$ is a phase factor resulting from the shift x_d of the intensity modulation. If the signal $S(x)$ in the plane of detection is expressed by its Fourier spectrum $s(f)$, one obtains

$$\begin{aligned} S(x) &= \int_{-\infty}^{\infty} s(f) \cdot \exp\left(2\pi i x f\right) \cdot df \\ &= \frac{1}{p_T} \cdot \sum_{m=-\infty}^{\infty} t_1\left(\frac{m}{p_T}\right) \cdot \exp\left(2\pi i x_d \frac{m}{p_T}\right) \cdot \exp\left(2\pi i x \frac{m}{p_T}\right). \end{aligned} \tag{2.39}$$

As the periodic intensity pattern contains only discrete spatial frequencies $f_m = m/p_T$, we can express the shift of the interference pattern caused by the sample by a phase factor $\Delta\varphi$

$$\Delta\varphi := 2\pi \frac{x_d}{p_T}, \tag{2.40}$$

so that the lateral intensity signal in the plane of detection is

$$S(x) = \frac{1}{p_T} \cdot \sum_{m=-\infty}^{\infty} t_1\left(\frac{m}{p_T}\right) \cdot \exp\left(im\Delta\varphi\right) \cdot \exp\left(2\pi i x \frac{m}{p_T}\right). \tag{2.41}$$

Combining Eq. (2.40) with Eqs. (2.33) and (2.30), the phase shift $\Delta\varphi$ can be written

$$\begin{aligned} \Delta\varphi(x,y) &= \frac{d \cdot \lambda}{p_T} \cdot \frac{\partial}{\partial x} \int_{-\infty}^{\infty} \Phi(\mathbf{r}) \cdot dz \\ &= 2\pi \frac{d}{p_T} \cdot \frac{\partial}{\partial x} \int_{-\infty}^{\infty} \delta(\mathbf{r}) \cdot dz. \end{aligned} \tag{2.42}$$

Thus, a connection between the measurable phase shift of the reference pattern $\Delta\varphi$, the phase shift of the wavefront $\Delta\Phi(\mathbf{r})$ and the refractive decrement $\delta(\mathbf{r})$ are obtained.

2.4 Spatial resolution - the analyzer grating

For the analysis of the phase shift $\Delta\varphi$ of the interference pattern as described by Eq. (2.42), the interference pattern first has to be recorded by a detector system. Digital solid state detectors have largely replaced analog detection systems based on photographic film. The resolution of digital systems is ultimately limited by the pixel size of the detector array. The use of a detector with a certain pixel pitch can be modeled analytically using the point spread function (PSF) of the detector, as derived in appendix A. If one period of the intensity modulation is described by a function $T_1(x)$, the measured signal strength $S(x)$ in each pixel of the detector is given by

$$S(x) = T_1(x) \otimes \Delta_{p_T}(x - x_d) \otimes P(x), \tag{2.43}$$

where $P(x)$ is the PSF of the detector. For the sake of simplicity, we will assume that the detector has an ideal, box-like modulation transfer function (MTF) with maximum spatial frequency $f_{\max}$ given by the inverse of the pixel pitch a, i.e. $f_{\max} = 1/a$. The signal strength (2.43) is given in Fourier domain by

$$s(f) = t_1(f) \cdot \frac{1}{p_T} \cdot \Delta_{\frac{1}{p_T}}(f) \cdot \exp(2\pi i x_d f) \cdot \frac{1}{f_{\max}} \mathrm{rect}(f/f_{\max}), \tag{2.44}$$

where

$$\mathrm{rect}(f/f_{\max}) := \begin{cases} 1 & \text{if } |f| < f_{\max} \\ \frac{1}{2} & \text{if } |f| = f_{\max} \\ 0 & \text{if } |f| > f_{\max} \end{cases} \tag{2.45}$$

is a rectangle function describing the MTF of the detector. If $f_{\max} = 1/a < 1/p_T$, the signal in each pixel can be given by

$$\begin{aligned} S(x) &= \frac{a}{p_T} \cdot \sum_{m=-\infty}^{\infty} t_1\left(\frac{m}{p_T}\right) \cdot \exp(im\Delta\varphi) \cdot \underbrace{\mathrm{rect}\left(a \cdot \frac{m}{p_T}\right)}_{=0 \quad \forall m \neq 0} \cdot \exp\left(2\pi i x \frac{m}{p_T}\right), \\ &= \frac{a}{p_T} \cdot t_1(0), \end{aligned} \tag{2.46}$$

which is equal to the intensity average of the intensity modulation over the width of one pixel. The detector thus acts as a low pass filter, eliminating all spatial frequencies higher than the inverse pixel pitch $f_{max} = 1/a$. Only the average of the intensity oscillation is measured if the pixel size is bigger than the period of the interference pattern. In state-of-the-art medical CT scanners, the pixel pitch is in the range 0.2 - 2 mm (Siemens Somatom Emotion, pixel pitch 600 μm, [Siemens11]), while typical detector pixel sizes for application in nondestructive testing are in the range of $50 - 250$ μm (Hamamatsu C7943, pixel pitch 100 μm, [Ham11]). Effective pixel sizes in the sub-micron range can be achieved by the conversion of x-rays to visible light in combination with magnifying optics, however, these techniques are mostly used in high-end applications at large research institutions. In conclusion, for commonly used detector systems in the most important x-ray applications, the pixel pitch is too crude to directly resolve the interference pattern and analyze the deflections caused by the sample in the beam path. Increasing the pitch of the gratings to a size sufficiently large to be resolved by a given x-ray detector comes at the cost of signal strength and thus signal-to-noise ratio, as will be highlighted in section 3.1.2. In this case, a direct Fourier approach to the analysis of the interference fringe pattern can be applied, as presented in Refs. [Wen08, Bennet10].

To overcome this problem in grating-based imaging, usually a fringe scanning approach is adopted for the analysis of the interference pattern. In this approach, an additional absorbing **analyzer grating G$_2$** is placed into the beam path downstream of the beam-splitter grating. The superposition of the intensity pattern with the grating profile creates Moiré-fringes, which exhibit a lower spatial frequency than the interference pattern itself and that can thus be measured using a detector with large pixel sizes. If an analyzer grating is placed into the beam path, the intensity at the plane of detection is given by the multiplication of the profile of the intensity modulation $T_1(x)$ at that distance with the intensity transmission function of the analyzer grating $T_2(x)$

$$S(x,x_r) = [(T_1(x) \otimes \Delta_{p_T}(x-x_d)) \cdot (T_2(x) \otimes \Delta_{p_2}(x-x_r))] \otimes P(x), \tag{2.47}$$

where x_r is the relative displacement between interference pattern and grating G$_2$. Ideally, the analyzer grating is placed at a distance from the beam-splitter grating which shows the highest lateral intensity modulation, with a period chosen equal to the period of the intensity modulation p_T at that distance

$$p_2 = p_T. \tag{2.48}$$

As the periods are chosen equal at the plane of detection, we will drop the indices in the following. With the G$_2$ in place, an analysis similar to the one leading to Eq. (2.46) now yields

$$\begin{aligned} S(x,x_r) &= \frac{a}{p^2}\sum_m\sum_n t_1\left(\frac{m}{p}\right)\cdot\exp\left(2\pi i x_d\frac{m}{p}\right)\cdot t_2\left(\frac{n}{p}\right)\cdot\exp\left(2\pi i x_r\frac{n}{p}\right) \\ &\quad \underbrace{\cdot\,\mathrm{rect}\left(a\cdot\frac{m+n}{p}\right)}_{=0\quad\forall m\neq -n}\cdot\exp\left(2\pi i x\left(\frac{m+n}{p}\right)\right) \\ &= \frac{a}{p^2}\sum_{n=-\infty}^{+\infty} t_1\left(\frac{-n}{p}\right)\cdot t_2\left(\frac{n}{p}\right)\cdot\exp\left(in\left(\varphi_r-\Delta\varphi\right)\right), \end{aligned} \tag{2.49}$$

where we have introduced the phase $\varphi_r = 2\pi x_r/p$. In words, the intensity measured at the detector will be given by the spectra of the two transmission functions, shifted proportional to the relative position x_r and the shift $\Delta\varphi$ caused by the sample. If the two gratings are chosen as binary gratings with a duty cycle of $\tau = 1/2$, a relative movement of the gratings will create an intensity oscillation which follows a triangular profile as a function of x_r. In the following, we will assume that a continuous scan of the relative position x_r was performed, which corresponds to a convolution of the intensity pattern T_1 with the intensity transmission function T_2 of the analyzer grating.

2.5 Spatial coherence - the source grating

So far, we have discussed DPC imaging using plane waves for illumination. Nevertheless, in compact laboratory setups, the lateral intensity profile of the x-ray source has to be included into the contrast generation. The lateral width of a focus of a laboratory x-ray tube ranges from several hundred nanometers for nanofocus tubes, up to a few millimeters for high-powered anodes. The impact of an extended source profile onto the interference pattern can be understood by considering each point in the profile as an independent point source. Each point in the source profile will therefore create an independent image of the beam-splitter grating, blurring the interference pattern at the plane of detection. If the lateral source width is given by

w, the projected source width q can be calculated using the source-to-beam-splitter distance l and the beam-splitter-to-analyzer distance d by

$$q = \frac{d}{l} \cdot w, \tag{2.50}$$

as indicated in Fig. 6 (a). Note, that the plane wave case is included in this definition by the limit $l \to \infty$. Analytically, the influence of an extended source can be described by a convolution of the lateral intensity profile of the interference pattern $T_1(x)$ with the projection of the lateral source distributions at the plane of the analyzer grating $T_0(x)$

$$S(x) = T_0(x) \otimes T_1(x) \otimes \Delta_p(x - x_d) \otimes T_2(x) \otimes \Delta_p(x - x_r) \otimes P(x). \tag{2.51}$$

If we express the intensity pattern by its spatial frequency spectrum, Eq. (2.51) can be written

$$S(x) \;=\; \frac{a}{p^2} \sum_{n=-\infty}^{\infty} t_0\left(\frac{n}{p}\right) \cdot t_1\left(\frac{n}{p}\right) \cdot t_2\left(\frac{n}{p}\right) \cdot \exp\left(2\pi i x \frac{n}{p} + in\left(\varphi_r - \Delta\varphi\right)\right). \tag{2.52}$$

The use of the relation $\exp(-ix) + \exp(ix) = 2 \cdot \cos(x)$, together with the assumption of symmetric intensity profiles, allows the summation of the negative and positive spatial frequencies. We obtain

$$S(x) = \frac{a}{p^2} \cdot t_0(0) \cdot t_1(0) \cdot t_2(0) \cdot \left[1 + \sum_{n=1}^{\infty} v_n \cos\left(2\pi x \frac{n}{p} + n(\varphi_r - \Delta\varphi)\right)\right], \tag{2.53}$$

where the amplitudes v_n are given by

$$v_n = 2 \cdot t_0\left(\frac{n}{p}\right) \cdot t_1\left(\frac{n}{p}\right) \cdot t_2\left(\frac{n}{p}\right). \tag{2.54}$$

Eqs. (2.53) and (2.54) describe the intensity oscillation in each pixel by its Fourier decomposition. These formulas will be the basis of the analytical description of the influence of grating errors and duty cycle changes in sections 7 and 8.

To evaluate the influence of an extended source on the interference pattern and to quantify the quality of the intensity oscillation, the well known concept of **interferometric visibility** is used. This parameter can be related to the complex degree of coherence, as shown in appendix D. The visibility v can in general be calculated from the maximum and minimum intensity $I_{\max}$ and $I_{\min}$ of an intensity modulation by

$$v := \frac{I_{\max} - I_{\min}}{I_{\max} + I_{\min}}. \tag{2.55}$$

For a binary beam-splitter and analyzer grating and $\varphi_r - \Delta\varphi = 0$, we may assume that $I_{\max} = S(x = 0)$ and $I_{\min} = S(x = p/2)$. Thus from Eq. (2.53), we obtain

$$v = \frac{\sum_{n=1}^{\infty} v_{2n-1}}{1 + \sum_{n=1}^{\infty} v_{2n}}. \tag{2.56}$$

If G_1 and G_2 are of binary type with duty cycles chosen equal to $\tau_1 = \tau_2 = 1/2$, we have $T_1(x) = T_2(x) = \mathrm{rect}(2x/p)$ and therefore $t_1(n/p) = t_2(n/p) = \mathrm{sinc}(n/2)$, where $\mathrm{sinc}(x) := \sin(\pi x)/(\pi x)$ is the normalized sinc function, the Fourier transform of the rectangle function. The amplitudes in Eq. (2.54) are then given by

$$v_n = 2 \cdot t_0\left(\frac{n}{p}\right) \cdot \mathrm{sinc}\left(\frac{n}{2}\right) \cdot \mathrm{sinc}\left(\frac{n}{2}\right). \tag{2.57}$$

This expression may be simplified by noting that

$$\operatorname{sinc}\left(\frac{n}{2}\right)=\begin{cases}0 & \text{if } n \text{ even}\\ \frac{2}{n\pi}\cdot(-1)^{\frac{n-1}{2}} & \text{if } n \text{ odd}\end{cases} \tag{2.58}$$

so that $v_{2n}=0$ for all $n\in\mathbb{N}$. Using Eqs. (2.54), (2.56) and (2.58), we arrive at

$$\begin{aligned} v &= \sum_{n=1}^{\infty} v_n \\ &= \frac{8}{\pi^2}\sum_{n=1}^{\infty}\cdot\frac{t_0\left(\frac{2n-1}{p}\right)}{(2n-1)^2}, \end{aligned} \tag{2.59}$$

where $t_0\left((2n-1)/p\right)$ is the Fourier transform of the projected source intensity distribution evaluated at spatial frequencies $(2n-1)/p$. For a laboratory x-ray tube, the lateral intensity distribution may be approximated by a Gaussian profile. This case was considered by Bech [Bech09]. Since a Gaussian-shaped intensity profile has a Gaussian shape in spatial frequency domain as well, the visibility is in this case given by

$$v=\frac{8}{\pi^2}\sum_{n=1}^{\infty}\frac{\exp\left(-2\pi^2\cdot(q/p)^2\cdot(2n-1)^2\right)}{(2n-1)^2}, \tag{2.60}$$

where the ratio q/p is the projected source width in multiples of the period of the interference pattern. The visibility and thus the modulation of the interference pattern decreases exponentially with growing source size. From Fig. 6 (b), it can be seen that the visibility decreases to nearly zero, if the width of the projected source is bigger than the period of the interference pattern, making phase-contrast imaging impossible. Thus, either the source has to be far away from the interferometer, which decreases the projected source size, or the focus of the tube has to be restricted to a few microns if the setup length is to be short. The restriction of the tube focus to widths of a few microns greatly limits the current and power of the x-ray tube and the achievable photon flux. Higher photon flux for a fixed anode voltage comes at the cost of higher current and thus larger focal size.

To overcome these restrictions and be able to use high-powered sources, an attenuating **source grating** G_0 is introduced. It splits the large focus of a high powered x-ray tube into an array of line sources, where each line source is thin enough to meet the lateral coherence requirements of the technique. Each line source will independently create an interference pattern downstream of the grating, which are superimposed at the plane of detection. If the period p_0 of the source grating G_0 is chosen equal to

$$p_0=\frac{l}{d}\cdot p_2, \tag{2.61}$$

where l is the inter-grating distance between G_0 and G_1 and d the inter-grating distance between G_1 and G_2, the images created by each line source overlap uniformly at the plane of detection. This principle is known as the **Lau effect** and is illustrated in Fig. 7 (a). If we assume that the source is described by a rectangular and binary source grating with a duty cycle τ_0, we obtain from Eq. (2.59)

$$v(\tau_0)=\frac{8}{\pi^2}\sum_{n=1}^{\infty}\frac{\operatorname{sinc}\left((2n-1)\cdot\tau_0\right)}{(2n-1)^2} \tag{2.62}$$

for the visibility as a function of the duty cycle of the source grating. The visibility as described by Eq. (2.62) together with the first and higher order Fourier expansion as a function of the

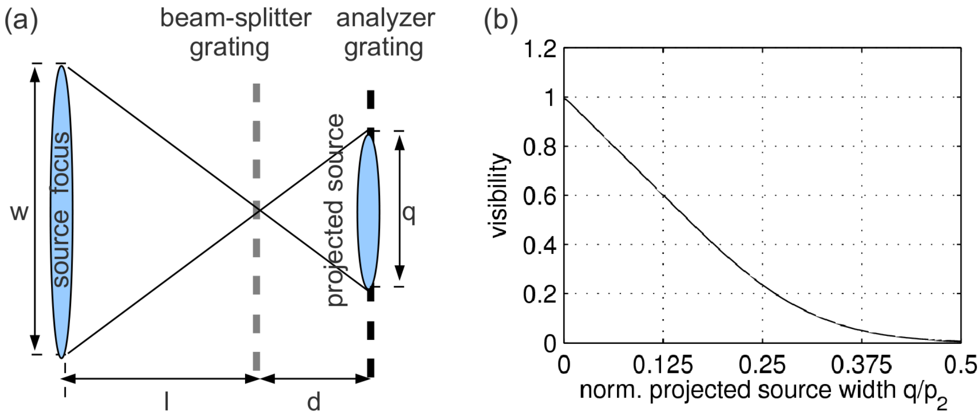

Fig. 6: *Illustration of the lateral coherence requirements of the technique: (a) An extended source will smear out the interference pattern, depending on the size of the projected source width q, which is given by the geometric relations of the interferometer. (b) The visibility as a function of the projected lateral source width, measured in multiples of the period of the interference pattern. The visibility decreases exponentially with the source size, being essentially zero for projected source sizes bigger than half the period of the interference pattern (after [Bech09]).*

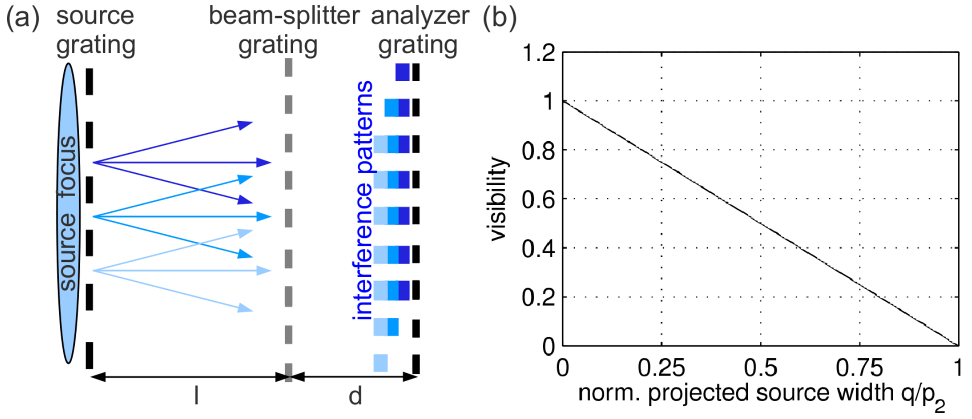

Fig. 7: *Illustration of the use of a source grating: (a) If the period of the source grating is adapted to the period of the analyzer grating, the interference patterns created by each slit of the source grating overlap with equal phase at the plane of detection. (b) The visibility decreases linearly as a function of the source grating's duty cycle* τ_0.

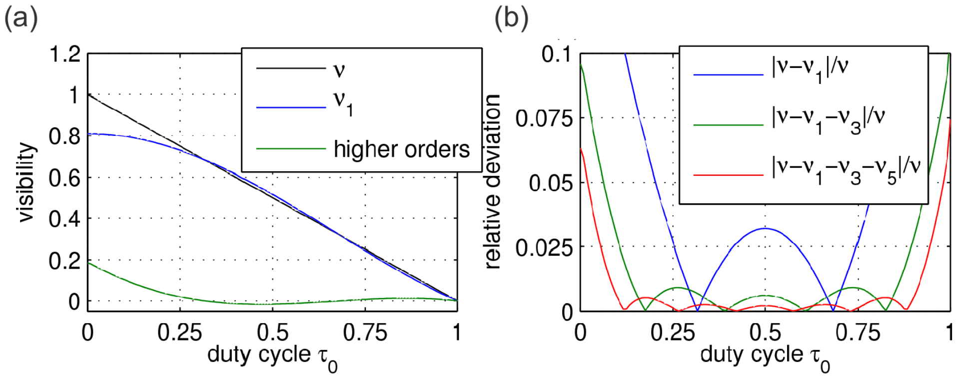

Fig. 8: *(a) The visibility as a function of the source grating's duty cycle* τ_0 *(black curve), together with the first (blue) and higher order Fourier coefficients (green) of the oscillation pattern. (b) For* $1/4 < \tau_0 < 3/4$*, the approximation of the interference pattern using only the first Fourier coefficient (blue curve) introduces a relative deviation lower than* 3.2%*. The deviation can be further reduced by including additional coefficients (green and red curves).*

duty cycle τ_0 are shown in Fig. 7 (b). If we note that $\mathrm{sinc}\left((2n-1)\cdot\tau_0\right) \approx \cos\left((2n-1)\cdot\tau_0\right)$ for small τ_0, one can see that Eq. (2.62) is approximately equal to the power series of a unit triangle function. Therefore, for a three-grating interferometer, the visibility of the intensity oscillation $S(x)$ as a function of the duty cycle of G_0 is equal to

$$\nu(\tau_0) = 1 - \tau_0. \tag{2.63}$$

The visibility decreases linearly with increasing duty cycle of G_0.
For a given duty cycle τ_0, the amplitudes ν_n decrease considerably with increasing n. Thus, the description of the visibility will be dominated by the lowest order Fourier coefficients. In Fig. 8 (a), the visibility with the first and the remaining higher order coefficients is shown as a function of duty cycle τ_0. It can be seen that for a wide range of duty cycles, the first order Fourier expansion is a good approximation to the visibility function. As shown in Fig. 8 (b), from the relative deviation of the approximation can be concluded that in the range of $1/4 < \tau_0 < 3/4$, the first order approximation ν_1 deviates from the visibility function ν by a relative error of $|\nu - \nu_1|/\nu \leq 32/\pi^3 - 1 \approx 3.2\%$. Thus, for source gratings with a duty cycle in the range of $1/4 < \tau_0 < 3/4$, the intensity oscillation in each pixel may be approximated by a Fourier series that is truncated after the first term with acceptable deviation. For binary attenuation gratings, we have $t_0(0) = p\cdot\tau_0$ and $t_2(0) = p\cdot\tau_2$. If we further define $S_0 := a/p\cdot t_1(0)$ as the signal that would be measured without the gratings in the beam path, Eq. (2.53) then simplifies to

$$\begin{aligned} S(x) &\approx S_0\cdot\tau_0\cdot\tau_2\cdot\left(1+\nu_1\cdot\cos\left(2\pi\frac{x}{p}+\varphi_r-\Delta\varphi\right)\right) \\ &:= a_0 + a_1\cdot\cos\left(2\pi\frac{x}{p}-\varphi\right). \end{aligned} \tag{2.64}$$

The parameter $a_0 := \tau_0\tau_2 S_0$ will be named the mean, $a_1 := a_0\cdot\nu_1$ the amplitude, $\nu = \nu_1$ the visibility and $\varphi := \Delta\varphi - \varphi_r$ the phase of the phase-stepping oscillation. For a source grating with a duty cycle of $\tau_0 = 1/2$ and an intensity oscillation approximated by a first order Fourier series, using Eq. (2.62), we obtain a maximum visibility of $\nu_1 = 16/\pi^3 \approx 0.516$. Thus, by the use of a source grating, grating-based imaging remains feasible at high powered laboratory x-ray sources with broad foci, while maintaining the lateral coherence requirements of the technique.

2.6 Sampling of the intensity oscillation

Due to limitations of flux and exposure time, the interference pattern cannot be scanned by the analyzer grating with infinite accuracy in a real experiment, i.e. at every lateral position x of the interference pattern. Instead, the interference pattern is sampled by the analyzer grating at a finite number of points, corresponding to different relative positions of the gratings. If we assume that the interference pattern was sampled at positions x_n with $n = 0,...,N-1$, the oscillation can be analytically given by

$$S(x_n) = a_0 + a_1\cdot\cos\left(2\pi\frac{x_n}{p}-\varphi\right). \tag{2.65}$$

As the intensity oscillation (2.65) has three independent parameters a_0, a_1 and φ, a minimum number of $N \geq 3$ steps and thus linear independent equations are necessary for a unique reconstruction of the oscillation. Less than three steps are feasible, but leave one parameter undetermined. Different approaches to sampling of the intensity oscillation can be conceived, as shown in Fig. 9. The most simple approach uses equidistant stepping with an integer number of steps over a full period of the intensity oscillation. In that case, the oscillation may be reconstructed using a simple Fourier based reconstruction approach, as presented in the following section 2.7.

Equidistant stepping in the linear part of the oscillation curve as shown in Fig. 9 (b) is reported in Ref. [Zhu10]. Approaches using non-equidistant sampling as shown in Fig 9 (c) have not been used so far. Although offering certain advantages, approaches using sampling over less than a full period, equidistant or not, have the drawback that the relative phase of the gratings has to be known beforehand to perform the sampling at the aimed position, thus introducing additional experimental challenges. Secondly, imperfections in grating fabrication can cause errors, distortions, bending or a waviness in the gratings, resulting in a spatially non-constant relative phase of the gratings. Therefore, in practice, it is difficult to fix the relative phase of the gratings to the same phase for all pixels in the image. Thirdly, these approaches would be more prone to instabilities in the relative phase of the gratings during the measurement in comparison to stepping over a full period. Therefore these approaches to sampling, although feasible, show drawbacks in practice due to reduced experimental simplicity, error tolerance and stability.

In the following, we will assume that a number of $N \geq 3$ equidistant steps over one period of the interference pattern were measured in the phase-stepping scan, i.e. $n = 0,...,N-1$ and $S_0 = S_N$. The oscillation may then be written

$$S_n = a_0 + a_1 \cdot \cos\left(2\pi \frac{n}{N} - \varphi\right). \tag{2.66}$$

If more than one period of the interference pattern has been scanned during the phase-stepping scan, the intensity oscillation in each pixel may be written $S_m = a_0 + a_1 \cdot \cos\left(2\pi \frac{P}{N} m + \varphi\right)$, where P is the number of scanned periods. If $S_n = a_0 + a_1 \cdot \cos\left(2\pi \frac{1}{N} n + \varphi\right)$ is the oscillation for a scan with one period of the phase-stepping oscillation, it can be easily shown that for integer P, for every m there is an $n = 0,...,N-1$ with $S_m = S_n$. For a fixed number of scan steps N, a phase-stepping scan with P periods of the interference pattern scanned can thus be transformed to a scan of one period of the interference pattern. Therefore, we can conclude that the reconstruction of the image information is essentially independent of the number of scanned periods. If P is not integer, the reconstructed mean, phase and amplitude of the phase-stepping oscillation are not independent of each other, as shown in appendix F. This case will thus be ignored in the following.

2.7 Data analysis and contrast generation

From the shape of the intensity oscillation in each pixel, described by the three parameters a_0, a_1 and φ, information considering the sample in the beam path can be obtained. The measured intensity oscillation S_n as described by Eq. (2.66) can be evaluated using the inverse discrete Fourier transform (DFT). The k-th Fourier coefficient c_k of the DFT is given by

$$c_k = \frac{1}{N} \sum_{n=0}^{N-1} S_n \cdot e^{\frac{2\pi i}{N} nk}. \tag{2.67}$$

As we assume that the intensity oscillation is harmonic, only the zeroth and first coefficient carry information. The offset a_0 of the oscillation can be reconstructed from the zeroth Fourier

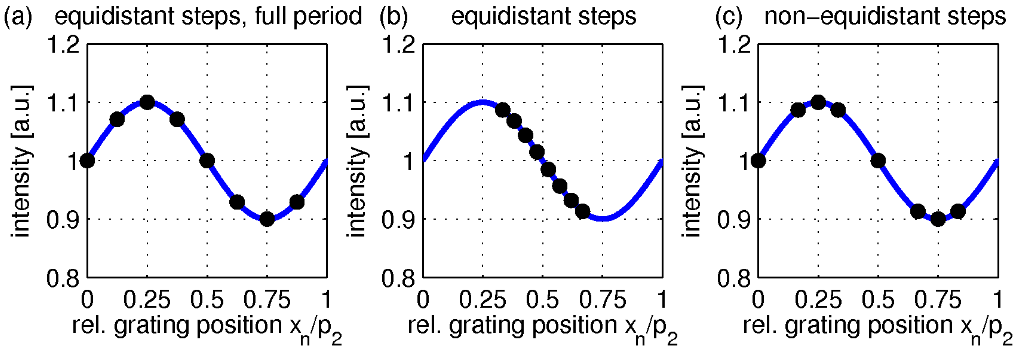

Fig. 9: *Different approaches to the sampling (black dots) of the intensity oscillation (solid blue line), (a) equidistant sampling over a full period, (b) equidistant sampling over the approximately linear part of the intensity oscillation, (c) non-equidistant sampling over a full period.*

coefficient c_0, which is simply the mean value of all projections S_n

$$a_0 = c_0. \tag{2.68}$$

The oscillation amplitude a_1 is identical to twice the amplitude of the first complex Fourier coefficient c_1

$$a_1 = 2 \cdot |c_1|. \tag{2.69}$$

The factor of two results from the equal contribution of negative frequency components. The oscillation phase φ is equal to the complex phase of the first complex Fourier coefficient

$$\varphi = \arg(c_1). \tag{2.70}$$

Eqs. (2.68)-(2.70) are derived in appendix F. For an evaluation of the attenuation, visibility decrease and phase shift caused by the measured sample, a reference scan has to be performed. If we denote the reference scan with the index r and a sample scan with the index s, the transmission T through the sample is calculated from the ratio of the mean values of the phase-stepping oscillation

$$T = \frac{a_{0,s}}{a_{0,r}}. \tag{2.71}$$

A similar definition can be made for the decrease of the amplitude, which will be named A

$$A = \frac{a_{1,s}}{a_{1,r}} = \left|\frac{c_{1,s}}{c_{1,r}}\right|. \tag{2.72}$$

The oscillation amplitude a_1 depends mainly on the coherence of the utilized beam, which can be quantified by the concept of visibility. For an oscillation pattern that is approximately harmonic, the visibility is identical to the oscillation amplitude a_1, normalized by the mean intensity a_0

$$v = \frac{a_1}{a_0}. \tag{2.73}$$

By quantifying the loss of visibility, one obtains a contrast which is denoted as dark-field contrast

$$D = \frac{v_s}{v_r} = \frac{A}{T}. \tag{2.74}$$

Note that the dark-field signal D is identical to the loss of oscillation amplitude A relative to the transmission T in the sample. The loss of visibility can be related to phase fluctuations of the

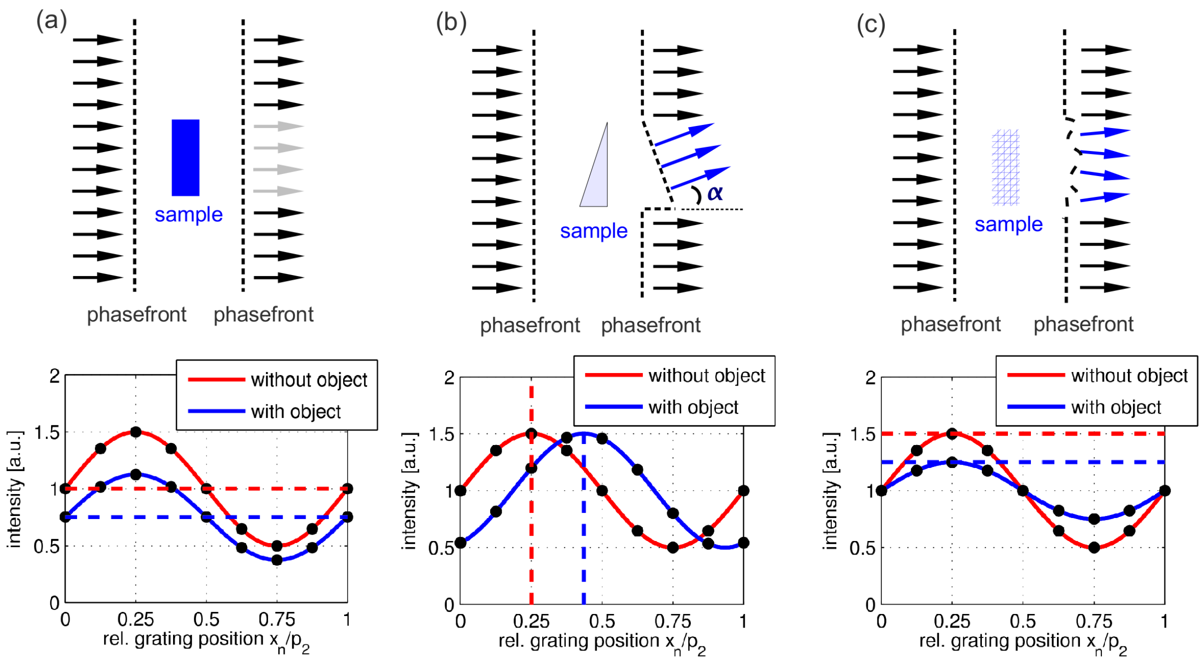

Fig. 10: *(a) The decrease of the mean value (dashed lines) of the phase-stepping oscillation is equal to the transmission T of the sample. (b) The phase shift $\Delta\varphi$ of the phase-stepping oscillation is related to beam deflections caused by a differential phase shift of the wavefront traversing the sample. (c) The amplitude decrease A of the phase-stepping oscillation is related to small-scale phase fluctuations of the wavefront, which can be related to sub-pixel structure of the traversed sample.*

x-ray wavefront caused by small-angle x-ray scattering at micron-sized structures within the sample [Pfeiffer08, Bech10, Jensen10, Yashiro10]. Therefore, a contrast similar to dark-field imaging in light microscopy can be achieved in the x-ray regime.

Using Eq. (2.42), the phase shift $\Delta\Phi$ can be reconstructed from the difference $\Delta\varphi$ between the oscillation phases of the sample and the reference scan

$$\Delta\varphi = \arg\left(\frac{c_{1,s}}{c_{1,r}}\right) = \operatorname{wrap}\left(\varphi_s - \varphi_r\right), \tag{2.75}$$

where $\operatorname{wrap}(x) = \operatorname{mod}(x, \pi)$ denotes phase wrapping. Note that in general $\arg\left(\frac{c_{1,s}}{c_{1,r}}\right) \neq \varphi_s - \varphi_r$ due to $\arg(z) \in [-\pi, \pi)$.

Thus, grating-based imaging offers three different contrast channels in a simultaneous measurement, namely attenuation contrast, differential phase-contrast and x-ray dark-field contrast. Contrast generation and data evaluation for the three contrast channels are shown in Fig. 10 (a)-(c). Depending on the sample, all three effects contribute to the the measured signal S_n in an experiment.

2.8 Interferometer design

As presented in the previous sections, the experimental requirements on a differential phase-contrast setup at low brilliance laboratory sources can be solved by the use of a three-grating interferometer. However, the previous discussion leaves many parameters unspecified, like the inter-grating distances, the arrangement of the gratings, or more general, the interferometer design, leaving space for optimizations. After discussing imaging at a magnifying setup in section 2.8.1, in section 2.8.2, a unified graphical approach to interferometer design will be

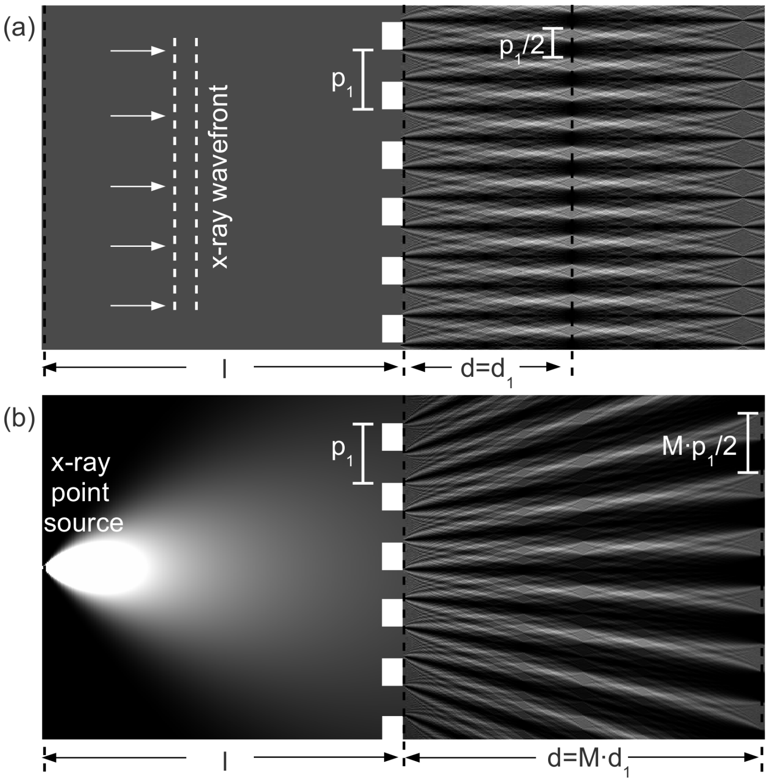

Fig. 11: *Interference pattern for a π-shifting phase grating in a) parallel-beam geometry and b) fan-beam geometry. b) shows how the period of the interference pattern and the fractional Talbot distance increase with magnification, relative to the parallel-beam situation.*

introduced, making the involved parameters and their dependencies more readily tangible. By following this approach, in section 2.8.3, three fundamental grating geometries will be identified and presented. Finally, in section 2.8.4, we will discuss how interferometer design can be performed and optimized under given experimental restrictions.
The results presented in section 2.8.3 were published in Ref. [Donath10A].

2.8.1 Imaging using fan- and cone-beam geometries

In fan-beam and cone-beam geometry, the distances between the gratings differ to the plane wave situations due to the fact that magnification has to be taken into account. The **geometric magnification** M of G_1 onto G_2 can be calculated by relating the inter-grating distances l and d to the total setup length $s = l + d$

$$M := \frac{s}{l} = \frac{l+d}{l}. \tag{2.76}$$

As the beam-splitter grating is magnified onto the analyzer grating, the period of the interference pattern increases proportional to the factor of the magnification, as shown in Fig. 11. The period of the analyzer grating p_2 has to be chosen equal to the period of the interference pattern

$$p_2 = M \cdot p_1/\eta, \tag{2.77}$$

where $\eta = 1$ for an attenuation and a $\pi/2$-shifting phase grating, while $\eta = 2$ for a π-shifting phase grating. The plane-wave case described by Eq. (2.48) is included as a special case for

$M = 1$. Additionally to the period of the interference pattern, the Talbot distance d_m increases proportional to the magnification

$$D_m = M \cdot d_m. \tag{2.78}$$

If the distance d between the beam-splitter and analyzer gratings is chosen equal to a Talbot distance $d = M \cdot d_m$, combining Eqs. (2.78) and (2.76) yields the magnified Talbot distance D_m as a function of the plane wave Talbot distance d_m

$$D_m = \frac{l \cdot d_m}{l - d_m}. \tag{2.79}$$

The period of the source grating has to be adjusted to the period of the analyzer grating as described by Eq. (2.61), just the same as in parallel-beam geometry.

2.8.2 Visualization of parameter dependencies

In the previous sections, the basic principles and parameters needed for the design of an interferometer for grating-based DPC imaging were deduced. As it is sometimes difficult and not directly visible how the different parameters are related and which of the parameters can be chosen or changed independently of one another, in this section an intuitive graphical approach to interferometer design will be presented. It is based on the idea that the interferometer parameters form a multidimensional parameter space. While some of the parameters are independent, others are related by various experimental specifications. Choosing a fixed value for one parameter singles out a hyperplane in this parameter space and therefore reduces the remaining space by one dimension. A fully characterized interferometer is represented by a single point in the parameter space. In our approach, each parameter describing the interferometer will be presented as a function of the G_0-G_1 distance l and the G_1-G_2 distance d in the following. As we shall see, this approach allows a compact description of interferometer design and at the same time a visualization of the different parameter dependencies.

We will begin with an overview over the parameters needed for the characterization of an interferometer. Of central importance is the design energy E_0 of the setup. In the following, we assume that the design energy is fixed by the requirements of the desired field of application and thus eliminated as a free parameter. If one assumes that the three gratings G_0, G_1 and G_2 are of binary and rectangular form, the gratings can be fully characterized by their periods p_0, p_1, p_2, their duty cycles τ_0, τ_1, τ_2, their heights h_0, h_1, h_2, and the grating material m_0, m_1, m_2. For the sake of simplicity, we assume that $\tau_0 = \tau_1 = \tau_2 = 0.5$. In practice, the grating material will be chosen by the manufacturing requirements in combination with the demand of high attenuation or phase shift. Additionally, we assume that the heights of the gratings will be adjusted to the design energy, and thus eliminated as a free parameter. Therefore, only the periods remain as free parameters for the description of the gratings. Furthermore, the interferometer geometry can be characterized by the total setup length s, measured from the source grating G_0 to the analyzer grating G_2, and the two inter-grating distance l and d. We assume that the analyzer grating is positioned at a fractional Talbot distance D_m, which is related to the plane wave Talbot distance d_m via the magnification M of the beam-splitter grating onto the analyzer grating. Finally, the plane wave Talbot distance d_m is determined by the period and the type of beam-splitter grating used.

The next step in our graphical approach to interferometer design is to list the equations that relate the mentioned parameters, where we will present each parameter as a function of the inter-grating distance. Beginning with the total setup length, each of the following relations will be based on the previous one. The total setup length s as a function of the inter-grating distances l and d is simply given by

$$s(l,d) = l + d. \tag{2.80}$$

The magnification of the interference pattern can be calculated by relating the inter-grating distances to the total length of the setup

$$M(l,d) = \frac{s(l,d)}{l}. \tag{2.81}$$

If we assume that G_2 is placed at a fractional Talbot distance of the beam-splitter grating G_1, we can calculate the plane wave Talbot distance d_m by

$$d_m(l,d) = \frac{d}{M(l,d)}. \tag{2.82}$$

If the type of beam-splitter grating is known, from the parallel-beam fractional Talbot-distance d_m, the full Talbot distance d_T can be obtained. For a given design energy, corresponding to a wavelength λ_0, this yields the period of the beam-splitter grating G_1

$$p_1(l,d) = \sqrt{\frac{1}{mn} \cdot \frac{\lambda_0}{2} \cdot d_m(l,d)} \qquad n = \begin{cases} 1/2 & \text{attenuation grating} \\ 1/4 & \pi/2\text{-shifting phase grating} \\ 1/16 & \pi\text{-shifting phase grating.} \end{cases} \tag{2.83}$$

The period p_2 of the analyzer-grating is adjusted to the period of the magnified interference pattern

$$p_2(l,d) = M(l,d) \cdot \frac{p_1(l,d)}{\eta}. \tag{2.84}$$

Finally, the period of the source-grating p_0 is adjusted to the period of the interference pattern p_2, so that the interference patterns created by each slit source overlap at the plane of detection

$$p_0(l,d) = \frac{l}{d} \cdot p_2(l,d). \tag{2.85}$$

From the above Eqs. (2.80)-(2.85), we see that all parameters are explicitly or implicitly dependent on the inter-grating distances l and d. If the design energy E_0, the fractional Talbot order m, and the type of beam-splitter grating which determine n and η are chosen, all remaining parameters can thus be simultaneously plotted as a function of the inter-grating distances. On this basis, in Fig. 12, the total setup length, the magnification, the fractional Talbot distance and the three grating periods are plotted as a function of the G_0-G_1 distance l along the x-axis and the G_1-G_2 distance d along the y-axis. For the numerical calculations in the example shown, a π-shifting beam-splitter phase grating at $E_0 = 40$ keV design energy was assumed, with the analyzer grating positioned in the first fractional Talbot order. In Fig. 12, the different interferometer parameters are represented as curves in the two-dimensional plane spread out by the two inter-grating distances. If, for example, the G_0-G_1 distance l is chosen to a fixed value, it will reduce the parameter space to a vertical line. Similarly, choosing a fixed value for d reduces the remaining parameter space to a horizontal line. Choosing a fixed value for the total setup length s will reduce the parameter space to a declining line, as visible by the color coding in Fig. 12 (a), while fixing one of the three periods reduces the parameter space to a non-linear curve. By fixing two parameters simultaneously, a point in the parameter space is

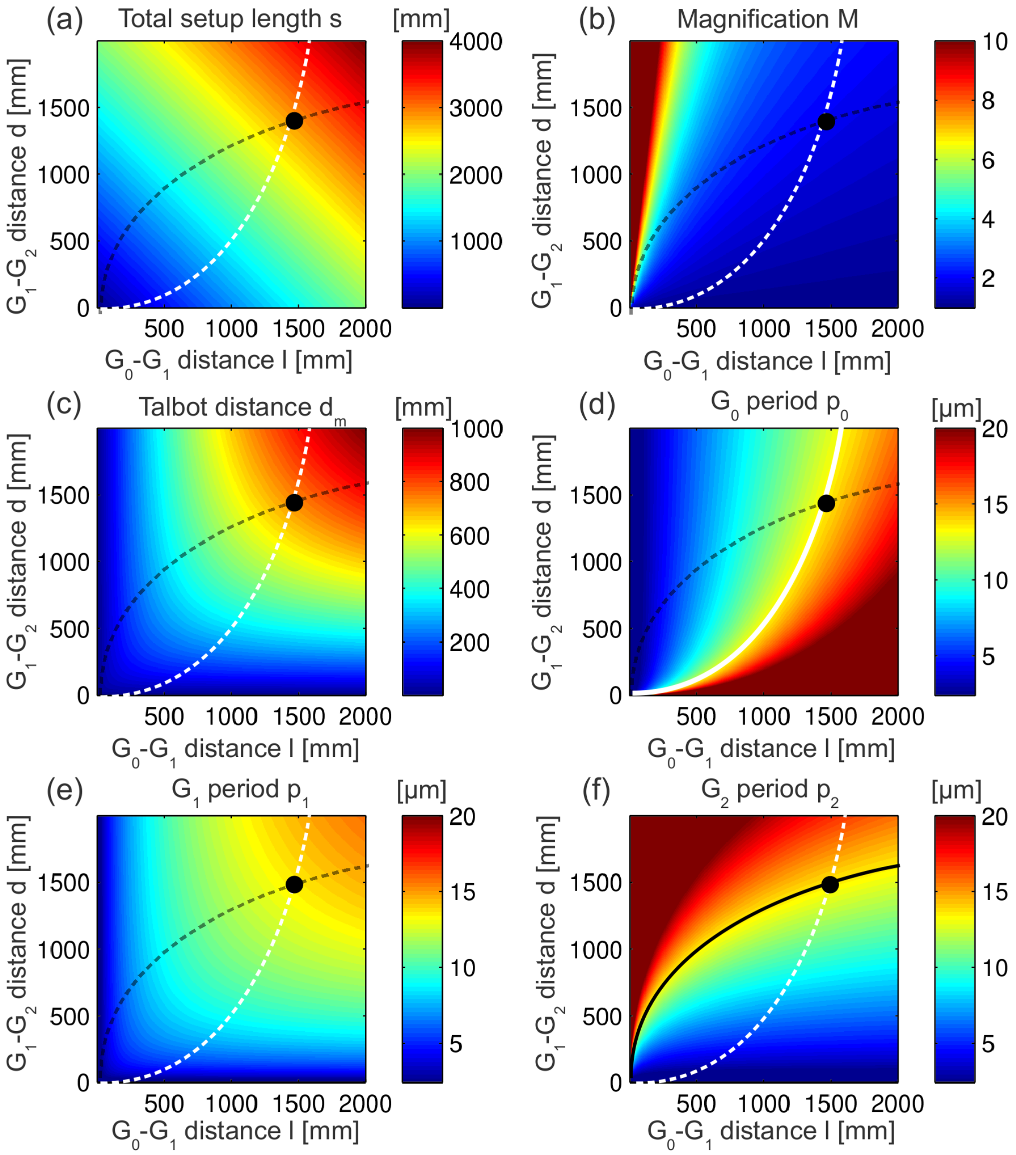

Fig. 12: *Grating parameters as a function of the inter-grating distances l and d, (a) the total setup length s, (b) the magnification M, (c) the plane wave fractional Talbot distance* d_m*, (d) the period of* G_0*, (e) the period of* G_1 *and (f) the period of* G_2*. In the shown example, the choice of* p_2 *(solid black curve) and* p_0 *(solid white curve) singles out a point in the parameter space (black dot) and thus fixes all the other parameters.*

singled out, given by the intersection point of the two curves, as shown in Fig. 12 exemplarily for the period of G_0 and G_1. As the parameter space is reduced to a single point there are no free parameters left and the interferometer is fully characterized. Therefore, one can see that by fixing any two free parameters, all other parameters will be fixed as well. For certain combinations of parameters the corresponding curves may not intersect, a case in which there is no solution for the desired interferometer.

By the graphical approach, interferometer design is transformed into a problem of analytic geometry, offering a unified guideline to interferometer design. By the representation of interferometer parameters by curves in a parameter space, the method is highly intuitive, offering a quick and visual analysis and overview of parameter dependencies. Finally, it is simple and fast to implement numerically. Nevertheless, on the back side, the method makes it necessary to fix a certain number of parameters for the calculation of the remaining parameter space. Of all the parameters fixed in our example, the beam-splitter grating type and the Talbot order m are of integer type, thus their influence can be evaluated with minor additional effort. A discussion of the design energy, as well as all polychromatic effects are not included in the approach, due to their analytical complexity. Also, it is implicitly assumed that the analyzer grating is placed exactly at a Talbot distance, which might be disadvantageous in certain situations. Therefore, in conclusion, working with the graphical approach has to be conducted with care, as valid solutions might go unnoticed.

2.8.3 Conventional, inverse and symmetric setups

In the following, we will apply the graphical approach to the discussion of different setup geometries. The combination of a fixed total setup length $s = l + d = l + D_m$ and a fixed beam-splitter period G_1 can be investigated analytically by combining Eq. (2.80) with Eq. (2.79), which leads to a quadratic equation for the solution of l

$$l^2 - s \cdot l + s \cdot d_m = 0, \tag{2.86}$$

with solutions

$$l_{1,2} = \frac{s}{2} \pm \sqrt{\frac{s^2}{4} - s \cdot d_m}. \tag{2.87}$$

Depending on the setup length s, three distinct cases for the solutions of l can be distinguished:

- For $s < 4 \cdot d_m$ the discriminant is imaginary and there is no solution.
- For $s = 4 \cdot d_m$ the discriminant is equal zero. This solution has the property $l = s/2 = d$. As the two inter-grating distances are equal in this case, this solution will be referred to as the **symmetric geometry**. In this case, we have $M = 2$ and thus $p_0 = 2 \cdot p_1 = p_2$ for an attenuation or $\pi/2$-shifting beam-splitter phase grating and $p_0 = p_1 = p_2$ for a π-shifting phase grating.
- For $s > 4 \cdot d_m$ there are two solutions. The solution with $l > d$ will be named the **conventional geometry**, as it has been utilized in most previous publications. For the second solution with $l < d$, the beam-splitter grating is closer to the source grating than to the analyzer grating. Compared to the conventional setup, the distances l and d are interchanged and, consequently, also the grating periods of G_0 and G_2 are interchanged. Thus, we will refer to the solution with $l < d$ as the **inverse geometry** since the inverse geometry is equivalent to the conventional geometry with reversed beam direction. This tells us that the three-grating interferometer can be used in either direction.

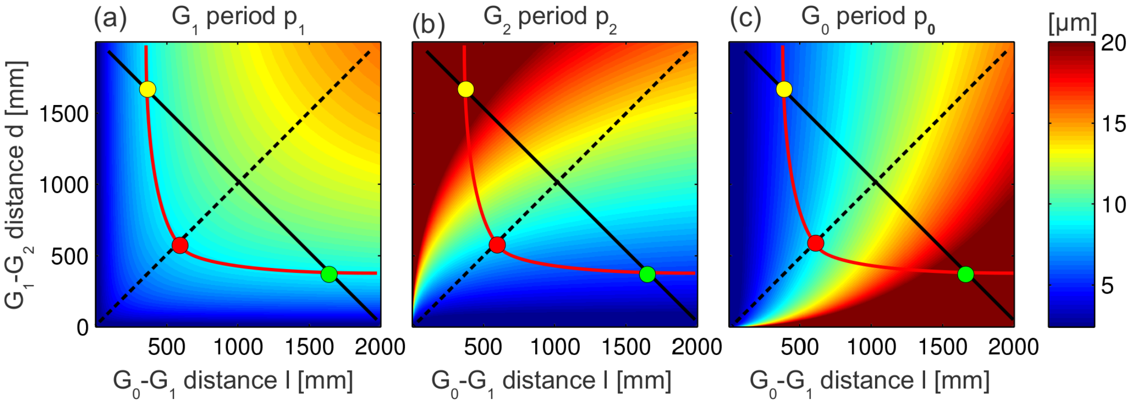

Fig. 13: *Visualization of setup geometries: (a) For a given total length s (solid black line) and G_1 period (solid red curve) solutions exist: a conventional (green dot) and an inverse (yellow dot). For a given G_1, the symmetric setup (red dot) is the shortest setup possible. (b) and (c) indicate that conventional and inverse setups are related by the exchange of G_0 and G_2, while their periods are equal in the symmetric geometry.*

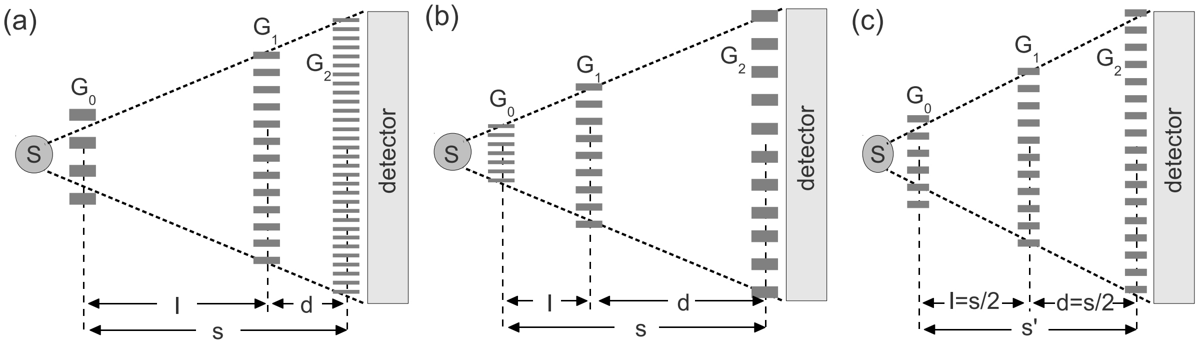

Fig. 14: *Schematics of the three fundamental interferomter geometries, (a) conventional setup with $p_2 < p_1 < p_0$, (b) inverse setup with $p_0 < p_1 < p_2$, and (c) symmetric setup with $p_0 = p_1 = p_2$.*

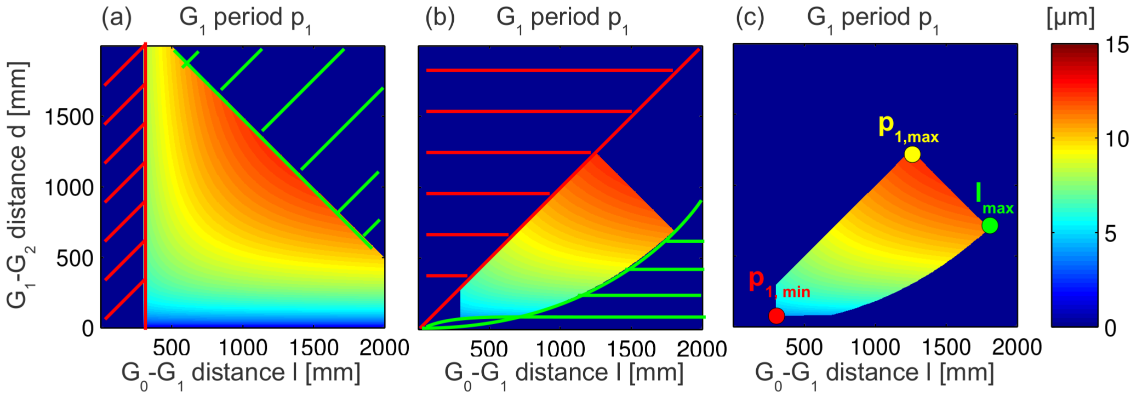

Fig. 15: *Optimization of the period of G_1 under given restrictions: (a) The red hatched area is excluded by the requirement $l > 0.3$ m, the green hatched area by $s < 2.5$ m, (b) the red hatched area is excluded by the requirement that the setup is conventional, the green hatched area by the requirement $p_0 < 20$ μm and $p_2 > 2.4$ μm. (c) The remaining parameter space allows a quick optimization of different parameters.*

The different solutions are presented graphically in Fig. 13. As symmetric solutions are characterized by $l = d$, in Fig. 13, they all lie along the diagonal line, which cuts the parameter space in two halfs. The lower half with $l > d$ corresponds to a setup in conventional geometry, while setups in inverse geometry with $l < d$ are given in the upper half. It can immediately be seen that for a given beam-splitter grating with period p_1, the symmetric setup is the setup with the shortest possible total length s_{min}. If s is chosen smaller than s_{min} there is no intersection point and thus no solution to the design problem, while there will be two solutions for $s > s_{\text{min}}$. It can also be seen that the conventional and inverse setup are related by a reflection across the axis $l = d$, i.e. an exchange of p_0, p_2 and l, d, respectively. The different grating arrangements are shown schematically in Fig. 14.

The inverse geometry with $l < d$ offers the following practical advantages over the conventional geometry in the realization of x-ray grating interferometers:

- The grating with the finest structures, and thus the grating which is the most challenging to produce by microfabrication, is G_0. It has a smaller total size than G_2 due to the high geometrical magnification. The grating with the largest area and the coarsest structures is G_2, which presents the least stringent requirements for microfabrication.

- Since the period of G_2 increases, the grating bars can easily be made higher so that the use of other materials than gold that are less dense and less expensive can be considered. This offers advantages with respect to the transmission of the gratings, process compatibility, and production costs.

- As grating G_1 is placed closer to the source, its dimensions can be reduced as well.

The symmetric geometry with $l = d$ also offers a variety of advantages in the realization of a DPC interferometer:

- A symmetric setup gives the shortest possible interferometer that can be realized for a given period p_1, with a total length of $s_{\text{min}} = 4 \cdot d_m$.

- Both attenuation gratings G_0 and G_2 have the same period $p_0 = p_2$ and can thus be produced using the same fabrication process. If a π-shifting phase grating is used as beam-splitter, all three gratings have the same period.

- If the attenuation gratings are not identical in terms of structure height or fabrication quality, both gratings can be exchanged, depending on their influence on image quality.

Due to the relative ease in grating fabrication and handling, the symmetric geometry will thus be the preferable solution for systematic investigations and method characterizations at a dedicated test setup.

Apart from the grating arrangement, the object position within the grating interferometer has to be chosen. In previous publications, the object was placed between source or G_0 and G_1. This was practical, since there is more space in front of the G_1 grating in the so far realized conventional geometry with $d > l$. For the inverse geometry, with $l < d$, it is favorable to place the object behind G_1. However, other applications such as laboratory micro-CT may still require the object to be close to the source in order to take advantage of the geometrical magnification in a cone-beam setup. The problem of sample positioning, as well as a comparison of conventional and inverse setups in terms of signal strength will be investigated in section 3.

2.8.4 Setup optimization under given restrictions

Additionally to the already mentioned advantages, the graphical approach to interferometer design allows the optimization of a realized or planned interferometer. Any experimental restrictions imposed on a given parameter reduces and excludes parts of the parameter space. For example, the total setup length s will be restricted by the length of the optical table or radiation protection hutch. In some situations, a compact setup is desirable. The size of the sample will impose a lower limit on one of the inter-grating distances, depending on whether the sample is placed upstream or downstream of the beam-splitter grating. Furthermore, the period of the gratings will have a lower bound due to manufacturing restrictions. An exemplary optimization procedure is presented in Fig. 15: in the example shown, the period of the beam-splitter grating G_1 is plotted as a function of the inter-grating distances. The possible values for p_1 are restricted by the requirement that the total setup length does not exceed $s < 2.5$ m; the sample is positioned between G_0 and G_1 in a conventional setup, with a minimum space of $l > 0.3$ m; finally, the three grating periods are restricted by $2.4\ \mu\text{m} < p_0, p_1, p_2 < 20\ \mu\text{m}$. The resulting reduced parameter space for the period of G_1 is shown in Fig. 15 (c). The remaining parameter space allows a quick evaluation of extremal points of the different parameters, either by their position relative to the axes, or by their color coding. For example, from Fig. 15 (c) can be concluded that under the given restrictions, the setup with the highest period $p_{1,\max}$ (and thus the highest sensitivity, see section 3.1.2) is at the same time the setup with the highest G_1-G_2 distance $d_{\max}$. As this solution lies along the diagonal for which $l = d$, the resulting setup will be in symmetric geometry. The restriction of the parameter space applies to all parameters shown in Fig. 12 simultaneously, therefore further information can be drawn by analyzing the other parameters under these restrictions.

2.9 Summary

In this section, the basics of grating-based x-ray differential phase-contrast imaging have been developed and presented. In section 2.1, the refractive index, its dependence on material and energy as well as its influence on an incoming wave were discussed. Based on the description of x-ray propagation by rays using the eikonal equation, the angular deflection of an x-ray beam was presented as a source of phase contrast in section 2.2. The gratings needed for a typical DPC interferometer were introduced in sections 2.3-2.5, motivated by experimental requirements on spatial reference, spatial resolution and spatial coherence. An analytical description of the visibility of the intensity oscillation revealed the resulting signal in each detector pixel to be approximately harmonic in shape. From the parameters of the intensity oscillation in each pixel, three different contrast channels can be evaluated using a DFT reconstruction approach, as described in section 2.7: attenuation contrast, connected to the transmission through the sample, differential phase contrast, connected to the gradient of the phase of the wavefront, and dark-field contrast, connected to sub-pixel phase fluctuations of the wavefront. In section 2.8.2, it was shown how interferometer design can be presented and guided by graphical means. By describing the different parameters characterizing the interferometer as a function of the inter-grating distances, parameter dependencies can be easily visualized. Based on this approach, in section 2.8.3, the characteristics of conventional, inverse and symmetric setups were worked out. The inverse and symmetric geometries both offer reduced requirements for grating manufacturing in comparison to the conventional geometry. Finally, in section 2.8.4, it was shown how the graphical approach to interferometer design can be used to optimize an interferometer under given restrictions.

3 Position dependence, sensitivity and tomography

In DPC imaging using a grating interferometer, x-rays contributing to the image formation do not propagate along straight lines. Instead, deflections caused by phase gradients are measured, causing lateral beam-shifts relative to an undeflected beam at the plane of detection. As the measured shifts caused by the deflections depend on the propagation distance to the detector, the measured signal strength in DPC imaging is expected to exhibit a strong dependence on the sample position within the interferometer. Additionally, while the attenuation along a beam path is monotonically increasing, deflections can be positive or negative with respect to the propagation direction, which might lead to ambiguities in data interpretation. Therefore, we will analyze the contrast formation as a function of sample position for all three contrast channels in section 3.1. Since in a computed tomography (CT) every point of the sample changes its position relative to the gratings during the measurement, a non-constant and position-dependent signal strength introduces an additional dependence of the projection angle in the tomographic reconstruction. Tomographic imaging modalities will therefore be investigated together with the sensitivity of the interferometer in section 3.2.
The results for the phase-contrast channel are based on Refs. [Donath10A] and [Chabior11A].

3.1 Sensitivity in grating-based x-ray imaging

In the following, by the expression **sensitivity of the interferometer**, we will understand the ratio of the measured signal relative to the physical effect involved in contrast generation, as a function of the sample position r within the interferometer

$$\text{Sensitivity}(r) := \frac{\text{measured signal}(r)}{\text{physical effect}}. \tag{3.1}$$

The sensitivity can be understood as a measure for the ability of the interferometer to transform physical effects into a measurable quantity. Because the measurement technique is capable of yielding three different contrasts in a single measurement, the sensitivity will be discussed for each contrast channel separately in sections 3.1.1-3.1.3.

3.1.1 Sensitivity in the attenuation-contrast channel

In the attenuation-contrast channel, contrast is generated by the attenuation of photons in the traversed matter. For the discussion of the sensitivity, we will define the negative logarithm of the transmission T as the measurement signal in the attenuation-contrast channel. The physical effect of attenuation can be quantified by the attenuation decrement $\beta(\mathbf{r})$. In a measurement, the total attenuation is given by summing the contributions of all materials along the beam path, i.e. by taking the line integral $\int \beta dz$. The sensitivity for the attenuation-contrast channel S_T is therefore given by

$$S_T(r) = \frac{-\ln\left(a_{0,s}/a_{0,r}\right)}{\int \beta(\mathbf{r}) \cdot dz} \equiv \frac{1}{2k}, \tag{3.2}$$

where the identity follows directly from Beer-Lambert's law. Thus, we can conclude that the ability of the interferometer to detect attenuation is independent of the position of the sample and thus the sensitivity for attenuation can be said to be constant within the interferometer. Classical attenuation tomography is thus feasible with grating-based x-ray imaging without alterations of the corresponding algorithms.

3.1.2 Sensitivity in the differential phase-contrast channel

While the measurement signal in DPC imaging is the phase $\Delta\varphi$ of the intensity oscillation in each pixel, the physical effect behind this signal is the deflection α of an x-ray beam by phase gradients in the sample, as described by Eq. (2.30). The sensitivity in the differential phase-contrast channel S_φ may thus be defined by

$$S_\varphi(r) = \frac{\Delta\varphi}{\alpha} = \frac{\arg\left(c_{1,s}/c_{1,r}\right)}{\partial_x \int \delta(\mathbf{r}) \cdot dz}. \tag{3.3}$$

Although Eqs. (3.2) and (3.3) show a similar mathematical structure, they differ from each other by the fact that the measured data are not logarithmized and that gradients of line integrals are measured in the phase-contrast channel. As the sample can in principle be placed up- and downstream of the beam-splitter grating, in the following, we will derive a general formula for the phase sensitivity that describes the two cases separately, based on the respective schemes in Fig. 16. We define the object position r relative to the origin which is the position of the phase grating G_1. Thereby, we distinguish between the case of negative r with the object between source point and G_1 $(-l < r < 0)$ and the case of positive r with the object between G_1 and G_2 $(0 < r < d)$. The rays from a point source, practically realized as either the spot of a microfocus tube or a slit in the source grating G_0, project the G_1 onto the G_2 grating. We consider a purely refractive flat object, symbolized by the wedge in Fig. 16, that changes the beam propagation direction by a given refraction angle α. The wedge displaces the projection of G_1 in the G_2 plane, or in other words, a different point of G_1 is projected onto the same point of G_2 when the wedge is inserted. Thus, a lateral displacement of G_1 by Δ_1 is needed to recover the same projection, i.e. to let the ray through the wedge project the same point of G_1 onto G_2 as for the central undisturbed ray. The displacement Δ_1 is directly related to the phase shift $\Delta\varphi$ measured in the DPC scan by

$$\frac{\Delta\varphi}{2\pi} = \frac{\Delta_1}{p_1/\eta} \tag{3.4}$$

with p_1 the period of the beam splitter grating and η a factor accounting for the period of the interference pattern relative to the beam splitter period. First, we will determine the displacement Δ_1 for the case $0 < r < d$ shown in Fig. 16 (a). From the figure, we see that the displacement is given by $\Delta_1 = \alpha_0 \cdot l$, where the angle α_0 is an auxiliary quantity that we have to determine. The angles α_0 and α_2 are geometrically related by the equations

$$\alpha = \alpha_0 + \alpha_2 \tag{3.5}$$

and

$$\Delta_s = \alpha_0(l + r) = \alpha_2(d - r), \tag{3.6}$$

where the auxiliary quantity Δ_s shown in Fig. 16 (a) and (b) is the beam separation of the undisturbed and the refracted beam at the object position. Note that we have again approximated the tangent with the angle in radians in paraxial approximation and that these equations are valid for both cases $r < 0$ and $r > 0$. Solving Eqs. (3.5) and (3.6) for α_0, we obtain the displacement

$$\Delta_1 = \alpha_0 \cdot l = \alpha \left(\frac{1}{l} + \frac{1}{d}\right)^{-1} \left(1 - \frac{r}{d}\right) \qquad \text{for } 0 < r < d. \tag{3.7}$$

For the case of $-l < r < 0$ shown in Fig. 16 (b), we determine the displacement $\Delta_1 = \alpha_2 \cdot d$. Since the displacement now depends on α_2, we solve Eqs. (3.5) and (3.6) for α_2 and obtain

$$\Delta_1 = \alpha_2 \cdot d = \alpha \left(\frac{1}{l} + \frac{1}{d}\right)^{-1} \left(1 + \frac{r}{d}\right). \tag{3.8}$$

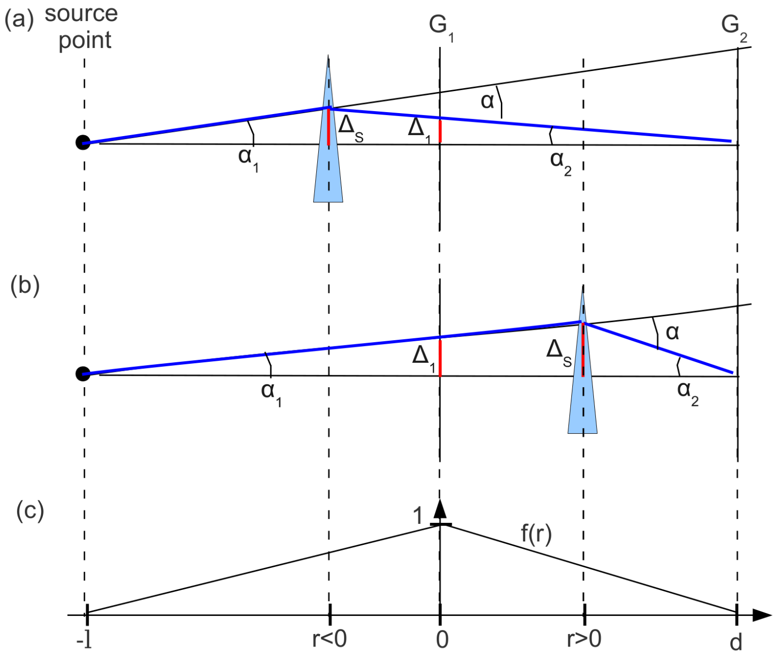

Fig. 16: *Illustration of beam paths for the calculation of angular sensitivity as a function of object position. The relative sensitivity as a function of the object position r is derived distinguishing the case: (a) refracting object between source and* G_1 *with* $-l < r < 0$*, and (b) refracting object between* G_1 *and* G_2 *with* $0 < r < d$*. (c) Plot of* $f(r)$*, which describes the linear scaling of the sensitivity. The source can either be a focal spot of a microfocus tube or slit in a* G_0 *grating.*

Combining Eqs. (3.7) and (3.8) yields a relation for the angular sensitivity

$$S_\varphi(r) = \frac{\Delta\varphi}{\alpha} = \left(\frac{1}{l} + \frac{1}{d}\right)^{-1} \frac{2\pi}{p_1/\eta} \cdot f(r), \tag{3.9}$$

where the position dependent function $f(r)$ is given by

$$f(r) = \begin{cases} 1 + r/l, & \text{for } -l < r \leq 0 \\ 1 - r/d, & \text{for } 0 \leq r < d. \end{cases} \tag{3.10}$$

Thus, we have separated the sensitivity into an interferometer-specific factor and the linear unit scaling function $f(r)$ shown in Fig. 16 (c), that only depends on the relative object position within the interferometer. The function $f(r)$ reaches its maximum of unity at the plane of G_1 for $r = 0$ and falls off linearly when the object is positioned closer towards G_0 or G_2. For $r = -l$ and $r = d$, i.e., when the object is in the plane of G_0 or G_2, respectively, we have $f(r) = 0$ and thus zero sensitivity. The maximum sensitivity S_0 is position independent and a constant of the interferometer. It can be calculated by

$$S_0 = S_\varphi(r = 0) = \left(\frac{1}{l} + \frac{1}{d}\right)^{-1} \frac{2\pi}{p_1} = 2\pi \frac{d}{M \cdot p_1/\eta} = 2\pi \frac{d}{p_2}, \tag{3.11}$$

where we have used the definition of magnification $M = (l + d)/l$ and $p_2 = M \cdot p_1/\eta$. We may thus abbreviate the position dependent sensivity in DPC imaging by

$$S_\varphi(r) = S_0 \cdot f(r), \tag{3.12}$$

where the maximum sensitivity S_0 may be equivalently expressed as

$$S_0 = 2\pi\frac{d}{p_2} = 2\pi\frac{l}{p_0} = 8\pi \cdot mn\eta \cdot \frac{p_1}{\lambda}. \tag{3.13}$$

Thus, we observe an increase in sensitivity with increasing G_1 period, which comes at the cost of an increased Talbot distance $d_m \sim p_1^2$ between G_1 and G_2. For fixed photon energy, grating type and Talbot order, the sensitivity is thus qualitatively equivalent to the period of G_1 in the graphical design approach presented in section 2.8.

To confirm Eq. (3.12) derived for the angular sensitivity and to compare the sensitivity of the conventional and the inverse grating geometry experimentally, the phase shift $\Delta\varphi$ was measured for both geometries as a function of sample position r using a simple phase object. For both geometries, nine object positions in front of the phase grating and another nine object positions behind the phase grating were recorded. The experiments were carried out at a laboratory setup at the Paul Scherrer Institut (PSI) in Villigen, Switzerland. As an x-ray source, a COMET MXR-160HP/11 tube with a tungsten anode and a target angle of 11° was used. It was operated at an anode voltage of 65 kV, an anode current of 10 mA, and with an effective focus diameter of 1 mm. Low energies in the spectrum were removed using a 10 mm thick aluminium filter. The detector consisted of three main components: a Hamamatsu caesium iodide (CsI) scintillator of 600 μm thickness, an optical lens and mirror system, and a charge-coupled device camera, model Proline of Finger Lakes Instrumentation with 1024×1024 pixels of 24×24 μm^2, which was read in 2 binning mode. The phase grating G_1 was manufactured at the Laboratory for Micro- and Nanotechnology of PSI in silicon with bars of 61 μm height and a period of 6.3 μm [David07]. The absorbing gold gratings were manufactured at the PSI and at the Karlsruher Institut für Technologie with periods of 8.5 and 5.0 μm and structure heights of 90 and 120 μm, respectively [Reznikova08]. The G_1 produces a relative phase shift of π at the design energy of 47.6 keV. This design energy results in inter-grating distances of $l = 514$ mm and $d = 303$ mm for the conventional setup and, vice versa, $l = 303$ mm and $d = 514$ mm for the inverse setup, according to the interferometer formulas in section 3.1.2. A reference scan was performed for each projection image. Phase-stepping was carried out with the G_1 grating in eight steps over one period of G_1 and each image was recorded with 4.5 s exposure time. The images were finally cropped to a size of 120×295 horiz. × vert. pixels. As a well-defined phase object, a homogeneous aluminium rod with 5×5 mm^2 square-shaped cross-section was used. Its diagonal was aligned along the beam direction, so that in good approximation, the rod exhibits a phase shift like a symmetric triangle or double wedge, with two areas of constant phase gradients of opposite sign. The expected absolute angle of refraction caused by the aluminium rod is

$$|\alpha| = \frac{\lambda}{2\pi}\frac{\partial\Delta\Phi}{\partial x} = 2\delta, \tag{3.14}$$

where δ is the refraction decrement. We have used the fact that the phase shift caused by the rod changes as $\Delta\Phi = (2\pi/\lambda)\cdot\delta\cdot 2\Delta x$, when moving toward the rod center by Δx. For our design energy of 47.6 keV, we determined $\delta = 0.238 \cdot 10^{-6}$ and $|\alpha| = 2\delta = 0.477$ μrad for the aluminium rod. The values for δ were calculated using tabulated data from Ref. [Mucal93].

Images of the phase object recorded at several selected object positions in the inverse geometry are displayed in Fig. 17. The images were cropped to a size of 120×295 pixels horiz. × vert. Note that the magnification of the rod decreases with increasing source-to-object distance. The images show the local oscillation phases $\Delta\varphi(x,y)$, which of course exhibit

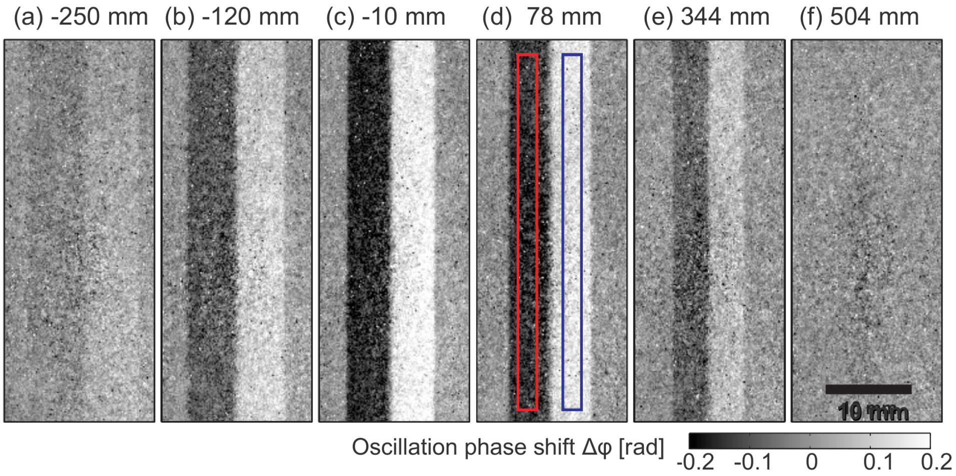

Fig. 17: *Images of the measured oscillation phase shift* $\Delta\varphi$ *(gray coded) of a square-shaped* 5×5 *mm*^{2} *aluminium rod, with the viewing angle along one of the diagonals of the rod. The sample was imaged in the inverse geometry and is shown for a few selected object positions r. From (a) to (f), the source-to-rod distance increases, while the geometric magnification and thus the size of the projection image decreases. The averaging boxes for the left side (red) and the right side (blue) of the rod are exemplarily shown in d).*

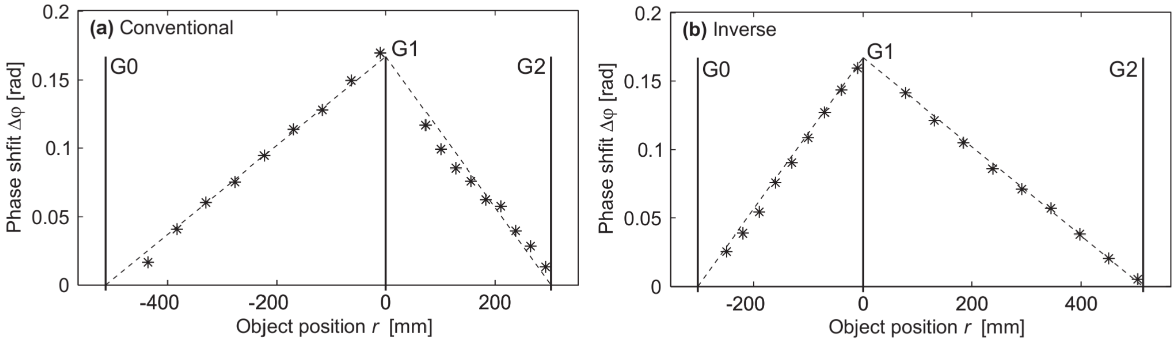

Fig. 18: *Oscillation phase shift* $\Delta\varphi$ *measured on a square-shaped* 5×5 *mm*^{2} *aluminium rod at 18 sample positions. (a) Conventional geometry with* G_0 *and* G_2 *grating at* $r_0 = -514$ *mm and* $r_2 = 303$ *mm and (b) inverse geometry with* G_0 *and* G_2 *gratings located at* $r_0 = 303$ *mm and* $r_2 = 514$ *mm.*

opposite direction and sign for the left and right half of the rod. For each image two regions of interest with each containing 16×260 pixels for the left and the right half of the rod were manually selected, as exemplarily shown in Fig. 17 (a). The phase shift for each side and object position was calculated as the mean over the defined region. The signals from the left and right sides were subtracted and divided by 2, in order to remove any signal offset, thus obtaining a quantitatively exact phase shift $\Delta\varphi$. The standard deviation σ_φ in the phase shift was determined by error propagation from the standard deviation of the mean value for each side of the rod. The measured phase shifts are plotted against the object position r in Fig. 18 for both the conventional and the inverse geometry. The plots exhibit the expected linear dependence of the measured phase shift on the object position, as described by Eq. (3.10). From this plot, the phase shift $\Delta\varphi(r = 0)$ of the object at the position of the phase grating G_1, i.e. for $r = 0$ and maximum sensitivity, were extrapolated using linear regression. The obtained values of $\Delta\varphi_c = 0.162 \pm 0.008$ rad for the conventional and $\Delta\varphi_i = 0.164 \pm 0.003$ rad for the inverse setup are equal within the limits of accuracy. The linear regression returns correlation coefficients of 0.990 for the conventional and 0.998 for the inverse setup, clearly showing that the linear change in sensitivity describes the data correctly. The measurement was limited mainly by the accuracy of object positioning, while the influence of noise from the images was negligible. The object position with the largest error of the determined mean phase shift exhibited a standard deviation of only $\sigma_\varphi = 0.853 \cdot 10^{-3}$ rad, which is too small to be plotted as an error bar in Fig. 18. The corresponding standard deviation for an individual pixel was determined to be 0.061 rad on the average, corresponding to a signal-to-noise ratio (SNR) of SNR < 2.7. This high noise level is clearly visible in the images of Fig. 17. One can also compare the measured absolute phase shift with the theoretical prediction for the refraction angle. The extrapolated phase shifts can be converted into refraction angles α_i and α_c using the definition of sensitivity in Eq. (3.12) according to $\alpha = \Delta\varphi/S_0$. For our conventional setup, with $d = 303$ mm and $p_2 = 5$ μm, there is $S_0(x) = 2\pi d/p_2 \approx 4.1 \cdot 10^5$. Thus, we obtain refraction angles of $\alpha_c = 0.425 \pm 0.021$ μrad and $\alpha_i = 0.431 \pm 0.008$ μrad for the conventional and inverse geometry, respectively. These values are about 10% smaller than the theoretically expected value of $\alpha = 0.477$ μrad. This difference can be explained by an x-ray spectrum that contributes to the phase measurement, which has a mean energy that is higher than the 47.6 keV assumed in the calculation of the theoretical value. The correct theoretical value of $\alpha = 0.428$ μrad average of α_c and α_i is obtained for a mean x-ray energy of 50.2 keV, which is reasonable.

In conclusion, our measurements clearly show that the analytical description of the position dependence of the phase signal by a linear scaling function is correct. The angular sensitivity for the conventional and inverse geometries is highest, when the object is in the plane of the phase grating G_1, and decreases linearly when the object is moved toward the gratings G_0 and G_2, respectively. Additionally, we showed that the inverse geometry offers equal sensitivity in comparison to the conventional geometry and that both geometries therefore perform equally well at phase measurements.

3.1.3 Sensitivity in the dark-field-contrast channel

The dark-field signal has been defined in section 2.7 as the decrease of the visibility caused by the sample. While the signal is easily accessible in measurements, the origin of the dark-field contrast is still an active area of research. In Refs. [Bech10, Wang09], it is assumed that the dark-field signal is created by a coherent multiple scattering of the x-rays traversing the sample. The resulting diffuse deflections of the x-rays behind the sample are modeled by a Gaussian angular distribution with a standard deviation σ_D.

$$f(\theta) = \frac{1}{\sigma_D\sqrt{2\pi}} \exp\left(\frac{\theta^2}{2\sigma_D^2}\right). \tag{3.15}$$

On the basis of this approach, in Ref. [Bech10] a change $\Delta\sigma^2$ in the variance of this angular distribution after passing a sheet of material of thickness Δz can be connected to a material-dependent **linear diffusion coefficient** ε by

$$\varepsilon := \Delta\sigma^2/\Delta z. \tag{3.16}$$

Analytically, we may therefore write

$$\sigma_D^2 = \int_{\infty}^{-\infty} \varepsilon \cdot dz. \tag{3.17}$$

This measure allows the dark-field contrast generation to be written as a line integral. In order to bring the sensitivity in the dark-field-contrast channel into analogy with the sensitivity in the attenuation-contrast channel as defined in Eq. (3.2), we will define the 'signal' in the dark-field-contrast channel as the negative logarithm of the visibility decrease D. The sensitivity in the dark-field-contrast channel S_D can therefore be written

$$S_D = \frac{-\ln D}{\sigma_D^2} = \frac{-\ln\left(\nu_s/\nu_r\right)}{\int \varepsilon(\mathbf{r}) \cdot dz}. \tag{3.18}$$

Similar to the differential phase-contrast channel, the dark-field signal depends on the position of the sample relative to the gratings. The dependence is introduced by the fact that the deflections of the angular distribution given in Eq. (3.15) have to be propagated to the detection plane. If we denote the sample position within the interferometer by r, an deflection by an angle θ causes a displacement of x at the plane of detection. Displacement an angle are related by

$$\theta = \frac{x}{d \cdot f(r)}, \tag{3.19}$$

where d is the G_1 to G_2 distance and $f(r)$ the unit scaling function defined in Eq. (3.10). This can be re-interpreted by a position dependent scattering width

$$\sigma_D = \sigma_D' \cdot f(r), \tag{3.20}$$

where σ_D' is the width after traversing the sample and σ_D the width at the detection plane. With these considerations, the derivations in Refs. [Bech10, Wang09] suggest that the sensitivity in the dark-field-contrast channel is therefore equal to

$$S_D(r) = 2\pi^2 \frac{d^2}{p_2^2} \cdot f(r)^2 = S_{0,D} \cdot f(r)^2, \tag{3.21}$$

where we have defined the maximum sensitivity of the dark-field signal by

$$S_{0,D} := 2\pi^2 d^2 / p_2^2. \tag{3.22}$$

Please note that $S_D = S_\varphi^2/2$, which reflects a close connection between the phase and dark-field-contrast channels.

In Refs. [Yashiro10, Bennet10] the assumption of a diffuse scatterer is extended to include the form and length scale of the scattering structures within the sample. By this model, the dark-field signal is not only described by the scattering width of a diffuse angular distribution, but also by the spatial autocorrelation γ of the wavefront. Following the model presented in Ref. [Yashiro10], the sensitivity can be written

$$S_D(r) = S_{0,D} \cdot f(r)^2 \cdot \left(1 - \gamma(x,y;-mp)\right), \tag{3.23}$$

where the normalized autocorrelation γ between two points x and $x + \Delta x$ can be modeled by

$$\gamma(x,y;\Delta x) \approx \exp\left[-\left(\frac{|\Delta x|}{\xi\,(x,y)}\right)^{2H(x,y)}\right], \tag{3.24}$$

with ξ the correlation length of phase fluctuations and $0 < H < 1$ the so-called Hurst exponent.

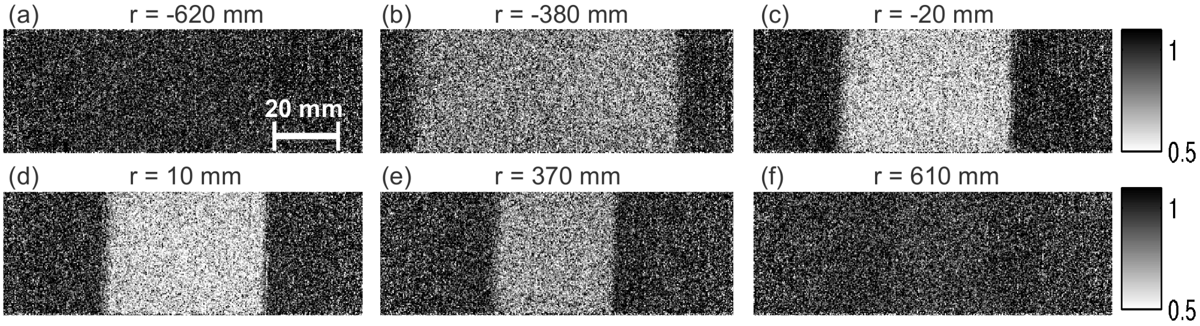

Fig. 19: *Measured dark-field signal for a paper stack at six different positions in the interferometer, (a)-(c) upstream of* G_1*, (d)-(e) downstream of* G_1*. The magnification is reduced as the sample position moves closer to the plane of detection.*

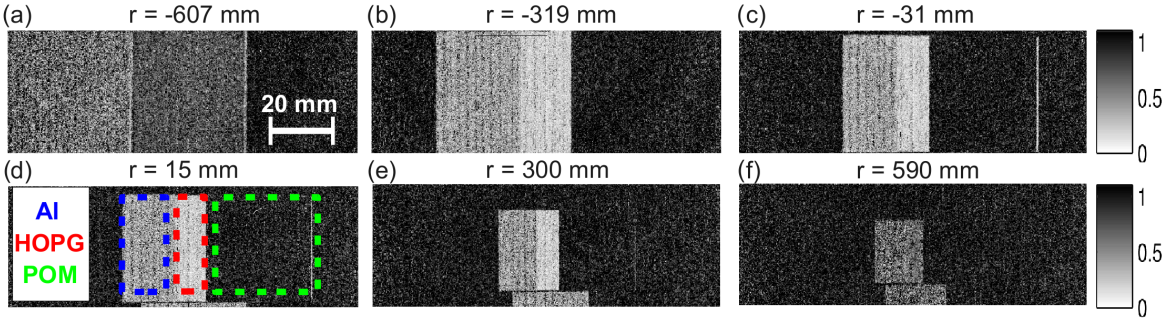

Fig. 20: *Measured dark-field signal for the Al, graphite and POM bar at six different positions in the interferometer, a)-c) upstream of* G_1*, d)-e) downstream of* G_1*. The magnification is reduced as the sample position moves closer to the plane of detection.*

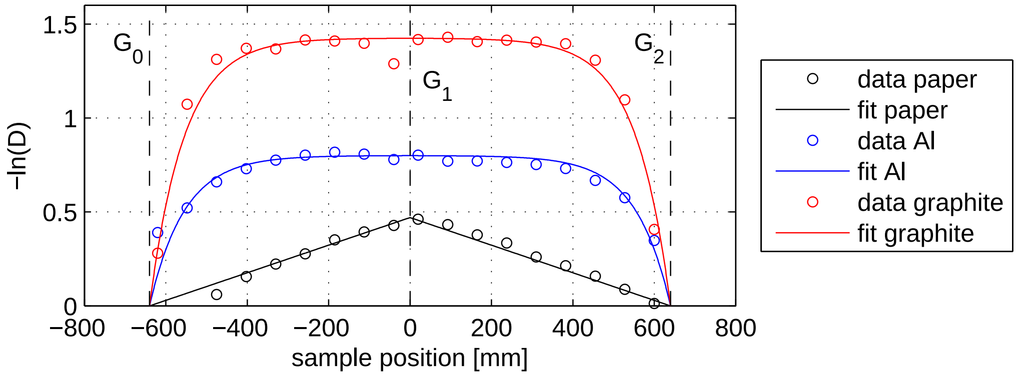

Fig. 21: *Negative logarithm of the measured dark-field signal D (circles) for the paper stack (black), the aluminium bar (blue) and the graphite bar (red) as a function of sample position, together with an analytical data fit (solid line). While the paper stack shows a linear dependence on the sample position, the dark-field signal for the aluminium and graphite bars is non-linear and approximately constant for positions close to the beam-splitter grating.*

To evaluate the position dependence in the dark-field-contrast channel, a series of measurements of a sample at different positions within the interferometer were performed, analogous to the measurements presented in section 3.1.2 for the phase-contrast channel. The measurements were carried out at the Technische Universität München in Garching, Germany. The source was a Phoenix XS 100 T microfocus transmission tube, with tungsten anode material on a diamond transmission target. For the measurements, the tube was operated at a voltage of 75 kV and a current of 20 W. No additional filtration was used. The gratings had a period of $p = 4.8\ \mu$m each, and structure heights of $h_0 = 105\ \mu$m, $h_1 = 16\ \mu$m, and $h_2 = 86\ \mu$m. All gratings were manufactured at the Karlsruhe Institute of Technology [Reznikova08]. The height of the phase grating corresponded to π-phase shift at the design energy of $E_0 = 45.9$ keV. The gratings were positioned in symmetric geometry, with the inter-grating distances set to the third fractional Talbot distance, corresponding to $l = d = 640$ mm. The distance from source point to source grating was 215 mm and the distance from analyzer grating to detector was 65 mm. As detector, a RadIcon Shad-o-Box 2048 flat panel detector was used, with a pixel pitch of 50 μm. The sensitivity area is 2048×1024 pixels horiz×vert, which equals 102×51 mm. The field of view was reduced to 1286×440 pixel by the lateral dimensions of the gratings. As samples, we used a paper stack of 10 sheets of paper, with approximately $d \approx 1$ mm thickness. Additionally, three rectangular bars were used, made from aluminium (Al), graphite (highly oriented pyrolytic graphite, HOPG) and polyoxymethylene (POM). The samples had a lateral extension of 5×10 mm^2, 2.5×10 mm^2 and 10×10 mm^2 horiz.×vert., respectively. Each sample was 10 mm thick. For each sample, nine positions upstream and nine downstream of the beam-splitter grating were measured, each separated by 72 mm. Each image was scanned with 10 s exposure time and 16 phase steps over one period of the interference pattern, using the analyzer grating for the stepping procedure. For each scan a reference scan was taken with identical parameters. The detector dependent data offset was corrected using five dark-field images.

The measured data for three positions upstream and three downstream of the beam-splitter grating can be seen in Fig. 19 for the paper stack and in Fig. 20 for the Al, HOPG and POM bars. Please note how the size of the samples reduces with decreasing magnification as the sample moves further away from the source. For the evaluation of the position dependence, the measured data for all samples and each position were averaged over the total area of the sample in the images. The negative logarithm of the resulting averaged dark-field signals as a function of sample position is shown in Fig. 21. For the paper stack, denoted by a subscript P, a maximum dark-field signal of $-\ln D_P(r = 0) = 0.47 \pm 0.02$ was determined by extrapolating the measured dark-field data shown in Fig. 21 at the position of the phase grating. For the Al and graphite bars, dark-field values of $\ln D_{Al}(r = 0) = 1.47 \pm 0.05$ and $\ln D_{HOPG}(r = 0) = 0.80 \pm 0.03$ were determined. The POM bar did not yield a well defined dark-field signal and will be omitted in the further discussion.

As can be seen in Fig. 21, the position dependence for the paper stack is essentially linear. In contrast, the Al and graphite bars exhibit an approximately constant dark-field signal for sample positions near the beam-splitter grating, while decreasing to zero in a non-linear way when moving the sample position towards the G_0 and G_2. It was tried to fit the measured data points with the function given by Eq. (3.23) as derived in Ref. [Yashiro10]. For the paper stack, a correlation length of $\xi \rightarrow 0$ and thus an autocorrelation of $\gamma = 0$ was assumed. Nevertheless, this leads to a quadratic dependence on the sample position if using Eq. (3.21), as opposed to the measured linear dependence. The sensitivity curves for the Al and HOPG bars cannot be fitted using the model given by Eq. (3.23). The position dependence in the measured data of the two bars as shown in Fig. 21 can be understood by a position dependence of the form

$$S_D(r) = S_{0,D}\left(1 - \exp\left(-c \cdot f(r)\right)\right), \tag{3.25}$$

where c is a constant. The reason for this discrepancy between measurement and theory is unknown and remains to be solved. Further discussions of this problem are given in section 9. In conclusion, the measurements show that the dark-field signal exhibits a strong dependence on the sample position within the interferometer. In contrast to the differential phase-contrast channel, where the position dependence is linear, in the dark-field channel it is non-linear and additionally dependent on the sample composition itself. This fact greatly complicates a correction of sensitivity-related effects in tomographic dark-field imaging, as the sample composition and its position dependence has to be known beforehand. For diffuse scatterers like the paper stack, the position dependence is linear. In this case the same correction approaches as in the differential phase-contrast channels can be applied.

3.2 Computed Tomography

In the previous section 3.1.2, we have shown that the measurement signals in differential phase-contrast and dark-field-contrast imaging depend on the sample position within the interferometer. In tomographic imaging, the recorded projections should ideally be line integrals of a constant function that represents an object property. Nevertheless, if the sensitivity of the interferometer varies along the beam path, the signal from a point outside the center of rotation will contribute differently to the reconstruction depending on the projection angle. While the position dependence is unproblematic for samples that are thin and that can therefore be approximated by a planar transfer function, an influence on tomographic reconstructions has to be expected for samples that are thick relative to the inter-grating distances. These considerations make a revision of the tomographic reconstruction algorithms necessary. In this section, we will therefore investigate tomographic imaging with a grating interferometer and work out an understanding and compensation for the artifacts introduced by sensitivity changes.

3.2.1 Computed attenuation tomography

The reconstruction of a three-dimensional linear attenuation coefficient distribution $\mu(\mathbf{r})$ from a given number of projections at different viewing angles is the fundamental problem of computed tomography. Pioneered in the 1970s, today CT is a standard tool for medical diagnostics and nondestructive testing. We will give a short introduction into the parallel-beam reconstruction algorithm, based on Ref. [Kak88]. For the sake of simplicity, we will reduce the formalism to two dimensions. An extension to three dimensions is straightforward.

Let the material distribution be described by the function $f(x,z)$. If (t,r) is the coordinate system obtained by rotating the rectangular coordinate system (x,z) by an angle θ

$$\begin{pmatrix} t \\ r \end{pmatrix} = \begin{pmatrix} \cos\theta & \sin\theta \\ -\sin\theta & \cos\theta \end{pmatrix} \cdot \begin{pmatrix} x \\ z \end{pmatrix}, \tag{3.26}$$

the projection $p(\theta,t)$ of $f(x,z)$ along the axis $r = -x\sin\theta + z\cos\theta$ onto the axis $t = x\cos\theta + z\sin\theta$ is given by

$$p(\theta,t) = \int_{-\infty}^{\infty} f(t,r)\, dr, \tag{3.27}$$

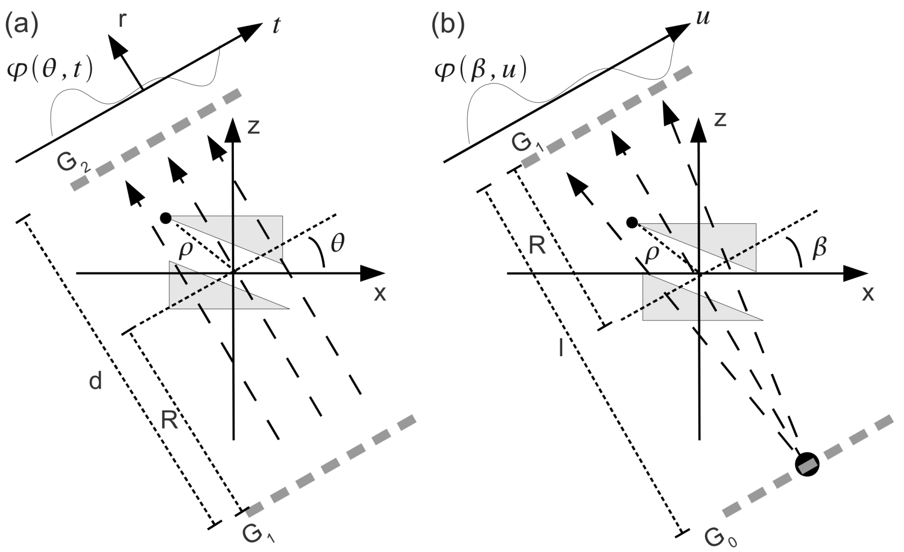

Fig. 22: *Schematic of the setup geometry, (a) parallel-beam CT with sample downstream of* G_1*, (b) fan-beam CT with sample upstream of* G_1*.*

as indicated in Fig 22 (a) for a phase-contrast measurement. Eq. (3.27) is known as the **Radon-transform** of $f(x,z)$ at angle θ. The Fourier transform of the projection with respect to the variable t

$$P(\theta,\tau) = \mathscr{F}\{p(\theta,t)\} \tag{3.28}$$

is connected to the Fourier transform of the material distribution

$$F(f,g) = \mathscr{F}\{f(x,z)\} \tag{3.29}$$

by the **Fourier-slice theorem**:

$$P(\theta,\tau) = F(f,g)|_{\substack{f\,=\,\tau\cos\theta \\ g\,=\,\tau\sin\theta}}. \tag{3.30}$$

In words, the Fourier transform of a projection $P(\theta,\tau)$ at angle θ is equal to a line through the Fourier transform of the material distribution parametrized by $(f,g) = (\tau\cos\theta,\tau\sin\theta)$. If the projections of the sample are known for all views, the spatial frequency representation of the material distribution is obtained, and thus the original material distribution may be reconstructed using inverse Fourier transform. This algorithm may be compactly written

$$f(x,z) = \int_0^{\pi} \mathscr{F}^{-1}\{P(\theta,\tau)\cdot H(\tau)\}\,d\theta. \tag{3.31}$$

The function $H(w)$ acts as a filter in Fourier domain and gives the algorithm its name **filtered backprojection algorithm** (FBP). The filter arises as the Jacobi-determinant from the coordinate transform between the rectangular coordinates (f,g) in frequency space and the polar coordinates (τ,θ) of the projections. In the simplest case, it is given by $H(\tau) = |\tau|$ and named ramp filter due to its shape. The band limited version of the ramp filter is known as filter of Ramachandran-Lakshminarayanan, or Ram-Lak in short. Because of

$$\mathscr{F}^{-1}\{P(\theta,\tau)\cdot H(\tau)\} = \mathscr{F}^{-1}\{P(\theta,\tau)\}\otimes\mathscr{F}^{-1}\{H(\tau)\} = p_\theta(t)\otimes h(t), \tag{3.32}$$

Eq. (3.31) can be rewritten

$$f(x,z)=\int_0^{\pi} p_\theta(t)\otimes h(t)\cdot d\theta. \tag{3.33}$$

The ideal filter function $H(\tau)$ is usually modified in practical CT applications to automatically include effects like the reduction image artifacts from sampling and noise. Apart from the ramp filter, the most commonly used filters are the Shepp-Logan, the cosine and the Hanning and Hamming-filters [Kak88].
In section 3.1.1, it was shown that the attenuation signal is not position-dependent in grating-based attenuation imaging, therefore, the standard algorithms may be applied to the reconstruction of the linear attenuation coefficient distribution without alterations.

3.2.2 Differential phase-contrast CT in parallel-beam geometry

In contrast to attenuation imaging, in differential phase-contrast imaging deflections are measured, causing the signal to exhibit a strong position dependence, as discussed in section 3.1.2. In the keV range, the deflection of x-rays is small compared to the size of the detector pixels. Therefore, the analytical description of the imaging process can be performed in paraxial approximation. As long as this approximation holds, we can model the sample by a straight-line projection onto a plane perpendicular to the beam direction, described by a two-dimensional transfer function. Using the sensitivity function defined by Eqs. (3.10) - (3.12), in the rotated coordinate system, a DPC projection φ can be compactly written as

$$\varphi(\theta,t)=\frac{\partial}{\partial t}\int_{-\infty}^{\infty} S_\varphi(r)\cdot\delta(t,r)\cdot dr. \tag{3.34}$$

Due to fundamental differences in the signal behavior in the two ranges upstream and downstream of G_1, in the following, we will discuss the contrast formation in tomographic imaging separately for both cases, first for parallel-beam geometry, then for fan-beam geometry. We will denote the DPC projections upstream of the beam-splitter grating $\hat{\varphi}$, while the projections downstream will be denoted $\check{\varphi}$.

Sample position between G_0 and G_1

If the sample is placed upstream of G_1 in parallel beam geometry, there is no dependence of the measured signal on the position of the sample and thus the sensitivity of the interferometer is constant with $S(z)=S_0$. This follows from Eqs. (3.12) and Eqs. (3.34) in the limit of $l\to\infty$. Using this property in Eq. (3.34), a DPC projection with the sample position upstream of G_1 can in this case be written

$$\hat{\varphi}(\theta,t) \quad = \quad S_0\cdot\frac{\partial}{\partial t}\int_{-\infty}^{\infty}\delta(t,r)\cdot dr, \tag{3.35}$$

with $S_0=2\pi d/p_2$. In Ref. [Pfeiffer07], it was shown that quantitative tomographic imaging of the refractive decrement distribution $\delta(x,y)$ is feasible with grating-based phase contrast. Following classical reconstruction approaches based on filtered backprojection [Kak88], a reconstruction formula for the parallel-beam geometry with sample position upstream of G_1 can be given by

$$\delta(x,z)=\frac{1}{S_0}\int_0^{\pi}\left[\hat{\varphi}(\theta,t)\otimes h(t)\right]\, d\theta, \tag{3.36}$$

where $\otimes$ denotes a convolution and $h_\varphi(t)$ is the DPC backprojection kernel. This kernel is obtained by including the integration of the differential data into the filtering step of the standard filtered backprojection algorithm. The spatial domain representation of the filter kernel is $h_\varphi(t) = \mathscr{F}^{-1}\{|\tau|/2\pi i\tau\}$, where $\mathscr{F}^{-1}$ is the inverse Fourier transform and the coordinate τ the Fourier space coordinate corresponding to t. Note that for the reconstruction of $\delta(x,z)$, only an angular range of π is needed in Eq. (3.36), since a projection at a projection angle of θ is related to the projection taken at an angle of $\theta+\pi$ by the relation $\hat{\varphi}(\theta,t) = -\hat{\varphi}(\theta+\pi,-t)$. We will denote two projections connected by this relation as being dual. In contrast to the corresponding relation for attenuation-contrast imaging, in DPC imaging, the dual projection has opposite sign due to the fact that gradient data are measured.

Sample position between G_1 and G_2

For a sample positioned between G_0 and G_1, the signal strength depends on S_0 and thus the propagation distance d between the gratings G_1 and G_2, as described by Eqs. (3.35). If, however, the sample is positioned downstream of G_1, a wavefront that is deflected by the sample has a reduced propagation distance to the plane of detection, depending on the sample's position relative to G_1 and G_2. The sensitivity of the interferometer $S(r)$ as described by Eqs. (3.10) - (3.12) therefore decreases linearly with decreasing distance between sample and the detection plane. A DPC projection downstream of G_1 can be written

$$\check{\varphi}(\theta,t) = \frac{\partial}{\partial t}\int_{-\infty}^{\infty} S_\varphi(r)\cdot\delta(t,r)\cdot dr. \tag{3.37}$$

Shifting the origin of the coordinate system to the axis of rotation, the sensitivity function is described by

$$S_\varphi(r) = S_0\cdot\left(1-\frac{R}{d}-\frac{r}{d}\right), \tag{3.38}$$

where R is the distance from the beam-splitter grating G_1 to the position of the axis of rotation, with $0<R<d$, as shown in Fig. 22 (a). Consequently, the sensitivity at the axis of rotation is

$$S_R = S_\varphi(r=0) = S_0\cdot\left(1-\frac{R}{d}\right). \tag{3.39}$$

The sensitivity function as given by Eq. (3.38) can be split into two parts: First, a constant term describing the sensitivity at the axis of rotation, and second, a term depending on the sample position r

$$S_\varphi(r) = S_R - S_0\cdot\frac{r}{d}. \tag{3.40}$$

By inserting Eq. (3.40) into Eq. (3.37) and separating both terms, we obtain

$$\check{\varphi}(\theta,t) = \frac{S_R}{S_0}\cdot\hat{\varphi}(\theta,t) - q(\theta,t), \tag{3.41}$$

where $\hat{\varphi}(\theta,t)$ is a projection as obtained upstream of G_1 after Eq. (3.35), while the function $q(\theta,t)$ is given by

$$q(\theta,t) = S_0\cdot\frac{\partial}{\partial t}\int_{-\infty}^{\infty}\frac{r}{d}\cdot\delta(t,r)\cdot dr. \tag{3.42}$$

Thus, a DPC projection $\check{\varphi}(\theta,t)$ for sample positions downstream of G_1 can be split into a term equal to the projection without position dependence $\hat{\varphi}(\theta,t)$, scaled down by a factor of S_R/S_0 which is determined by the position of the axis of rotation relative to the gratings, plus an additive term $q(\theta,t)$. This additive term introduces deviations to measurements with the sample position upstream of G_1 and therefore leads to differences in the tomographic reconstructions.

Since the sensitivity is known in the experiment for all projection angles, its linear characteristic can be used for the correction of the position dependence. Various methods can be conceived, ranging from iterative numerical methods, algebraic reconstruction approaches, to weighted Fourier-based backprojection algorithms. Nevertheless, the most simple approach to avoid artifacts in the reconstruction of the refractive decrement can be found by extending the angular range of the tomographic scan from π to 2π: By using the symmetries $\hat{\varphi}(\theta,t) = -\hat{\varphi}(\theta+\pi,-t)$ and $q(\theta,t) = q(\theta+\pi,-t)$, one easily arrives at the relation

$$\check{\varphi}(\theta,t) - \check{\varphi}(\theta+\pi,-t) = \frac{2S_R}{S_0} \cdot \hat{\varphi}(\theta,t). \tag{3.43}$$

In other words, combining two dual projections with projection angles apart by π cancels the position dependence introduced by the additive term $q(\theta,t)$ and one obtains an image corresponding to a position-independent projection upstream of G_1, scaled by a constant factor determined by the sensitivity at the axis of rotation. Using this property, a simple reconstruction formula for tomographic data sets with projections affected by the sensitivity changes downstream of G_1 can be given: extending the angular range in Eq. (3.36) from π to 2π and using Eq. (3.43), we obtain an artifact-free reconstruction of the distribution of the decrement of refraction by

$$\delta(x,z) = \frac{1}{2S_R} \int_0^{2\pi} \left[\check{\varphi}(\theta,t) \otimes h_\varphi(t)\right] \, d\theta. \tag{3.44}$$

In comparison to the reconstruction formula for parallel-beam data upstream of G_1 as described by Eq. (3.36), this result exhibits two significant differences: First, when using the standard filtered backprojection algorithm, an angular range over the full circle is needed for an artifact-free reconstruction of the refractive decrement distribution. Second, the reconstructed data are scaled down by a factor determined by the sensitivity at the axis of rotation S_R/S_0. This can be understood by considering that, for a full circle scan, the sensitivity at the axis of rotation corresponds to the mean propagation distance towards the plane of detection for every point in the slice. When comparing tomographies with the sample position upstream and downstream of G_1, this factor causes an overall reduction of the signal-to-noise ratio (SNR) for tomographies downstream of G_1. These considerations remain valid even if other reconstruction approaches like iterative methods or weighted backprojection are utilized.

If less than a full angular range is used for imaging, tomographic reconstruction cannot be performed with standard algorithms. The position dependent signal strength has to be compensated in the reconstruction algorithm by an increased weighting of the areas in the slice with low sensitivity for a quantitatively correct reconstruction. Nevertheless, not only the signal, but also the noise is enhanced by this increased weight. Tomographic reconstructions with reduced angular ranges will therefore exhibit position dependent and non-uniform SNR properties. The SNR will depend on the angular range and the distance of a given point in the slice to the axis of rotation. Let θ_{min} and θ_{max} be the projection angles in the first and in the last measurement projection, respectively, and ρ the distance of a given point to the axis of rotation. For this object point in the reconstructed slice, the weight will be determined by the mean sensitivity that this point is subjected to during the tomographic measurement, given by

$$\overline{S}(\rho, \theta_{min}, \theta_{max}) = S_R + S_0 \cdot \frac{\rho}{d} \cdot \int_{\theta_{min}}^{\theta_{max}} \cos\theta \, d\theta, \tag{3.45}$$

By the position dependence of the measured signal, the SNR in each point of the reconstructed slice is reduced by a factor of $\overline{S}/S_0$ relative to the situation upstream of G_1. For a tomography

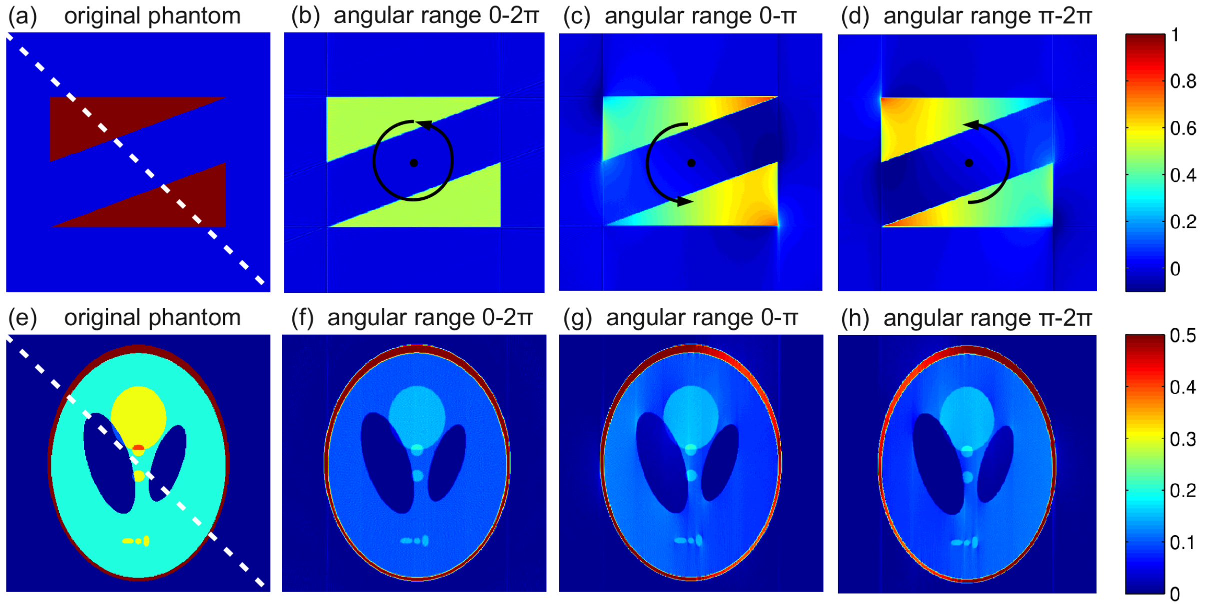

Fig. 23: *Simulated tomographic slices of two wedges and a Shepp-Logan head phantom: (a) the phantom used as input for the simulation, (b) the reconstruction result for a full range scan from* $0-2\pi$*, (c) for an angular range from* 0 *to* π *and d) for an angular range from* π *to* 2π*, (e)-(h) same images for the head phantom. The angular projection ranges are indicated by arrows in (b)-(d). The* 2π*-range reconstruction leads to a correct reconstruction of the phantom, albeit scaled-down by a factor of* $S_R/S_0 = 0.5$*. In contrast, reconstruction (c) and (d) clearly show artifacts. The data are scaled relative to the original phantom. In (a) and (e), the position of the profiles in Fig. 24 is indicated by a dashed white line.*

with an angular range of 2π, we obtain $\overline{S}(\rho, 0, 2\pi) = S_R$, the SNR in the slice is globally reduced relative to the situation upstream of G_1 by the factor $S_R/S_0 = 1 + R/d$, as described by Eq. (3.44). Therefore, placing the sample downstream of G_1 is the more disadvantageous, the closer the axis of rotation is placed to the plane of detection.

In order to verify the above considerations for sample positions between G_1 and G_2, a simulation was performed in parallel-beam geometry. Beginning from an initial refractive decrement distribution, each point in the sample is first weighted with the sensitivity at its corresponding position relative to the gratings, projected towards the detector along straight lines and subsequently differentiated. The tomographic scan was simulated by rotating the refractive decrement distribution, where bicubic interpolation was used for the calculation of the rotated sample. After collecting the projections for all angular views, the resulting sinogram is reconstructed using the standard algorithm given in Eq. (3.36), ignoring the sensitivity dependence in the reconstruction. The axis of rotation was halfway between G_1 and G_2, so that $R = d/2$ and $S_R = \pi/p_2 \cdot d$. The field of view in the slices was chosen to encompass the complete space between the two gratings. Thus, the sensitivity decreases from its maximum value at the top of the slice to zero at the bottom. Three simulations were performed for each sample, using an angular range of 2π, a range from 0 to π and a range from π to 2π, respectively. An angular increment of 1° was used for the tomographies over the half circle, while the increment was 2° for the full circle, thus keeping the total number of projections equal in all simulations. As samples, a pair of homogeneous unit-valued wedges and a standard Shepp-Logan head phantom [Kak88] were used, as shown in Fig. 23 (a). The resolution of both phantom slices was chosen as 512×512 pixels^2. The results are summarized in Fig. 23.

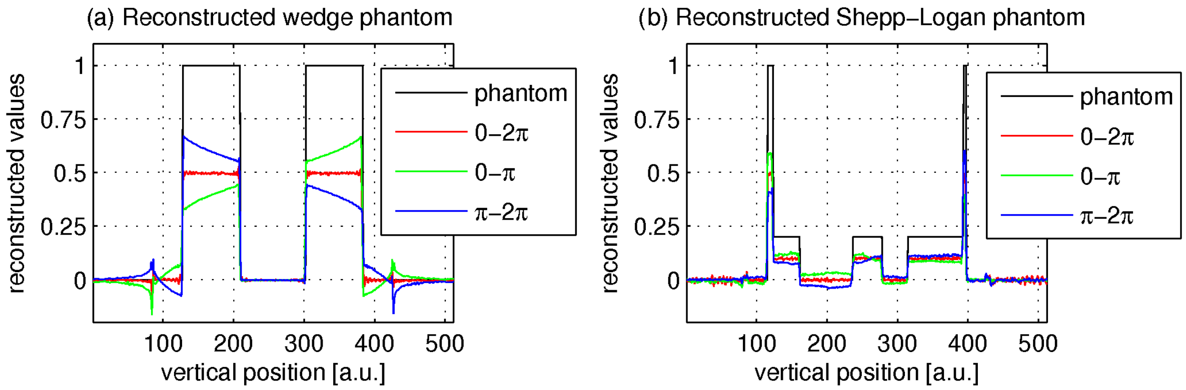

Fig. 24: *Vertical profiles through the reconstructed slices, (a) for the wedge phantom, (b) for the Shepp-Logan head phantom, as indicated in Fig. 23 (a) and (e). The full scan reconstruction is artifact-free, but scaled down by a factor of the sensitivity at the axis of rotation, i.e.* $S_R/S_0 = 1/2$. *In contrast, the two half-circle reconstructions show deviations. It can be seen that the sum of both half-circle reconstructions is equal to the full circle reconstruction, as the artifacts are exactly opposite in sign to each other.*

The original phantoms are shown in Figs. 23 (a) and (d). If the data are collected over an angular range of 2π, the phantoms are reconstructed without artifacts, as shown in Figs. 23 (b) and (f). Nevertheless, quantitatively, the reconstructed values are scaled down relative to the original phantom by a factor corresponding to the sensitivity at the axis of rotation, in the simulation by $S_R/S_0 = 1/2$. However, if collecting the data over an angular range of less than 2π leads to image artifacts when using the standard reconstruction algorithms. This can be seen in Figs. 23 (c) and (d) for the wedge phantom and (f) and (g) for the head phantom, where angular ranges of $0-\pi$ and $\pi-2\pi$ were chosen. Fig. 24 shows a diagonal profile through the original phantom and the reconstructed images, as indicated by the dashed line in Figs. 23 (a) and (e). The deviations in the two half circle reconstructions can be seen to be exactly dual to each other. Thus, by summing both half-circle reconstructions, one obtains the artifact-free full-circle reconstruction. These simulation results prove the correctness of the performed analysis in the case of a sample positioned downstream of G_1.

3.2.3 Differential phase-contrast CT in fan-beam geometry

In fan-beam geometry and for sample positions between G_0 and G_1, the measured signal depends on the sample position due to the fact that the gradients measured in differential data scale with magnification M, as first described by Ref. [Engelhardt07]. This consideration is consistent with measurements in parallel-beam geometry, as the magnification is constant with $M = 1$ and therefore independent of sample position in this case. This additional dependence on the magnification has to be included into the fan-beam reconstruction algorithm to obtain correct quantitative results. The measured signal is reduced when the sample is positioned closer to G_0. Same as in parallel beam geometry between G_1 and G_2, this decrease has to be compensated in the reconstruction algorithm by an increased backprojection weight. For tomographies in fan-beam geometry with a sample position between G_0 and G_1, the sensitivity reduction is equivalent to the SNR reduction as observed in parallel-beam geometry with a sample position between G_1 and G_2. Nevertheless, the reason for the SNR reduction is a dependence on the magnification in the first case, and a dependence on the propagation distance to the plane of detection in the latter. For reduced angular ranges, the SNR will again not be uniform in the slice, but instead depend on the angular range and the distance of each point to the axis of rotation, as described by Eq. (3.45).

The schematic of a fan-beam projection $\varphi(\beta,u)$ is shown in Fig. 22 (b), where β and u are the fan-beam projection angle and projection axis, respectively. Since a set of fan-beam projections can be reordered into parallel-beam projections [Kak88], a direct DPC fan-beam reconstruction formula can be derived from Eq. (3.36) (sample between G_0 and G_1) and Eq. (3.44) (sample between G_1 and G_2) by nothing more than a coordinate transform, as presented for example in Ref. [Qi08]. Changes to the classical reconstruction algorithm are solely caused by the fact that the measured data are differential and scale with magnification. Therefore, we can conclude that in fan-beam geometry, the DPC interferometer performs equally well for sample positions upstream and downstream of the beam splitter grating.

3.2.4 Sensitivity in dark-field CT

In contrast to the results obtained for the differential phase-contrast channel in section 3.2.2, the position dependence of the dark-field signal introduces further complications into tomographic reconstructions. For a diffuse scatterer with a vanishing phase correlation in the wavefront like the paper stack in section 3.1.3, the measurement signal shows a linear dependence on the sample position, the same as in the phase-contrast channel. The algorithms presented in section 3.2.2 can therefore be used in this case without further alterations. For materials like the Al or graphite bar however, the position dependence shows a different, non-linear relationship. Therefore the position dependence itself depends on the material composition, which is unknown beforehand in the measurement. Therefore, no a priori correction of the position dependence is possible in dark-field CT during the reconstruction procedure. Instead, for a correction, iterative and algebraic methods have to be used and developed, greatly increasing reconstruction complexity and time. The additional dependence of the dark-field signal on the orientation of the sample structures [Jensen10] introduces further complexity to the problem of developing appropriate reconstruction algorithms.

Analogous to the differential phase-contrast channel, if standard reconstruction algorithms are used, it is preferable to position the sample as close as possible to the beam-splitter grating G_1.

3.3 Summary

In this section, the dependence of the three contrast channels on the position of the sample within the interferometer has been investigated. The position dependence was generalized in the concept of interferometer-sensitivity in section 3.1. While the attenuation does not show any position dependence, the phase signal is highest at the position of the beam-splitter grating and falls off linearly towards G_0 and G_2. The dark-field signal shows a non-linear position dependence and additionally is dependent on the sample composition. Only for diffuse scatterers it show a linear relationship, while the measurement signal is highest near the G_1 and falls off in a non-linear way towards G_0 and G_2 for other samples. Additionally, the conventional and inverse geometries were shown to exhibit equal sensitivity in theory and in measurement, due to the dependence of the sensitivity on the period of the beam splitter. Based on these basic results for radiographies, tomographic imaging using a grating interferometer was investigated for all three contrast channels in section 3.2. The attenuation CT and parallel-beam phase-contrast CT may be performed with standard reconstruction algorithms. For DPC imaging, there are principal differences in image formation depending on the position of the sample, upstream or downstream of the beam-splitter grating. While the DPC signals scales with magnification between G_0 and G_1, for sample positions between G_1 and G_2 the position dependence is introduced by propagation effects. Nevertheless, artifact-free reconstructions from tomographic data sets are feasible for all sample positions. When the sample is positioned downstream of G_1, a wider angular range is needed for artifact-free reconstructions. Measurements with the sample position upstream of the beam-splitter grating are therefore preferable, as, with correctly adapted algorithms, the image reconstruction is in this case artifact-free even for reduced angular ranges and additionally exhibits a higher SNR in the parallel-beam case. Dark-field tomography remains difficult and an unresolved problem, due to the non-linear and material-specific position-dependence of the signal strength.

4 Imaging with atomic number contrast

The grating-based x-ray imaging technique is capable of delivering three contrast channels simultaneously, namely attenuation, phase-contrast and dark-field contrast. While each contrast is interesting in itself, in this section, we will investigate how the combination of the data from the attenuation and phase-contrast channels allows the calculation of the atomic number of the sample under investigation. In section 4.1, it is shown how the basic dependencies of the attenuation and refraction decrements on material parameters can be used for the calculation an atomic number contrast. In sections 4.2 and 4.3, the basic idea of the technique will be extended to be applicable to compound materials and different modes of imaging, while in section 4.4, an experimental verification is presented. In section 4.5 finally, the numerical stability of the calculation of the contrast is discussed.
The results presented in this section have been published in [Chabior11B].

4.1 Basic principles of atomic number contrast

The attenuation of x-rays in a sample of known thickness depends on the atomic number, the density of the material and the energy of the utilized x-ray photons, as discussed in section 2.1. Analytically, the measured attenuation can be considered a function of those three unknowns. By performing a measurement at two different and well defined energies, a separation of the density and atomic number can be achieved, allowing the calculation of an atomic number contrast. This is the basis for the dual energy approach in classical attenuation imaging [Engeler90].
In grating-based imaging, a determination of the atomic number is simplified, since the measurement does not only provide information on the attenuation of the sample, but also on the phase shift. In section 2.1, the basic dependencies of the attenuation and refraction decrements were given by

$$\delta = \frac{r_e \lambda^2}{2\pi} \cdot \rho_N \cdot Z \qquad \text{and} \qquad \beta = \frac{\lambda}{4\pi} \cdot \rho_N \cdot \left(C_1 \cdot \frac{Z^{C_2}}{E^3} + Z\sigma_{KN}(E) \right). \tag{4.1}$$

By taking the ratio between the attenuation and refraction decrements for a given material, the dependence on the atomic density ρ_N is canceled out. We obtain

$$\frac{\beta}{\delta} = \frac{1}{2r_e\lambda} \cdot \left(C_1 \cdot \frac{Z^{C_2-1}}{E^3} + \sigma_{KN}(E) \right), \tag{4.2}$$

where C_1 and C_2 are constants and r_e is the classical electron radius. This expression can be solved for the atomic number Z, yielding a quantity that is computable from measurement data

$$Z = \left(2r_e\lambda \cdot \frac{E^3}{C_1} \cdot \frac{\beta}{\delta} - \frac{E^3}{C_1}\sigma_{KN}(E) \right)^{\frac{1}{C_2-1}}. \tag{4.3}$$

By the definition of new, energy dependent constants c_1, c_2 and c_3, the above relation can be simplified to [Qi10]

$$Z = \left(c_1 \cdot \frac{\beta}{\delta} - c_2 \right)^{c_3}. \tag{4.4}$$

Since $c_1 \sim E^2$ and $c_2 \sim E^3\sigma_{KN}(E)$ depend only on the energy and natural constants and the exponent c_3 is approximately constant with $c_3(Z,E) \approx 1/3$, the three parameters can in

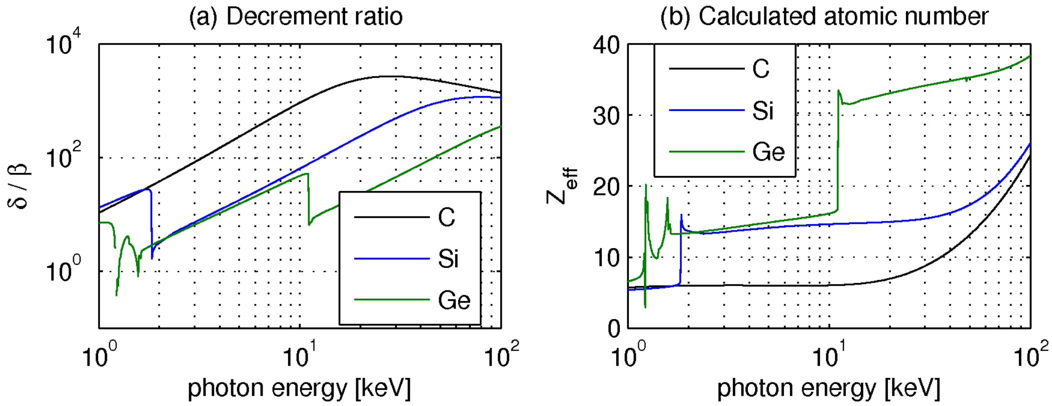

Fig. 25: *(a) The ratio* δ/β *of the refraction and attenuation decrements as a function of photon energy and (b) the resulting calculated effective atomic number. Above the K-edge of the element, the calculated atomic number is approximately constant. For higher energies and low atomic numbers, the rising contribution of Compton scattering leads to a rise in the calculated atomic number. The calculation is optimized for the reconstruction of carbon. Thus the calculated atomic number for material Ge is not strictly constant due to its different dependence on the energy.*

principle be fully determined if the energy is known in the measurement. Alternatively, they can be determined by a calibration measurement using well defined samples and experimental conditions, with one calibration measurement for each unknown. The constant c_2 accounts for Compton scattering and is negligible for energies below 20 keV.

An exemplary calculation of the ratio of the attenuation and refraction decrements can be seen in Fig. 25 (a). The δ/β-ratio rises approximately with E^3 for all materials for low energies. For higher energies and with increasing contribution of Compton scattering, the differences in the δ/β-ratios between the materials decrease, making a separation of the different elements difficult for energies $>$ 100 keV. In Fig. 25 (b), the effective atomic number was calculated from the data shown in Fig. 25 (a). For the calculation, $c_3 = 1/3$ was chosen, while c_1 was determined by reproducing the atomic number of carbon at low energies. The contribution of Compton scattering was ignored, i.e. $c_2 = 0$. As a result, the calculated atomic numbers are not constant at high energies, but instead begin to rise with increasing contribution of Compton scattering, the more, the lower the atomic number Z. It can be seen, that above the K-edges of the elements involved, the calculated values correspond to the atomic number of the material. The material-dependence of c_3 causes the calculated atomic number for germanium to rise marginally with increasing energy.

4.2 Radiography versus tomography

The refraction and attenuation decrements are directly obtainable from tomographic reconstructions alone. Nevertheless, a calculation of an atomic number contrast is also feasible using solely radiographic image data. In radiography, only the projections, or in other words, the line-integrals of the material distribution along the x-ray path are obtainable, thus containing the thickness of the sample as an additional unknown. Nevertheless, if the measured differential phase and attenuation images are combined in a meaningful way, the dependence on the material thickness can be canceled out. Two approaches may be conceived for the reconstruction of the ratio of the attenuation and refraction decrement: First, by the integration of the differential phase-contrast image, and second, by the differentiation of the attenuation-contrast image. The integration of the DPC image $\varphi(x,y)$ along x yields the phase shift $\Delta\Phi$ of the wavefront

$$\Delta\Phi(x_j,y_k)=\frac{a\cdot p_2}{\lambda\cdot d}\sum_{i_1}^{j}\varphi(x_i,y_k)=\int_0^L\gamma\cdot dz, \tag{4.5}$$

with a the pixel size, p_2 the period of the analyzer grating, λ the wavelength, d the inter-grating distance and L the thickness of the sample. For a homogeneous material (μ=const., no variation of material, only sample thickness), the ratio between the integrated phase shift $\Delta\Phi$ and attenuation T thus yields

$$\frac{\Delta\Phi}{T}=\frac{\gamma\cdot L}{\mu\cdot L}=\frac{1}{2}\cdot\frac{\delta}{\beta}, \tag{4.6}$$

which is the decrement ratio needed for the calculation of the atomic number. The dependence on the material thickness is thereby canceled out.

The second approach uses the differentiation of the attenuation image. One obtains

$$\partial_x T=\frac{\partial}{\partial x}\int_0^L\mu\cdot dz=\mu\partial_x L. \tag{4.7}$$

For a homogeneous sample, taking the ratio of the two differential images yields

$$\frac{\varphi}{\partial_x T}=\frac{\frac{\lambda d}{p_2}\cdot\gamma\cdot\partial_x L}{\mu\cdot\partial_x L}=\frac{\lambda d}{2p_2}\cdot\frac{\delta}{\beta}, \tag{4.8}$$

and thus, as all scaling factors are known from the measurement, the calculation of the atomic number remains feasible in this case as well.

4.3 Multi-material and polychromatic approach

So far, we have considered homogeneous and elementary materials only. If compounds or material mixtures are taken into consideration, Eq. (4.4) has to be altered. Instead of using the elemental decrements, one has to work with effectively averaged decrements. In radiographic imaging, if the sample consists of multiple materials along the path of the beam, the effective decrements are calculated by a weighted average, where the weights are given by the thickness of each material

$$\delta_{\text{eff}}=\frac{1}{L}\int_0^L\delta\cdot dz. \tag{4.9}$$

with L is the total sample thickness. Similarly, for the attenuation decrement one obtains

$$\beta_{\text{eff}}=\frac{1}{L}\int_0^L\beta\cdot dz. \tag{4.10}$$

If the sample consists of a stacked layer of different materials along the path of the ray, the integral will become a sum over the different layers.

As explained in more detail in section 2.1, for a single compound material, the effective decrements may be be obtained by

$$\delta_{\text{eff}}=\rho_{\text{eff}}\sum_i w_i\cdot\left(\frac{\delta}{\rho}\right)_i, \tag{4.11}$$

and

$$\beta_{\text{eff}}=\rho_{\text{eff}}\sum_i w_i\cdot\left(\frac{\beta}{\rho}\right)_i, \tag{4.12}$$

with ρ_{eff} the mass density of the compound material, w_i the weight fraction of element i,

$$\left(\frac{\beta}{\rho}\right)_i = \frac{\lambda}{4\pi} \cdot \frac{N_A}{M_i} \cdot \left(C_1 \cdot \frac{Z_i^{C_2}}{E^3} + Z_i \sigma_{KN}(E)\right) \tag{4.13}$$

is the mass attenuation decrement and

$$\left(\frac{\delta}{\rho}\right)_i := \frac{r_e \lambda^2}{2\pi} \cdot \frac{N_A}{M_i} \cdot Z_i, \tag{4.14}$$

the mass refraction decrement of element i. Analogous to Eq. (4.4), taking the ratio of the effective decrements yields a dependence on the atomic numbers Z_i of the constituents of the compound by

$$\frac{\beta_{\text{eff}}}{\delta_{\text{eff}}} \sim \frac{\sum_i w_i Z_i^{C_2}/M_i}{\sum_i w_i Z_i/M_i}. \tag{4.15}$$

In comparison to Eq. (4.2) for elemental materials, this relation motivates the definition of an **effective atomic number** Z_{eff} by

$$Z_{\text{eff}}^{C_2-1} := \frac{\sum_i w_i Z_i^{C_2}/M_i}{\sum_i w_i Z_i/M_i}. \tag{4.16}$$

The effective atomic number can be understood as the atomic number of a hypothetical element yielding the same measurement results as the compound material. In attenuation imaging, the effective atomic number is usually defined using only the material dependence of the attenuation index by [Engeler90]

$$Z_{\text{eff}}^{C_2-1} = \sum_i f_i Z_i^{C_2-1}, \tag{4.17}$$

where $C_2(Z,E) \approx 4$ and f_i is the electron fraction of element i. From Eqs. (4.16) and (4.17), it can be seen that high Z materials contribute more to the calculated effective atomic number than low Z materials.

If a polychromatic spectrum is used, the measured decrements will be an average of the decrements for each monochromatic photon energy that contributes to imaging (see section 6 for a discussion of polychromatic effects). As the dependencies for phase and attenuation are different, the effective decrements will be given by the two effective energies $\overline{E}_\delta$ for the phase and $\overline{E}_\beta$ for the attenuation contrast. If the different effective energies are taken into account, the effective atomic number can be calculated by

$$Z_{\text{eff}} = \left(2 r_e hc \frac{\overline{E}_\beta^2}{\overline{E}_\delta^2} \cdot \frac{\overline{E}_\beta^2}{C_1} \cdot \frac{\beta}{\delta} - \frac{\overline{E}_\beta^3}{C_1} \sigma_{KN}(\overline{E}_\beta)\right)^{\frac{1}{C_2-1}}, \tag{4.18}$$

where h is Planck's constant and c the speed of light. In its mathematical structure, Eq. (4.18) is equal to Eq. (4.4), only with minimally altered values for the three parameters c_1, c_2 and c_3. Thus, if both effective energies are known, the constants c_1, c_2 and c_3 can be calculated or calibrated in the same way as in the monochromatic case. Since the difference between both effective energies is small in a well designed setup, Eq. (4.4) can be used instead of Eq. (4.18) without introducing large deviations from the measured data.

It should be noted that the dependence on two different effective energies introduces a complicated dependence on beam hardening and other polychromatic effects into the calculation of the atomic number contrast (see section 6.2). Nevertheless, an in-depth discussion of beam-hardening effects in the calculation of the effective atomic number will not be performed in this thesis.

4.4 Experimental verification

In order to test the validity of the analytical approach, a measurement was performed using some well defined test samples. The measurements were performed by M. Bech et al. at the coherence beamline ID19 at the European Synchrotron Radiation Facility (ESRF) in Grenoble, France. A monochromatic beam of 35 keV photon energy was used, with an energy width of $\Delta E/E = 10^{-4}$. The beam was attenuated with 3 mm of aluminium. As beam-splitter, a π-phase grating with $p_1 = 3.995$ μm period was used. The inter-grating distance was chosen as $d = 408$ mm, corresponding to the fifth fractional Talbot distance of the beam-splitter grating. The analyzer grating had an period of $p_2 = 2.0$ μm. Both gratings were manufactured at the IMT [Reznikova08]. With this grating arrangement, a mean visibility of $\overline{v} = 0.245$ was achieved. Using a magnifying optic, an effective pixel size of 31.15×31.15 μm^2 over a field-of-view of 1400×330 pixels was achieved. The phase stepping was performed with three steps (four points) over one period. For the tomography, 499 projections of 0.721° over the full circle with 0.5 s exposure time were taken. Additionally 21 dark images and 10 reference images were taken. The sample arrangement consisted of several plastic cylinders with a diameter of 5 mm each, made from the materials polypropylene (PP, $[C_3H_6]_n$), polyethylene (PE, $[C_2H_4]_n$), polymethylmethacrylate (PMMA, $[C_5H_8O_2]_n$), polyoxymethylene (POM, $[CH_2O]_n$) and polyvinyl chloride (PVC, $[C_2H_3Cl]_n$). Two cylinders with diameter 6 mm, filled with water (H_2O) and ethanol (EtOH, C_2H_6O), respectively, were added for calibration purposes. The measurements were performed in a water bath. The reconstructed quantitative results for the attenuation and refraction decrements can be seen in Fig. 26.

From the data for β and δ, the effective atomic number was computed using Eq. (4.4). We assumed $c_3 = 1/3$ and used the water cylinder as a fixpoint for the calculation of the coefficients c_1 and c_2, which were determined as $c_1 = 2.56 \cdot 10^6$ and $c_2 = 835$. The computed atomic numbers are given in Fig. 27 (a). For each cylinder, the atomic number data were averaged over the area of the cylinders to obtain a higher signal to noise ratio. The resulting effective atomic numbers for the different sample materials, together with the corresponding literature values as determined by Eq. (4.17) with atomic masses after Ref. [NIST09], are shown in Fig. 27 (b). The calculated atomic numbers show a good agreement with the literature values, with the relative deviation being below 5% for all used materials. Thus, we can conclude that the analytical approach leads to correct results and may be recommended for quantitative analysis of unknown material distributions.

4.5 Numerical stability

For an assessment of the image quality in the calculated atomic number images, an analysis of the noise properties has to be performed. For the image quality in the atomic number contrast, the mathematical structure of Eq. (4.4) has to be considered: First, the ratio of the phase and attenuation-contrast images is computed. A constant is subtracted and from the resulting number, the root is taken. In this algorithm, firstly, the calculation of the ratio of the attenuation and refraction decrement is problematic, as in areas without sample, forming the ratio is equivalent to a division of zero by zero. Secondly, as a constant number c_3 is subtracted from the resulting ratio, high noise variance may lead to the discriminant to become negative in some pixels. In both cases, the calculation of the atomic number will become numerically unstable, especially in the presence of high variance noise and in the absence of a sample.

Fig. 28 illustrates the numerical instability of the calculation of the atomic number contrast, showing the measured attenuation and refraction decrements for a PMMA cylinder of 10 mm

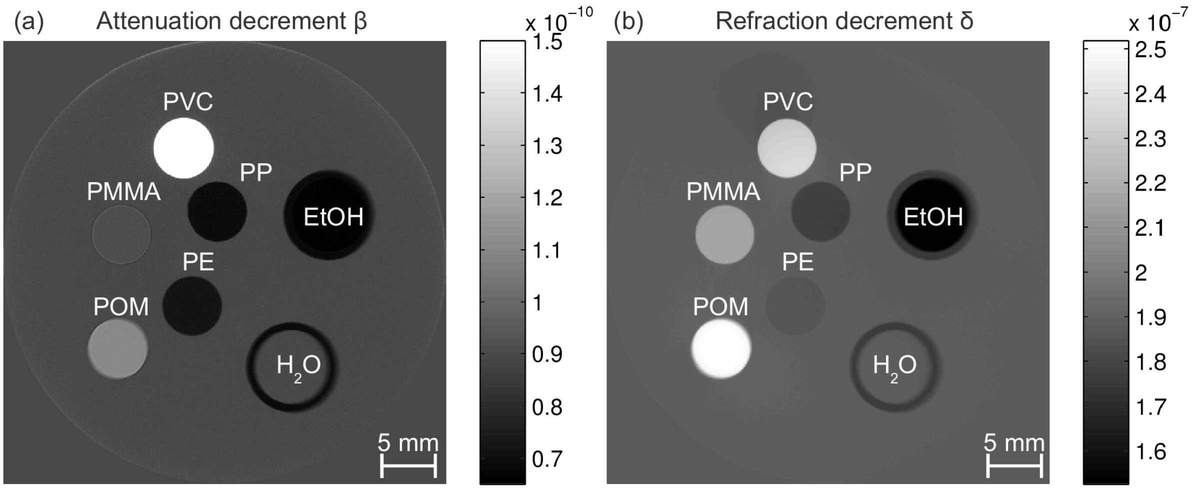

Fig. 26: *(a) Reconstructed attenuation decrement β and (b) reconstructed refraction decrement δ for different polymers and liquids in a water bath, measured with a monochromatic synchrotron beam of $E_0 = 35$ keV.*

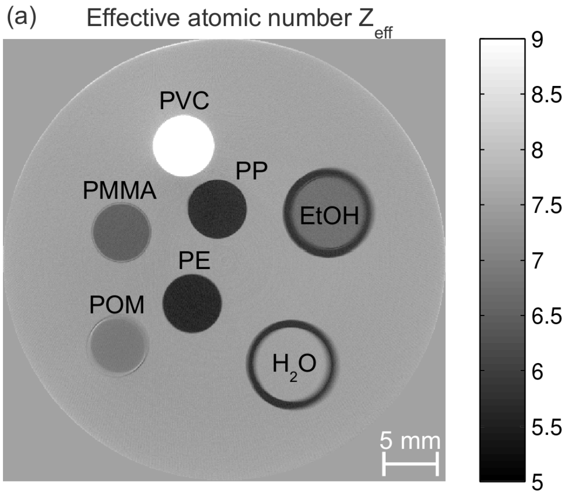

(b) Numerical results

Material	measured	literature	deviation
PP	5.77	5.60	3.0 %
PE	5.66	5.53	2.4 %
PMMA	6.55	6.56	0.1 %
POM	6.95	7.03	1.1 %
PVC	14.4	14.3	0.8 %
EtOH	6.77	6.47	4.7 %

Fig. 27: *(a) Effective atomic number of different plastic cylinders as calculated from the measured decrements presented in Fig. 26. (b) Averaged effective atomic numbers for the different cylinders shown in (a), in comparison to calculated literature values.*

diameter, measured relative to air. The measurements were performed at the PSI in Villigen, Switzerland. The setup is identical to the conventional setup described in section 3.1.2, with identical recording parameters. For the calculation of the atomic number we assumed $c_3 = 1/3$ and adjusted the parameters c_1 and c_2 so that the correct value for the atomic number of PMMA is obtained. In Fig. 28 (c), it can be seen that the relatively high noise variance in the attenuation and differential phase image causes the calculation of the atomic number to become unstable in the areas where no sample is present. This causes the high fluctuations of the calculated values in the empty area around the PMMA cylinder.

The numerical calculation of the atomic number can be made more stable by introducing a correction parameter $\varepsilon > 0$ into the calculation of the atomic number according to

$$Z_{\text{eff}} = \left| c_1 \cdot \frac{\beta}{\delta + \varepsilon} - c_2 \right|^{c_3} . \tag{4.19}$$

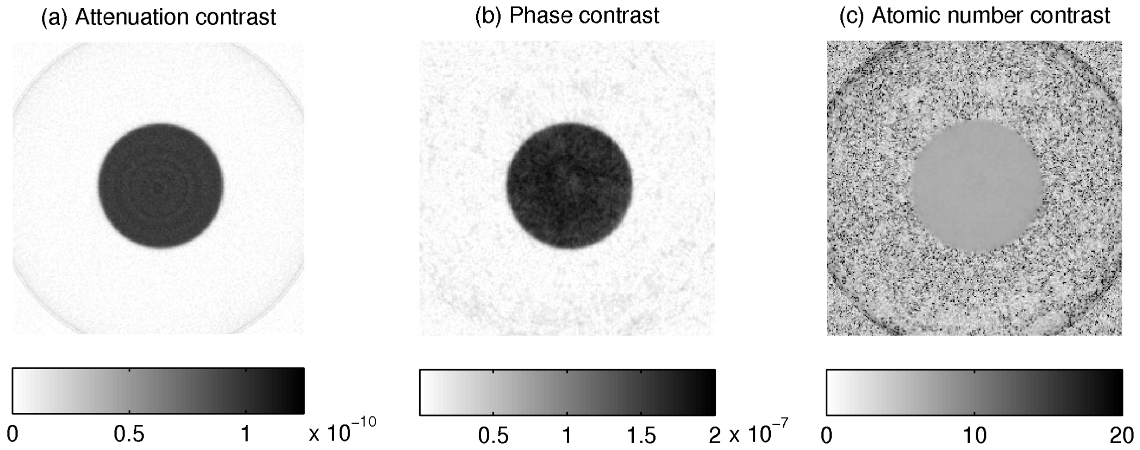

Fig. 28: *(a) Reconstructed attenuation decrement β and (b) refraction decrement δ for a PMMA cylinder of 10 mm diameter. (c) Atomic number contrast as calculated from the data shown in (a) and (b). In regions without sample, the numerical instability of the algorithm caused by high variance noise in images (a) and (b) the calculation of the atomic number causes considerable fluctuations of the calculated data.*

By choosing an adequate value for ε, a lower bound for the refraction decrement δ is introduced, and a division by zero can be avoided in Eq. (4.19). Additionally, the problem of negative discriminants is overcome in Eq. (4.19) by taking the absolute value of the discriminant before taking the root. While the lower bound ε for the refraction decrement δ offers the advantage of rendering the calculation more stable, it necessarily introduces an offset into the calculation of the atomic number, depending on the designated value of ε.

Another approach to noise reduction in atomic-number images is to use the parameter ε as a threshold, instead of using it as an additive lower bound for the refraction image. If the refraction decrement is lower than the threshold, the attenuation decrement β is set to zero. When this approach is made in the presence of a significant contribution of Compton scattering, the calculated atomic number will not be zero, but instead exhibit an offset of $|c_2|^{c_3}$. This offset can conveniently be eliminated by setting the attenuation decrement not to zero, but by setting the ratio of the decrements equal to $\beta/\delta = c_2/c_1$ in pixels where the refraction decrement is lower than the threshold. This measure causes the discriminant and thus the calculated atomic number to be equal to zero.

Both the lower bound and the threshold approach to noise reduction can be seen in Fig. 29 (b) and (c). Both approaches lead to a significant noise reduction and increase in image quality in comparison to the uncorrected image shown in Fig. 29 a). While the noise in Fig. 29 (b) for the lower bound method can be seen to be greatly reduced, its average value is not zero, due to the offset introduced by the specific choice of ε. The threshold method shown in Fig. 29 (c) leads to an excellent noise reduction, with the calculated atomic numbers being zero in the absence of a sample. Nevertheless, the hard edges at the borders of the sample in the corrected image give the image an artificial look, in comparison to the image corrected by the lower bound method. Also, by the hard thresholding, important image information hidden under high variance noise may be truncated and thus be lost for the observer. Thus, while both methods offer a significant noise reduction, none is perfect in itself. We thus advise a further investigation in the suppression of noise in the calculated atomic-number images.

So far we have discussed the properties of the calculation of the effective atomic number using the attenuation and refraction decrements, which can only be obtained in a tomographic scan. Nevertheless, similar problems occur as well if radiographies are used as a basis

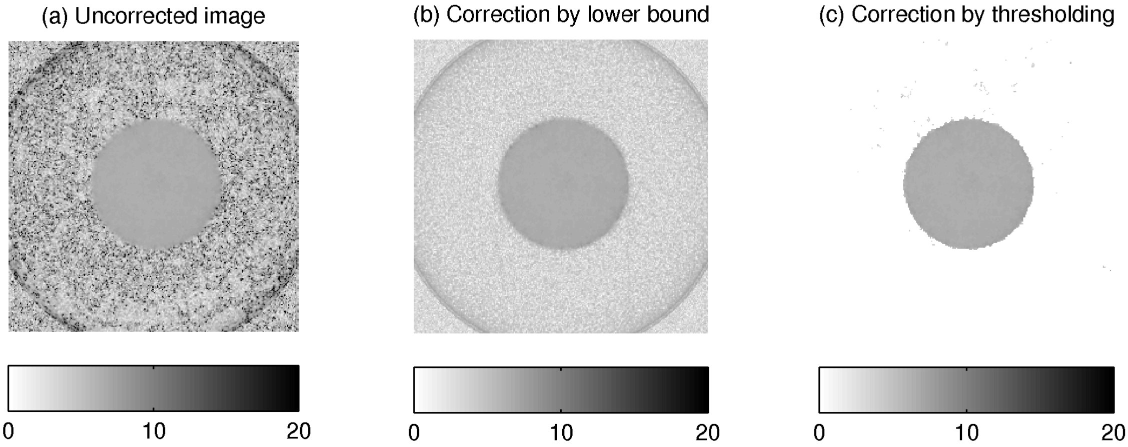

Fig. 29: *(a) Uncorrected atomic-number image, (b) atomic-number image as calculated by applying a lower bound ε to the refraction-decrement image, (c) atomic-number image as calculated by applying a threshold to the refraction-decrement image.*

for the calculation of the effective atomic number. As discussed in section 4.2, there are two possibilities to calculate an effective atomic number from radiography data: either by integrating the differential phase-contrast image or by differentiating the attenuation-contrast image. If the attenuation-contrast image is differentiated, most of the image in both contrast channels consists of values close to zero, since in a differential image, most image information is concentrated at the edges of the object, where the largest thickness gradients can be found. Taking the ratio of the two differential images therefore corresponds to a division by zero in a significant number of pixels of the image. On the other hand, the integration of the DPC image creates long ranged correlations in the image, visible as streaks along the direction of integration. In the presence of high variance noise, these streak artifacts dominate the image and greatly lower the image quality of the integrated phase image. These artifacts influence the calculation of the atomic number and thus lead to a deterioration of the image quality in the atomic number image as well. As a result, for radiography data, the calculation of the atomic number in the presence of high variance noise is effectively rendered impossible.

4.6 Summary

In this section, by using the basic dependencies of the refraction and attenuation decrement on energy, the combined measurement of attenuation and refraction was shown to allow the calculation of a contrast which is related to the atomic number of the material. The calculation was shown to be feasible for elemental as well as multi-material and compound samples, with radiographic as well as tomographic data, using monochromatic as well as polychromatic radiation. In exemplary measurements using well defined plastic samples, the method was shown to lead to good agreement with nominal values. Nevertheless, in section 4.5 the calculation was shown to be become unstable in the presence of noise fluctuations, especially in the absence of a sample in the region of interest. While the corresponding problems can be overcome by various methods in tomographic images, for low SNR, effective atomic-number calculations in the radiographic imaging mode are largely rendered unfeasible. Nevertheless, the approach as highly interesting for quantitative evaluation of calcifications and contrast agents in medical imaging, material and impurity discrimination in non-destructive testing, to metals and explosives detection in security applications.

5 Analysis of signal and noise properties

For an understanding of the image quality in grating-based differential phase-contrast imaging, an analysis of the noise properties of the images reconstructed from the measured raw data and an assessment of the signal-to-noise ratio (SNR) are essential. In this section, the characteristics of the noise in the three contrast channels in grating-based imaging will be investigated. Based on the propagation of noise through the reconstruction algorithm, the fundamental probability density functions (PDF) of the three parameters of the phase-stepping oscillation, the mean value a_0, the amplitude a_1 and the phase φ of the phase-stepping oscillation will be investigated in sections 5.1.1-5.1.5. The noise properties of the attenuation, differential phase and dark-field contrasts will then be derived and validated by exemplary measurements in sections 5.1.6 - 5.1.7. In section 5.2, approaches to the parameter estimation from noisy images is discussed, while in section 5.3 the dependence on the dose and the number of scan steps is investigated. In section 5.4, the results are extended to an analysis of the noise properties of tomographic reconstructions.

The results for the dark-field contrast channel have been published in Ref. [Chabior11C].

5.1 Image noise and noise propagation

Measured data are subject to signal fluctuations of various origins, which are referred to as noise. Noise can be characterized and quantified by the concept of correlation, as described in appendix E. The noise in the recorded raw images $S_n(x,y)$ propagates through the DFT algorithms given by Eqs. (2.67)-(2.70) and influences the reconstruction of the phase-stepping oscillation and thus the quality of the images derived from the raw data.

To simplify the analysis of the noise behavior of the images, we will assume that the only source of noise is the quantum noise caused by photon counting statistics, ignoring all other sources of noise, as positioning jitter, alignment instabilities, electronic noise, etc. In that case, the probability of detecting a certain number of photons in a given pixel follows a Poissonian PDF. When an average of M photons per pixel is measured, the probability to detect m photons in a single given pixel is

$$f(m,M) = \frac{M^m}{m!} e^{-M}. \tag{5.1}$$

The expectation value of the Poissonian distribution is

$$E(m) = M \tag{5.2}$$

and its variance is

$$V(m) = M. \tag{5.3}$$

The SNR for a pure Poissonian process is therefore

$$\frac{E(m)}{\sqrt{V(m)}} = \sqrt{M}. \tag{5.4}$$

In a DPC measurement, the signal strength per pixel S_n is thus equal to the number of photons detected per pixel and phase-step, with variance $V(S_n) = S_n$, following Poissonian statistics. We further assume an equidistant phase-stepping over an integer number of periods of the interference pattern, yielding a measurement signal as presented exemplarily in Fig. 30 (a). As can be seen from Fig. 30 (b), the Gaussian distribution is a good approximation to the Poissonian distribution for all count rates of practical interest. Therefore, we will model the noise analysis by the assumption that the raw data S_n are corrupted by an additive zero-mean Gaussian white noise with variance $V(S_n)$.

5.1.1 PDF of the mean of the phase-stepping oscillation

If an integer number of periods of the interference pattern is scanned with equidistant steps, the mean of the phase-stepping oscillation is equal to the zeroth Fourier coefficient and thus simply given as the mean of the phase-stepping data

$$a_0 = c_0 = \frac{1}{N}\sum_{n=0}^{\infty} S_n. \tag{5.5}$$

As the calculation of a mean value is a linear function, the noise properties of the averaged phase-stepping images are identical in the raw images. Therefore, the PDF of the mean value a_0 is that of a Poissonian distribution, as shown in Fig. 30 (b). If the distribution is approximated by a Gaussian distribution, its expectation value is given by

$$E(a_0) = a_0, \tag{5.6}$$

while its variance is

$$V(a_0) = \frac{a_0}{N}, \tag{5.7}$$

as shown in appendix G.1. In the following, we will use the normalized standard deviation $\tilde{\sigma} := \sqrt{V(a_0)}/E(a_0)$ for the quantification of noise, and for comparison with other x-ray imaging modalities, like classical x-ray radiography. Note that $1/\tilde{\sigma}$ is equal to the SNR in the attenuation-contrast channel. Using Eqs. (5.6) and (5.7), $\tilde{\sigma}$ can be rewritten

$$\tilde{\sigma} := \sqrt{V(a_0)}/E(a_0) = \frac{1}{\sqrt{a_0 \cdot N}}. \tag{5.8}$$

Assuming a minimum of $N = 3$ phase steps and a minimum number of $a_0 = 10$ photons per step and pixel to be able to apply the Gaussian approximation to the Poissonian distribution, the results are expected to be valid for $\tilde{\sigma} < 0.2$.

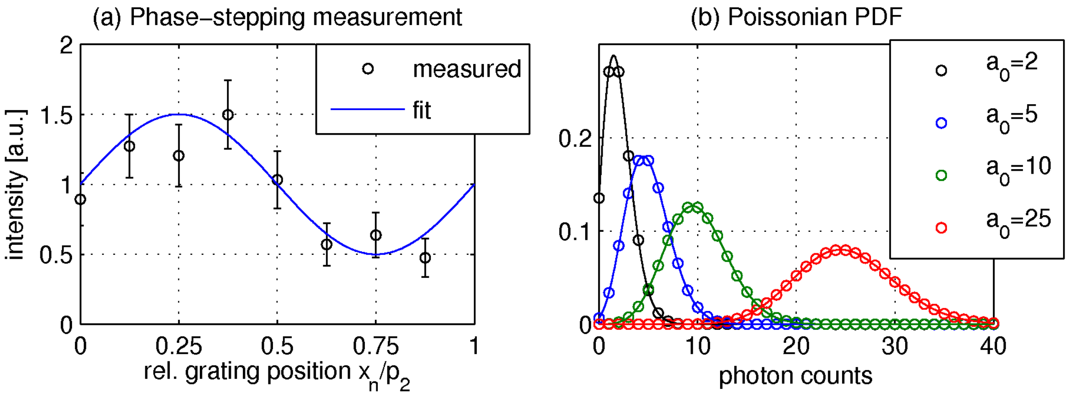

Fig. 30: *(a) The noise fluctuations in the measured raw data (black circles) influence the accuracy of the reconstruction of the intensity oscillation (solid blue line). (b) Poissonian distribution for the measured photon counts in each detector pixel for different values of* a_0. *The discrete Poissonian distribution can be well approximated by a continuous Gaussian PDF for values larger than* $a_0 > 10$ *photons per step.*

5.1.2 PDF of the first complex Fourier coefficient

Since the amplitude a_1 and the phase φ of the phase-stepping oscillation are both calculated from the first complex Fourier coefficient c_1, it is instructive to analyze the noise properties of this parameter separately. The Fourier coefficient is calculated by

$$c_1 = \frac{1}{N}\sum_{n=0}^{\infty} S_n \cdot \exp\left(2\pi\frac{n}{N}\right). \tag{5.9}$$

In appendix G.2, it is shown that in the presence of zero mean noise in the raw data S_n, the expectation value of the first complex Fourier coefficient is simply

$$E(c_1) = c_1. \tag{5.10}$$

As the coefficient is a number in the two-dimensional complex plane, its variance has to be analyzed separately for its real and imaginary part. The variances can be shown to be equal and given by (see appendix G.2)

$$\begin{aligned} V(\mathrm{Re}(c_1)) &= V(\mathrm{Im}(c_1)) \\ &:= \sigma_c^2 \\ &= \frac{1}{2}\cdot a_0^2 \cdot \tilde{\sigma}^2. \end{aligned} \tag{5.11}$$

A schematic of the distribution of the first complex Fourier coefficient in the presence of noise in the raw data is plotted in Fig. 31. If the noise in the raw data can be approximated by Gaussian noise, the complex Fourier coefficient follows a two-dimensional Gaussian distribution in the complex plane, due to the linearity of the Fourier transform. Nevertheless, the amplitude a_1 and phase φ of a complex number are calculated from the real and imaginary part of the complex number using non-linear functions. As indicated in Fig. 31, the amplitude and phase of the phase-stepping oscillation will be approximately Gaussian distributed for high SNR, while for low SNR, their distributions will be more complicated. In the following sections, we will therefore describe these two parameters by both a low and a high SNR limit.

5.1.3 PDF of the phase of the phase-stepping oscillation

The phase φ of the phase-stepping oscillation is calculated by the argument of the first complex Fourier coefficient c_1

$$\varphi = \arg(c_1) = \mathrm{atan}\left(\frac{\mathrm{Im}(c_1)}{\mathrm{Re}(c_1)}\right), \tag{5.12}$$

where atan is the arc tangent function, extended to the complex plane. As the Fourier transform is a linear functional, the noise properties of the complex Fourier coefficients as well as their real and imaginary parts equal the noise properties of the raw data. If the noise in the raw images is negligible and thus the determination of the phase of the phase-stepping oscillation can be achieved with good accuracy and minor deviations, the distribution of the reconstructed phases will be that of the raw data, a Gaussian PDF. Nevertheless, in contrast to the calculation of the mean a_0 of the phase-stepping oscillation, the calculation of phase data from the raw intensity data contains a non-linearity due to the fact that phase data are confined to the interval $[-\pi, \pi)$. If the sample shifts the intensity pattern by more than one period of the interference pattern, the phase will be wrapped back to the interval $[-\pi, \pi)$, leading to the well known phenomenon of **phase-wrapping** [Ghiglia98]. In this section, we will primarily be concerned with **statistical**

phase wrapping, i.e. an experimental situation, where phase-wrapping does not occur due to large deflections caused by the sample, but is caused by statistical fluctuations for low SNR. The statistics of the calculation of the phase of a complex number can be conveniently formalized by defining the normal distribution on the unit circle, yielding a **wrapped normal distribution**. The PDF of a wrapped normal distribution may be written

$$f(x;\varphi,\sigma_\varphi) = \frac{1}{\sqrt{2\pi\sigma_\varphi^2}} \cdot \sum_{k=-\infty}^{\infty} \exp\left(\frac{-(x-\varphi+2\pi k)^2}{2\sigma_\varphi^2}\right), \tag{5.13}$$

where x is the random variable, φ the mean and σ_φ^2 the variance of the unwrapped normal distribution. Eq. (5.13) describes a series of Gaussian distributions with identical standard deviations σ_φ, but mean values shifted relative to each other by multiples of 2π. Due to difficulties in its mathematical handling, the wrapped normal distribution is usually approximated by the **von Mises distribution** in directional statistics [Fisher93]. The von Mises distribution may in its importance for directional statistics be considered as the correspondence to the normal distribution on the unit circle. Its PDF is given by

$$f(x;\varphi,\sigma_\varphi) = \frac{1}{2\pi \cdot I_0\left(\frac{1}{\sigma_\varphi^2}\right)} \exp\left(\frac{\cos(x-\varphi)}{\sigma_\varphi^2}\right), \tag{5.14}$$

where $I_0(x)$ is the modified Bessel function of the first kind of order zero. The PDF of a von Mises distribution for $\varphi = 0$ and different values of σ_φ is shown in Fig. 32 (a).
Due to its mathematical intuitiveness, in the following, we will not describe the reconstructed phase by a wrapped normal or a von Mises distribution, but instead by its distributions in the high and low SNR limit, respectively. We will therefore denote the phase as reconstructed from a high and low SNR measurement by $\hat{\varphi}$ and $\check{\varphi}$, respectively. For high SNR (low σ_φ), statistical phase wrapping does not occur, so that the PDF may be simply approximated by a Gaussian PDF, with the expectation value

$$E(\hat{\varphi}) = \varphi. \tag{5.15}$$

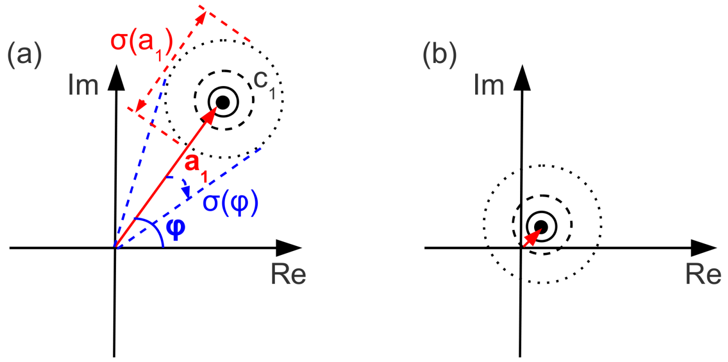

Fig. 31: *Schematics indicating the distribution of the reconstructed Fourier coefficient c_1 in the complex plane. Exemplarily, the 1σ, 2σ and 3σ surroundings of the expectation value for c_1 (black dot) are indicated by a solid, dashed and dotted black circles, respectively. For high SNR as shown in (a), the distribution of the complex amplitude and phase will be Gaussian with standard deviations $\sigma(a_1)$ and $\sigma(\varphi)$. In (b) can be seen that the phase will be approximately even distributed on the interval $[-\pi,\pi)$ if the visibility and thus the amplitude a_1 is lowered, while the positive definite amplitude a_1 will rise with the noise level.*

As the phase is calculated from the raw data S_n, the noise in the phase image can be related to the noise in the attenuation-contrast channel. In appendix G.4, it is shown that for high SNR, the noise variance in the differential phase-contrast channel is given by

$$V(\hat{\varphi}) = \sigma_\varphi^2 = \frac{2}{v^2} \cdot \tilde{\sigma}^2, \tag{5.16}$$

where $v = a_1/a_0$ is the visibility of the phase-stepping oscillation.
For low SNR, statistical phase-wrapping causes the phase distribution to approach a uniform distribution on the interval $[a,b) = [-\pi,\pi)$, with a constant PDF given by

$$f(x) = \frac{1}{b-a} = \frac{1}{2\pi}. \tag{5.17}$$

The expectation value of a uniform distribution is given by

$$E(\check{\varphi}) = \frac{1}{2}(a+b) = 0, \tag{5.18}$$

while its variance is

$$V(\check{\varphi}) = \frac{(b-a)^2}{12} = \frac{\pi^2}{3}. \tag{5.19}$$

In conclusion, for high SNR, the reconstructed oscillation phase will scale linearly with the noise in the raw data and be Gaussian distributed, as described by Eq. (5.15). The noise variance in the reconstructed phase is increased for decreasing visibility v of the phase-stepping oscillation and determined by the noise level $\tilde{\sigma}$. For high SNR, the noise in the phase-contrast channel rises linearly with the noise level $\tilde{\sigma}$. If one considers that $\tilde{\sigma}$ equals the normalized standard deviation in the attenuation-contrast channel, one can conclude that the noise in the phase-contrast channel is always higher than in the attenuation-contrast channel, by a factor of $\sqrt{2}/v$. For a realistic visibility of $v = 0.25$ at a polychromatic three-grating laboratory setup, the noise in the phase-contrast channel is higher by a factor of approximately 5.6 than the normalized standard deviation of the reconstructed mean value a_0. In the low SNR limit instead, phase-wrapping causes the reconstructed phase to be arbitrarily distributed in the interval $[-\pi,\pi)$, so that the phase shift φ caused by the sample will be impossible to reconstruct. We thus can conclude that by the transition in the statistical behavior of the underlying parameters, a lower bound for the necessary photon counts, or dose, is required to obtain reasonable differential phase-contrast images.

5.1.4 PDF of the amplitude of the phase-stepping oscillation

The amplitude a_1 of the phase-stepping oscillation is calculated as twice the magnitude of the first complex Fourier coefficient c_1

$$a_1 = 2 \cdot |c_1| = 2 \cdot \sqrt{\mathrm{Re}^2(c_1) + \mathrm{Im}^2(c_1)}. \tag{5.20}$$

If the real and imaginary part of a complex number are corrupted by a zero mean Gaussian noise with variance $V(\mathrm{Re}(c_1)) = V(\mathrm{Im}(c_1)) = \sigma_c^2$, it is well known in signal processing that consecutive measurements of the magnitude of that complex number follow a Rician distribution [Rice45, Lindsey64, Sijbers99]. The probability density function (PDF) of a Rician process can be described by

$$f(x,a_1,\sigma_c) = \frac{x}{4\sigma_c^2} \cdot \exp\left(-\frac{\left(x^2+a_1^2\right)}{8\sigma_c^2}\right) \cdot I_0\left(\frac{x \cdot a_1}{4\sigma_c^2}\right), \tag{5.21}$$

where x is the random variable or reconstructed amplitude, a_1 and σ_c the parameters of the distribution, and I_0 the modified Bessel function of the first kind of order zero. The expectation value of a Rician PDF is equal to

$$E(x) = \sigma_c\sqrt{2\pi}\cdot L_{\frac{1}{2}}\left(-\frac{a_1^2}{8\sigma_c^2}\right), \tag{5.22}$$

with $L_{1/2}(x)$ being a Laguerre polynomial $L_m(x)$ with $m = 1/2$, while its variance is

$$V(x) = a_1^2 + 8\sigma_c^2 - E(x)^2. \tag{5.23}$$

Please note that Eqs. (5.21)-(5.23) are different from the classical definition of a Rician PDF due to the fact that a_1 equals twice the amplitude of a complex number. The Rician PDF for four SNR values is shown in Fig. 32 (b).

Instead of describing the statistics of the reconstructed parameters in terms of the Rician distribution, similar to the differential phase signal in section 5.1.3, we chose the more insightful approach to model the statistical behavior as a transition between the two characteristic noise distributions in the high and low SNR limit, namely a Gaussian distribution and a Rayleigh distribution, respectively. In the following, we will denote the oscillation amplitude by a_1, the reconstructed amplitude in the high SNR limit by $\hat{a}_1$ and in the low SNR limit by $\check{a}_1$. In the high SNR limit ($a_1/\sigma_c > 3$), the amplitude distribution follows a Gaussian PDF

$$f(\hat{a}_1, \sigma_c) = \frac{1}{\sqrt{8\pi\sigma_c^2}}\exp\left(-\frac{(\hat{a}_1 - a_1)^2}{8\sigma_c^2}\right), \tag{5.24}$$

with the expectation value

$$E(\hat{a}_1) = a_1 \tag{5.25}$$

and the variance

$$V(\hat{a}_1) = 4\sigma_c^2. \tag{5.26}$$

For decreasing SNR, the distribution of the reconstructed amplitudes $\check{a}_1$ will tend towards a Rayleigh distribution. Its PDF can be obtained from Eq. (5.21) in the limit of $a_1 \to 0$, leading to

$$f(\check{a}_1, \sigma_c) = \frac{\check{a}_1}{4\sigma_c^2}\exp\left(-\frac{\check{a}_1^2}{8\sigma_c^2}\right). \tag{5.27}$$

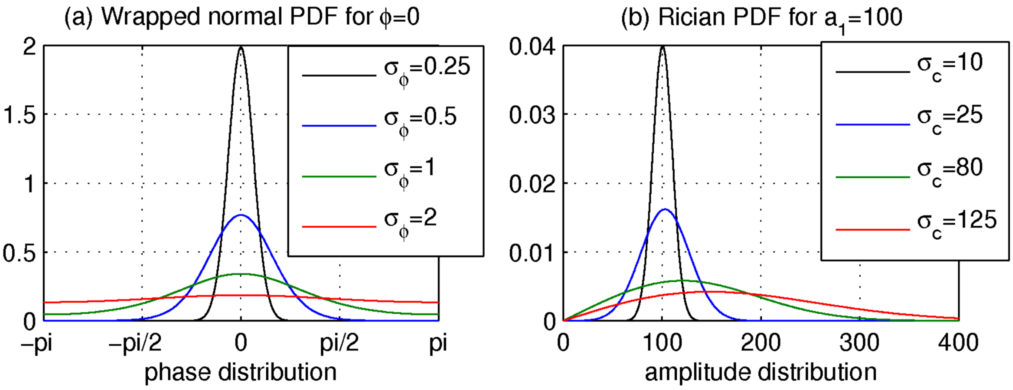

Fig. 32: *(a) Wrapped normal PDF for* $\varphi = 0$ *and four different settings of* σ_φ*. For high SNR (low* σ_φ*), the distribution can be approximated by a Gaussian distribution, while for low SNR, it converges towards a uniform distribution on the interval* $[-\pi, \pi)$*. (b) Exemplary Rician PDF for* $a_1 = 100$ *and four different settings of* σ_c*. For decreasing SNR, the distribution becomes skew and its mean shifts to higher values.*

Using $a_1 \rightarrow 0$ and $L_{\frac{1}{2}}(0) = 1$ in Eqs. (5.22) and (5.23), its expectation value is given by

$$E(\check{a}_1) = \sigma_c \cdot \sqrt{2\pi} \tag{5.28}$$

and its variance by

$$V(\check{a}_1) = \sigma_c^2 (8 - 2\pi). \tag{5.29}$$

The variance σ_c^2 of the real and imaginary part of the complex Fourier coefficients is connected to $\tilde{\sigma}$ by Eq. (5.11). Combining Eqs. (5.25), (5.26) and (5.11), the relative reconstruction error of the amplitude in the high SNR limit as a function of $\tilde{\sigma}$ is

$$\frac{\sqrt{V(\hat{a}_1)}}{E(\hat{a}_1)} = \tilde{\sigma} \cdot \frac{\sqrt{2}}{v}, \tag{5.30}$$

while in the low SNR limit the relative reconstruction error can be obtained by combining Eqs. (5.28) and (5.29), leading to

$$\frac{\sqrt{V(\check{a}_1)}}{E(\check{a}_1)} = \sqrt{\frac{4-\pi}{\pi}}. \tag{5.31}$$

For low SNR limit, the noise in the amplitude becomes independent of $\tilde{\sigma}$ and thus independent of the noise in the raw images. These considerations on the reconstruction of the amplitude can be used for an analysis of the noise behavior of the visibility.

5.1.5 PDF of the visibility of the phase-stepping oscillation

As the visibility is defined by a ratio between the amplitude and the mean according to Eq. (2.73), the statistical properties of the amplitude reconstruction make it necessary to distinguish between a high and low SNR limit for the visibility as well. We will write $\hat{v}$ and $\check{v}$ for the reconstructed visibilities in the high and low SNR limit, respectively. In the following, we will not explicitly derive the PDF of the visibility, but instead describe its expectation value and variance by the PDFs of the amplitude and mean. If the function $v(a_0, a_1) = a_1/a_0$ is expanded into a power series around $E(a_0)$ and $E(a_1)$ as shown in appendix G.5, the expectation value of the reconstructed visibility in the absence of correlation between a_0 and a_1 is given by

$$E(v) = \frac{E(a_1)}{E(a_0)} \sum_{k=0}^{\infty} \frac{M_k(a_0)}{E^k(a_0)}, \tag{5.32}$$

where $M_k(a_0)$ is the k-th central moment of the distribution of a_0. Therefore, we may approximate the expectation value of the reconstructed visibility by $E(v) \approx E(a_1)/E(a_0)$ up to second order, as long as $V(a_0)/E^2(a_0) = \tilde{\sigma}^2 \ll 1$. Under these conditions, the variance of the reconstructed visibility $V(v)$ is given by

$$V(v) \approx \frac{E^2(a_1)}{E^2(a_0)} \cdot \left(\frac{V(a_1)}{E^2(a_1)} + \frac{V(a_0)}{E^2(a_0)} \right). \tag{5.33}$$

This approximation will be implicitly used in the following, greatly simplifying the analysis, while not leading to major deviations from measurement results.

While for high SNR, the expectation value is

$$E(\hat{v}) \approx \frac{E(\hat{a}_1)}{E(a_0)} = v, \tag{5.34}$$

by combining Eqs. (5.8) and (5.30), the relative reconstructed error of the visibility can be calculated by

$$\frac{\sqrt{V(\hat{v})}}{E(\hat{v})} = \tilde{\sigma} \cdot \sqrt{\frac{2}{v^2} + 1}. \tag{5.35}$$

Eq. (5.35) holds for high SNR, while the statistical behavior of the reconstructed visibility changes as the flux or exposure time decreases and the noise in the images increases. In the low SNR limit, the PDF of the reconstructed visibility will be a quotient distribution formed by the ratio of a Rayleigh and Gaussian distributed parameter. Using again $E(\check{v}) \approx E(\check{a}_1)/E(a_0)$ in combination with the expectation value of the amplitude $E(\check{a}_1)$, in the limit of low SNR described by Eq. (5.28), we arrive at

$$E(\check{v}) = \tilde{\sigma}\sqrt{\pi} \tag{5.36}$$

for the expectation value and for its relative reconstruction error

$$\frac{\sqrt{V(\check{v})}}{E(\check{v})} = \sqrt{\frac{4-\pi}{\pi} + \tilde{\sigma}^2}. \tag{5.37}$$

The visibility reconstructed from noisy raw data S_n in the limit of high and low SNR exhibits interesting properties: The visibility reconstruction is dominated by the statistical properties of the amplitude distribution. If the SNR is lowered in a measurement, the noise characteristics in the measured visibilities will show a transition from Gaussian distributed noise, as given by Eq. (5.35), to Rayleigh distributed noise as described by Eq. (5.37). For high SNR, the relative errors of the reconstructed amplitude $\sqrt{V(\hat{a}_1)}/E(\hat{a}_1)$ and visibility $\sqrt{V(\hat{v})}/E(\hat{v})$ in Eqs. (5.30) and (5.35) rise linearly with the noise level $\tilde{\sigma}$. Same as in the differential phase-contrast channel, the normalized standard deviations for the reconstructed amplitude and visibility are higher than in the attenuation-contrast channel, by a factor of $\sqrt{2}/v$ and $\sqrt{2/v^2+1}$, respectively. Additionally, the variance of the reconstructed amplitude and visibility rises with decreasing visibility, in opposition to the attenuation contrast, which is independent of the oscillation visibility. For an assumed visibility of $v = 0.25$, the noise in the reconstructed visibility is higher by a factor of approximately 5.7 than the noise of the attenuation contrast image. In the limit of low SNR, Eq. (5.36) predicts that the expectation value of the reconstructed visibility is not constant, but instead a function of the noise level, eventually becoming larger than the visibility in the reference image. As the visibility is the carrier of information in a dark-field measurement, it is obvious that this corresponds to a loss of information by the application of the reconstruction algorithms. Similar to the differential phase-contrast channel, in dark-field imaging, a lower bound for the necessary photon counts has to be imposed to be able to reconstruct the corresponding information from the sample.

5.1.6 Calculation using a noisy reference image

In most experimental situations, the reference images, which are needed for a proper evaluation of the image data, can in principle be acquired with arbitrary accuracy and can be considered approximately noise free. In this case, The formulas presented in the previous sections are sufficient for the understanding of the noise properties. If, however, the reference images are assumed to be noisy as well, further analysis has to be performed. For the sake of simplicity, we will assume that the noise level in the reference images is equal to the noise level in the sample images. Using $T = a_{0,s}/a_{0,r}$ and the approximation given in Eq. (5.32), the expectation value of the reconstructed transmission equals

$$E(T) \approx E(a_{0,s})/E(a_{0,r}) = T, \tag{5.38}$$

while the normalized reconstruction error is

$$\frac{\sqrt{V(T)}}{E(T)} = \tilde{\sigma} \cdot \sqrt{1 + \frac{1}{T}}. \tag{5.39}$$

This relation for the attenuation contrast holds for all noise levels of interest in grating-based imaging, as long as a Gaussian distribution is a valid approximation for the noise in the raw data.

If the phase shift $\Delta\varphi$ of the phase-stepping oscillation is calculated by $\Delta\varphi = \arg(c_{1,s}/c_{1,r})$, its expectation value is

$$E(\Delta\hat{\varphi}) = \Delta\varphi \tag{5.40}$$

for all signal-to-noise ratios (see also section 5.2). Its variance in the high SNR limit can be calculated by the combination of the sample and reference measurements following Eq. (5.16),

$$V(\Delta\check{\varphi}) = \tilde{\sigma}^2 \cdot \frac{2}{v_r^2}\left(1 + \frac{1}{T \cdot D^2}\right), \tag{5.41}$$

where v_r is the visibility in the reference measurement. The noise in the differential phase-contrast channel thus increases with decreasing visibility v_r. Additionally, the noise increases with both decreasing transmission T and decreasing dark-field signal D. Strongly absorbing or scattering samples will thus be visible in the differential phase images by their different noise characteristics, even if they do not exhibit a phase shift. For low SNR, the oscillation phase of sample and reference measurement both converge towards a uniform distribution. As the reconstructed phase of the combined measurement is a phase as well, its variance will similarly tend towards the variance of a uniform distribution, given by

$$V(\Delta\check{\varphi}) = \frac{\pi^2}{3}. \tag{5.42}$$

In the low SNR limit, the differential phase-contrast channel will thus consist of plain noise with mean zero and constant variance.

For a discussion of the noise properties in the dark-field-contrast channel, first the statistical properties of the amplitude decrease A have to be investigated. The expectation value of the reconstructed amplitude decrease is

$$E(\hat{A}) \approx \frac{E(\hat{a}_{1,s})}{E(\hat{a}_{1,r})} = A \tag{5.43}$$

for high SNR, while the relative reconstruction error reads

$$\frac{\sqrt{V(\hat{A})}}{E(\hat{A})} = \tilde{\sigma} \cdot \sqrt{\frac{2}{v_r^2}\left(1 + \frac{1}{T \cdot D^2}\right)}. \tag{5.44}$$

Similarly, the expectation value of the dark-field signal is

$$E(\hat{D}) \approx \frac{E(\hat{v}_s)}{E(\hat{v}_r)} = D. \tag{5.45}$$

Using Eqs. (5.39) and (5.44), it is possible to calculate the relative reconstruction error of the dark-field signal by

$$\frac{\sqrt{V(\hat{D})}}{E(\hat{D})} = \tilde{\sigma} \cdot \sqrt{\frac{2}{v_r^2}\left(1 + \frac{1}{T \cdot D^2}\right) + \left(1 + \frac{1}{T}\right)}. \tag{5.46}$$

These formulas only hold for high SNR, while in the limit of low SNR, the transition in the statistical behavior dictates other relationships. Taking into account the results of section 5.1.4, from Eq. (5.31), it immediately follows that the expectation value of the amplitude decrease $E(\check{A}) \approx E(\check{a}_{1,s})/E(\check{a}_{1,r})$ can be written in the low SNR limit as

$$E(\check{A}) = \sqrt{T} \tag{5.47}$$

and its relative reconstruction error can be calculated to be

$$\frac{\sqrt{V(\check{A})}}{E(\check{A})} = \sqrt{2 \cdot \frac{4-\pi}{\pi}}. \tag{5.48}$$

If we assume $E(\check{D}) \approx E(\check{A})/E(T)$, finally we can write the dark-field signal in the low SNR limit using Eq. (5.47) as

$$E(\check{D}) = \frac{1}{\sqrt{T}}, \tag{5.49}$$

with a relative reconstruction error of

$$\frac{\sqrt{V(\check{D})}}{E(\check{D})} = \sqrt{2 \cdot \frac{4-\pi}{\pi} + \tilde{\sigma}^2 \left(1 + \frac{1}{T}\right)}. \tag{5.50}$$

In the limit of low SNR, the dark-field signal will not consist of plain noise, but instead will converge towards an image which is proportional to the inverse square root of the transmission image. This dependence can be understood since for low SNR, the visibility is a function of the noise level, following Eq. (5.36), and thus inherently of the attenuation in the sample.
A summary of the noise properties of the different contrast channels as analyzed in the previous sections is given in appendix G.6 in tables 1 and 2.

5.1.7 Experimental verification

In order to prove the correctness of the analytical approach and the resulting formulas, a series of measurements on some well defined test samples were performed as a function of exposure time and thus image noise. The measurements were done at a laboratory setup at the Paul Scherrer Institut in Villigen, Switzerland. As x-ray source, a Seifert DX-W8x0.4-L x-ray tube was used, operated at an anode voltage of 40 kV and an anode current of 25 mA. No filtration was applied. As detector, a Dectris Pilatus 100K was used. Detection is achieved by photon conversion in a reverse-biased Si diode array with 320 μm sensor thickness. The sensitive area consisted of a 487×195 pixel array with a pixel size of 172×172 μm^2, offering a total field of view of 83.8×33.5 mm^2. The single photon counting detector could handle count rates of up to 2×10^6 photons per second and a dynamic range of 20 bit. All gratings were manufactured at the PSI [David07]. The phase grating G_1 had Si bars of 35 μm height and a period of 3.5 μm, exhibiting a phase shift of π for a design energy of $E_0 = 27.3$ keV. The attenuation gratings G_0 and G_2 had Au structure heights of $h_0 = 42$ μm and $h_2 = 26$ μm with periods of $p_0 = 14$ μm and $p_2 = 2.0$ μm, respectively. The distance between G_1 and G_2 was $d = 200$ mm, corresponding to the 5th Talbot distance. The G_0-G_1 distance was $l = 1400$ mm, giving a total setup length of 1600 mm. The phase stepping was done by scanning G_1, with 9 stepping positions over 2 periods of the interference pattern for each scan. The noise in the images was increased by lowering the exposure time in each consecutive phase-stepping scan by a factor of two. Starting with 41 s exposure time per step, a total of 14 scans were performed, the exposure times varied from 41 s to 0.005 s per step, or from 369 s to 0.045 s for the total exposure time, respectively. Identical parameters were used to record the reference images. As samples, a square 10×10 mm^2 PMMA (polymethyl methacrylate) bar and a square 5×5 mm^2 Al bar were used. The PMMA bar was aligned along its diagonal, so that, in projection, it exhibits a phase shift like a symmetric triangle. The two bars were arranged in a way that leaves an empty area on one side of our field of view, allowing the analysis of image noise in the absence of a sample. The sample was positioned between G_0 and G_1, 100 mm upstream of G_1.

Analyzing the measured data for all exposure times by the DFT formulas presented in Eqs. (2.67)-(2.69), the mean, phase, amplitude and visibility of the phase-stepping oscillation in each pixel were reconstructed. The attenuation-, differential phase- and dark-field contrast images reconstructed from the sample and reference measurement for four different exposure times can be seen in Fig. 33. Three regions-of-interest (ROIs) were chosen in the region of the PMMA wedge, the strongly absorbing Al bar and the reference region to its right where no sample was positioned, as indicated in Fig. 33 (a). The ROIs for the Al bar and the reference region had a size of $28 \times 194 = 5432$ and $105 \times 194 = 20370$ pixels, respectively. The mean visibility in the reference was calculated from the measurement with the highest exposure time, resulting in a value of $v_r = 0.154 \pm 0.006$. The mean transmission of the Al bar was $T = 0.132 \pm 0.002$, while its mean dark-field signal was $D = 0.34 \pm 0.06$. As the PMMA wedge exhibits a two-sided rectangular-shaped phase shift of opposite sign, two ROIs with a size of $2 \times 56 \times 194 = 21728$ pixels were used for its evaluation. The measured data were averaged over the left and right side of the PMMA wedge, yielding an oscillation phase shift of $\Delta\varphi = \pm(0.59 \pm 0.04)$ rad.

Since we use a photon-counting x-ray detector with an almost ideal, rectangular point-spread function, the response of each pixel can be interpreted as an independent statistical process. The statistical behavior of the calculated parameters can be analyzed using a well defined ensemble of pixels, as represented by the ROIs. From the data measured in the ROIs, the average and the standard deviation over the area of each ROI were extracted and plotted against the exposure time. Since the exposure time, interpreted as a noise measure, depends on the utilized imaging system, we choose $\tilde{\sigma}$ as a reference parameter to quantify noise. This parameter can be calculated by the use of Eq. (5.8). For a source with constant flux F per pixel, the number of detected photons and thus the mean a_0 is proportional to the exposure time. The noise parameter $\tilde{\sigma}$ can therefore be related to the exposure time per step t by $\tilde{\sigma} = 1/\sqrt{N \cdot t \cdot F}$. As the flux is unknown in the experiment, $\tilde{\sigma}$ was calculated by extracting the average number of detected photons from the ROI in the reference scan.

The measured oscillation mean a_0 for the reference measurement and the Al bar as a function of image noise can be seen in Fig 34 (a). As described by Eq. (5.8), the curves decline proportional to $a_0 \sim 1/\tilde{\sigma}^2$. The ratio between the Al and the reference curve is equal to the transmission of the Al bar as a function of $\tilde{\sigma}$. It can be seen from Fig 34 (a) that the transmission is constant for all noise levels. Similarly, the measured oscillation amplitude a_1 for the reference measurement and the Al bar as a function of image noise is shown in Fig. 34 (b). In contrast to the oscillation mean, the amplitude shows a transition in its behavior if the SNR is reduced. While for high SNR, the amplitude is given by $\hat{a}_1 = a_0 \cdot v \sim 1/\tilde{\sigma}^2$, for low SNR the dependence on the image noise is described by Eq. (5.28) with $\check{a}_1 \sim 1/\tilde{\sigma}$.

The reconstructed oscillation phase $\Delta\varphi$ of the phase-stepping oscillation as a function of $\tilde{\sigma}$ is shown in Fig. 35 (a). While the reconstructed phase is constant for high SNR levels, it

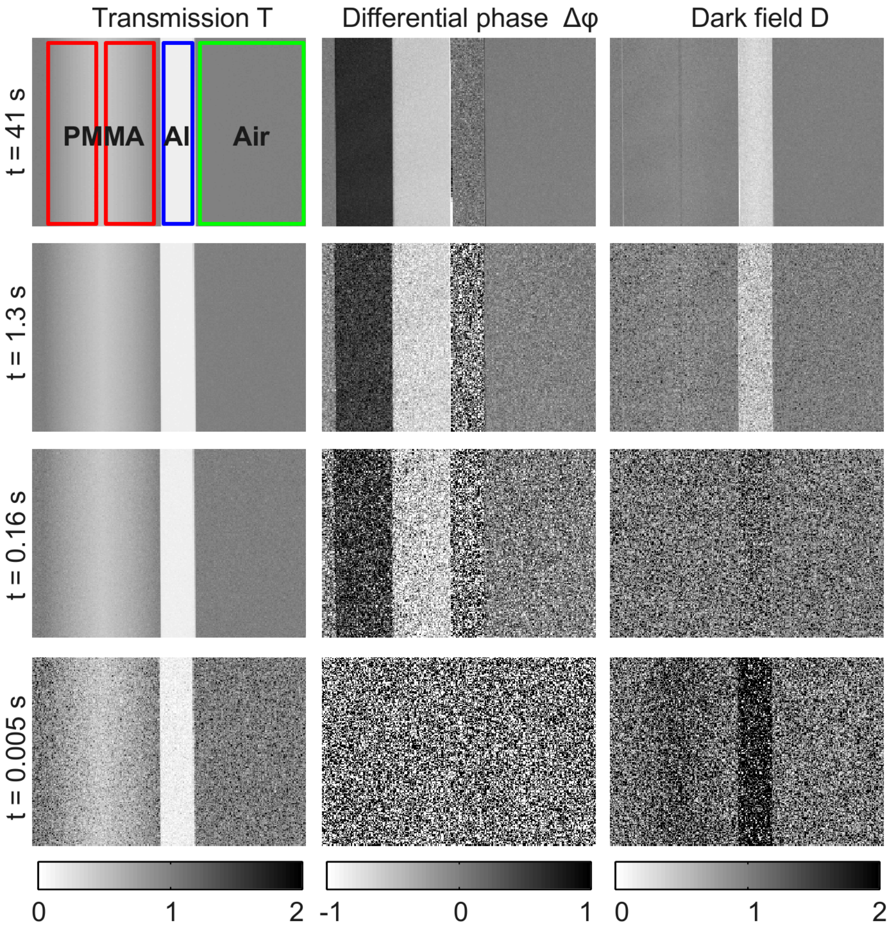

Fig. 33: *Comparison between reconstructed transmission T (left column), differential phase shift Δφ (mid column) and dark-field signal D (right column) of an exemplary phantom for four different exposure times (from top to bottom, $t = 41$ s, $t = 1.3$ s, $t = 0.16$ s, $t = 0.005$ s). The phantom consisted of a PMMA wedge, an Al bar and an empty reference region. The ROIs used for the evaluation are indicated by two red rectangles for the PMMA wedge, a blue rectangle for the Al bar and a green rectangle for the reference region. As the exposure time decreases and the noise level increases, the differential phase-contrast channel reduces to plain noise, while the inverse of the transmission image becomes visible in the dark-field-contrast channel.*

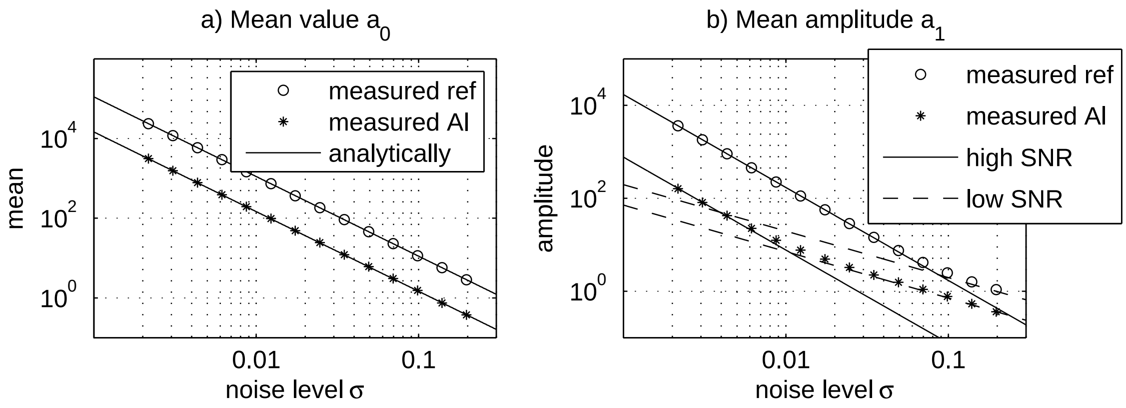

Fig. 34: *(a) Measured mean value a_0 and (b) amplitude a_1 as a function of the noise level $\tilde{\sigma}$, both for the Al bar (asterisks) and the reference scan (circles). In contrast to the mean value, the amplitude reconstruction shows a transition from its statistical behavior for high and low SNR, as indicated by the solid and dashed black lines.*

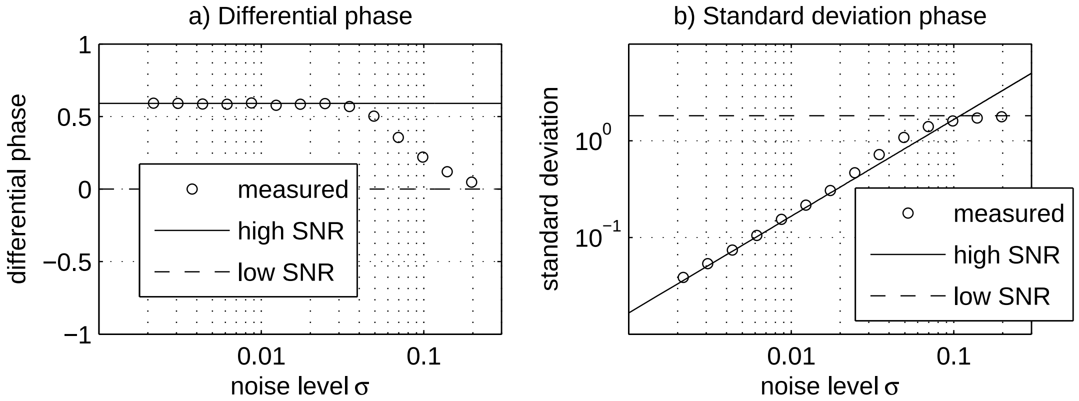

Fig. 35: *(a) Reconstructed differential phase signal* $\Delta\varphi$ *from a PMMA wedge, obtained by averaging over the left and right slope of the wedge. (b) Standard deviation of the reconstructed differential phase in the ROI of the PMMA wedge. For low noise levels* $\tilde{\sigma}$*, the calculated phase is constant and its standard deviation rises linearly with the noise level. For high noise level, the phase distribution approaches a uniform distribution on* $[-\pi,\pi)$*, with mean zero and standard deviation* $\pi/\sqrt{3}$*.*

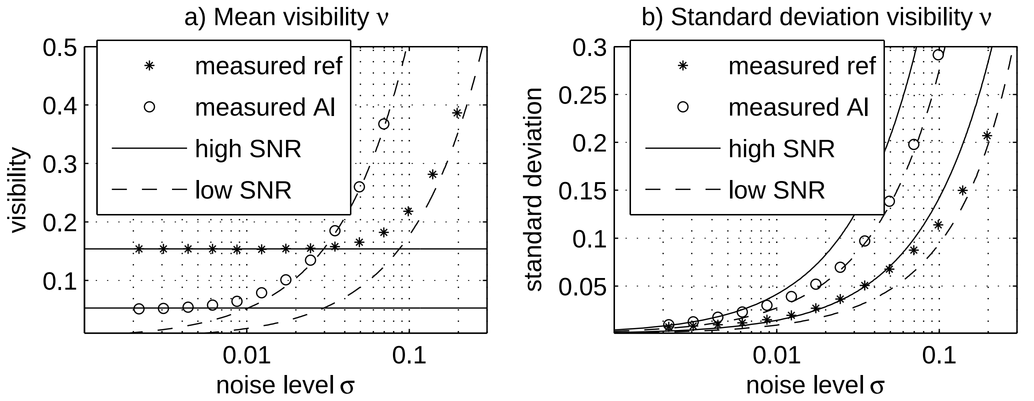

Fig. 36: *(a) Measured mean visibility for the reference region-of-interest (asterisks) and the Al bar (circles) and (b) its standard deviation* $\sqrt{V(\nu)}$ *as a function of the noise level* $\tilde{\sigma}$*. The solid and dashed lines describe the analytically expected values in the limit of high and low SNR, respectively. The rise of the visibility with increasing noise level indicates a breakdown of the information transfer.*

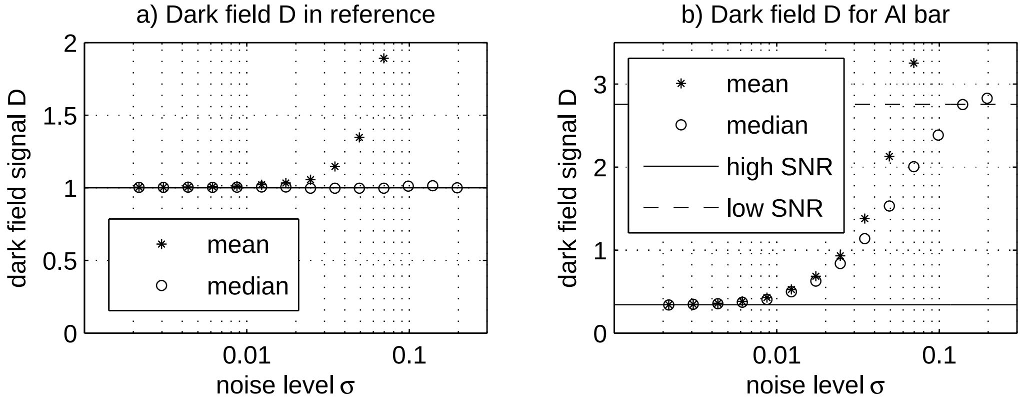

Fig. 37: *Measured mean (asterisks) and median (circles) dark-field signal for (a) the reference region and (b) the Al bar. The solid and dashed lines describe the analytically expected values in the limit of high and low SNR, respectively. In the limit of low SNR, the dark-field signal approaches a value related to the transmission of the sample, while it remains constant in the absence of a sample. The median is a better suited estimator for the expectation value than the mean due to the skewness of the underlying distribution.*

approaches zero for decreasing SNR, the expectation value of the uniform distribution. The transition in the statistical behavior can also be seen in the evaluation of the standard deviation of the reconstructed phase as shown in Fig. 35 (b). While for high SNR the standard deviation rises linearly with the noise level following Eq. (5.41), for low SNR it converges towards the standard deviation of the uniform distribution on $[-\pi, \pi)$ as described by Eq. (5.19), i.e. $\sigma(\Delta\breve{\varphi}) = \pi/\sqrt{3}$.

The plots for the mean visibility and its reconstruction error for the reference ROI and the Al bar as a function of $\tilde{\sigma}$ can be seen in Fig. 36 (a) and b), respectively: While the visibility is constant for low values of $\tilde{\sigma}$, it rises asymptotically towards the values predicted by the Rayleigh distribution in the limit of low SNR. While the dependence of the visibility on the noise level can be described by $E(\hat{v}) = v$ and Eq. (5.35) for high SNR, the dependence changes to Eqs. (5.36) and (5.37) for low SNR. This transition corresponds to a breakdown of information transfer from the raw images to the derived dark-field image.

The median dark-field signal over the reference ROI and the Al bar as a function of $\tilde{\sigma}$ are shown in Fig. 37 (a) and (b), respectively. At low noise levels (high SNR), the dark-field signal is constant for both regions. For the Al bar, the rise of the signal with increasing noise level is not related to physical effects but again indicates a breakdown of information transfer. In the limit of low SNR, the median dark-field signal approaches $1/\sqrt{T} \approx 2.75$, as predicted by Eq. (5.49). Similarly, in the absence of absorption, the mean over a pixel ensemble increases with noise level, while the median remains constant with $E(D) = 1$, as shown in Fig. 37 (a).

The median instead of the arithmetic mean has been used for data evaluation in the dark-field-contrast channel due to the underlying statistics: In our calculations, we use averaging over a finite ensemble of pixels as an estimator for the expectation value $E(D)$. This estimator leads to good results as long as the statistical distributions are symmetric and fall off exponentially towards infinity, like the Gaussian PDF for high SNR. For low SNR, the distribution of the dark-field signal has a lower bound of zero, but is unbound and heavy-tailed towards high values. Thus, the estimation of the expectation value by averaging over a finite ensemble of pixels has a tendency to lead to values that are too high, due to the high variance of the underlying ratio distribution. In this case, taking the median over the ROI as an estimator is a better choice, as the median is less sensitive to extreme outliers in the pixel ensemble.

These results show that the physical meaning of the information presented in differential phase and dark-field images has to be interpreted with caution in the presence of high noise variance, due to the transitions in the statistical behavior of the underlying noise PDFs. A fixed upper bound for the image noise, below which the reconstructed data are reliable, cannot be readily given, as the reconstruction errors depend on the transmission T and the dark-field signal D of the sample. Nevertheless, we can estimate an upper bound for the noise level $\tilde{\sigma}$ by demanding that the relative reconstruction errors of the dark-field signal for high SNR, as described by Eq. (5.46), have to be lower than the reconstruction errors for low SNR, described by Eq. (5.50). Equating both formulas yields the relation

$$\tilde{\sigma} \leq v_r \cdot \sqrt{\frac{4-\pi}{\pi} \cdot \frac{TD^2}{TD^2+1}}. \tag{5.51}$$

For the dark-field signal of the Al-bar presented in Fig. 37 (b), we obtain an upper bound of $\tilde{\sigma} \leq 0.01$. In the absence of a sample ($T = D = 1$), one obtains

$$\tilde{\sigma} \leq v_r \sqrt{(4-\pi)/2\pi} \approx 0.37 \cdot v_r. \tag{5.52}$$

This corresponds to $\tilde{\sigma} \leq 0.057$ for the reference visibility presented in Fig. 36 (a). Eq. (5.51) may just as well be used as an upper bound for the differential phase contrast, as can be seen from Fig. 35 (a).

The agreement of theory and measurement as presented in Figs. 34 - 37 is convincing, so that the correctness of the analytical approach to describe the noise characteristics of the image data in grating-based x-ray dark-field images can be asserted.

5.2 Averaging and noise estimation using maximum likelihood

The easiest way to reduce the noise in the images is via averaging. If the noise in the images is additive with zero mean, averaging over a number of K consecutive measurements of x reduces the standard deviation of x by a factor of $1/\sqrt{K}$, since the uncorrelated noise contributions in the images will level out. Even if only a single measurement is performed, in some experimental situations averaging over a symmetry axis of the sample or a certain constant region-of-interest can yield a higher SNR for a given application. In the following, the average over a number of K measurements of a variable x will be denoted $\overline{x}$.

In DPC imaging, the assumption of additive noise with zero mean does only apply to the raw data and the attenuation-contrast channel, i.e. the calculation of the mean of the phase-stepping oscillation, due to the linearity of the reconstruction algorithm. In contrast, the calculation of the amplitude and phase of the phase-stepping oscillation is non-linear and shows a transition in its statistical behavior, from Gaussian in high SNR for both parameters, to a uniform distribution for the differential phase-contrast and a Rayleigh distribution for the amplitude. Therefore, the noise properties of these two contrast channels cannot be described by an additive noise with zero mean. For this reason, the arithmetic average over a number of measurements will converge towards the expectation values of the noise distributions, not however towards the parameters φ and a_1 of the phase-stepping oscillation that are desired. From a more abstract and analytical point of view, when performing averaging, we are actually interested in an adequate estimator for the parameters φ and a_1 of the underlying distributions of an ensemble of reconstructed data. While arithmetic averaging is an appropriate estimator only for the mean of the phase-stepping oscillation, for the estimation of the phase φ and the amplitude a_1 from a number of noisy measurements, more elaborate means are necessary.

That the arithmetic average is an unsuitable estimator for the phase can be seen by averaging $\varphi_1 = \pi - \varepsilon$ and $\varphi_2 = -\pi + \varepsilon$, with $\varepsilon > 0$. The arithmetic mean is $\overline{\varphi} = 0$, whereas the desired result would be $\overline{\varphi} = -\pi$. This problem can be solved by choosing an estimator adapted to the circular character of the underlying distribution. The distribution of the phase φ is a wrapped normal distribution after Eq. (5.13). Instead of describing the statistical moments of the wrapped distribution by the random variable x, the properties of the distribution can be described more directly by a circular variable $z = e^{ix}$. The expectation value of the circular variable z is given by [Fisher93]

$$E(z) = \exp\left(i\varphi - \sigma_\varphi^2/2\right). \tag{5.53}$$

The expectation value of the original angular variable x can therefore be calculated by taking the complex argument of the expectation value of z

$$E(x) = \arg\left(E(z)\right) = \varphi. \tag{5.54}$$

If the standard definition of variance is applied to the measured data, the variance of φ will also be affected by the transition from a Gaussian distribution to a uniform distribution and converge towards a value of $V(\hat{\varphi}) = \pi^2/3$ as described by Eq. (5.19). Therefore, the concept

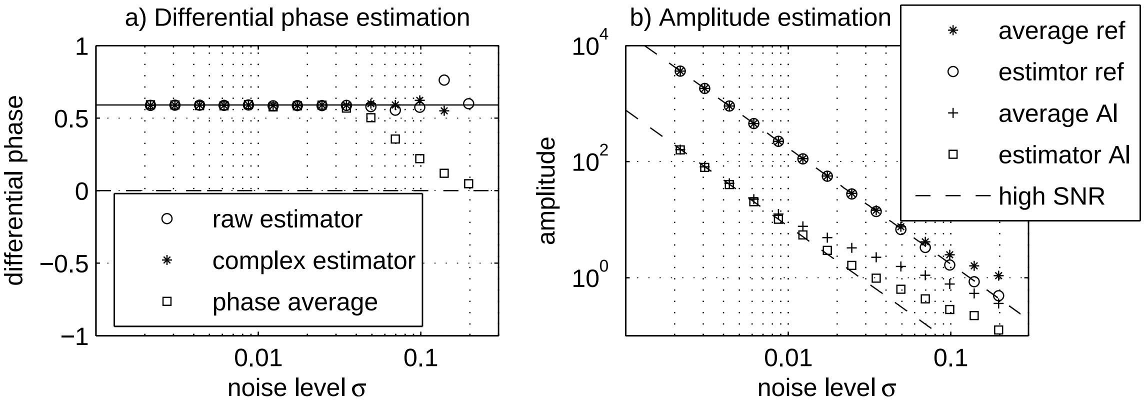

Fig. 38: *Different estimators for the (a) the differential phase and (b) for the amplitude. (a) shows that while averaging over the reconstructed phases leads to a decrease of the mean phase, estimation by averaging over the raw and complex data respectively leads to a correct estimation of the phase, only with different noise properties. In (b), the amplitude estimator is shown relative to the mean estimator, for both the reference ROI and the Al bar.*

of circular variance was developed in directional statistics. It is equal to the variance of z and can be calculated by

$$V(x) = \ln\left(\frac{1}{|E(z)|^2}\right) = \sigma_\varphi^2. \tag{5.55}$$

If these considerations are taken into account, we see that the average of the phase of the phase-stepping oscillation should be calculated by identifying $z = c_1$ and thus performing the averaging over the complex first Fourier coefficient. The average complex Fourier coefficient $\overline{c_1}$ is known as mean resultant vector in directional statistics

$$\overline{c_1} = \overline{a_1} \cdot \exp\left(i \cdot \overline{\varphi}\right). \tag{5.56}$$

The average phase $\overline{\varphi}$ can be derived from the resultant vector by

$$\overline{\varphi} = \arg\left(\overline{c_1}\right), \tag{5.57}$$

while the circular variance of φ is

$$V(\overline{\varphi}) = \ln\left(1/\left|\overline{c_1}\right|^2\right). \tag{5.58}$$

The mean of an ensemble of phase measurements has to be calculated by the average over the complex Fourier coefficients. In other words: $\arg(\overline{c_1})$ is a biased estimator for the average phase $\overline{\varphi}$ and $\ln(1/\left|\overline{c_1}\right|^2)$ is a biased estimator for the circular variance $V(\overline{\varphi})$. The average over the reconstructed phases will tend towards zero for low SNR and can thus be excluded as an estimator for $\Delta\varphi$.

For the reconstruction of the differential phase shift $\Delta\varphi$ caused by the sample, an additional possibility has to be taken into account: averaging over the raw data S_n and averaging over the complex Fourier coefficients. While both methods lead to the correct reconstruction of the parameter φ of the phase distribution, there are differences in the variance of the estimation. This is due to the fact that

$$\arg\left(\frac{\overline{c_{1,s}}}{\overline{c_{1,r}}}\right) \neq \arg\left(\overline{\left(\frac{c_{1,s}}{c_{1,r}}\right)}\right). \tag{5.59}$$

As the step from raw data to Fourier coefficient is linear, the right hand side is obtained by averaging over the raw data, while the left hand side can only be obtained by averaging the

Fourier coefficients in the complex plane. The estimation of the oscillation phase from the ROI of the PMMA wedge by the use of the three averaging methods can be seen in Fig. 38 (a). While the arithmetic average decreases towards zero for increasing noise level, the raw and complex estimators remain constant. Nevertheless, there are differences in their noise properties.

Similarly, the average $\overline{a_1} = 2|\overline{c_1}|$ is an unbiased estimator for $E(a_1)$. Nevertheless, in a low SNR measurement, it is not the expectation value of the amplitude that is of interest, but the parameter a_1 of the Rician distribution as presented in Eq. (5.21). While for high SNR, the expectation value of the Rician distribution is approximately equal to a_1 as described by Eq. (5.28), for low SNR, the expectation value of the amplitude rises with the noise level, as described by Eq. (5.25). Thus, while the mean reconstructed amplitude is easily obtainable by Eq. (5.58), the actual oscillation amplitude and thus the parameter that carries information considering the sample remains unknown. The simplest estimator for the parameter a_1 of the Rician distribution can be found by solving Eq. (5.30) for the amplitude

$$a_1 = \sqrt{V(x) + E(x)^2 - 4 \cdot a_0^2 \cdot \tilde{\sigma}^2}. \tag{5.60}$$

While $E(x)$ can be estimated by averaging over the measured data and $V(x)$ by the squared standard deviation of the data, $\tilde{\sigma}$ can be extracted from the attenuation-contrast channel. The estimation of the amplitudes for the reference and sample measurements from the ROI of the Al bar as presented in section 5.1.7 can be seen in Fig. 38 (b). The calculations were performed by the use of the arithmetic average on the one hand and by Eq. (5.60) on the other.

While the estimation leads to better results than the estimation using solely averaging, for low SNR, the estimator still leads to deviations. Following the argumentation in Ref. [Sijbers99], this is due the biased nature of this estimator. The problem of estimating the parameters a_1 and $V(a_1)$ from a given number of amplitude data has been widely studied in the literature and will not be followed further in this work. The interested reader is referred to three different methods: the methods of moments [Talukdar91], the method of maximum likelihood [Bonny96] and the method of least squares [Sijbers99].

5.3 Dependence on the number of phase steps and dose

In the following, we will analyze the dependence of the image noise in the reconstructed data on the number of scan steps N and thus of the sampling of the interference pattern in the phase-stepping scan. Two different cases have to be distinguished: Constant total dose and constant dose per step. As the noise in all three contrast channels depends on $\tilde{\sigma}$ following Eqs. (5.8), (5.16) and (5.30), we will perform the analysis based on this parameter.

If the dose per step is kept constant, the oscillation is being sampled at more points, while the three parameters of the phase-stepping oscillation are constant as a function of N. In this case, the noise level $\tilde{\sigma}$ is proportional to

$$\tilde{\sigma} = 1/\sqrt{a_0 \cdot N} \sim 1\sqrt{N}, \tag{5.61}$$

since the mean of the phase-stepping oscillation a_0 is constant per step. Thus, increasing the number of scan steps with equal dose per step leads to an increase in SNR proportional to $\sqrt{N}$ in all three contrast channels. If the dose per step is kept constant, an increase in the number of scan steps naturally leads to a rise in total dose, proportional to N.

If the total dose is kept constant instead, increasing the number of scan steps decreases the dose per step. As the total total dose in the measurement is equal to $\sum_n S_n = a_0 \cdot N$, therefore

$$\tilde{\sigma} = 1/\sqrt{a_0 \cdot N} = const. \tag{5.62}$$

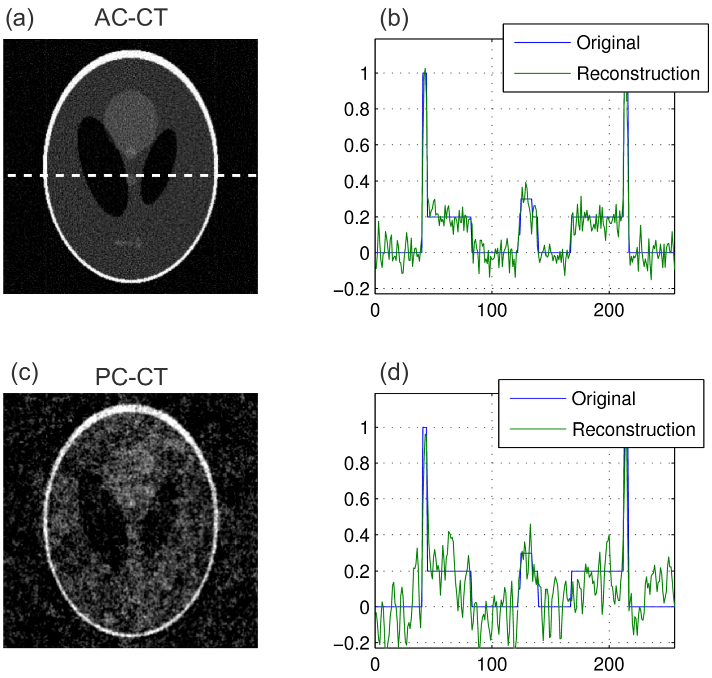

Fig. 39: *Reconstructed Shepp-Logan head phantom for (a) attenuation contrast and (c) phase contrast. (b) and (d) show the corresponding profiles for the dashed line indicated in (a). The increased noise power at low spatial frequencies in phase contrast leads to a different noise texture, causing difficulties in the discrimination of sample details.*

is constant in this case. Thus, the noise in the reconstructed images for a given fixed total dose is independent of the total number of scan steps.

Therefore, we can conclude that the image noise in the three contrast channels is determined by the total dose applied in the measurement. For a given and fixed total dose, the quality of the reconstructed differential phase and dark-field images is independent of the number of phase steps N.

5.4 Noise in tomographic imaging

Similarly to the noise propagation from the measured raw data to the different images reconstructed from the phase-stepping oscillation, the noise in the three reconstructed contrast channels will influence the image quality in a tomographic reconstruction. In this section, we will highlight the propagation of noise through the CT-reconstruction algorithms, which were presented in section 3.44. The results for the differential phase-contrast channel are based on Ref. [Raupach11] and will only be briefly discussed for completeness sake.

Due to the linearity of the reconstruction, for the attenuation-contrast channel, the noise in the reconstructed tomographic slices is equal to the well understood noise properties of conventional x-ray CT imaging. For a discussion of these properties, the reader is referred to [Barret96].

For the differential phase-contrast channel, an important difference has to be taken into account: As the measured oscillation phase $\Delta\varphi$ is proportional to the gradient of the phase $\partial_x\Phi$, an integration has to be performed during the reconstruction of the refractive decrement $\delta(\mathbf{r})$. This integration, or summation in the discrete case, introduces long ranged correlations into the image reconstruction. The reconstructed slices will thus be dominated by a low frequency noise. As shown in Ref. [Raupach11], the noise power spectrum (NPS) of the phase-contrast image $NPS_{\Delta\Phi}$ can be related to the noise power spectrum of the differential phase-contrast image $NPS_{\Delta\varphi}$ by

$$NPS_{\Delta\Phi}(f) = \left(\frac{p_2}{\lambda d}\frac{a}{2}\right) \cdot \frac{NPS_{\Delta\varphi}(f)}{\sin(\pi f a)} = \left(\frac{p_2}{\lambda d}\frac{a}{2}\frac{\sqrt{2}}{\nu}\right) \cdot \frac{NPS_T(f)}{\sin(\pi f a)}, \tag{5.63}$$

where a is the pixel size, p_2 the period of the analyzer grating, λ the x-ray wavelength, and d the distance between the beam-splitter and analyzer grating. By the factor $1/\sin(\pi f a)$ the $NPS_{\Delta\Phi}$ diverges like $\sim 1/f^2$ for $f \to 0$. The reconstructed slices in phase-contrast imaging will thus be dominated by low frequency noise, which may render the identification of small structures in the slice more difficult, as shown exemplarily in Fig. 39 for the well known Shepp-Logan head phantom [Kak88].

In the dark-field-contrast channel, the noise is Gaussian distributed for high SNR and no additional step is needed for data reconstruction. The NPS will thus be the same as is the attenuation-contrast channel, only with a higher noise variance.

5.5 Noise reduction using adaptive wavelet thresholding

An interesting and promising approach to the reduction of noise is given by the use of wavelets. In the wavelet domain, the image is represented by wavelet coefficients, in number equal to the number of pixels in the original image. While the relevant image information is enclosed in a small number of wavelet coefficients with high amplitude, the noise in the image remains diffusely distributed across the image with low amplitude. By applying a global threshold in the wavelet domain representation of the image, the noise in the image can be suppressed, while only marginally influencing the image data. The difficulty in this approach is to estimate a correct level of thresholding. If the threshold is set too high, relevant image information will be lost, if it is set too low, image noise will only be marginally suppressed. While various threshold estimators exist in the research field of wavelet noise reduction, we would like to follow a similar approach as presented in Refs. [Borsdorf06, Borsdorf08]: As noise is essentially an uncorrelated signal from an analytical point of view, image noise can be distinguished from image information by a cross-correlation analysis. Two consecutive neighboring views of a tomographic scan differ only little in their image information and can thus be cross-correlated to obtain a local measure of the relevant image information. From this correlation, a local measure for the threshold in wavelet domain can be obtained. For attenuation contrast, this approach is only possible in CT imaging. Nevertheless, the grating-based DPC technique offers an additional approach: Instead of using neighboring views of a tomographic scan for cross-correlation analysis as described in Refs. [Borsdorf06, Borsdorf08], in DPC imaging, the images obtained in a phase-stepping scan can be correlated. By the phase-stepping method, the DPC-technique necessarily delivers at least three images of an object with essentially equal and thus correlated image information, overlaid with additional uncorrelated noise. The cross-correlation between the different images recorded in the phase-stepping scan can be used to obtain a local estimate of the noise threshold in wavelet domain. By this approach, noise can even be reduced if only a single DPC scan was performed. In the course of this work, first steps towards an application of this approach were performed, with promising results. Nevertheless, an in-depth assessment of this denoising technique would require an extensive analysis of the MTF of the algorithm, as a function of a great number of relevant parameters. A decisive conclusion on the quality of the approach has not been developed.

5.6 Summary

In this section, the noise characteristics of the different contrast channels obtainable by grating-based imaging were investigated and analyzed. In section 5.1, the basic noise characteristics and the propagation of noise from the raw data were highlighted, under the assumption of pure quantum noise. The Poissonian distribution was identified as the noise distribution of the mean value a_0, while the phase φ and the amplitude a_1 of the phase-stepping oscillation are described by a wrapped Gaussian PDF and a Rician PDF, respectively. Based on these results, the expectation values and variances of the visibility, the transmission, the differential phase and the dark-field signal were derived using a Taylor approximation. While the attenuation-contrast channel was shown to depend only on the total dose applied, the noise in the differential phase and dark-field-contrast channel depends on the visibility, transmission and scattering in the sample itself. Explicit analytical formulas showing the dependencies were derived for all parameters involved, and compared to measurements. Both the phase and dark-field-contrast channels exhibit a breakdown of information transfer for decreasing SNR. While the DPC signal converges towards a uniform distribution due to phase wrapping effects, the dark-field signal approaches an image related to the inverse of the transmission image for low SNR. An upper bound for the noise level and thus dose was presented, below which the noise in the differential phase and dark-field-contrast channel is approximately Gaussian. Due to these statistical properties, in section 5.2, maximum likelihood estimators adapted to reconstruct the parameters of the underlying distribution from an ensemble of pixels were presented. For the estimation of the phase, it was shown that the non-linearities in the phase reconstruction make it necessary to perform averaging over the raw data instead of the reconstructed phase data. A simple biased estimator for the amplitude was introduced, leading to a better parameter estimation. In section 5.3, the reconstructed contrasts were shown to depend only on the total dose applied and to be independent on the number of scan steps. In section 5.4, the analysis was extended to the noise properties in tomographic reconstructions. The noise characteristics in the dark-field-contrast channel were shown to be equal to the well known characteristics of the attenuation channel. In contrast, the noise properties in the differential phase-contrast channel exhibit an enhancement of low spatial frequencies due to the integration of the differential data, which introduces long ranged correlations into the image.

6 Imaging with polychromatic radiation

High-powered laboratory x-ray sources emit polychromatic radiation. As the different energies of the spectrum are averaged into a single effective value by the imaging system, an analysis on how a given source spectrum contributes to the resulting measured data has to be performed. The energy-dependence of the visibility gives rise to the spectral sensitivity of the interferometer, which will be described in section 6.1. The obtained results find application in the discussion of beam-hardening effects in section 6.2, which will be presented for all three contrast channels. First, in section 6.2.1, the beam-hardening effect and the resulting image artifacts in classical attenuation contrast will be discussed, followed by an introduction into beam hardening in phase and dark-field imaging in sections 6.2.2 and 6.2.3, respectively. In section 6.2.4, a linearization approach to the correction of beam-hardening artifacts will be presented, followed by an experimental verification in section 6.2.5.
The analysis of beam-hardening effects in DPC imaging is based on and has been published in Ref. [Chabior11D].

6.1 Spectral sensitivity of the interferometer

For a given a beam-splitter grating, the interference pattern shows maximum modulation at a certain distance d downstream of the grating. If a phase grating is used, this distance corresponds to a fractional Talbot distance

$$d_m = m \cdot n \cdot \frac{2p^2}{\lambda}, \tag{6.1}$$

with m the fractional Talbot order and n a factor depending on the type of the beam-splitter grating. As the Talbot distance depends on the energy, for a fixed inter-grating distance, the modulation will only be maximum for a **design energy** E_0, which is determined by the height and material of the grating structures. For energies that differ from the design energy, the position of maximum modulation will be at another distance from the beam-splitter grating, while at the position d, the intensity pattern for this energy will have a reduced modulation. A reduced modulation is equivalent to a reduced visibility and thus to a reduced signal strength for this energy. The visibility as a function of energy for a certain grating and inter-grating distance, denoted **visibility spectrum** in the following, thus is of vital importance for DPC imaging with polychromatic radiation. In a measurement with a polychromatic source, the visibility spectrum describes how much the different energies in the source spectrum contribute to the image formation in phase and dark-field contrast. The visibility as a function of monochromatic energy at different Talbot distances for a $\pi/2$-shifting beam-splitter grating with a design energy of $E_0 = 40$ keV can be seen in Fig. 40 (a)-(c).
The visibility $\nu(E,z)$ for a given grating at energy E and propagation distance z obeys the symmetry relations

$$\nu(a \cdot E, b \cdot z) = \nu(E/b, z/a) \quad \text{and} \quad \nu(a \cdot E, a \cdot z) = \nu(E,z), \tag{6.2}$$

where a and b are real constants. The origin of this symmetry is the dependence of the Fresnel propagator on z/E: Since the intensity modulation behind a grating is caused by the propagation of the wavefront modulation imposed by the beam-splitter grating, the characteristics of the intensity modulation at any given distance are determined by the properties of the Fresnel propagator. For a π and $\pi/2$ shifting grating with a duty cycle of

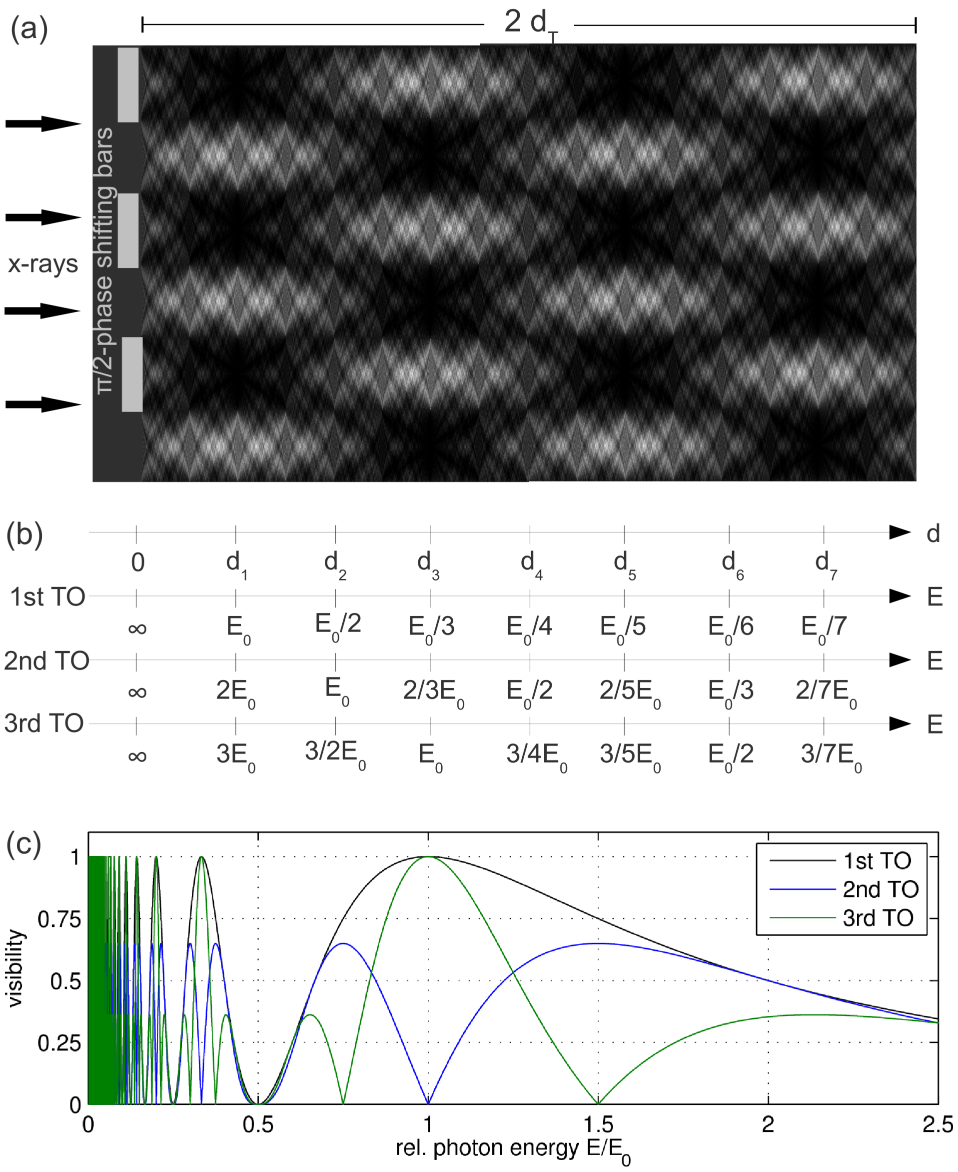

Fig. 40: *(a) Intensity distribution downstream of a* $\pi/2$*-shifting phase grating, shown for a propagation distance of* $2d_T$*. (b) The fractional Talbot distances* d_m *belonging to the intensity pattern. The propagation axis can be rescaled to an energy axis for a given inter-grating distance by the use of Eq. (6.2), shown here in the case of the first, second, and third Talbot order (TO). (c) Calculated visibility spectrum* $\nu(E)$ *of the interferometer in multiples of the design energy* E_0 *in first (black line), second (blue line) and third (green line) Talbot order.*

$\tau_1 = 1/2$, the visibility at the first fractional Talbot order can be calculated by

$$\nu(E, d_1) = \sin\left(\frac{\pi}{2} \cdot \frac{E_0}{E}\right)^2. \tag{6.3}$$

The following relation allows the calculation of the visibility spectrum at the higher Talbot orders

$$\nu(E, d_m) = \nu(E, d_1) \cdot \left|\sin\left(m \cdot \frac{\pi}{2} \cdot \frac{E_0}{E}\right)\right|. \tag{6.4}$$

Eq. (6.4) was used for the calculation of the visibility spectra as shown in Fig. 40 (c) for the first three Talbot orders. The spectrum can be understood by noting that the energy axis can be translated into a propagation distance by the use of Eq. (6.2). The form of the spectrum therefore is identical to the transversal shape of the interference pattern, as indicated by the different axes in Fig. 40 (b).

In the following, we will assume that the imaging system is linear with respect to the energy, i.e. that the resulting polychromatic contrast can be modeled as a linear superposition of the different monochromatic energies of the source spectrum [Engelhardt08]. For a polychromatic source, the measured intensities have to be integrated over all energies of the source spectrum $I(E)$, additionally weighted with the energy dependent efficiency $D(E)$ of the detector. Energy-averaged quantities will be denoted by an overline in the following. The measured polychromatic intensity oscillation $\overline{S}_n$ is therefore given by the integral over the monochromatic intensity oscillations as described by Eq. (2.66) in section 2

$$\overline{S}_n = \int_E \left[a_0(E,L) + a_1(E,L)\cdot\cos\left(2\pi\frac{n}{N} - \varphi(E)\right)\right] dE, \tag{6.5}$$

where we have introduced the mean value

$$a_0(E,L) = D(E)\cdot I(E)\cdot\exp\left(-\int_0^L \mu(E)dz\right) \tag{6.6}$$

and the amplitude

$$a_1(E,L) = \nu(E)\cdot a_0(E,L) = \nu(E)\cdot D(E)\cdot I(E)\cdot\exp\left(-\int_0^L \mu(E)dz\right), \tag{6.7}$$

of the phase-stepping oscillation as a function of energy E and sample thickness L. The function $\nu(E)$ is the visibility as a function of energy as shown in Fig. 40 (c).

6.2 Beam hardening and its correction

Common x-ray tubes as used in laboratory setups emit a spectrum of energies, which are averaged into an effective value by the detection system. As low energy components of the spectrum are absorbed more strongly than high energy components, an absorbing sample in the beam path will alter the spectrum along the path of a line integral. Thus, a dependence on the sample geometry is introduced into the measured effective data. In this section, we will discuss this so-called beam-hardening effect and evaluate its influence on the three contrast channels in grating-based x-ray imaging.

6.2.1 Beam hardening in attenuation-contrast imaging

In conventional radiography, the measured signal $a_{0,s}$ of a projection relative to a reference $a_{0,r}$ yields the transmission T of x-rays along the projection axis z, following Beer-Lambert's law

$$\Gamma = -\ln\left(\frac{a_{0,s}}{a_{0,r}}\right) = \int_0^L \mu(\mathbf{r},E)\cdot dz, \tag{6.8}$$

where Γ is the negative logarithm of the measured transmission of the sample, $\mu = \mu(\mathbf{r},E)$ the linear attenuation coefficient as a function of position $\mathbf{r} = (x,y,z)$ and photon energy E, and $L = L(x,y)$ the sample thickness along the z axis. For a polychromatic source, the measured polychromatic intensities are given by

$$\overline{a}_{0,s} = \int_E a_0(E,L)\cdot dE \tag{6.9}$$

for a measurement with absorbing sample and

$$\overline{a}_{0,r} = \int_E a_0(E,0)\cdot dE \tag{6.10}$$

for the reference intensity in the absence of a sample. The polychromatic attenuation $\overline{\Gamma}$ is therefore given by

$$\begin{aligned}\overline{\Gamma} &= -\ln\left(\frac{\overline{a}_{0,s}}{\overline{a}_{0,r}}\right)\\ &= -\ln\left[\frac{\int_E D(E)\cdot I(E)\cdot \exp\left(-\int_0^L \mu(E)dz\right)\cdot dE}{\int_E D(E)\cdot I(E)\cdot dE}\right].\end{aligned} \tag{6.11}$$

Despite the non-linear relationship between traversed thickness L and linear attenuation coefficient $\mu(E)$, it is convenient to interpret the measured polychromatic data by the use of an **effective linear attenuation coefficient** $\overline{\mu}$ [Kak88]. The usage of $\overline{\mu}$ corresponds to the approximation of the exponential and logarithm in Eq. (6.11) with $\exp(x) \approx 1+x$ and $\ln(1+x) \approx x$, which is valid for small L. Using these approximations, Eq. (6.11) simplifies to

$$\overline{\Gamma} \approx \int_0^L \overline{\mu}\cdot dz, \tag{6.12}$$

where the effective linear attenuation coefficient $\overline{\mu}$ is given by a weighted average of the monochromatic linear attenuation coefficients, with the detected spectrum $D(E)I(E) = a_0(E,0)$ as the weight

$$\overline{\mu} := \frac{\int_E a_0(E,0)\cdot\mu(E)\cdot dE}{\int_E a_0(E,0)\cdot dE} = \frac{\int_E D(E)\cdot I(E)\cdot\mu(E)\cdot dE}{\int_E D(E)\cdot I(E)\cdot dE}. \tag{6.13}$$

By this approximation, the relation between the penetrated thickness and the logarithmic gray value is linearized. Thus, as $\overline{\mu}$ is approximately constant for small sample thickness and attenuation, we can define an **effective energy** $\overline{E}_\mu$ of the setup by

$$\mu(\overline{E}_\mu) := \lim_{\mu L\to 0}\overline{\mu}. \tag{6.14}$$

The effective energy is defined as the monochromatic energy that yields the same linear attenuation coefficient as measured with the polychromatic source. Since $\mu(E) \sim E^{-3}$ for energies where the photoelectric effect is dominant ($E < 40$ keV, see section 2.1 for a detailed discussion of the energy and atomic number dependence of the different interaction processes contributing to μ), we may alternatively define the effective energy as the center of energy of the detected spectrum by

$$\overline{E}_\mu \approx \left(\frac{\int_E a_0(E,0)\cdot E^{-3}\cdot dE}{\int_E a_0(E,0)\cdot dE}\right)^{-3}. \tag{6.15}$$

This specific energy dependence causes low energy components of the spectrum to be absorbed more intensely than high energy components. Therefore, the beam spectrum hardens the thicker the penetrated object is. As this aspect is disregarded by the applied linear approximation, beam hardening leads to a decrease of $\overline{\mu}$ with the absorber thickness, or, if $\overline{\mu}$ is assumed to be constant in the measurement, to a systematic underestimation of the absorber thickness L via Eq. (6.12). In CT images, this well-known effect causes streak artifacts along edges and cupping artifacts in areas of constant thickness, which severely affect image quality and quantitative evaluation [Kak88].

6.2.2 Beam hardening in differential phase-contrast imaging

Since the refractive decrement δ is energy-dependent with $\delta \sim 1/E^2$ following Eq. (2.17), the phase shift $\Phi = k\int \delta dz$ of a wavefront caused by a sample is proportional to $\Phi \sim 1/E$. Thus, for the measured oscillation phase $\varphi = d\lambda/p_2 \cdot \partial_x \Phi$, we obtain an energy dependence proportional to

$$\varphi \sim 1/E^2. \tag{6.16}$$

Because of the energy dependence of δ and Φ, all phase-contrast imaging techniques using polychromatic radiation are also affected by beam-hardening effects. When using a polychromatic spectrum, the explicit analytical calculation of the first Fourier coefficient $\overline{c}_1$ from Eq. (6.5) using DFT yields the relation

$$\overline{c}_1 = \frac{1}{2}\int_E a_1(E,L) \cdot \exp\left(i\varphi(E)\right) dE, \tag{6.17}$$

and thus

$$\overline{\varphi} = \arg\left(\frac{1}{2}\int_E a_1(E,L) \cdot \exp\left(i\varphi(E)\right) \cdot dE\right). \tag{6.18}$$

By the exponential attenuation term $\exp(-\int_0^L \mu(E)dz)$ in $a_1(E,L)$, beam-hardening effects are introduced in DPC imaging. If the oscillation phase $\varphi(E)$ is assumed small for all energies, Eq. (6.18) can be simplified by approximating the exponential by $\exp(i\varphi) \approx 1 + i\varphi$ and the argument function by $\arg z \approx \mathrm{Im}\, z/\mathrm{Re}\, z$, which leads to

$$\overline{\varphi} \approx \frac{\int_E a_1(E,L) \cdot \varphi(E) \cdot dE}{\int_E a_1(E,L) \cdot dE}, \tag{6.19}$$

an expression in analogy to Eq. (6.13) for the attenuation-contrast channel. Nevertheless, it should be stressed that this approximation is valid only in a limited number of cases.

By applying the monochromatic Eq. (2.42) to the polychromatic case, an effective wavefront phase shift $\overline{\Phi}$ can be determined from the measured oscillation phases by integrating the image data $\overline{\varphi}(x,y)$ along the phase-stepping scan direction x:

$$\overline{\Phi} = \frac{p_2}{\overline{\lambda} d}\int_0^x \overline{\varphi} \cdot dx. \tag{6.20}$$

Additionally, from Eq. (6.18), an effective refraction decrement $\overline{\delta}$ can be calculated by

$$\overline{\delta} = \frac{p}{2\pi d}\int_0^x \overline{\varphi} \cdot dx. \tag{6.21}$$

In Eq. (6.20), $\overline{\lambda}$ denotes the wavelength at the effective energy $\overline{E}_\delta$ of the spectrum. This energy can be defined in analogy to the effective energy in attenuation imaging as shown in Eq. (6.14): Since $\overline{\delta}$ is independent of sample thicknesses for vanishing attenuation, we can thus define the effective energy $\overline{E}_\delta$ in DPC imaging by

$$\delta(\overline{E}_\delta) := \lim_{\mu L \to 0} \overline{\delta}. \tag{6.22}$$

Similar to Eq. (6.15), the effective energy may be equivalently defined by

$$\overline{E}_\delta \approx \left(\frac{\int_E a_1(E,0) \cdot E^{-2} \cdot dE}{\int_E a_1(E,0) \cdot dE}\right)^{-2}. \tag{6.23}$$

If the effective energy is assumed to be constant and independent of the sample thickness in the measurement, its use in Eq. (6.20) will lead to beam-hardening artifacts in the calculated phase $\overline{\Phi}$. Despite the similar definitions, the effective energies in attenuation and DPC imaging differ from each other, due to the additional dependence of $\overline{\delta}$ on the visibility $\nu(E)$ and the different energy dependences of $\delta(E)$ and $\mu(E)$.
By defining

$$\overline{\gamma} := \frac{2\pi}{\overline{\lambda}} \overline{\delta}, \tag{6.24}$$

Eq. (6.21) takes the form $\overline{\Phi} = \int_0^L \overline{\gamma} \cdot dz$ and thus a similar relation corresponding to Eq. (6.12) in attenuation imaging can be derived for DPC imaging. Since the structure of the Eqs. (6.12) and (6.21) is similar, in phase-contrast imaging, artifacts resulting from beam hardening will exhibit qualitatively comparable characteristics as in attenuation imaging. Quantitatively however, the effect is less pronounced in phase-contrast imaging as a result of the reduced energy dependence of $\mu(E) \sim E^{-3}$ relative to $\gamma(E) \sim E^{-1}$ (apart from absorption edges, in detail see 2.1) for the energy range considered in X-ray medical imaging. This was previously experimentally observed in Ref. [Donath10B]. The similarities are remarkable considering the differences between attenuation and phase contrast: in attenuation-contrast imaging, beam-hardening artifacts are introduced by linearizing the exponential dependence on the absorber thickness, thus creating a deviation from the equations used for thick absorbers, as described by Eqs. (6.8) - (6.12). In DPC imaging however, the attenuation term $\exp(\int_0^L \mu(E) dz)$ in Eq. (6.18) cannot be effectively approximated for thin absorber thickness, since the phase data are not logarithmized as in attenuation imaging. Instead, beam-hardening artifacts are introduced by assuming an effective energy that is independent of the object geometry in Eq. (6.21). Another difference lies in the fact that beam-hardening effects depend on the thickness of the absorber, whereas in DPC imaging, the measured quantity φ depends on the gradient of the absorber thickness perpendicular to the direction of propagation. Hence, the measured oscillation phases φ do not allow the direct analysis and correction of beam-hardening effects.
To exemplify beam-hardening effects in DPC imaging, in Fig. 41, a typical visibility spectrum for a two-grating setup at 40 keV design energy in the first fractional Talbot distance, together with a typical source spectrum and a spectrum hardened by a 10 mm sheet of silicon is shown. The hardened spectrum leads to an increase in the effective amplitude of the imaging system, and thus to an increased effective energy.

6.2.3 Beam hardening in dark-field-contrast imaging

For the discussion of beam-hardening effects in the dark-field-contrast channel, the behavior of the amplitude of the phase-stepping oscillation in the presence of absorption has to be investigated. Using a similar reasoning as the one leading to Eq. (6.17) in section 6.2.2, the effective amplitude $\overline{a}_{1,s} = 2|\overline{c}_1|$ of the polychromatic phase-stepping oscillation $\overline{S}$ in the presence of a sample can be calculated by

$$\overline{a}_{1,s} = \left| \int_E a_1(E,L) \cdot \exp\left(- \int_0^L \varepsilon(E) dz \right) \cdot \exp\left(i\varphi(E)\right) dE \right|. \tag{6.25}$$

In this equation, we have introduced the linear diffusion coefficient $\varepsilon(E)$, as presented in section 3.1.3 and Ref. [Bech10], accounting for the visibility decrease by small angle scattering. The polychromatic reference oscillation amplitude $\overline{a}_{1,r}$ can be obtained from Eq. (6.25) by setting

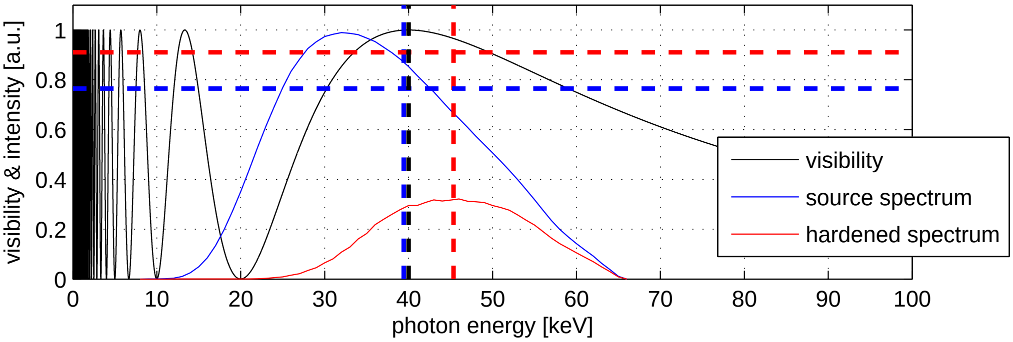

Fig. 41: *Calculated visibility spectrum* $\nu(E)$ *in first Talbot distance, together with an unfiltered source intensity spectrum at* 65 *keV (solid blue line) and a spectrum hardened by a* 10 *mm silicon sheet (solid red line). While the effective energy* $\overline{E}_\delta$ *of the unfiltered spectrum (vertical dashed blue line) is near the design energy of* $E_0 = 40$ *keV (vertical dashed black line), beam hardening leads to an increase of the effective energy for the hardened spectrum (vertical dashed red line).*

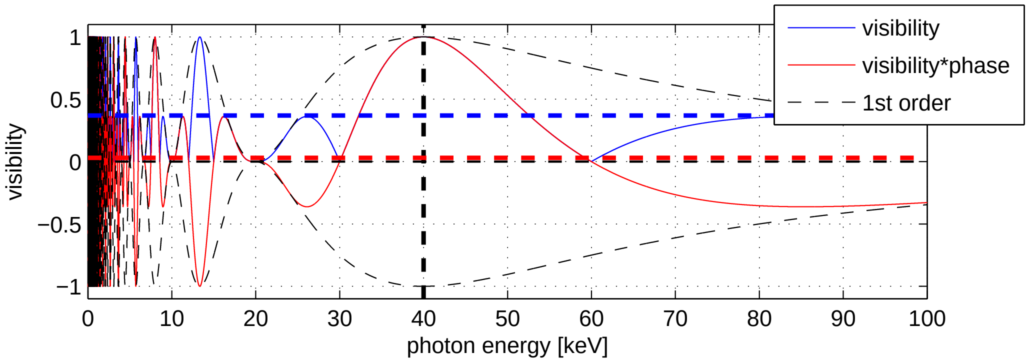

Fig. 42: *Influence of the phase of the interference pattern on the visibility spectrum, by the example of a* $\pi/2$*-shifting phase grating in 3rd Talbot order at 40 keV design energy, without phase dependence (solid blue line) and with phase dependence (solid red line). If the phase of the interference pattern is taken into account, the mean visibility (dashed red line) is close to zero, in contrast to the mean visibility if the phase is not taken into account (dashed blue line).*

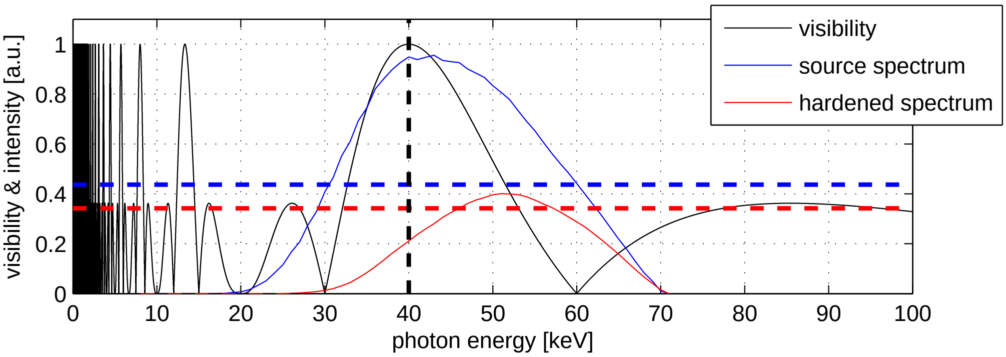

Fig. 43: *Example for an experimental situation with a mean visibility decrease caused by beam hardening: the setup is designed for an energy of 40 keV at 3rd Talbot order with a* $\pi/2$*-shifting grating. The mean visibility (dashed blue line) for the unfiltered 70 kV tungsten spectrum (solid blue line) is higher than the visibility (dashed red line) for the spectrum filtered with 20 mm of Silicon (solid red line).*

$\varepsilon(E) = \mu(E) = \varphi(E) \equiv 0$

$$\bar{a}_{1,r} = \left| \int_E a_1(E,0) \cdot dE \right|, \tag{6.26}$$

with $a_1(E,0) = \nu(E) \cdot D(E) \cdot I(E)$. Thus for the visibility for the reference measurement we obtain

$$\overline{\nu}_r = \frac{\bar{a}_{1,r}}{\bar{a}_{0,r}} = \frac{\int_E a_1(E,0) \cdot dE}{\int_E a_0(E,0) \cdot dE}, \tag{6.27}$$

while in presence of a sample this relation changes to

$$\overline{\nu}_s = \frac{\bar{a}_{1,s}}{\bar{a}_{0,s}} = \frac{\left| \int_E a_1(E,L) \cdot \exp\left(- \int_0^L \varepsilon(E) dz \right) \cdot \exp\left(i\varphi(E) \right) \cdot dE \right|}{\int_E a_0(E,L) \cdot dE}. \tag{6.28}$$

The dark-field signal $\overline{D}$ when using polychromatic radiation is by definition given by the ratio of the polychromatic visibilities defined by Eqs. (6.28) and (6.27)

$$\overline{D} = \frac{\overline{\nu}_s}{\overline{\nu}_r}. \tag{6.29}$$

As can be seen from Eq. (6.28), the polychromatic dark-field signal depends not only on the phase fluctuations described by the diffusion coefficient ε, but also on the attenuation in the sample as well as the phase shift $\varphi(E)$ of the oscillation. The dependence on the attenuation introduces beam-hardening effects in dark-field imaging. The dependence on the phase can be understood by noting that the interference patterns for each energy overlap in the plane of detection. If, for example, the interference patterns for two different energies and otherwise equal amplitude overlap at the plane of detection, their modulation will level out if they are shifted by a phase of π relative to one another. This situation is given if a $\pi/2$-shifting phase grating with inter-grating distance chosen to the 3rd Talbot order is used for imaging: As can be seen from the intensity modulation downstream of the grating in Fig. 40 (a), the interference pattern at the 3rd (and 7th, 11th, ...) fractional Talbot distance is phase shifted by half a period relative to the interference pattern at the 1st (and 5th, 9th, ...) fractional Talbot distance. Thus the superposition of the interference patterns of all energies causes a decrease in modulation and thus visibility even if the visibility for each monochromatic energy is high. The influence of an interference pattern phase shift of π can be included into the calculation of the mean visibility by extending the visibility spectrum to the negative numbers, as discussed in Fig. 42. In contrast to the differential phase-contrast channel, beam-hardening effects can enter the measured dark-field signal in two different ways: first, by the energy dependence of the visibility, and second, by a possible energy dependence of the linear diffusion coefficient $\varepsilon = \varepsilon(E)$. The explicit energy dependence of the linear diffusion coefficient is unknown. As the effective energies $\overline{E}_\mu$ and $\overline{E}_\delta$ are defined over the energy dependence of the underlying parameter $\mu(E)$ and $\delta(E)$, respectively, an effective energy $\overline{E}_\varepsilon$ cannot be readily determined in the dark-field contrast channel. Nevertheless, due to the energy dependence of the visibility, beam-hardening effects may enter dark-field imaging even in the absence of refraction or scattering in the sample. Additionally, depending on the combination of source spectrum and visibility spectrum, beam hardening in dark-field imaging can lead to a decrease as well as to an increase in the measured signal. A example for an increase of the mean visibility caused by beam hardening is shown in Fig. 41, while a decrease with beam hardening is depicted in Fig. 43.

6.2.4 Beam-hardening correction using linearization

For homogeneous objects, the linearization technique [Kak88] proved to be useful for the correction of beam-hardening artifacts in attenuation radiography. In the following, it will be utilized for the correction of beam-hardening artifacts in phase-contrast measurements. As shown in Fig. 44, if $\overline{\mu}$ and $\overline{\gamma}$ are assumed to be constant, a growing absorber thickness and thus growing beam hardening leads to an increasing underestimation of sample thickness.

The aim of the linearization is to transform the non-linear gray values $\overline{\Gamma}$ measured with polychromatic sources into gray values Γ which are linearly proportional to the sample thickness:

$$\Gamma = \overline{\Gamma} \cdot H(L_p). \tag{6.30}$$

Like beam hardening itself, the correction function $H(L_p)$ depends on the absorber thickness L_p as obtained in measurements with polychromatic radiation. Since the oscillation phase φ in DPC imaging is not proportional to the absorber thickness but to its gradient, the measured phases φ cannot give a direct measure of the amount of beam hardening caused by the sample. For a beam-hardening correction, first the phase shift Φ and thus a quantity that is proportional to the sample thickness has to be determined by integration. Alternatively, instead of integrating the measured oscillation phases φ, the required thickness information can be extracted from the attenuation-contrast image. The correction function $H(L_p)$ can be calculated by taking the quotient of the thickness L of an adequately chosen calibration sample with known geometry and the corresponding thickness L_p as obtained from the measurement:

$$H(L_p) = \frac{L}{L_p}. \tag{6.31}$$

In attenuation radiography, usually an absorption stair is used as a test object for the measurement of the correction curve. Thickness and thus beam hardening are constant for each step and can be averaged over the area of each step to improve the signal-to-noise ratio. In contrast to attenuation imaging, in DPC imaging a step with constant thickness would not exhibit a phase gradient and therefore would not give a signal in the DPC measurement, while objects with non-zero phase gradient would exhibit non-constant beam hardening over the area of one step. By choosing an absorption stair for which the absorber thickness and thus the phase shift varies only marginally over the width of one step, a correction curve can be obtained while keeping the systematic error negligible.

The correction curve is only valid for homogeneous objects and only for a certain configuration of source, detector, and gratings. If central measurement parameters of the setup are changed, the correction curve has to be calculated anew: A change in the tube settings, for example a higher anode voltage, would lead to a change of the source spectrum $S(E)$, while a change of the detector, or the detector settings, would alter the detection efficiency $D(E)$, leading to a change in the effective attenuation coefficient $\overline{\mu}$ after Eq. (6.13) and the effective refraction decrement $\overline{\delta}$ via Eqs. (6.18) - (6.21). Additionally, a change in the interferometer geometry leads to a change in $\overline{\delta}$ via the dependence on the visibility $V(E)$. A variation of the setup would lead to a change in the effective energies, following Eqs. (6.14) and (6.22), and thus to an altered correction curve.

In a well calibrated system, correction curves are saved in look-up tables for all materials under investigation. If a priori knowledge of the material distribution in the sample is included into the reconstruction algorithm, the linearization technique can easily be applied in an automated way to multi-material and non-homogeneous samples. For complicated and unknown material distributions, more elaborate methods like iterative algorithms have to be used [Kak88].

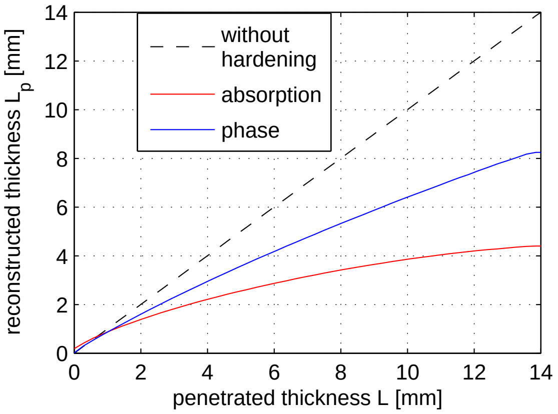

Fig. 44: *Reconstructed absorber thickness L_p from a measurement of a* 10×10 *mm*^{2} *square aluminium bar as a function of the real absorber thickness L. Beam-hardening effects lead to an increasing underestimation of the absorber thickness. The deviation is smaller for the phase-contrast channel due to the reduced energy dependence of γ relative to μ.*

6.2.5 Experiments

In order to demonstrate beam-hardening effects in differential phase-contrast and dark-field-contrast imaging, several simple test objects were measured in a laboratory setup at the Paul Scherrer Institut (PSI) in Villigen, Switzerland. The source was a Seifert DX-W8x0.4-L X-ray tube, operated at an anode voltage of 40 kVp and an anode current of 25 mA. No additional filtration was used. The effective focus size of 0.8×0.4 mm^2 is achieved by an electron beam of 8×0.4 mm^2, using a tungsten anode with a take-off angle of 6°. As detector, a PILATUS 100K (Dectris Ltd., Baden, Switzerland) was used. The single photon counting detector consisted of a 487×195 pixel array with a pixel size of 172×172 μm^2. The phase grating G_1 was manufactured at the PSI [David07] with Si bars of 35 μm height and a period of 3.5 μm, exhibiting a phase shift of π for a design energy of $E_0 = 27.3$ keV. The attenuation gratings G_0 and G_2 [Reznikova08] had Au structure heights of $h_0 = 42$ μm and $h_2 = 26$ μm with periods of $p_0 = 14$ μm and $p_2 = 2$ μm, respectively. The distance between G_1 and G_2 was chosen as the 5th Talbot distance with $d = 200$ mm at a G_0-G_1 distance of $l = 1400$ mm. The phase stepping was done by scanning G_1, with 8 steps over 2 periods of the interference pattern, with an exposure time of 32 s for the complete scan.

For a discussion of beam hardening in DPC imaging, we used a number of geometrically well-defined homogeneous objects as samples: (i) square aluminium bar of 10×10 mm^2 cross-section, (ii) square aluminium bar of 5×5 mm^2 cross-section, (iii) aluminium cylinder of 5 mm diameter. For both bars, the diagonal was aligned along the beam direction z, leading to a phase shift corresponding to a symmetric triangle or double wedge. This gives two constant phase gradients of opposite sign in the differential phase-contrast image. The samples were positioned 100 mm upstream of G_1.

The resulting projection for attenuation-contrast and differential phase-contrast can be seen in Fig. 45 (a) and (b). Using the symmetry of the sample, the measured data were averaged along the vertical axis of the images to gain in signal-to-noise ratio, leading to the averaged cross-sections shown in Fig. 45 (c) and (d), respectively. It can be seen in the DPC profile in Fig. 45 (d) that although the phase gradient of the sample is constant along the horizontal axis of the image, the increasing absorber thickness towards the middle of the aluminium bar leads to a growing hardening of the source spectrum and thus to a decreasing DPC signal $\overline{\varphi}$.

In order to demonstrate the applicability of beam-hardening correction by linearization in phase-contrast imaging, a correction curve $H(L_p)$ as seen in Fig. 44 was calculated from the measured 10×10 mm^2 aluminium bar. First, the 'effective' values of $\overline{\mu}$ and $\overline{\delta}$ have to be calculated. As effective values we have defined those values of $\overline{\mu}$ and $\overline{\delta}$ that arise from a measurement with negligible beam hardening, i.e. for vanishing object thickness, in our measurement the left and right edge of the aluminium bar. As the geometry and material composition of the sample is known, attenuation and phase shift can be calculated for each given monochromatic energy. By fitting the thus obtained theoretically expected monochromatic curves to the measured polychromatic values, as seen in Fig. 45 (c) and (d), the effective energy for our measurements can be reconstructed. From the measurements, the values of $\mu_p = 8.2 \pm 0.3$ cm^{-1} and $\delta_p = (1.37 \pm 0.02) \cdot 10^{-6}$ were calculated. These values correspond to effective energies of $\overline{E}_\mu = 19.9 \pm 0.3$ keV for attenuation and $\overline{E}_\delta = 19.8 \pm 0.2$ keV for phase contrast [Mucal93]. Assuming that these values are constant in the measurement, the thickness distribution of the bar can be reconstructed from the profiles of the sample by use of Eq. (6.12) for the attenuation and Eq. (6.21) for the phase, respectively. After averaging over both slopes of the triangular height profile, the correction curve is calculated by taking the ratio between the measured and the ideal values for both attenuation and phase contrast, as presented in Fig. 44. The stronger energy dependence for the attenuation contrast manifests itself in a stronger decrease of the curve with increasing absorber thickness L.
In order to test the correction algorithm, additionally to the 10×10 mm^2 bar, two other aluminium objects were measured as shown in Fig. 46 (a) for attenuation contrast and (b) differential phase contrast: a square bar of 5×5 mm^2 cross-section and a cylinder with a diameter of 5 mm. After averaging the measured DPC values along the vertical axis of the image, the object thicknesses L_p were reconstructed and then corrected for beam hardening using the calculated correction curve $H(L_p)$. The measured and corrected results together with the real object's dimensions are given in Fig. 46 (c) and (d), respectively. It can be seen that the corrected profiles are in good agreement with the theoretically expected values for the 10×10 mm^2 bar and the cylinder. The small deviation for the 5×5 mm^2 bar results from a misalignment of the bar during the measurement, giving the projected thickness profile a slightly trapezoidal instead of a perfectly triangular shape. Nevertheless, the results prove that the linearization technique leads to a successful compensation of beam-hardening effects in phase-contrast imaging in the case of homogeneous objects.

For the discussion of beam-hardening effects in dark-field imaging, the dark-field signal of an exemplary test sample as a function of the hardening of the source spectrum was measured. As sample, we used a stair made out of paper. The stair was created by stacking sheets of common printer paper, with a step width of approximately 2.5 mm and a step length large enough to fill the field of view. Each paper sheet had a thickness of approximately 0.1 mm, stacked in 12 sheets up to a maximum thickness of 1.2 mm. The source spectrum was hardened by filtering with aluminium. Instead of performing consecutive measurements using aluminium filters of different thickness, we chose the approach to perform a single measurement with different effective spectra in one image, by the use of an aluminium stair: Similar to the paper stair, the stair was created by stacking sheets of 1 mm thick Al plates onto each other, up to a maximum thickness of 10 mm. The step width was approximately 5 mm, with a step length large enough to fill the field of view. The aluminium stair was placed into the beam path in the reference measurement and remained unchanged in the sample measurement with the additional paper stair. In the measurement, the steps of the aluminium stair were oriented perpendicular to the steps of the paper stair. By this measure, we obtain an image of the paper stair with different

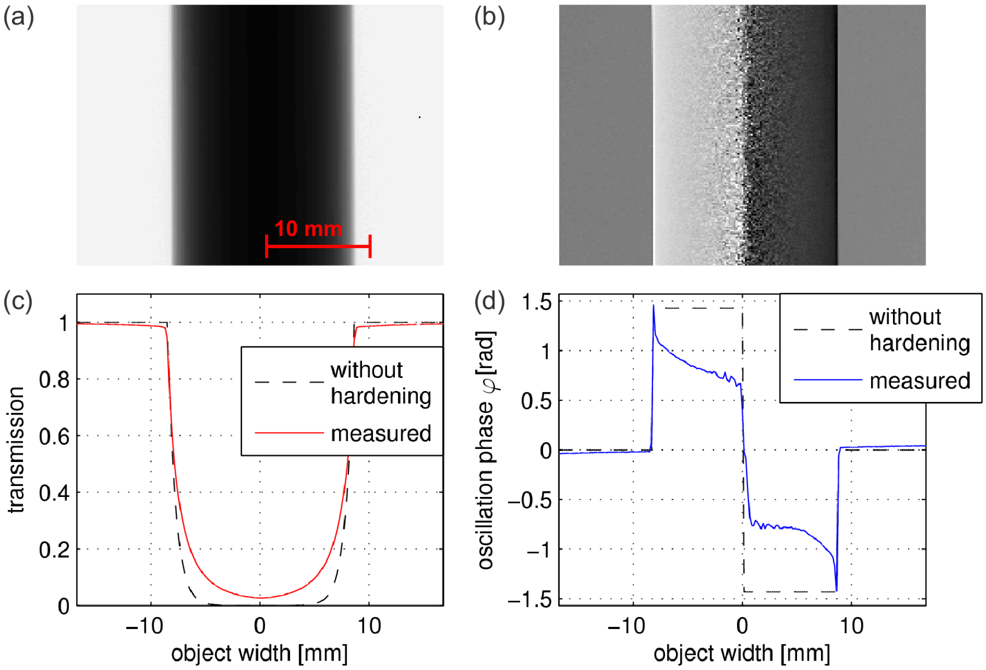

Fig. 45: *(a) Attenuation-contrast and (b) differential phase-contrast radiography of a square aluminium bar with* 10×10 *mm*^{2} *cross-section. (c) and (d) the respective horizontal profiles averaged along the vertical direction of the image. Unlike the ideal values at the monochromatic effective energy (dashed line), the measured values (solid line) decrease with growing absorber thickness due to beam hardening.*

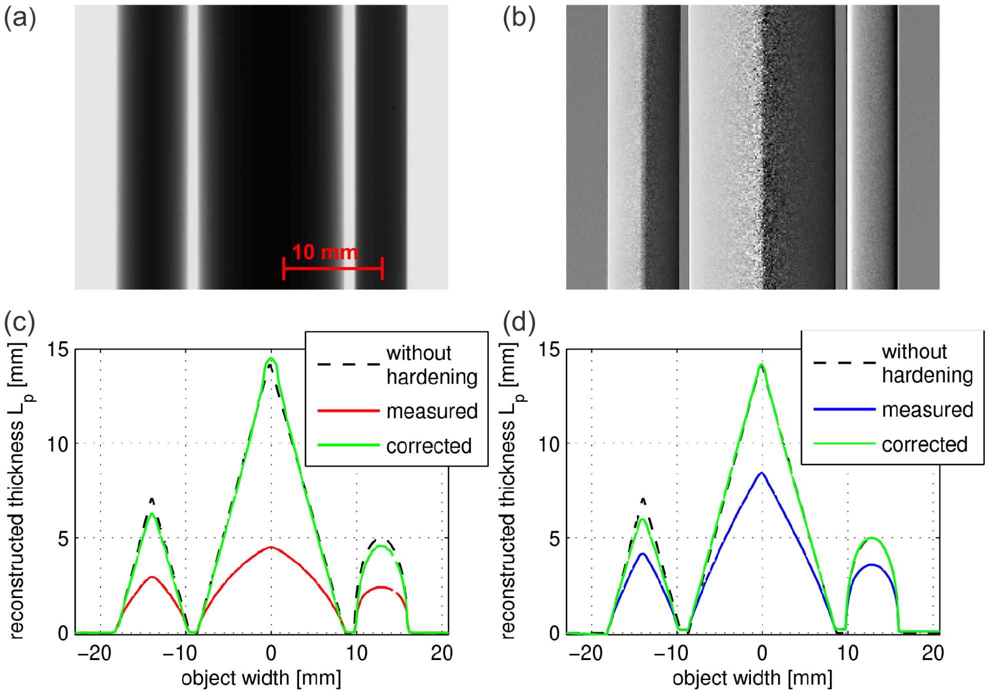

Fig. 46: *(a) Attenuation-contrast and (b) differential phase-contrast radiography of two square aluminium bars with* 5×5 *and* 10×10 *mm*^{2} *cross-section and a cylinder of 5 mm diameter. (c) and (d) show the corresponding reconstructed height profiles of the vertically averaged samples, as measured with beam hardening (attenuation solid red line, phase solid blue line), corrected for beam hardening (solid green line), compared to the real thickness of the samples (dashed line).*

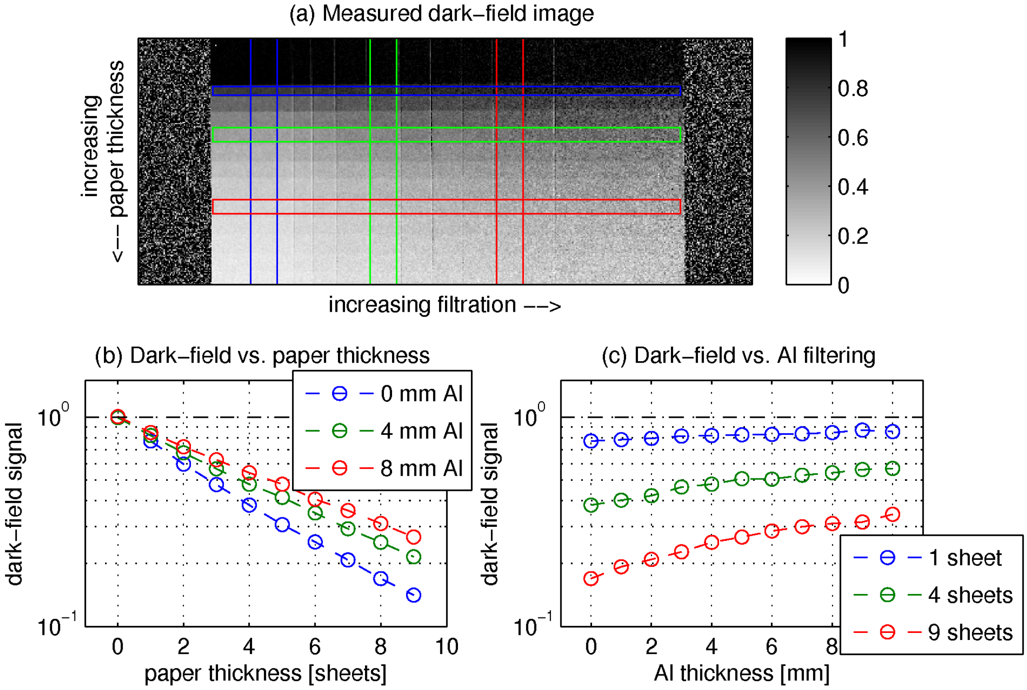

Fig. 47: *Measurement demonstrating beam-hardening effects in dark-field imaging: (a) Measured paper-stack phantom (gray coded), with increasing paper thickness towards the bottom of the image. The source spectrum was hardened by an Al stair (1 mm per step), with increasing Al thickness towards the right side of the image. (b) Average dark-field signal as a function of paper thickness for three different filtrations (vertical ROIs, blue 0 mm, green 4 mm, red 8 mm Al). (c) Average dark-field signal as a function of filtrations for three different paper thicknesses (horizontal ROIs, blue 1 sheet, green 4 sheets, red 8 sheets of paper). The dependence of the measured dark-field signal on the filtration is caused by beam hardening.*

effective source spectra in one single measurement. The resulting dark-field image is shown in Fig. 47 (a).

The superposition of paper stair and aluminium stair divides the dark-field image into a matrix of areas with piecewise constant paper thickness and spectrum filtering, as indicated by the colored rectangles in Fig. 47 (a). The measured dark-field data were averaged over each constant area of the matrix for an increase in signal-to-noise ratio. The resulting averaged dark-field signal as a function of paper thickness for three different source filtrations can be seen in Fig. 47 (b), while the averaged dark-field signal as a function of source filtration for three different paper thicknesses is shown in Fig. 47 (c).

The results clearly show a dependence of the measured dark-field signal on the filtering of the source spectrum, proving beam-hardening effects in dark-field imaging. Nevertheless, an interpretation of the obtained data remains difficult. This is caused by the fact that quantitative data for the linear diffusion coefficient of a given material at monochromatic energies are not readily available or tabulated in literature. For this reason, neither the effective energy $\overline{E}_\varepsilon$ nor the correction curve needed for the linearization technique can be determined. Additionally, it is unknown whether the diffusion coefficient is a function of energy $\varepsilon = \varepsilon(E)$. Since beam-hardening in the dark-field contrast channel can occur even in the absence of a scattering sample, in our measurement we cannot determine whether the measured decrease of the dark-field signal is solely caused by a change in the mean visibility, or by the energy dependence of the linear diffusion coefficient, or by a combination of both.

6.3 Summary

In this section, polychromatic effects in x-ray imaging using a grating interferometer were discussed. The basis for the discussion was given by an analytical discussion of the visibility spectrum in section 6.1. The problem of beam hardening in grating-base x-ray imaging has been addressed in the context of attenuation contrast (section 6.2.1), differential phase-contrast (section 6.2.2 and dark-field imaging (section 6.2.3) using a grating interferometer. The concept of effective energy has been introduced and has been shown to be different from each other in attenuation-, phase- and dark-field contrast due to the contribution of the energy-dependent visibility spectrum. Beam hardening was demonstrated to be a problem for all contrast channels theoretically and in measurement. The effect is less distinct in phase-contrast radiography due to the reduced energy dependence of the refractive decrement relative to the attenuation coefficient. Since differential phase data depend on the gradient of the sample thickness, beam-hardening effects are introduced in DPC imaging in an indirect way compared to the attenuation data. In dark-field imaging, beam hardening is introduced in two ways: by an energy dependent visibility and by an energy dependent diffusion coefficient. Additionally, beam hardening may lead to a decrease as well as an increase of the measured dark-field signal. Due to the lack of data for the linear diffusion coefficient, a explicit discussion of beam hardening in dark-field imaging remains difficult. In section 6.2.4, a linearization technique for the correction of beam-hardening effects was presented. The results show that for homogeneous objects, a beam-hardening correction based on linearization leads to a good agreement with the theoretical values and can thus be advocated for practical implementation in all application fields.

7 Imaging with imperfect gratings

The three gratings are the central part for the understanding of the grating-based differential phase-contrast technique. High-quality gratings adapted to the imaging application are the key for a good performance of the interferometer. Nevertheless, the gratings will in reality never be ideal, due to physical restrictions and errors during fabrication. In this section will be investigated how grating errors influence the image quality in DPC imaging. First the grating alignment and the influence of alignment errors will be reviewed in section 7.1. Typical deviations from the ideal rectangular shape of a grating bar profile will be discussed in the following sections, ranging from deviations in the height of the bars (section 7.2), deviations in form (section 7.3) and deviations in period and duty cycle (section 7.4). The investigations will be performed mostly analytically, supplemented by simulations and exemplary measurements where helpful or necessary. In section 7.5, it is shown that the divergent beam geometry in a compact laboratory setup makes it necessary to utilize bent grating structures, instead of plane structures.

7.1 Grating alignment

For an optimal performance of the interferometers, the grating structures have to be aligned parallel to each other and positioned at the correct distances. Due to the involved length scales of just a few microns, alignment has to be precise and stable. A misalignment will create distortions and a decrease in visibility and thus imaging performance. In our discussion, we will restrict ourselves to the superposition of two gratings. In a three-grating interferometer, the gratings have to be aligned pairwise to each other, as well as to the source. The alignment techniques presented in the following are known and widely used in the DPC imaging community, and shall be summarized in this section for completeness sake.

Alignment using optical lasers

Besides a rough mechanical alignment using ruler and a steady hand, a fine mechanical pre-alignment can be achieved by the use of common visible light lasers. As the wavelength of visible light is in the order of the gratings period, the gratings will act as diffraction gratings, and reflect a diffraction pattern when illuminated. If the laser beam is aligned along the optical axis of the setup, the orientation of the gratings can be optimized by adjusting the diffraction pattern to a reference line on a screen, as illustrated in Fig. 48 (a). If the screen is positioned far way from the grating and the diffraction pattern is thus strongly magnified, a high alignment accuracy can be achieved.

Alignment using grating geometry

Since the gratings structures are aligned parallel or perpendicular to the gratings outer boundaries and wafer dimensions, the gratings can be roughly aligned around the z-axis by rotating them parallel to the detector lines. As the attenuation gratings exhibit an inhomogeneous transmission when using a divergent source, the transmission profile of the grating can be used for optimizing the grating alignment around the y-axis, as illustrated in Fig. 48 (b) (see also section 7.5).

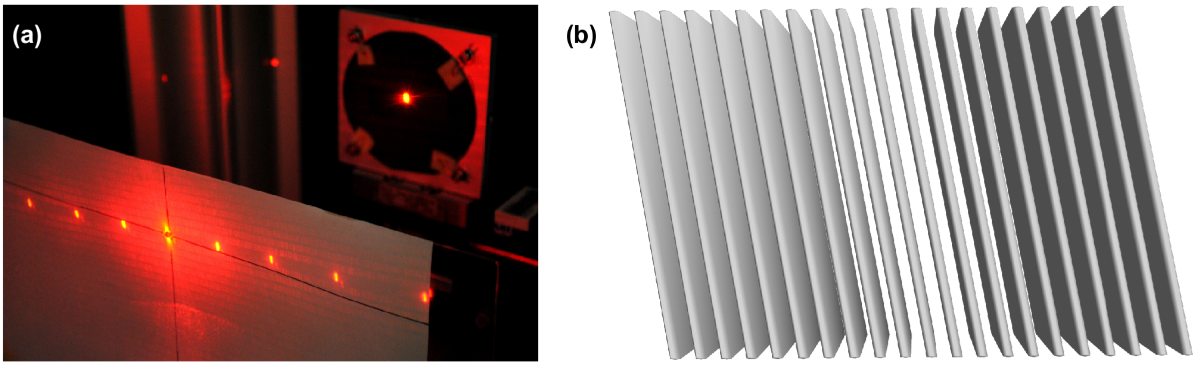

Fig. 48: *(a) Grating alignment using diffraction of visible laser light. In the shown example, the grating is misaligned around the z-axis. (b) Illustration of the shadowing effect caused by an attenuation grating, which can be used to determine the orientation of the grating bars.*

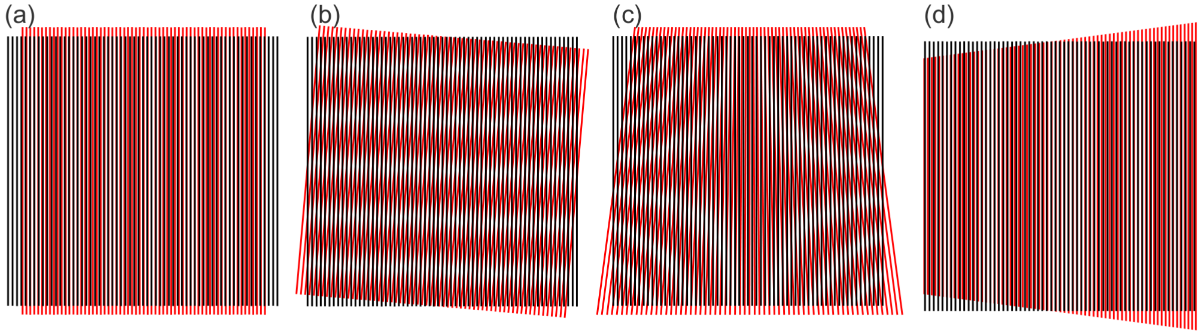

Fig. 49: *Schematics of interference fringes caused by misalignment of two 1D gratings (solid black and red lines), (a) lateral misalignment in z creates vertical fringes, (b) a rotational misalignment around z creates horizontal fringes, (c) rotational misalignment around x and (d) rotational misalignment around y, creating vertical fringes with a period that increases with misalignment.*

Alignment using Moiré fringes

If the distances and orientations of the gratings are misaligned, the superposition of the two periodic structures will create Moiré fringes on the detector screen. In the following, we will assume that the gratings are one-dimensional, with structures oriented parallel to the y-axis, and the phase stepping is performed along the x-axis. Thus, lateral misalignments along the y-axis do not change the imaging performance as it is the symmetry axis of the gratings, while a lateral change of one of the gratings in x-direction only changes the relative phase of the flat field. Only a displacement in z is of importance for imaging. A translation in z-direction causes the magnification of the first grating onto the second grating to differ from the design value, thus the projected period of the first grating will be smaller or larger than that of the grating further downstream. This global period misalignment causes vertical Moiré fringes, as shown in Fig. 49 (a). Additionally to translation, the gratings may be misaligned by rotations around all three axes, where all misalignments cause different fringes. A rotational misalignment around the z-axis is shown in Fig. 49 (b), causing horizontal fringes at the plane of detection. A rotation around the x-axis causes the upper/lower part of the grating be be nearer/farther to/from the other grating, thus creating a gradient in the projected period in the vertical direction, as shown in Fig. 49 (c). Finally, a rotation around the y-axis causes the left/right part of the grating to be nearer/farther to/from the other grating, causing a horizontal gradient in the projected period, which creates the interference fringes shown in Fig. 49 (d). Each of the different misalignments can be superimposed onto the other, complicating the identification of the misaligned grating.

Fine alignment using the phase of the flatfield

If the misalignment is only small and the noise in the images very high, the contrast of the interference fringes may be small and therefore the fringes barely visible. For certain sources, the intensity distribution of the source itself can be confused with a fringe. In situations like these, it becomes difficult to perform the final steps in the optimization of the grating alignment. Usually these problems can be resolved by a fast phase-stepping scan. The calculation of the phase of the flat field image generally yields a higher fringe contrast than achievable by a mere estimation of the intensity at the detector. By this measure, the alignment of the gratings can be optimized to its greatest quality.

7.2 Deviations in the height

Attenuation gratings:

As the attenuation gratings necessarily have a finite height, they will not be ideally absorbing. Instead, they will exhibit a finite transmission at the bars as a function of energy. Additionally, due to imperfections in the fabrication, the bar height will not be constant, but will vary around the nominal value. In the following, we will perform the analysis based on a source grating with finite height. Since the interferometer is symmetric with respect to the source and the analyzer grating, the results are in principle valid for both gratings.

The basis for the analytical evaluation of grating height variations is the intensity oscillation in each pixel as described by Eq. (2.53) in section 2.5

$$S(x) = t_0(0) \cdot \tau_2 \cdot \frac{S_0}{p} \left[1 + \sum_{n=1}^{\infty} v_n \cos\left(2\pi n \frac{x}{p} \right) \right], \tag{7.1}$$

with $t_0(n/p)$ the Fourier spectrum of the source intensity distribution. For rectangular grating profiles, the amplitudes v_n are given by

$$v_n = 2 \cdot t_0\,(n/p) \cdot \mathrm{sinc}\,(n \cdot \tau_1) \cdot \mathrm{sinc}\,(n \cdot \tau_2)\,. \tag{7.2}$$

If the gratings have a duty cycle of $\tau_1 = \tau_2 = 1/2$, the visibility $v = (S_{\max} - S_{\min})/(S_{\max} + S_{\min})$ is given by

$$v = \sum_{n=1}^{\infty} v_n = \frac{8}{\pi^2} \sum_{n=1}^{\infty} \frac{t_0\,((2n-1)/p)}{(2n-1)^2}, \tag{7.3}$$

In practice, the bars of the source and analyzer gratings will not be capable of absorbing all x-ray photons incident on them due to their finite height. Instead of being described by a rectangle function of period p, width $p\tau$ and unit height, the intensity transmission profile $T_0(x)$ of an attenuation grating with non-zero transmission T at the bars can be modeled by the sum of two rectangle functions

$$T_0(x) = T \cdot \mathrm{rect}\left(\frac{x}{p} \right) + (1-T) \cdot \mathrm{rect}\left(\frac{x}{p\tau_0} \right), \tag{7.4}$$

as shown schematically in Fig. 50 (a). The Fourier transform of Eq. (7.4) is

$$t_0(f) = \frac{T \cdot p \cdot \mathrm{sinc}\,(f \cdot p)}{T \cdot p + (1-T) \cdot \tau_0 \cdot p} + \frac{(1-T) \cdot p \cdot \tau_0 \cdot \mathrm{sinc}\,(f \cdot p \cdot \tau_0)}{T \cdot p + (1-T) \cdot \tau_0 \cdot p}. \tag{7.5}$$

Since only multiples of the inverse grating frequency contribute, i.e. $f_n = n/p$, and $\mathrm{sinc}(n) = 0$

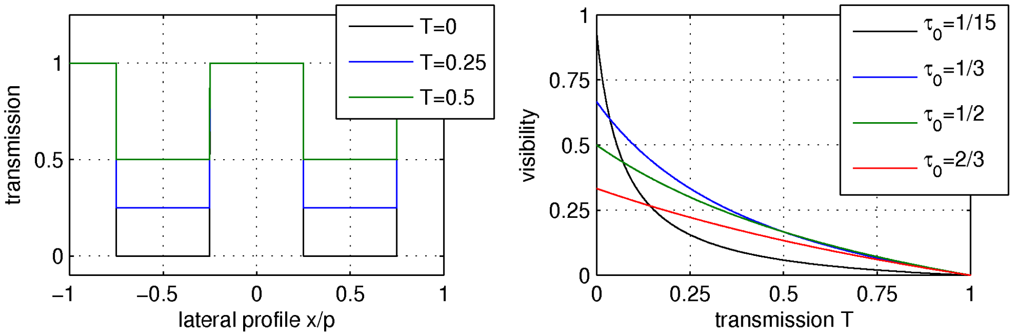

Fig. 50: *(a) Transmission profile of an attenuation grating with different bar heights and thus different transmission T at the grating bars, (b) dependence of the visibility on the transmission for four different duty cycles τ_0 of the source grating.*

for all n, the first term is equal to zero. By inserting Eq. (7.5) into Eq. (7.3), the visibility as a function of transmission can be shown to be

$$v(T) = \frac{1-T}{T/\tau_0 + (1-T)} \cdot \frac{8}{\pi^2} \sum_{n=1}^{\infty} \frac{\operatorname{sinc}((2n-1)\cdot\tau_0)}{(2n-1)^2}. \tag{7.6}$$

The dependence of the visibility on the transmission is shown in Fig. 50 (b) for different duty cycles of the source grating. It can be seen that for small duty cycles, the visibility is affected strongly by a nonzero transmision of the attenuation gratings. The positive effect of a coherence increase by the use of a small duty cycle will thus be cancelled out when the transmission of the grating bars increases. For high duty cycles, the visibility decline exhibits an approximately linear dependence on the transmission.

From Eq. (7.6), it can immediately be concluded that the visibility spectrum $v(E,T)$ as obtained with imperfectly attenuating gratings can be directly calculated from the visibility spectrum $v(E,0)$ with ideal gratings (as described by Eq. (6.4) in section 6.1)

$$v(E,T) = \frac{1-T(E)}{T(E)/\tau_0 + 1 - T(E)} \cdot v(E,0). \tag{7.7}$$

For a given homogeneous grating material and monochromatic energy, the transmission T of a grating with duty cycle $\tau_0 = 0.5$ can be related to the height h of the attenuating grating bars by Beer-Lambert's-law $T = e^{-\mu\cdot h}$, resulting in

$$v(h) = \frac{1-e^{-\mu\cdot h}}{1+e^{-\mu\cdot h}} \cdot \frac{8}{\pi^2} \sum_{n=1}^{\infty} \frac{\operatorname{sinc}((2n-1)\cdot\tau_0)}{(2n-1)^2}. \tag{7.8}$$

where $\mu = \mu(Z,E)$ is the linear attenuation coefficient of the grating material with atomic number Z for energy E. The dependence of the visibility on the bar height is thus non-linear, as shown in Fig. 51 (a) for a gold (Au) grating at 40 keV. It can be seen, that for low grating heights, an increase in grating height leads to a significant increase in visibility. On the other hand, if the attenuation of the grating bars approaches 1, the visibility and attenuation as a function of grating height rise only marginally with further increase of the bar height. While the effort in grating manufacturing greatly increases with increasing height, the benefits of a further increase for imaging are thus minimal above a certain bar height. Therefore, the analysis suggests that an increase of grating height beyond 90% attenuation at the bars is, although desirable, dispensable from a cost-benefit point-of-view.

Due to instabilities and difficulties in grating fabrication, the bars will not be equally high.

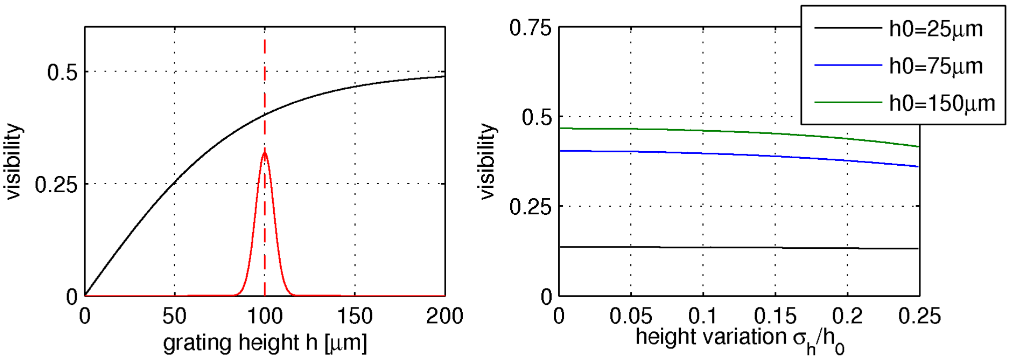

Fig. 51: *(a) Dependence of the visibility (left axis) and the attenuation (right axis) on the height h of one of a Au attenuation grating with a duty cycle of* $\tau = 0.5$ *at* 40 *keV. Due to fabrication errors, the heights of the bars will be distributed around a nominal value of* $h_0 = 75$ *µm (dashed red line), following a certain distribution (solid red line). (b) Dependence of the visibility on the variation of the attenuation bar heights, modeled with a Gaussian distribution with width* $h_0 \cdot \sigma_h$ *for three different nominal heights.*

Instead, their heights will vary around a certain nominal value h_0, as indicated in Fig. 51 (a). To evaluate the influence of height variations, we assume a Gaussian height distribution for the bars, with the nominal height h_0 as the mean and a standard deviation of σ_h. For the analysis, we will assume that each single grating bar can be connected to a certain visibility. As the visibility is different for bars of different height, the resulting mean visibility $\overline{v}(\sigma_h)$ as a function of height variations will be a weighted average of the visibilities $v(h)$ for each different height, where the weight is given by the probability $P(h, h_0, \sigma_h)$ of the height distribution

$$\overline{v}(\sigma_h) = \int_{-\infty}^{+\infty} P(h, h_0, \sigma_h) \cdot v(h) \cdot dh. \tag{7.9}$$

Note that the use of a continuous integral in Eq. (7.9) corresponds to the assumption of an infinitely extended detector pixel. The relation can easily be made to apply to arbitrarily sized detector pixels by replacing the integral by a finite sum over the grating bars in the pixel area. In Fig. 51 (b) the visibility for a three-grating interferometer at 40 keV design energy as a function of the normalized width σ_h/h_0 of the Gaussian function is shown. For the calculation, all gratings were assumed to have a duty cycle of $\tau = 1/2$. As can be seen, the beneficial contributions of the grating bars that are too high approximately cancel the disadvantageous contributions of bars that are too low, leading to an only marginally decreasing visibility as a function of height variations. We can thus conclude that height variations in the attenuation gratings exert only a minor influence on DPC imaging quality.

Phase gratings:

The analysis so far applies only to attenuation gratings. For phase gratings, the dependence on height and height variations is different, since the height of the phase grating affects the shape of the interference pattern in a non-trivial way. The height of the bars affects the interference pattern in two ways: first, by the attenuation of the bars, which should ideally be zero, and second, by a change in the desired phase shift. The influence of the transmission of the grating bars on the intensity profile of the interference pattern at a fractional Talbot distance is shown in Fig. 52 for a π and $\pi/2$-shifting phase grating. The profiles were simulated using a Fresnel propagation method with monochromatic energy. As can been seen, a reduced transmission at the grating bars causes a simple reduction in intensity for the $\pi/2$ shifting grating, while the intensity pattern of the π-shifting grating becomes asymmetric. This result can be understood

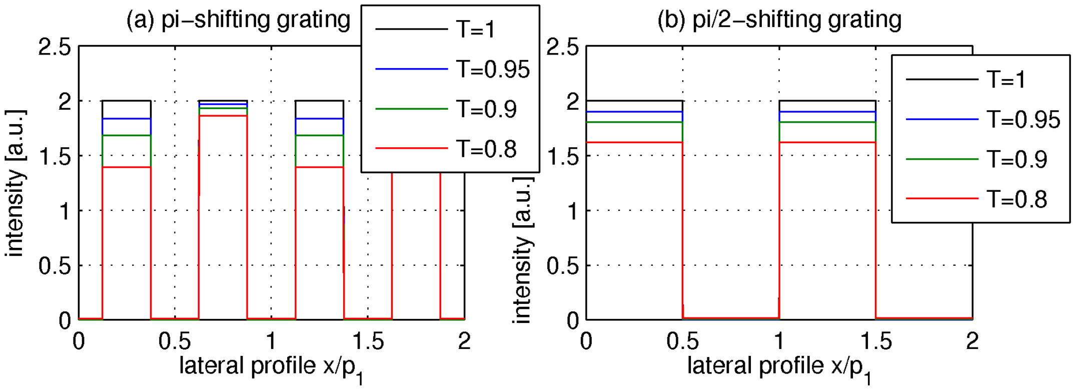

Fig. 52: *Simulated lateral profile of the intensity pattern at the first fractional Talbot distance for different transmission of the grating bars of (a) a π-shifting and (b) a $\pi/2$-shifting phase grating. While the reduced transmission only causes a reduction of intensity fo the $\pi/2$-grating, the intensity pattern of the π-grating becomes asymmetric.*

by noting that the interference pattern at the Talbot distance will be a mixture between the intensity pattern of a pure phase and a pure attenuation grating. As the π-shifting phase grating creates an interference pattern with twice the period as the corresponding attenuation grating, a non-zero attenuation at the grating bars causes an asymmetry in the resulting interference pattern. Thus, when using a π-phase grating with non-negligible attenuation, a scan over two periods of the intensity pattern and adapted evaluation algorithms are necessary.

The influence of height variations of the bars of a phase grating can be conveniently modeled by the use of the concept of the visibility spectrum $\nu(E)$, as presented in section 6.1. The key idea in this approach is that the grating height of the phase grating corresponds to a certain phase shift and design energy for a given grating material. The connection between design phase shift Φ_0 of the grating on the one side and design energy E_0 and design height h_0 on the other is given by Eq. (2.14)

$$\Phi_0 = k_0 \cdot \delta(E_0) \cdot h_0, \tag{7.10}$$

where $k_0 = E_0 2\pi/(hc)$ is the wave vector at the design energy, h Planck's constant and c the speed of light. Using the material dependence of $\delta(E)$ as given by Eq. (2.17), the design energy E_0 as a function of material and grating height can be given by

$$E_0(h) = 2\pi\hbar c r_e \cdot \frac{\rho_Z}{\Phi_0} \cdot h \tag{7.11}$$

where $\hbar$, c, r_e and ρ_Z are the reduced Planck constant, the speed of light, the classical electron radius and the electron density of the grating material. Using Eq. (7.11), each bar height can be connected to a different design energy. The visibility spectrum of a grating, as given in Fig. 40, can thus be expressed in terms of grating height by a linear rescaling of the x-axis, as shown in Fig. 53 (a). The dependence of the visibility as a function of grating height is thus equivalent to the visibility spectrum of the grating. Height variations can be modeled by connecting each bar with height $h \neq h_0$ to a different visibility spectrum, with its maximum at $E_0(h)$, as shown in Fig. 53 (a) for $h = h_0 - 2.5\ \mu$m and $h = h_0 + 2.5\ \mu$m. By this approach, the mean visibility as a function of height variations with standard deviation σ_h, denoted $\overline{\nu}(\sigma_h)$, can be obtained by a weighted average over the visibility spectra $\nu(E, E_0)$ for each bar, evaluated at the design energy $E = E_0(h_0)$:

$$\overline{\nu}(\sigma_h) = \int_0^{-\infty} P(h, h_0, \sigma_h) \cdot \nu\left(E_0(h_0), E_0(h)\right) \cdot dh, \tag{7.12}$$

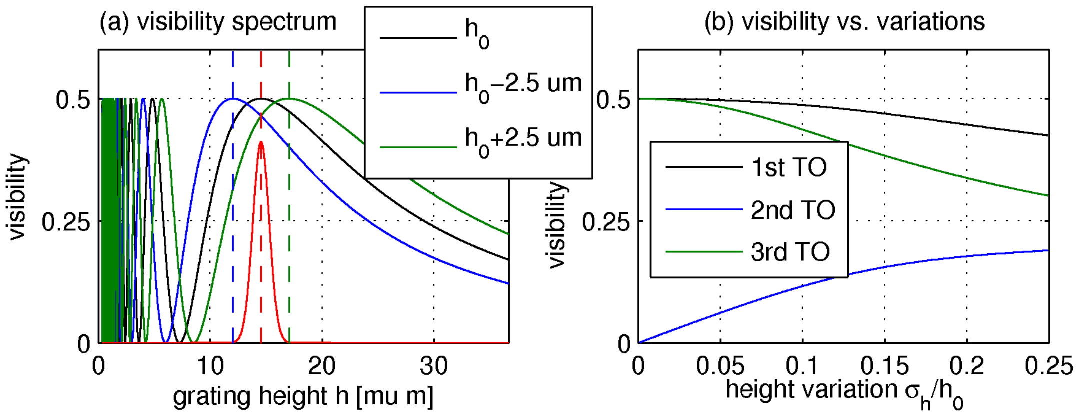

Fig. 53: *(a) Visibility spectra corresponding to three different grating heights (nominal height* h_0*, black,* $h_0 - 2.5$ *µm, blue,* $h_0 + 2.5$ *µm, green), obtained by a linear rescaling of the energy axes, for a* π*-shifting Ni-grating at* 40 *keV. The heights of the grating bars will be distributed around the nominal value (solid red curve), where bars with higher or lower height contribute with a reduced visibility to the mean visibility at the design energy (dashed red line). (b) Dependence of the visibility on height variations of the phase grating for the first three Talbot orders of the grating.*

where $P(h, h_0, \sigma_h)$ is the probability for the grating having a bar with height h. The function $\overline{v}(\sigma_h)$ is shown in Fig. 53 (b) for the first three fractional Talbot orders of a π-shifting Ni-grating at the design energy of $E_0 = 40$ keV. It can be seen that height variations have a higher impact on imaging when going to higher Talbot orders, since high values for the visibility can only be achieved in a small energy range around the design energy (compare with Fig. 40). If the dependence on the height variations in the phase grating is compared to the height variations of the attenuation gratings as shown in Fig. 51 (b), it can be concluded that height variations in the phase grating show a steeper decrease in visibility. From the obtained results, we suggest an upper limit for the relative height variations of $\sigma_h/h_0 < 10\%$ for the phase and $\sigma_h/h_0 < 20\%$ for the attenuation grating.

7.3 Deviations in the shape

Rounded bars:

Perfectly rectangular grating profiles, as assumed in the derivation of Eq. (7.3), are an idealization. In reality, the grating profiles will deviate from a rectangular form, where the most obvious deviation is obtained by the rounding of the edges of the bars. Since a rectangular shape carries infinite spatial frequencies, rounded edges can be introduced by a suitable low-pass filter in frequency domain. In the following, we will model rounded edges by the convolution of transmission function of a grating by a disturbance $T_\sigma(x)$ of Gaussian shape with a standard deviation of σ, as shown in Fig. 54 (a). The convolution with a Gaussian function introduces an additional Gaussian factor in the visibility calculation of Eq. (7.2)

$$v_n = 2 \cdot \sum_{n=1}^{\infty} \mathrm{sinc}^3\left(\frac{n}{2}\right) \cdot \exp\left(-2\pi^2 \cdot \sigma^2 \cdot n^2\right), \tag{7.13}$$

where we have assumed that all gratings have a duty cycle of $\tau = 1/2$. Using Eq. (7.13), the dependence of the visibility on the width of the disturbing Gaussian function $v(\sigma)$ can thus be calculated analytically. It is shown in Fig. 54 (b).

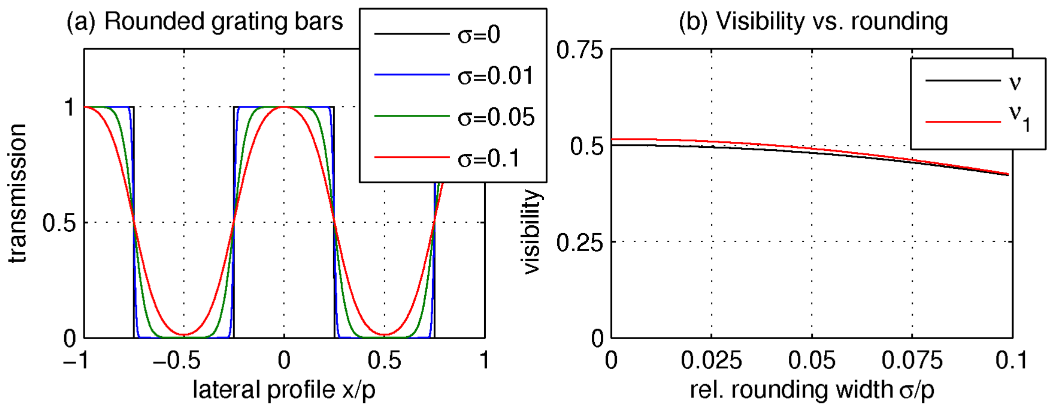

Fig. 54: *(a) Rounded deviations from a rectangular profile, modeled with the convolution of a Gaussian with width σ, (b) dependence of the visibility (solid black line) and its first order approximation (solid red line) on the width σ of the Gaussian modeling the rounded bars.*

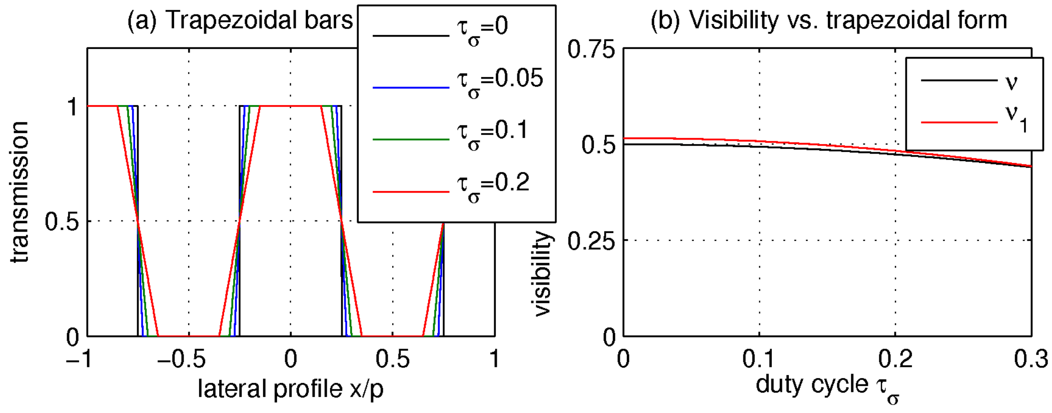

Fig. 55: *(a) Trapezoidal deviations from a rectangular profile, modeled with the convolution of a rectangular function with a duty cycle τ_σ, (b) dependence of the visibility (solid black line) and its first order approximation (solid red line) on the duty cycle τ_σ of the rectangular function modeling the trapezoidal bars.*

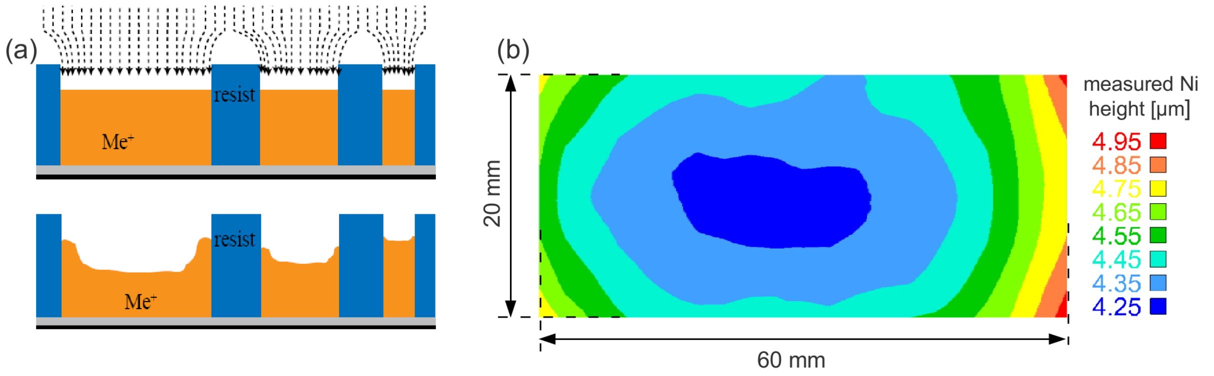

Fig. 56: *(a) Caused by inhomogeneities in current density during the galvanization procedure, the metal structures are higher near the resist (schematic courtesy of J. Kenntner). (b) Grating height as measured with an x-ray fluorescence spectrometer. The average bar height decreases towards the middle of the grating.*

Trapezoidal bars:

Similar to the rounded grating profiles, trapezoidal profiles, as shown in Fig. 55 (a), can be modeled by the convolution of the transmission function of the gratings with an additional rectangle function of width $p \cdot \tau_\sigma$ and a duty cycle τ_σ. The additional rectangle function introduces another sinc-function in Eq. (7.2)

$$v_n = 2 \cdot \sum_{n=1}^{\infty} \mathrm{sinc}\left(\frac{n}{2}\right)^3 \cdot \mathrm{sinc}\left(n \cdot \tau_\sigma\right), \tag{7.14}$$

where we have again assumed that the three interferometer gratings have a duty cycle of $\tau = 1/2$. The visibility as a function of the duty cycle τ_σ of the rectangular disturbance as given by Eq. (7.14) can be seen in Fig. 55 (b). From Figs. 54 and 55, it can be seen that rounded and trapezoidal deviations from the ideal rectangular grating profile introduce only a marginally decreasing visibility and can thus be tolerated for a wide range of deviations. Additionally, the difference between the visibility v and the usually applied first order approximation v_1 is reduced with growing grating errors. The shape of the oscillation in each pixel thus approaches a harmonic oscillation with increasing grating errors.

Bathtub effect:

Another deviation from the ideal grating shape is introduced by the so-called bathtub effect, as shown schematically in Fig. 56 (a): Due to the structure of the grating, the current density during galvanization is higher near the resist structures than in the middle of the grating bar. This causes the galvanized metal ions Me^+ to be inhomogeneously deposited within one grating bar. Instead of having a constant height, the bars are overgrown near the resist structures, creating a lateral profile that resembles a 'bathtub'. This effect is observed within every bar, as well as over the entire area of the grating, where the structures at the grating's perimeter are higher than in the middle of the grating.

The effect is negligible for attenuation gratings, since overgrown structures in each bar will be equivalent to a mean increase of bar height and thus a higher attenuation, if the pixels are big enough to average over multiple grating bars. The bathtub effect for attenuation gratings therefore exhibits a negligible influence on imaging. Considered over the entire surface of the grating, the bathtub effect will create higher grating structures at the outer ranges of the grating, thus potentially increasing the visibility there in a measurement.

The situation becomes more complicated for phase gratings. The bathtub-effect increases with the height of the galvanized structures. As the bars of the phase grating are comparatively low, the bathtub effect within a single bar can be assumed to be negligible and leads only to a mean increase of bar height. If the bathtub effect is considered over the entire surface of the phase grating and the nominal grating height is achieved in the center of the grating, the outer reaches of the grating will exhibit a phase shift that is higher than the design phase shift at the design energy. This will lead to an overall visibility decrease when close to the edges of the grating, which can be calculated using the visibility spectrum of the grating, as explained in section 7.2. Exemplarily, the bathtub effect for a nickel (Ni) phase grating with a nominal height of $h_0 \approx 8$ μm was measured, exploiting the Ni Kα fluorescence radiation of the grating material. For the measurement, a FischerScope X-Ray XDV SD fluorescence spectrometer was used. From the fluorescence yield of the sample, the material thickness under the assumption of homogeneous material layer was calculated. As the grating surface is not homogeneous but structured into bar material and resist structure, the grating heights that are calculated from the measured data are reduced by a factor of approximately 0.5. The grating was scanned at 30×15 points horiz×vert, each for 60 s integration time. The fluorescence signal was averaged over the area of the beam focus at the sample, which had a diameter of d= 1 mm. No filtration was used. The resulting measured heights for all points were rendered numerically into the surface shown in Fig. 56 (b). It can be seen that the bar height changes by approximately 20 % from the nominal height in the middle of the grating towards the outside. Additionally, it can be seen that the bathtub effect is higher along the long side of the grating. The reason for this is the higher inhomogeneity in current density in this case, as shown in Fig. 56 (a).

7.4 Deviations in the period and duty cycle

Attenuation gratings:

Closely related are shifts in the period and the duty cycle of the grating and will thus be analyzed together in this section. A typical fabrication error connected to the grating period can be seen in Fig. 57 (a): the SU8-polymer structures were distorted and shifted by capillary forces occurring in the fabrication procedure. During galvanization of the grating material, some grating bars are produced in a deformed shape, essentially corresponding to period and duty cycle shifts in the lateral grating profile. The length of those vertical 'rifts' in the grating period can extend from a few microns to a few millimeters. The widening of the period at the rift causes the grating structures to the left and right hand side of the rift to be out of phase, which articulates itself in a DPC measurement by jumps in the phase of the flat field, as shown Fig. 57 (b). Two different phase jumps can be seen: first, large scale phase shifts, where the whole structure of the grating is shifted by the rift, and second, small scale period variations, where the phase is altered by a small margin and confined to a small area around the rift. If the phase of the grating is averaged over the area of one pixel, in the presence of a phase change in that area all visibility can be destroyed in the worst case. On the other hand, large scale phase shifts only reduce the visibility in the pixel immediately at the position of the shift, while only shifting the phase of the flat field in the adjacent pixels. As the phase of the flat field has no direct influence on imaging quality, large scale period shifts only impose higher demands on alignment stability during measurements.

Apart from sporadic shifts in the period, the influence of statistical duty cycle variations in the attenuation gratings on the visibility has to be assessed. The dependence can be easily modeled by using $\nu(\tau)$ as given by Eq. (7.3). Assuming again a Gaussian duty cycle variation, the dependence of the mean visibility on the variations $\overline{\nu}(\sigma_\tau))$ is given by a weighted average with the probability $P(\tau,\tau_0,\sigma_\tau)$ for each duty cycle

$$\overline{\nu}(\sigma_\tau) = \int_0^{-\infty} P(\tau,\tau_0,\sigma_\tau)\cdot\nu(\tau))\cdot d\tau. \tag{7.15}$$

As discussed in section 2.4, the dependence of the visibility on the duty cycle is linear and remains linear for the first order approximation ν_1 for duty cycles in the range of $0.25 < \tau < 0.75$. Due to this linearity, the beneficial and disadvantageous contributions of the duty cycle variations approximately cancel each other out. The visibility $\nu(\sigma_\tau)$ is thus approximately constant and independent of duty cycle variations in the attenuation gratings.

Phase gratings:

The influence of period and duty cycle variations of the phase gratings is difficult to model, since it has a complicated influence on the shape of the interference pattern. To evaluate this influence, a simulation of the wavefields behind a flawed phase grating was performed using Fresnel wave propagation. Two examples for shifts and variations in the duty cycle are shown in Fig. 58 (a) and (b), respectively. Comparable simulations using shifts and variations in the

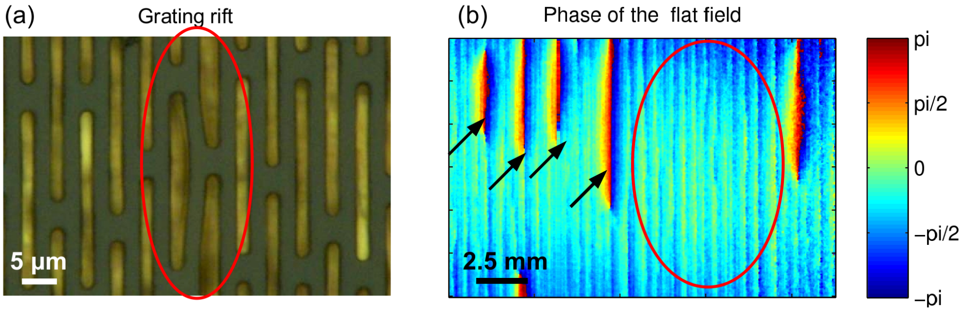

Fig. 57: *(a) Visible light microscopy image of the surface of an attenuation grating which exhibits shifts in grating period and duty cycle (red circle), (b) phase of the flat field measured with this grating. If the whole grating structure is shifted, jumps in the relative phase occurs, as indicated by the black arrows. Small period variations give rise to a fluctuation and a decrease in the visibility (red circle).*

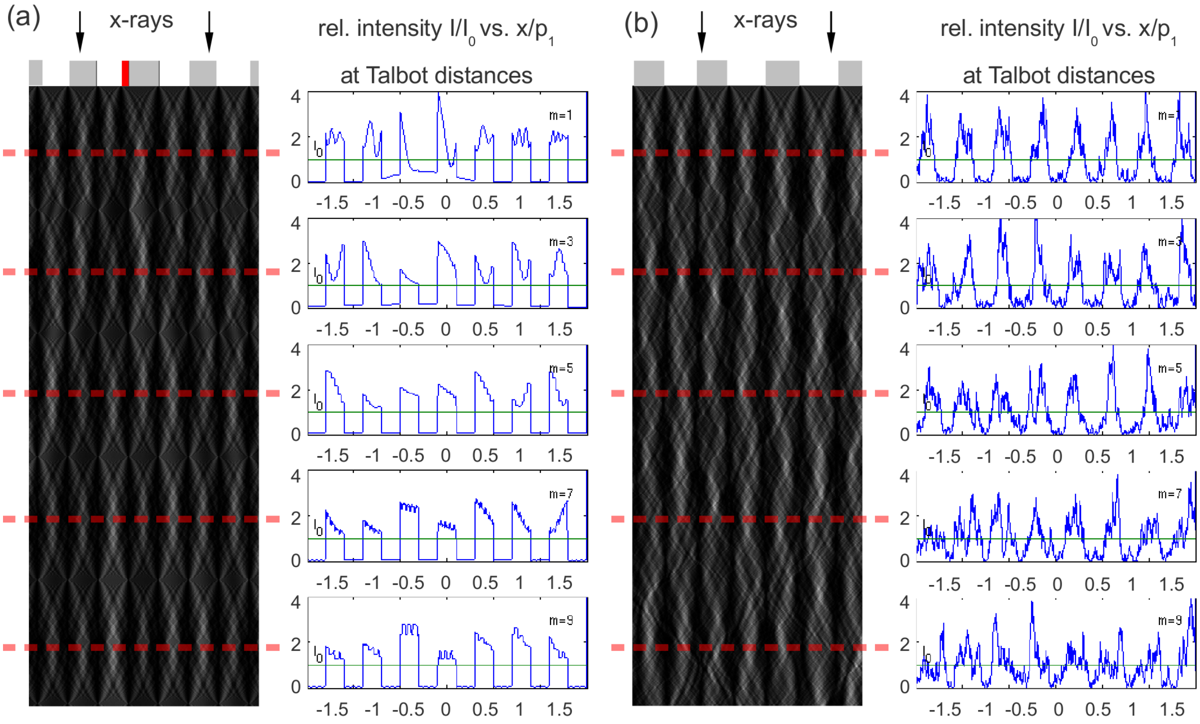

Fig. 58: *Intensity patterns behind a π shifting phase grating, together with the lateral intensity profiles at the first five fractional Talbot distances (dashed red lines) using (a) a grating with a single bar of reduced duty cycle (indicated red) and (b) a grating with variations in the duty cycle of* $\sigma_\tau/\tau = 0.1$.

period of the grating lead to analogous results. In Fig. 58 (a), a single bar of a π-shifting phase grating with nominal duty cycle of $\tau_0 = 0.5$ was given a duty cycle of $\tau = 0.375$. As can be seen, the shift in the duty cycle greatly distorts the intensity pattern near the grating, but confined to a small area downstream of the grating. With increasing propagation distance, the distortion spreads out laterally and its influence on the quality of the intensity pattern decreases. Thus, shifts in single bars are assumed to exhibit a bigger influence near the beam-splitter grating than at a distance. Fig. 58 (b) shows the interference pattern behind a phase grating with stochastic variations in the duty cycle, modeled by Gaussian distribution with a standard deviation of $\sigma_\tau/\tau = 0.1$. The resulting shape of the interference pattern can be seen to be highly distorted. In contrast to the distortions caused by single shifts, the distortion of the interference pattern increases with the propagation distance from the grating.

In conclusion, flaws in the phase grating show a distinct dependence on the distance from the grating: For single shifts and errors, the distortion of the interference pattern is higher near the grating than at a distance, while for variations of the grating quality, the distortions are more significant at a distance than near the grating.

7.5 Imaging with bent gratings

7.5.1 Geometric shadowing of unbent gratings

So far, we have only considered the dependence of the interferometer performance on the inter-grating distances l and d. Nevertheless, in an experiment, the distance between source and each grating has to be considered as well. When a magnifying setup with divergent rays is used, grating structures adapted to the curvature of the wavefront have to be utilized, while flat rectangular gratings are only applicable without error if a parallel beam is used for illumination. If unbent gratings are used with a divergent source, off-axis rays will be attenuated by their crossing of grating structures on their path, the more, the further they are away from the optical axis, as indicated in Fig. 59 a). Geometric shadowing can be characterized by the **shadowing angle** θ_0, corresponding to a ray that traverses the grating through the diagonal in the grating gap between two bars. It can be defined by

$$\tan\theta_0 := \frac{p\cdot\tau}{h}, \tag{7.16}$$

where p is the period, τ the duty cycle and h the height of the grating. The angle θ_0 will be used to quantify shadowing effects in the following. If the angle between the ray and the optical axis is larger than θ_0, the ray will necessarily traverse some grating structures and thus be attenuated.

For an evaluation of the influence of shadowing effects on image quality, not only the grating geometry is of importance, but also the size and distance to the detector has to be included into the analysis. By the width and distance of the detector from the source, a maximal lateral field of view is chosen, corresponding to an angle θ_m, as indicated in Fig. 59 (a). This angle will be denoted the **acceptance angle** of the setup in the following. If a is the lateral detector size and d the distance from the grating to the detector, the angular acceptance can be calculated by

$$\tan\theta_m := \frac{a}{2\cdot s}, \tag{7.17}$$

where s is the total setup length $s = l_S + l_D$, with l_S the source-to-grating and l_D the grating-to-detector distance. As the corresponding angles are usually small, the paraxial approximation $\tan\theta \approx \theta$ can be used for the tangent function in Eqs. (7.16) and (7.17). Geometric shadowing effects from a grating can be reduced by an increase of the ratio

$$\frac{\theta_0}{\theta_m} = \frac{2\cdot p\cdot\tau\cdot(l_S + l_D)}{a\cdot h}. \tag{7.18}$$

If a compact setup is desired, bent gratings instead of plane gratings have to be used. In the following, we will consider cylindrically bent gratings, with the grating structures aligned along the symmetry axis of the cylinder. Apart from structure height, period and duty cycle, bent gratings are characterized by their focal length, or radius of curvature, denoted f. In a properly aligned setup, the focal point of the grating has to be located at the focal point of the x-ray source. Not meeting this condition results in misalignment of the interferometer and Moiré fringes in the images. For a given grating with focal length f, an upper and lower bound l_+

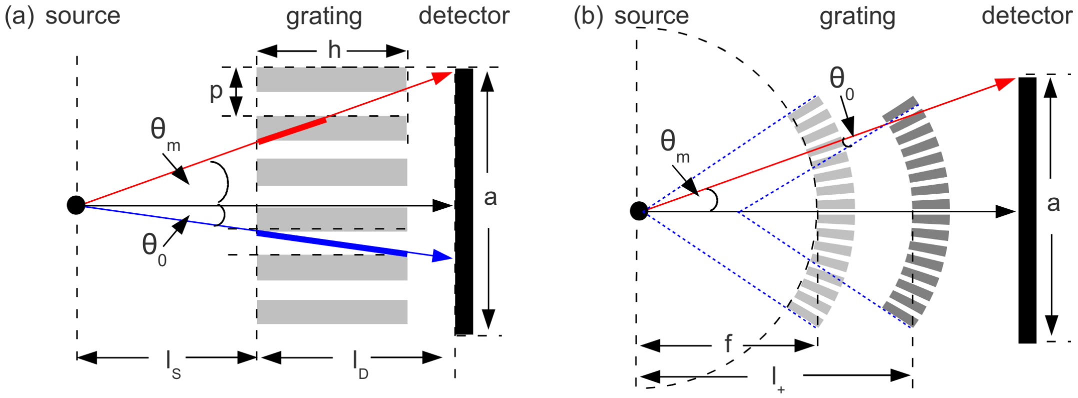

Fig. 59: *(a) Geometric shadowing of an unbent grating: while the central ray (solid black arrow) passes the grating undisturbed, rays with a divergence greater than* θ_0 *(solid blue arrow) will be shadowed by the crossing of one or more grating bars. The acceptance angle* θ_m *of the setup is determined by the detector distance and size (solid red arrow). (b) Geometric shadowing of a bent grating with focus* f*, with correct transversal alignment (light gray) and with misalignment* l_+ *(dark gray).*

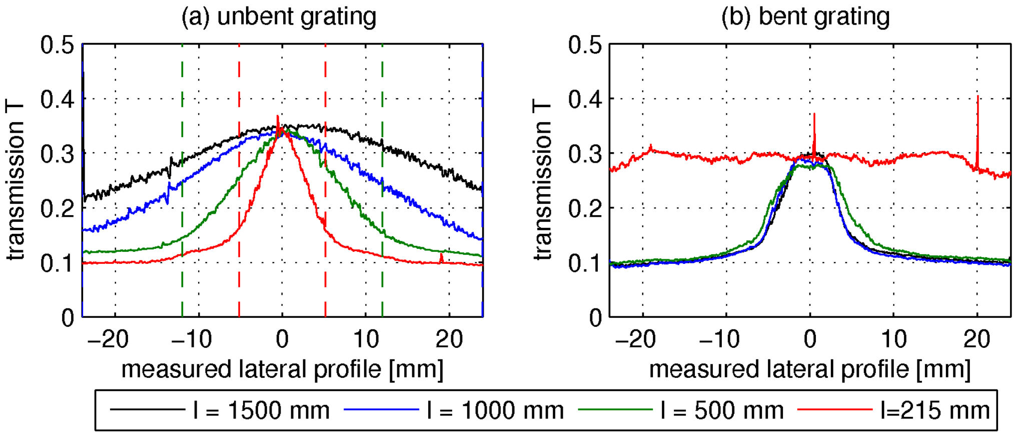

Fig. 60: *Transmission through (a) an unbent attenuation grating with* $h = 85\ \mu m$ *grating height and (b) a bent attenuation grating with* $h = 85\ \mu m$ *height and focus of* $f = 215$ *mm, each for four different source-to-grating distances. The detector was positioned directly behind the grating in each measurement. In (a), the range* $s \cdot tan(\pm\theta_0)$ *is indicated by vertical dashed lines for each grating distance. It can be seen how the shadowing decreases the field-of-view with decreasing source-to-grating distance, while the bent grating shows a flat intensity distribution only at its focal distance.*

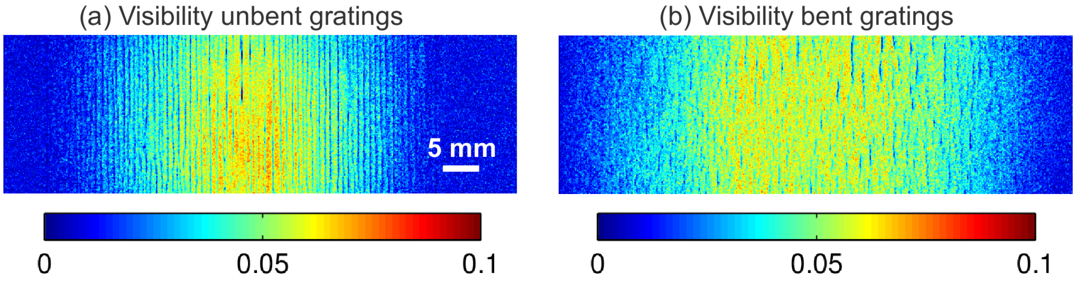

Fig. 61: *Measured visibility at a symmetric interferometer with, (a) unbent gratings and (b) with* G_0 *and* G_1 *bent. The reduction of geometric shadowing effects by the use of bent gratings leads to a wider FOV with a visibility acceptable for imaging purposes.*

and l_- for the positioning tolerance along the optical axis can be derived. The two distances l_+ and l_- are defined as the two positions of the grating, where the maximal ray, described by θ_m, traverses the bent grating through the diagonal of the gap between two grating bars, described by θ_0, as indicated in Fig. 59 (b). These considerations lead to the relations

$$l_+ = f \cdot \left(\frac{\sin\theta_0 + \sin\theta_m}{\sin\theta_m} \right) \quad \text{and} \quad l_- = f \cdot \left(\frac{\sin(\theta_m - \theta_0)}{\sin\theta_0 + \sin(\theta_m - \theta_0)} \right). \tag{7.19}$$

In paraxial approximation, these relations reduce to

$$l_\pm = f \cdot \left(1 \pm \frac{\theta_0}{\theta_m} \right). \tag{7.20}$$

In order to give an impression on the distances involved, we consider the following example: suppose we have a grating with period $p = 4.8$ μm, height $h = 100$ μm and grating focal length of $f = 215$ mm, a detector at a distance of $s = 1000$ mm with a lateral size of $a = 100$ mm. Thereby one obtains $\theta_m = 0.05$ rad for the acceptance angle and $\theta_0 = 0.024$ rad for the shadowing angle, $l_+ = 112$ mm and $l_- = 318$ and thus a positioning range of $l_S = 215 \pm 113$ mm. Nevertheless, for a significant reduction of shadowing effects, the requirements leading to Eq. (7.20) will have to be chosen more stringent.

In order to exemplify shadowing effects with bent and unbent gratings, transmission measurements were performed at the microfocus setup at the Technische Universität München , as described in section 3.1.3. The measurements were done at tube settings of 65 kV for the anode voltage and at 20 W power. The unbent grating had a height of $h \approx 105$ μm and the bent grating of $h \approx 100$ μm. The bent grating was mounted into a grating holder with a curvature radius of $f = 215$ mm. Both gratings had a period of $p = 4.8$ μm. Four exemplary distances from the source to the grating were chosen, namely $l_S = 1500$ mm, $l_S = 1000$ mm, $l_S = 500$ mm and $l_S = 215$ mm. The detector was positioned as close to the grating as mechanically possible, in the measurements at $l_D = 30$ mm for all positions. The measured lateral transmission of the unbent and the bent grating for the different distances from the source is shown in Fig. 60 (a) and (b), respectively. From Fig. 60 (a) can be seen how the grating shadowing reduces the transmission of the grating with growing distance from the optical axis with decreasing distance to the source. Additionally, the range corresponding to the shadowing angle $s \cdot \tan\theta_0$ is shown. In contrast, for the bent grating shown in Fig. 60 (b), the intensity profile at the distance corresponding to its focal length is flat, while showing strong shadowing effects for all other distances.

To assess the influence of bent and unbent gratings on a DPC measurement, a symmetric three-grating interferometer was realized. For the source and beam-splitter gratings, bent and unbent grating were available. All gratings had a period of $p = 4.8$ μm. The bent and unbent source gratings had a height of $h_0 = 100$ μm and $h_0 = 105$ μm, respectively, while the bent and unbent beam-splitter gratings had a height of $h_1 \approx 15$ μm and $h \approx 16$ μm. The analyzer grating was unbent, with a height of $h_2 = 86$ μm. The height of the unbent phase gratings corresponds to a phase shift of π at a design energy of ≈ 46.5 keV. The source was operated at 70 kV and 20 W. The setup was realized in first Talbot order, with distances $l_S = l = d = 215$ mm. The distance from source to source grating was $f = 215$ mm and the detector was $l_D = 30$ mm away from the analyzer grating. The phase-stepping was performed with the grating G$_2$ with an exposure time of 3 s and 16 steps over two periods of the interference pattern. The resulting visibility maps for a measurement with all gratings unbent and with the first two gratings bent can be seen in Fig. 61 (a) and (b), respectively. It can be seen that the use of bent gratings lessens the shadowing-induced decrease of the visibility away from the optical axis.

7.5.2 Phase-stepping using bent gratings

The alignment of an interferometer consisting of bent gratings poses additional challenges due to the increased number of degrees of freedom. The gratings do not only have to be aligned to each other pairwise, but additionally, the grating's focus for each grating has to be at the position of the source point. For flat gratings, a lateral misalignment along the x-axis simply causes a change in the relative phase of the gratings and is thus used for the phase-stepping technique. For bent gratings, a lateral misalignment causes Moiré fringes, since it moves the focus of the grating out of the optical axis. For this reason, the phase-stepping cannot be performed along a straight line when using bent gratings. Instead, stepping of the grating has to be performed along a circular arc, with the axis of rotation in the source focus. Since this is difficult to implement in practical situations, we will investigate the deviations created by using a straight line phase-stepping scan instead of a bent one. Performing a lateral scan of a bent grating along a straight line introduces a deviation Δp between the period p along the arc and the projected period p' along the straight line, given by

$$\Delta p = \frac{p'}{p} = \frac{\tan\theta}{\theta}. \tag{7.21}$$

Since $\Delta p = \Delta p(\theta)$ depends on the angle θ between the ray and the optical axis, the deviation will be different in each pixel, being the higher, the more the ray is tilted away from the optical axis. In an experiment, the field of view and therefore the maximal error that is produced by a linear movement of the bent grating is limited by the detector size. In order to estimate the maximal error, it is therefore sufficient to take a look at the behavior for the largest angle that is still captured by the detector, given by the angular acceptance θ_m. A phase-stepping scan along a circular arc, using a distance of a single period p of the bent grating, corresponds to an angular range of $\Delta\theta = p/f$, with f the focal length of the grating. Under these considerations, the deviation Δp for the period can be shown to be smaller than

$$\Delta p \leq \frac{\tan\theta_m - \tan(\theta_m - \Delta\theta)}{\Delta\theta}. \tag{7.22}$$

Please note that the maximal deviation is independent of the focal length of the bent grating and thus of the source-to-grating distance l_S. This can be understood by the cancellation of two opposing effects: On the one hand, the deviations between straight line and curved arc increase with increasing grating curvature. On the other hand, the simultaneous reduction of the source-to-grating distance reduces the visible field-of-view of the grating to an area with reduced influence of grating shadowing. It is therefore irrelevant which of the gratings is used for the phase-stepping procedure.

To give a numerical example on the deviations involved, we consider the gratings and setup from the preceding section 7.5.1: With $\theta_m = 0.05$ rad and $\theta_p = 2.23 \cdot 10^{-5}$ rad, a linear stepping approach introduces a relative error of only $(p' - p)/p \leq 0.25\%$. Therefore, a phase-stepping procedure along a circular arc is not necessary in this case.

While the linear scanning technique is a good approximation in most situations, the numerically correct approach would be to alter the data analysis routines by declaring the period a variable, and adjusting it in the reconstruction algorithms relative to the distance of each pixel to the optical axis by $p \cdot \Delta p$, following Eq. (7.21). Nevertheless, since the results with a linear scanning technique offer good results in all but the most extreme experimental cases, this approach will not be followed further.

7.6 Summary

In this section, the influence of grating errors on the imaging quality have been analyzed. In section 7.1, the four different degrees of freedom in the grating alignment, namely the transverse and the three rotational alignments, were investigated. Typical Moiré patterns caused by misalignment and measures for the optimization of the alignment were presented. In section 7.2, the dependence of the visibility on the attenuation in the analyzer gratings was shown to be $\nu(E,T) = (1-T)\nu(E)$. Based on a non-linear relationship between visibility increase and height increase, a recommendation of 90% attenuation is given for the attenuation gratings. The visibility was found to be approximately constant as a function of height variations σ_h in the attenuation grating. While attenuation in a π-shifting phase grating was shown to lead to an asymmetric interference pattern, for a $\pi/2$ shifting phase grating, attenuation merely leads to a decrease in the photon flux. For a phase grating, height-variations were shown to be describable by the concept of the visibility spectrum. Height variations in the phase grating have a bigger impact on image quality than corresponding variations in attenuation gratings, with a recommended error tolerance in fabrication of $\sigma/h < 10\%$ relative to $\sigma/h < 20\%$ for the attenuation grating, respectively. The dependence of the visibility on the shape of the grating bars of an attenuation grating was investigated in section 7.3. A rounded shape of the bars was modeled by a convolution with a Gaussian factor, where the dependence of the visibility on the width σ of the Gaussian function can be given by $\nu(\sigma) \sim \exp(\sigma^2)$. For trapezoidal grating bars, a dependence of $\nu(\tau_\sigma) \sim \mathrm{sinc}(\tau_\sigma)$ was found. The bathtub effect was presented as a deviation from the ideal grating shape, with consequences for the phase gratings. It was shown analytically that the bathtub effect in phase gratings can be modeled using the height dependence of the visibility, leading to a visibility decrease towards to outer areas of the grating. In section 7.4, period variations in the attenuation gratings were presented and shown to lead to phase jumps and to a decrease of visibility in the measurement. Variations in the duty cycle of the attenuation grating do not exhibit significant influence on imaging quality. Shifts and variations in the period and the duty cycle of a phase grating distort the interference pattern behind the grating, exhibiting a distinct dependence on the propagation distance from the grating. Section 7.5 provided an introduction into the measurement with bent gratings. Shadowing effects were characterized by defining two angles, the acceptance angle θ_m and the shadowing angle θ_0. Grating shadowing and the benefits of the use of bent gratings were verified in concept and measurement. Additionally, particular characteristics of phase-stepping with bent gratings were addressed in section 7.5.2.

8 Imaging using gratings with a duty cycle of 1/3

In previous publications and measurements, mostly gratings with a duty cycle of $\tau = 1/2$ have been used or taken into account. In this section, we will evaluate the possible gains of the use of gratings with different duty cycles. Since the beam-splitter and the two attenuation gratings have different purposes in the interferometer, we will focus on the different gratings separately, in section 8.1 on the attenuation gratings and in section 8.2 on the phase grating. In both cases, we will derive and emphasize the benefits of gratings with duty cycles of $\tau = 1/3$. Additionally, this section serves as an application of the results obtained in the previous sections. The discussion will follow the layout of this thesis: After an explanation of the basic layout of the gratings, the use of these phase gratings will be evaluated in terms of sensitivity, noise characteristics, polychromatic characteristics and performance in an imperfect setup. In section 8.3, the obtained results will be combined and the overall performance assessed.

8.1 Attenuation gratings with a duty cycle of 1/3

In section 2.5, we have derived an analytical expression for the visibility as a function of the duty cycle of the source-grating, which will serve as a basis for the following analysis. In section 2.5, the visibility of the interferometer was described by

$$v = \frac{\sum_{n=1}^{\infty} v_{2n-1}}{1+\sum_{n=1}^{\infty} v_{2n}}, \tag{8.1}$$

where the Fourier coefficients v_n for binary gratings are given by

$$v_n = 2 \cdot \operatorname{sinc}(n \cdot \tau_0) \cdot \operatorname{sinc}(n \cdot \tau_1) \cdot \operatorname{sinc}(n \cdot \tau_2), \tag{8.2}$$

with τ_0, τ_1, and τ_2 the duty cycles of the source, beam-splitter and analyzer grating, respectively. Eq. (8.1) thus allows a quick evaluation of the imaging performance of combinations of gratings with different duty cycles. If the beam-splitter and analyzer grating have duty cycles of $\tau_1 = \tau_2 = 1/2$, the visibility was shown to depend linearly on the duty cycle τ_0, as depicted in Fig. 62 (a). In this case, the visibility can be calculated by

$$v = \frac{8}{\pi^2} \sum_{n=1}^{\infty} \frac{\operatorname{sinc}((2n-1) \cdot \tau_0)}{(2n-1)^2}. \tag{8.3}$$

Since the photon flux in the experiment depends on the duty cycle of G_0 as well, in this section, we will extend the analysis by SNR considerations. The SNR in DPC imaging can generally be given by $\mathrm{SNR}_\varphi = \varphi/\sigma(\varphi)$. The signal strength φ can be expressed by the sensitivity S_0 and the deflection angle α by

$$\varphi = S_0 \cdot \alpha. \tag{8.4}$$

The sensitivity is influenced only by the interferometer geometry, while the deflection angle depends on the sample. Both parameters and thus the signal strength φ are therefore independent of the source width. On the other hand, the noise variance σ_φ^2 depends on the source grating's duty cycle due to its dependence on both visibility and flux, after Eq. (5.16)

$$\sigma_\varphi = \frac{\sqrt{2}}{v} \tilde{\sigma}. \tag{8.5}$$

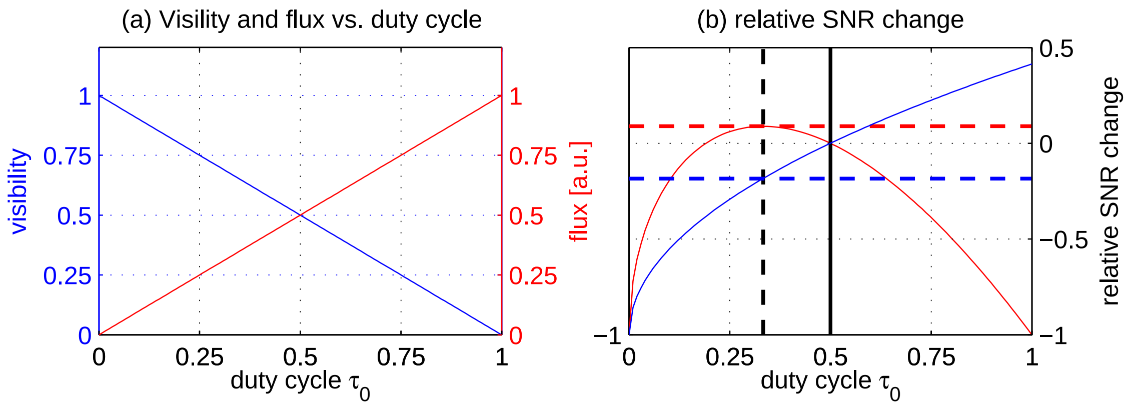

Fig. 62: *(a) Visibility (blue, left axis) and photon flux (red, right axis) are both linear functions of the duty cycle of the source grating. (b) Relative change in* SNR_φ *(solid red line) and* SNR_T *(solid blue line) when changing from* $\tau_0 = 1/2$ *to the shown duty cycle of the source grating. If the source flux is kept constant, the* SNR_φ *can be increased (dashed red line) by changing the duty cycle from* $\tau_0 = 1/2$ *(solid black line) to* $\tau_0 = 1/3$ *(dashed black line), at the cost of a loss in* SNR_T *(dashed blue line).*

The noise level $\tilde{\sigma}$ is connected to the number I of detected photons per pixel by $\tilde{\sigma} = 1/\sqrt{I}$. The SNR is therefore given by

$$\mathrm{SNR}_\varphi = \frac{\varphi}{\sigma_\varphi} = \frac{1}{\sqrt{2}} \cdot S_0 \cdot \alpha \cdot \nu \cdot \sqrt{I}. \tag{8.6}$$

Assuming that the flux density F of the source is constant over the width of one period, it is easy to see that the photon counts I per pixel will increase linearly when the duty cycle and thus the slit widths in the source grating are increased. If we denote the total exposure time as t, we can write

$$I \sim F \cdot t \cdot \tau_0. \tag{8.7}$$

Inserting Eqs. (8.3) and (8.7) into Eq. (8.6), we see that the dependence of the SNR_φ on the duty cycle of the source grating is

$$\Rightarrow \mathrm{SNR}_\varphi(\tau_0) \quad \sim \quad (1-\tau_0) \cdot \sqrt{\tau_0}. \tag{8.8}$$

The relative change in SNR_φ when changing from a duty cycle of $\tau_0 = 1/2$ to any given duty cycle is plotted in Fig 62 (b). It can be seen that under the given assumptions, the maximum of the SNR in the differential phase-contrast channel will be achieved for a duty cycle of $\tau_0 = 1/3$. In comparison to a source grating with $\tau_0 = 1/2$ duty cycle, a relative increase in SNR by

$$\frac{\mathrm{SNR}_\varphi(\tau_0 = 1/3) - \mathrm{SNR}_\varphi(\tau_0 = 1/2)}{\mathrm{SNR}_\varphi(\tau_0 = 1/2)} \approx +8.9\% \tag{8.9}$$

can be achieved. Please note that as the attenuation contrast does not depend on the visibility of the interference pattern, reducing the slit width of the source grating and thus the flux will lead to a net SNR loss in the attenuation-contrast channel. As the SNR in the attenuation-contrast channel is proportional to $\sqrt{I}$ after Eq. (5.8),

$$SNR_T(\tau_0) = \frac{1}{\tilde{\sigma}} = \sqrt{I} \sim \sqrt{\tau_0}, \tag{8.10}$$

the change in performance can be calculated by

$$\frac{\mathrm{SNR}_T(\tau_0 = 1/3) - \mathrm{SNR}_T(\tau_0 = 1/2)}{\mathrm{SNR}_T(\tau_0 = 1/2)} \approx -18.4\%. \tag{8.11}$$

We may instead increase the duty cycle of the source grating with the aim of a maximization of flux. A change of the duty cycle from 1/2 to 2/3 for example causes a relative increase in the SNR in the attenuation-contrast channel by $\approx +15.5\%$, while this will lead to a SNR decrease in the phase-contrast channel by $\approx -23.0\%$. In conclusion, the SNR in the differential phase-contrast channel may be maximized by changing to a source grating with a duty cycle of $\tau_0 = 1/3$. Nevertheless, this increase has to be bought at the expense of a decrease of SNR in the attenuation-contrast channel, if the flux of the tube is kept constant. On the other hand, an increase in the SNR of the attenuation-contrast channel comes at the expense of decreasing visibility and thus SNR_φ.

In principle, this analysis can be performed for the analyzer grating G_2 as well, while keeping the duty cycle of the source grating constant at $\tau_0 = 1/2$. Due to the symmetry of Eq. (8.2) in terms of the duty cycles of the two gratings, a reduction of the duty cycle of G_2 would lead to identical results in the description of the visibility. Nevertheless, the reduction of the duty cycle of the source grating is advantageous, since the additional attenuation introduced by the reduced duty cycle does not affect the dose incident on the sample/patient, in contrast to the case when the duty cycle of the analyzer grating is reduced.

8.2 Phase gratings with a duty cycle of 1/3

Basic grating design

Additionally to the different distances of the fractional Talbot orders, the interference patters of binary phase gratings may differ with respect to the **compression ratio** κ of the interference pattern. We define the compression ratio as the ratio between the numbers of intensity maxima per period of the beam-splitter grating at a fractional Talbot distance. It may be understood as an analogon to the duty cycle for the intensity modulation. For example, the intensity pattern of a $\pi/2$ shifting pattern has one intensity maximum for one period of the grating, thus a compression ratio of $1/2$. The intensity pattern of a π-shifting phase grating has half the periodicity of the period of the grating and thus a compression ratio $2/4$.

So far only phase gratings with a duty cycle of $1/2$ were used in experiments, exhibiting either π or $\pi/2$ phase shift. Following Suleski [Suleski97], we will consider phase gratings with a duty cycle of $1/3$ and $2/3$. The intensity pattern for binary gratings with $1/3$ or $2/3$ duty-cycle are distinguished from $\pi/2$ and π-shifting gratings by having a compression ratio of $1/3$. Higher compression ratios than $1/3$ can only be achieved with non-binary phase gratings, which are more difficult to fabricate. The necessary design phase shift Φ_0 at the bars for the creation of a well defined interference pattern, together with the duty cycle τ_1, the shortest fractional Talbot distance n, the compression ratio κ and period η of the resulting interference pattern are summarized in the following table:

grating no.	design phase shift Φ_0 $[1/\pi]$	duty cycle τ_1	shortest Talbot distance n $[1/d_T]$	compression ratio κ	period factor η
1	$1/2$	1/2	1/4	1/2	1
2	1	1/2	1/16	2/4	2
3	$2/3$	2/3	1/3	1/3	1
4	$4/3$	1/3	1/3	1/3	1
5	$2/3$	1/3	1/6	1/3	1
6	$4/3$	2/3	1/6	1/3	1

The interference patterns created by the gratings pairs #3 and #4 on the one hand, and #5 and #6 on the other hand, are identical, only laterally shifted by half a period. In the following, we will therefore focus on a comparison between gratings #4 and #5, using the terms duty cycle and compression ratio interchangeably. The interference patterns created by those two gratings are shown in Fig. 63.

Sensitivity considerations

The gratings discussed in this section differ in the distance at which the maximum intensity modulation can be found. If the analyzer grating is positioned into a fractional Talbot order, the different inter-grating distances translate linearly into different sensitivities of the interferometer. Differences in the sensitivity correspond to different signal strengths for a given sample and therefore have to be evaluated for an assessment of the imaging performance. Following Eq. (3.13) in section 3.1.2, the sensitivity is given by

$$S_0 = 8\pi \cdot mn\eta \cdot \frac{p_1}{\lambda}, \tag{8.12}$$

where p_1 is the period of the interference pattern, m the fractional Talbot order, n the shortest fractional Talbot distance relative to the full Talbot distance and η the period of the grating relative to the period of the interference pattern. If the period of the gratings, the wavelength λ and the Talbot order are chosen equal for comparison, the sensitivities of the setups with gratings A and B are related by

$$\frac{S_{0,A}}{S_{0,B}} = \frac{n_A}{n_B}\frac{\eta_A}{\eta_B}. \tag{8.13}$$

For example, the sensitivity of grating #1 will be higher by a factor of 2 in relation to grating #2, higher by a factor of 4/3 compared to grating #3 and higher by a factor of 3/2 compared to grating #5. Nevertheless, despite the loss of sensitivity, a reduced inter-grating distance might prove useful in experimental situations where a more compact setup is required.

Noise properties

An evaluation of the imaging performance when using an interference pattern with a compression ratio of $1/3$ requires the analysis of the visibility and the shape of the intensity oscillation in each pixel. The shape and visibility of the interference pattern influence the noise propagation through the algorithms for the retrieval of the phase from the measured raw data. The influence of the shape of the interference pattern on the visibility can be evaluated by inserting $\tau_1 = 1/3$ into Eq. (8.2) while keeping $\tau_2 = 1/2$. From the resulting curve shown in Fig. 64 (a) we can see that the visibility when using phase gratings with a compression ratio of $1/3$ is always higher than with a compression ratio of $1/2$, for any given duty cycle τ_0 of the source grating or lateral source width. This is due to the fact that the interference pattern is less influenced by the smearing of the source intensity distribution if it is more compact.

Additionally, if only the first Fourier coefficient is used for the analysis, one can see from Fig. 64 (b) that the deviation from the full Fourier expansion is lower for gratings with $1/3$ compression ratio. The intensity oscillation in each pixel for a interference pattern with a compression ratio of $1/3$ is therefore more closely approximated by a harmonic oscillation than the oscillation for a interference pattern with $1/2$ compression ratio. As a harmonic intensity oscillation is the most advantageous in terms of noise propagation (compare Ref. [Raupach11]), the use of phase gratings with a duty cycle of $\tau_1 = 1/3$ shows beneficial properties in terms of data evaluation and phase retrieval. From Eq. (8.1) we can express the ratio of the visibilities of two beam-splitter gratings A and B by

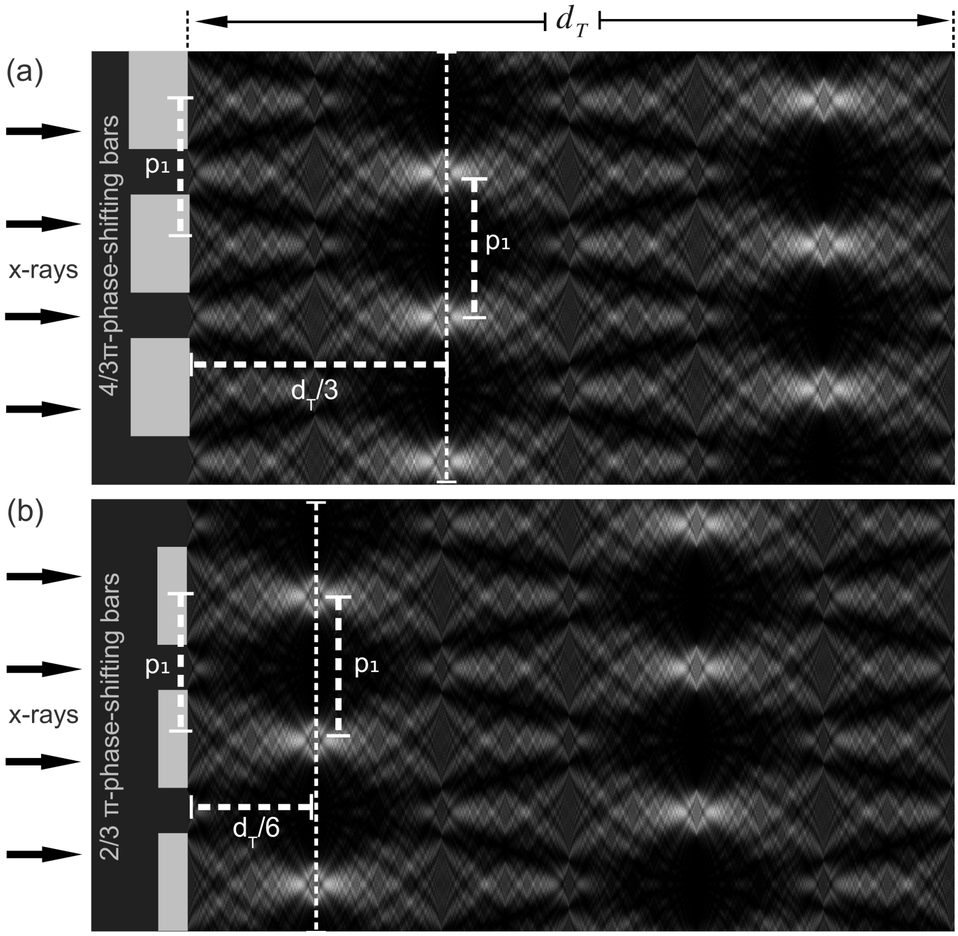

Fig. 63: *Monochromatic intensity patters downstream of (a) a phase grating with a duty cycle of 2/3 and* $4/3\pi$ *phase shift and (b) with a duty cycle of 1/3 and* $4/3\pi$ *phase shift at the bars. The propagation distance shown in the figure corresponds to the full Talbot distance* d_T*. The first fractional Talbot distance* d_1 *is marked for each grating (dashed white lines).*

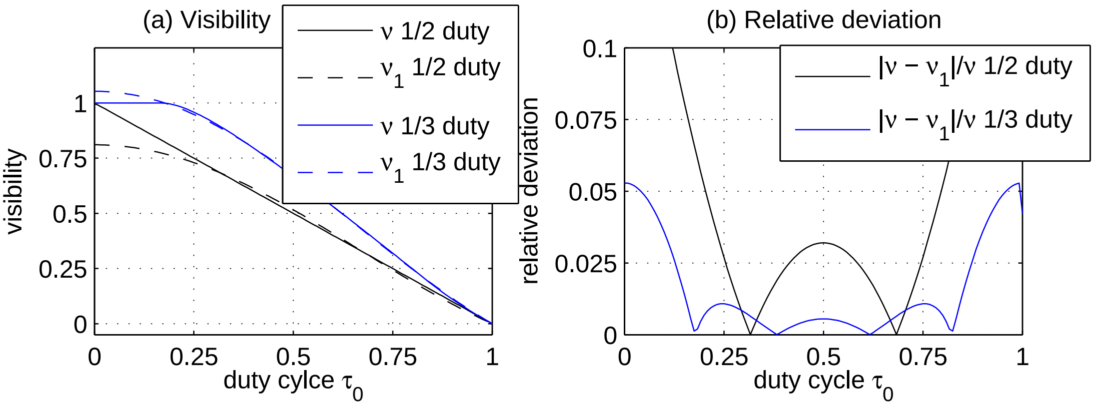

Fig. 64: *(a) Visibility as a function of duty cycle for interference patterns with compression ratio* $\tau_1 = 1/2$ *(solid black) and* $\tau_1 = 1/3$ *(solid blue). The first Fourier coefficient is shown with a dashed line for both duty cycles. (b) Relative error for the approximation with the first Fourier coefficient for the gratings under consideration.*

$$\frac{v_A}{v_B} = \frac{\sum_{n=1}^{\infty} \mathrm{sinc}(n\tau_0)\mathrm{sinc}(n\tau_{1,A})\mathrm{sinc}(n\tau_2)}{\sum_{n=1}^{\infty} \mathrm{sinc}(n\tau_0)\mathrm{sinc}(n\tau_{1,B})\mathrm{sinc}(n\tau_2)}. \tag{8.14}$$

For the harmonic first order approximation v_1 of the visibility, this expression becomes independent of the source and analyzer grating. Comparing an interference pattern with compression ratios of $\tau_{1,A} = 1/3$ and $\tau_{1,B} = 1/2$ yields

$$\frac{v_{1,A}(\tau_{1,A} = 1/3)}{v_{1,B}(\tau_{1,B} = 1/2)} = \frac{\mathrm{sinc}(1/3)}{\mathrm{sinc}(1/2)} = \frac{3}{4}\sqrt{3} \approx 1.299. \tag{8.15}$$

In this case, the relative increase in visibility is

$$\frac{v_{1,A}(\tau_{1,A} = 1/3) - v_{1,B}(\tau_{1,B} = 1/2)}{v_{1,B}(\tau_{1,B} = 1/2)} \approx +29.90\%, \tag{8.16}$$

which is reflected by the dashed graphs shown in Fig. 64 (a). Therefore, we can conclude that a relative visibility increase of about 30% can be achieved by the use of an interference pattern with $1/3$ compression ratio. It should be noted that due to the symmetry of Eq. (8.1) in terms of the duty cycles of the three gratings, identical results for the visibility can be achieved by the change of the duty cycle of the analyzer grating from $\tau_2 = 1/2$ to 1/3, while keeping the compression ratio of the interference pattern at $\tau_1 = 1/2$. Nevertheless, this would decrease the photon flux, due to the increased attenuation in the analyzer grating. Changing the duty cycle of the phase grating is thus advantageous, since the phase grating exhibits negligible attenuation and therefore has only negligible influence on the photon flux available for imaging.

Apart from visibility considerations, for an analysis of the SNR performance of the different gratings, the total flux I at the detector has to be analyzed. Since the duty cycle is equal to the transmission of an ideal attenuation grating, changing the duty cycle of the attenuation gratings will change the flux incident on the detector. Additionally, in a magnifying setup, the photon flux through a given detector area decreases with increasing total setup length $s = l + d$. While the dependence on the duty cycle is linear, the reduction of the photon counts from I_A to I_B follows an inverse square law when changing the distance from s_A to s_B. The intensity ratio between I_A to I_B is thus given by

$$\frac{I_A}{I_B} = \frac{s_B^2}{s_A^2} \cdot \frac{\tau_{0,A}}{\tau_{0,B}} \cdot \frac{\tau_{2,A}}{\tau_{2,B}}. \tag{8.17}$$

The total setup length s_A and s_B cannot be analytically related to the grating parameters without making additional assumptions on the grating periods or the inter-grating distances l and d (see also section 2.8). Nevertheless, for divergent beam geometries, we can conclude that a higher sensitivity, obtained by an increase of the total setup length, reduces the flux at the plane of detection and thus introduces a disadvantageous influence on the SNR.

Polychromatic radiation

For a given bar height and material, the design phase shift Φ_0 can only be achieved for a certain monochromatic energy, the design energy E_0. For energies different from the design energy, the visibility of the interference pattern at a Talbot distance will be lower. As discussed in more detail in section 6, if imaging is done using a laboratory x-ray source, the measured visibility at the plane of detection will be an average over the resulting visibility spectrum, weighted with the intensity of the source for each energy. For an evaluation of the visibility spectra of the different phase gratings under investigation, a Fresnel propagation approach was implemented

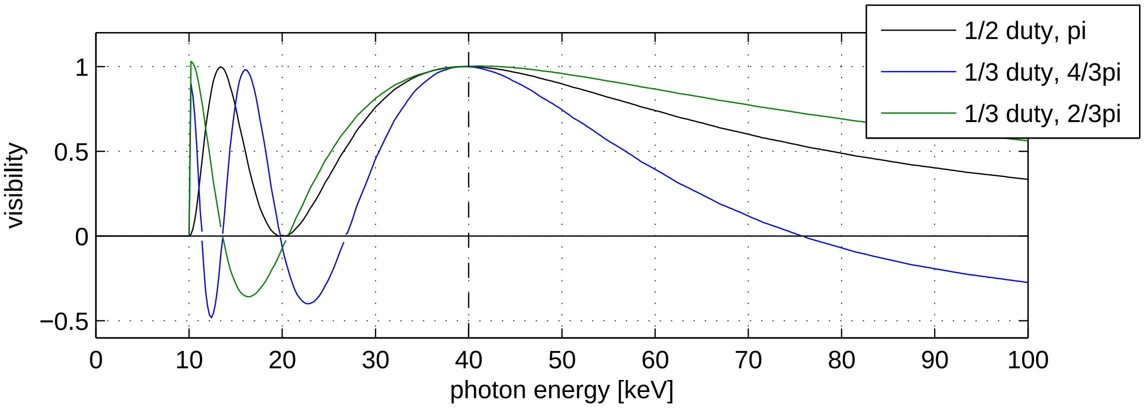

Fig. 65: *Visibility spectra for phase gratings with different duty cycles* τ_1 *and design phase shifts* Φ_0*:* $\tau_1 = 1/2$, $\Phi_0 = \pi/2$ *(black),* $\tau_1 = 1/3$, $\Phi_0 = 4/3\pi$ *(blue),* $\tau_1 = 1/3$, $\Phi_0 = 2/3\pi$ *(green), all calculated for a design energy of* $E_0 = 40$ *keV and first Talbot order. The interference pattern in the negative parts of the spectra exhibits a compression ratio of* $2/3$ *instead of* $1/3$ *and intensity maxima shifted by half a period relative to the solid-lined parts of the spectra.*

numerically. A one-dimensional representation of the grating was propagated using the Fresnel propagator in Fourier domain (see appendix C), and the visibility was consecutively calculated from the squared magnitude at a fractional Talbot order for each given energy. The resulting visibility spectra of the different gratings as a function of energy for a fixed design energy of 40 keV at the first fractional Talbot distance can be seen in Fig. 65.

The different phase gratings show significant differences in their visibility spectra: Compared to the standard $\pi/2$ or π shifting gratings with $1/2$ duty cycle, phase gratings with 1/3 duty cycle and 2/3π phase shift exhibit a visibility spectrum with a higher average visibility. Especially the energies above the design energy contribute more to imaging compared to the standard phase gratings with 1/2 duty cycle. This option offers an advantage in experimental situations where a high flux and thus the contribution of a broad energy band of photons is desired. Nevertheless, since the deflections angles measured in DPC imaging depends on the energy, this approach causes a polychromatic smearing of the measured signal and may introduce polychromatic artifacts like beam hardening. Phase gratings with 4/3π phase shift exhibit a high visibility in a small energy band around the design energy, compared to the other gratings gratings with 1/2 duty cycle. They may thus be used for an optimization of the image quality by the reduction of polychromatic effects, at the expense of an overall flux decrease in the DPC and dark-field-contrast channel.

Apart from the visibility for a given photon energy, the phase of the interference pattern has an influence on the visibility spectrum, as discussed in section 6.1. Nevertheless, the interference pattern of a phase grating with 1/3 duty cycle does not only exhibit a phase change, but also a change in its compression ratio at the Talbot distance for certain energies. The spectral bands which exhibit a shift of the interference pattern by half a period and a change in the compression ratio from 1/3 to 2/3 are plotted with negative values in Fig. 65. Averaging over the contributions from positive and negative visibility bands will result in a loss of mean visibility. In a measurement, those energy bands should therefore be excluded from the source spectrum for a maximization of the mean visibility.

8.3 Attenuation and phase-gratings combined

In this section, we will combine the discussions of the previous sections for an overall assessment of the imaging performance of gratings with 1/3 duty cycle. As discussed in section 8.1, the SNR in DPC imaging can be expressed by

$$\mathrm{SNR} = \frac{\varphi}{\sigma(\varphi)} = \frac{1}{2} \cdot S \cdot \alpha \cdot \nu \cdot \sqrt{I}. \tag{8.18}$$

Taking the SNR ratio between the two gratings A and B allows a comparison of the imaging performance

$$\frac{\mathrm{SNR}_A}{\mathrm{SNR}_B} = \frac{S_{0,A}}{S_{0,B}} \cdot \frac{\nu_A}{\nu_B} \cdot \sqrt{\frac{I_A}{I_B}}. \tag{8.19}$$

Note that the dependence on the sample is canceled out in this representation. By inserting the results of the previous discussions given by Eqs. (8.13), (8.14) and (8.17), we obtain

$$\frac{\mathrm{SNR}_A}{\mathrm{SNR}_B} = \frac{n_A}{n_B} \cdot \frac{\eta_A}{\eta_B} \cdot \frac{\nu_A}{\nu_B} \cdot \frac{s_B}{s_A} \cdot \sqrt{\frac{\tau_{0,A}\tau_{2,A}}{\tau_{0,B}\tau_{2,B}}} \tag{8.20}$$

for a three-grating setup. Eq. (8.20) allows the comparison of the imaging performance of two given setups A and B.

For an exemplary comparison of the performance of 1/3 duty gratings, we will keep the total setup length s and the period of the phase grating fixed, while positioning the analyzer grating at the first fractional Talbot distance. Furthermore, for the comparison, we choose setup B to consist of a $\pi/2$-shifting phase grating and two ideal attenuation gratings with duty cycles of 1/2. This leads to the parameters $n_B = 1/4$, $\eta_B = 1$, $\nu_B = 1/2$, $s_A = s_B$ and $\tau_{0,B} \cdot \tau_{2,B} = 1/4$, which results in the relation

$$\frac{\mathrm{SNR}_A}{\mathrm{SNR}_B} = 16 \cdot \eta_A \cdot \nu_A \cdot n_A \cdot \sqrt{\tau_{0,A}\tau_{2,A}}. \tag{8.21}$$

For an evaluation of the SNR-ratio for a setup with 1/3 duty cycle gratings, first the visibility has to be calculated. The visibility after Eq. (8.1) for different combinations of compression ratios of the interference patterns and duty cycles of the analyzer grating is shown in Fig. 66, as a function of the duty cycle of G_0. While the compression ratio of the interference pattern can take values of 1/2 and 1/3, the duty cycle of the analyzer grating allows arbitrary settings. We exemplarily chose to evaluate the settings 1/2, 1/3 and 2/3, where the last setting could bring advantages in SNR due to the higher transmission of the grating.

From Fig. 66 we can see that the only grating combination offering visibility advantages over the conventional 1/2 duty cycle approach is by the use of either an interference pattern with 1/3 compression ratio or by an analyzer grating with 1/3 duty (solid blue line). The change in the duty cycle of the analyzer grating will be disadvantageous over the latter case as it increases the visibility at the cost of photon flux. The SNR analysis for a number of interesting grating combinations is summarized in the following table:

$\tau_{0,A}$	$\tau_{1,A}$	$\Phi_{0,A}$	$\tau_{2,A}$	n_A	ν_A	SNR ratio
$1/2$	$1/2$	$\pi/2$	$1/2$	$1/4$	0.50	1.000
$1/2$	$1/2$	$\pi/2$	$1/3$	$1/4$	0.66	1.089
$1/2$	$1/3$	$2/3\pi$	$1/2$	$1/6$	0.66	0.889
$1/2$	$1/3$	$4/3\pi$	$1/2$	$1/3$	0.66	1.778

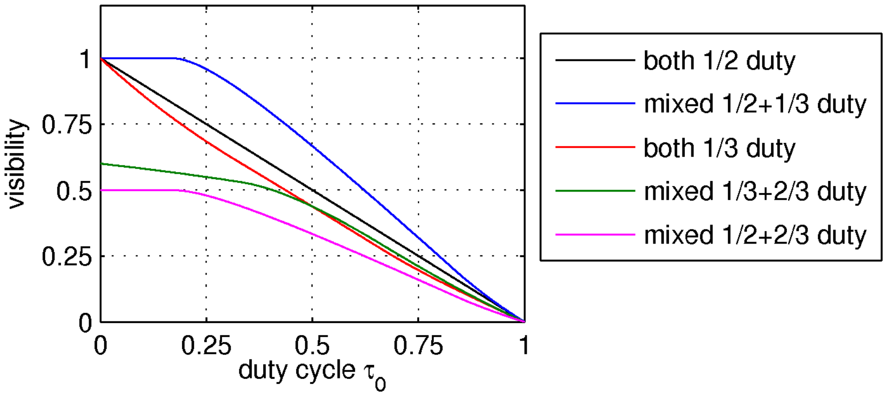

Fig. 66: *Visibility as a function of the duty cycle of* G_0 *for different combinations of compression ratios and duty cycles of the interference pattern and analyzer grating, respectively.*

We see from the table that the SNR ratio will be slightly higher if only the duty cycle of the attenuation grating is changed, as already discussed in section 8.1. The difference in the SNR ratio between the two phase gratings comes mostly from different sensitivities due to different setup lengths. A setup with a $2/3\pi$-shifting phase grating is shorter, while a setup with a $4/3\pi$ shifting phase grating is longer than a setup with a $\pi/2$ phase grating.

We can thus conclude that the grating combinations presented exhibit various advantages, either by an increase of the SNR, a compactification of the setup or an optimization of the visibility spectrum. Nevertheless, as we have made various assumptions like equal total setup length and first Talbot order in our exemplary analysis, a much larger number of additional combinations of grating and setup parameters than discussed above exits and that can be chosen depending on the experimental requirements. Eq. (8.20) now offers the means for their comparison.

8.4 Summary

In this section, the use of binary attenuation and phase gratings with a duty cycle different from $\tau = 1/2$ was discussed. At the same time, this section served as an application and demonstration of the research results of this work. In section 8.1, a duty cycle of 1/3 for either the source or the analyzer grating was shown to maximize the SNR in DPC imaging, if the source flux is kept constant. As the visibility influences only the phase and dark-field-contrast channels, this measure has the drawback of simultaneously decreasing the SNR in the attenuation-contrast channel. In section 8.2, phase gratings with 1/3 or 2/3 duty cycle were shown to offer a compression ratio of the interference pattern of 1/3. This leads to a higher visibility for a given source size in comparison to interference patterns with 1/2 compression ratio, as well as a shape of the intensity oscillation which is closer to a harmonic oscillation. Besides these advantageous noise properties, these gratings exhibit intensity modulations at fractional Talbot distances different from the ones used so far, opening new possibilities in interferometer design. As a grating with a duty cycle of 1/3 or 2/3 can create well defined interference patterns for two design phase shifts of $2/3\pi$ and $4/3\pi$, the visibility spectrum of a given grating can be optimized to allow a relatively thin or broad energy band to contribute to imaging. Finally, different conceivable combinations of gratings with 1/3 duty cycles were assessed in section 8.3, on the basis of the ratio between their expected SNR. The analysis showed that the use of gratings with 1/3 duty cycle offers new possibilities and advantages in interferometer design and imaging, which can be adapted to given experimental requirements.

9 Summary, conclusions and outlook

In this section, we will conclude with a summary and discussion of the main results, with a highlight on open questions and possible future studies.

The basis for the research results presented in this work was provided in section 2 by an analytical description of the contrast formation in DPC imaging. Consecutively, the adopted graphical approach to interferometer design allowed the identification of three basic interferometer geometries, namely conventional, symmetric and inverse. These different grating arrangements open new possibilities in the experimental realization of a grating interferometer [Donath10B]. The combination of the graphic approach with the sensitivity considerations as described in section 3 establishes a unified guideline for the assessment of the interferometer performance. Nevertheless, the graphical approach is presented from a strictly monochromatic point of view. Extending the design approach to the use of polychromatic radiation as emitted by laboratory x-ray sources could yield new insights and advantageous interferometer designs that might otherwise go unnoticed. Polychromatic performance studies, however, exhibit a much higher degree of complexity due to the increased number of parameters: Properties of the source spectrum, of the sample, the detection efficiency, dose and the signal-to-noise ratio have to be considered. While such a discussion is feasible, an insightful unified presentation showing the dependencies between the different parameters needs further consideration.

In section 3, the experimental and analytical investigation on the origin of the DPC signal led to a quantification of the sensitivity of the interferometer [Donath10B]. The measurement signal was shown to exhibit a linear dependence on the sample position for the phase-contrast channel, with far-reaching implications for the reconstruction of tomographic data. For the phase-contrast channel, the observed linear dependence can be compensated by an appropriate alteration of the reconstruction algorithms [Chabior11A]. For the dark-field contrast channel however, the position dependence is only linear for diffusely scattering samples, while being non-linear for others. Since the position dependence is a function of the unknown material composition of the sample itself, an *a priori* compensation of the sensitivity change cannot be performed. In this case iterative or algebraic methods of image reconstruction have to be developed. This challenge may be well combined with the current efforts of developing a tomographic reconstruction algorithm for the directional dark-field contrast.

In section 4, it was shown how the energy and material dependence of the attenuation and refraction decrement can be used for the calculation of an atomic number contrast. The method is compatible with radiographic and tomographic imaging modes, using monochromatic and polychromatic radiation, as well as elemental and compound materials [Chabior11B]. The calculation of the contrast in the presence of high-variance noise was shown to be problematic, but manageable using adapted algorithms. This promising new contrast opens new possibilities in the quantitative discrimination of different materials, either in medical diagnostics, nondestructive testing or security applications. Interesting effects could be studied near the absorption edges of a given material or marker, for example at the iodine K-edge. The use of multiple markers could also be conceived, utilizing different characteristic ratios between attenuation and refraction for the identification of each single marker.

The influence of noise on the image quality has been addressed in section 5. The fundamental statistical noise distributions of the three contrast channels were worked out by analytical means, identifying the Poissonian, the wrapped-normal and the Rician distribution as the probability density functions of the mean, the phase and the amplitude of the phase-stepping oscillation, respectively. Based on these results, the signal-to-noise properties in the transmission, phase and dark-field signals can be understood [Chabior11C]. The full understanding of the fundamental PDFs of the reconstructed parameters is essential for signal processing applications and approaches to the denoising of the images. A first application was given in section 5.2 by the discussion of data averaging and parameter estimation techniques. Noise is especially crucial in the differential phase-contrast channel, as the integration of the differential data introduces highly disadvantageous noise-power characteristics to the reconstructed data. Alternative integration methods and approaches adapted to the noise signature should therefore be investigated.

How the use of polychromatic radiation influences the measurement data has been investigated in section 6. An analytical expression for the visibility spectrum was given, describing the spectral sensitivity of the interferometer. By deriving analytical expressions for the measured effective polychromatic signals for all three contrast channels, a better understanding of polychromatic effects in grating-based imaging could be achieved. These results were applied to the analysis of beam-hardening effects in all three contrast channels, demonstrating these effects experimentally for the first time in grating-based imaging [Chabior11D]. The discussion of polychromatic effects in dark-field imaging was shown to be difficult, since tabulated data for the diffusion coefficient and its energy dependence are not yet available. As the origin of the dark-field signal is essentially a phase measurement at sub-pixel scales, the energy dependence is expected to be the related to the energy dependence of the phase measurement. Nevertheless, this assumption will have to be verified experimentally.

Based on analytical expressions for the visibility as a function of the grating profiles, in section 7, the influence of different grating errors on the imaging performance was investigated. Deviations and variations in the height, the period, the duty cycle of the grating, as well as the bathtub effect were evaluated [Chabior11E]. The results allow the definition of explicit tolerance limits for grating fabrication, serving as a guideline for the ongoing optimization of the fabrication procedures. A successive experimental investigation of the shadowing effects in plane gratings proved the experimental advantages of cylindrically bent gratings. This experimental work is a first step towards the realization of a compact setup suitable for medical imaging.

In section 8, the results obtained from the previous investigations were applied to the assessment of gratings with a duty cycle of 1/3 in DPC imaging. After a discussion of the basic properties of the gratings in consideration, the sensitivity, polychromatic performance and noise characteristics relative to the achievable flux were studied for each grating. An optimization of the SNR in DPC imaging can be achieved by a change in the duty cycle of G_0, nevertheless only at the expense of SNR in the attenuation-contrast channel. The results show that the use of phase gratings with 1/3 and 2/3 duty cycle offers advantages over state-of-the-art gratings with a duty cycle of 1/2, depending on the experimental requirements.

In conclusion, the results obtained in this work clearly show the value of the developed tools and concepts and expand the understanding of the grating-based x-ray imaging technique. Advancements have been achieved in the understanding of the contrast formation ([Donath10A], [Chabior11A], [Chabior11B]), as well as the assessment of the influence of different imperfections of the setup on the image quality ([Chabior11C], [Chabior11D], [Chabior11E]). The presented results are intended to provide understanding and clarity for other researches and to pave the way for further advancements of the imaging technique. While grating-based imaging can already be said to be useful for the application in non-destructive testing, various challenges and open questions still remain for its effective utilization in widely used applications. I hope that the research will continue incessantly and lead to further fruitful results, new intriguing insights and helpful applications.

Appendix

A Characterization of optical systems

This section gives a brief introduction into the theory of linear and shift-invariant systems, deriving a number of important concepts for the characterization of optical systems. The derivations are based on Ref. [Goodman05].

Assume that the action of an optical system is described by an operator S, mapping an incoming signal u_0 at position (x_0, y_0) onto the outgoing signal u_1 at position (x_1, y_1):

$$u_1(x_1, y_1) = S(u_0(x_0, y_0)). \tag{A.1}$$

Using the properties of the delta distribution δ, the incoming signal may be rewritten

$$u_0(x_0, y_0) = \int_{-\infty}^{\infty}\int_{-\infty}^{\infty} u_0(\xi, \eta)\cdot\delta(x_0-\xi, y_0-\eta)\cdot d\xi d\eta \tag{A.2}$$

If the system is linear, i.e. if $S(a\cdot u_0 + b\cdot u_1) = aS(u_0) + bS(u_1)\ \forall a, b \in \mathbb{C}$, the effect of the optical system onto an incoming signal can be described by the action of the operator S onto the decomposition of the input function

$$\begin{aligned} u_1(x_1, y_1) &= S\left(\int_{-\infty}^{\infty}\int_{-\infty}^{\infty} u_0(\xi, \eta)\cdot\delta(x_0-\xi, y_0-\eta)\cdot d\xi d\eta\right) \\ &\overset{\text{linearity}}{=} \int_{-\infty}^{\infty}\int_{-\infty}^{\infty} u_0(\xi, \eta)\cdot S\left(\delta(x_0-\xi, y_0-\eta)\cdot d\xi d\eta\right) \\ &= \int_{-\infty}^{\infty}\int_{-\infty}^{\infty} u_0(\xi, \eta)\cdot h(x_1, y_1; \xi, \eta)\cdot d\xi d\eta, \end{aligned} \tag{A.3}$$

where we have introduced the image function

$$h(x_1, y_1; \xi, \eta) := S\left(\delta(x_0-\xi, y_0-\eta)\right), \tag{A.4}$$

which is called the **impulse response** or **point spread function** (PSF) of the system. It is the response of the system to a delta impulse at position (ξ, η) in the input plane, evaluated at point (x_1, y_1) in the image plane.

Far-reaching implications can be obtained for the special case of shift-invariant optical systems. A system is called shift-invariant, if its impulse response depends only on the difference $x_1 - \xi$ and $y_1 - \eta$:

$$h(x_1-\xi, y_1-\eta) = S\left(\delta(x_0-\xi, y_0-\eta)\right). \tag{A.5}$$

Shift-invariance means that a shift of the source of illumination only shifts the resulting image in the image plane, without introducing any additional distortions. Thus, for linear, shift-invariant systems, the outgoing signal can be written

$$u_1(x_1, y_1) = \int_{-\infty}^{\infty}\int_{-\infty}^{\infty} u_0(\xi, \eta)\cdot h(x_1-\xi, y_1-\eta)\cdot d\xi d\eta. \tag{A.6}$$

Mathematically, this integral represents the convolution of the incoming signal u_0 with the impulse response h:

$$u_1 = u_0 \otimes h. \tag{A.7}$$

The action of any linear, shift-invariant system onto an arbitrary input signal is thus completely characterized by its impulse response.
Taking the Fourier transform of Eq. (A.7) yields

$$U_1(f_1, g_1) = U_0(f_0, g_0) \cdot H(f_0, g_0), \tag{A.8}$$

where the function H is the Fourier transform of the impulse response h and is called the **optical transfer function** (OTF), or simply transfer function of the system. In spatial frequency domain, the action of the optical system is thus a simple multiplication of the frequency representation of the input signal $U_0(f_0, g_0)$ with the OFT. Usually the complex-valued OTF is split into a real-valued amplitude and a phase factor

$$\begin{array}{rrcll} & H(f_0,g_0) & = & |H(f_0,g_0)| \quad \cdot & \exp\left(i \cdot \arg\left(H(f_0,g_0)\right)\right) \\ \Leftrightarrow & \mathrm{OTF}(f_0,g_0) & = & \mathrm{MTF}(f_0,g_0) \cdot & \mathrm{PTF}(f_0,g_0) \end{array} \tag{A.9}$$

The functions MTF and PTF are called **modulation transfer function** and **phase transfer function**, respectively. The MTF is widely used for the characterization of optical systems, describing the ability of the system to transmit spatial frequencies. As real optical systems cannot transmit infinitely high frequencies, the MTF of the system will in general be monotonically decreasing. Usually, the **resolution of the optical system** is defined by the length scale for which the MTF has dropped to a value of 10 % .
The real- and imaginary part of the transfer function are connected by a Kramers-Kronig-relation, a special case of the Hilbert transform

$$\begin{aligned} \mathrm{Im} H(x) &= -\frac{2}{\pi} P \int_0^{+\infty} \frac{x \cdot \mathrm{Re} H(x)}{t^2 - x^2} dt \\ \mathrm{Re} H(x) &= \frac{2}{\pi} P \int_0^{+\infty} \frac{t \cdot \mathrm{Im} H(x)}{t^2 - x^2} dt. \end{aligned} \tag{A.10}$$

Here, P is the Cauchy principal value of the integral. If the MTF or the PTF are known $\forall x \in \mathbb{R}$, the corresponding counterpart can be calculated.

B The scattering factor

Scattering from a single bound electron

If an electromagnetic wave passes through a sample, it interacts with the bound electron in matter. If the energies of the incoming photon are below the 1 GeV, pair production and relativistic effects can be disregarded and the interaction can be explained in a semi-classical picture. In this approach, the electron can be described as a dipole oscillator with a natural frequency of ω_0 equal to its binding energy in the atomic shell, being driven by the oscillating electric field component $\mathscr{E} = \mathscr{E}_0 \cdot e^{i\omega t}$ of the incoming photon. The forced oscillation of the electron can be described by the differential equation

$$\ddot{x} + \gamma \dot{x} + \omega_0^2 x = -\frac{e}{m_e} \cdot \mathscr{E}_0 \cdot e^{i\omega t}, \tag{B.1}$$

where x is the position of the electron, γ a damping constant and e and m_e the electron charge and mass, respectively. Eq. (B.1) has the solution

$$x = \frac{e}{m_e} \frac{\mathscr{E}_0 e^{i\omega t}}{\omega^2 - \omega_0^2 + i\gamma\omega}. \tag{B.2}$$

The excited electron will emit an electromagnetic field that can be modeled as a point source e^{ikR}/R. At distance R from the interaction point, the ratio of the incoming and outgoing field can be shown to be [Nielsen00]

$$\frac{\mathscr{E}_{\text{out}}}{\mathscr{E}_{\text{in}}} = -r_e \frac{\omega^2}{\omega^2 - \omega_0^2 + i\gamma\omega} \cdot \frac{e^{ikR}}{R} = -r_e \cdot f \cdot \frac{e^{ikR}}{R}. \tag{B.3}$$

The atomic scattering factor f is the amplitude of the outgoing wave. It is given by

$$f(\omega, \omega_0) = \frac{\omega^2}{\omega^2 - \omega_0^2 + i\gamma\omega} = 1 + \frac{\omega_0^2 - i\omega\gamma}{\omega^2 - \omega_0^2 + i\gamma\omega} \approx 1 + \frac{\omega_0^2}{\omega^2 - \omega_0^2 + i\gamma\omega}, \tag{B.4}$$

where the approximation is valid if $\gamma \ll \omega$. The scattering factor can be written $f = f_0 + f_1 + if_2$, where $f_0 = 1$. f_1 and f_2 can be obtained from Eq. (B.4) by separating the right hand side of Eq. (B.4) into a real-valued function

$$f_1 = \frac{\omega_0^2 \left(\omega^2 - \omega_0^2\right)}{\left(\omega^2 - \omega_0^2\right)^2 + (\omega\gamma)^2} \tag{B.5}$$

and an imaginary function

$$f_2 = -\frac{\omega_0^2 \omega\gamma}{\left(\omega^2 - \omega_0^2\right)^2 + (\omega\gamma)^2}. \tag{B.6}$$

The functions f_1 and f_2 are the dispersion corrections of the electron system. In the language of linear systems theory (see appendix A), the scattering factor can be considered the impulse response of a bound electron to a harmonic driving force. The real and imaginary parts of the dispersion correction are thus connected by the Kramers-Kronig relation.
In a scattering experiment, the total interaction cross-section is given by

$$\sigma_{\text{total}} = \left(\frac{8\pi}{3}\right) r_e^2 |f|^2 = \left(\frac{8\pi}{3}\right) r_e^2 \frac{\omega^4}{\left(\omega^2 - \omega_0^2\right)^2 + (\omega\gamma)^2}. \tag{B.7}$$

For $\omega \gg \omega_0$, the electron can be considered free, which yields $f = 1$ and the classical Thomson cross-section

$$\sigma_{\text{total}} = \left(\frac{8\pi}{3}\right) r_e^2. \tag{B.8}$$

For $\omega \ll \omega_0$, one obtains $f = \omega^2/\omega_0^2$ and thus the Rayleigh cross-section is

$$\sigma_{\text{total}} = \left(\frac{8\pi}{3}\right) r_e^2 \left(\frac{\omega}{\omega_0}\right)^4. \tag{B.9}$$

Scattering from an atom

Eqs. (B.4)-(B.6) describe the energy dependent scattering factor of a single bound oscillator. Nevertheless, in an atom, multiple bound electrons with independent energy levels will interact with the photon. If the Coulomb interaction between the electrons is ignored, the scattering factor of the atom can be calculated by a linear superposition of the scattering factors f_k of each single oscillator, with natural frequencies ω_k and damping factors γ_k

$$f = \sum_k g_k(\omega_k) f_k(\omega_k, \omega). \tag{B.10}$$

The weight g_k is called the oscillator strength, which is the probability of a transition of the electrons of from their shell to all permissible states

$$g_k(\omega_k) = \int_{\omega_k}^{\infty} \left(\frac{dg}{d\omega}\right)_k d\omega, \tag{B.11}$$

where $dg/d\omega$ is the density of the oscillator states [Crystallography04]. The sum of all oscillators strengths is equal to the number of electrons contributing to the cross-section. For energies above the K-edge, one obtains

$$f_0 = \sum_k g_k = Z, \tag{B.12}$$

where Z is the atomic number of the atom.

Scattering from a molecule

If scattering from a molecule is considered, the molecular scattering factor F_m is simply given by a superposition of the contributions of the single atomic scattering factors f_j

$$F_\mathrm{m}(\mathbf{q}) = \sum_j f_j(\mathbf{q}) \exp\left(i\mathbf{q}\mathbf{r}_j\right), \tag{B.13}$$

where $\mathbf{r}_j$ are the positions of the different atoms of the molecule. The vector $\mathbf{q} = \mathbf{k} - \mathbf{k}$' is the momentum transfer between the incoming and the scattered wave.

Scattering from a crystal

If the scattering atoms are not isolated, but part of a crystal lattice, the influence of the long-range order has to be taken into account. The crystal scattering amplitude F_c is calculated by including the influence of the form factors of all atoms of the crystal. The formalism can be simplified by using the symmetry of the crystal, which can be described by the concept of the unit cell of the crystal. Scattering from a crystal is described by the **structure factor F_c**, given by

$$F_\mathrm{c}(\mathbf{q}) = \sum_{j=1}^{\text{crystal}} f_j(\mathbf{q}) \cdot e^{i\mathbf{q}\cdot\mathbf{r}_j} = \sum_{n}^{\text{lattice}} e^{i\mathbf{q}\mathbf{R}_n} \sum_{j}^{\text{unit cell}} f_j(\mathbf{q}) e^{i\mathbf{q}\mathbf{r}_j}. \tag{B.14}$$

In this relation, $\mathbf{r}_j$ is the position of each atom, $\mathbf{R}_n$ is a crystal lattice vector and f_j the atomic form factor of the j-th atom in the crystal or unit cell, respectively. Additionally, the position of the atoms within the crystal lattice is not constant, but subject to thermal drifts and lattice vibration modes. The influence of temperature can be taken into account by the Debye-Waller-factor, while the influence of phonon scattering can be neglected in the energy range of interest in this work.

C Wave propagation and the Talbot effect

Propagation in space

If a light perturbation can be described by a scalar function $u(r,t) = u(r)u(t)$, a starting point for the discussion of its propagation is given by the Rayleigh-Sommerfeld integral [Goodman05]:

$$u(x,y,z) = \frac{1}{i\lambda} \iint u\left(x_0, y_0, 0\right) \frac{e^{i\mathbf{k}\mathbf{r}}}{r} \cos(\mathbf{n},\mathbf{r})\, dx_0\, dy_0. \tag{C.1}$$

Eq. (C.1) is an analytical formulation of the Huygens-Fresnel principle: Every point of the incoming wavefront $u(x_0, y_0)$ in the plane $z = 0$ can be considered as the source of a spherical wave $\exp(ikr)/r$. The superposition of these point sources, multiplied by an inclination factor $\cos(\mathbf{n}, \mathbf{r})$, propagates the wavefront to the image plane. The unit vector $\mathbf{n}$ points into the direction of propagation, while $\mathbf{r}$ is a vector reaching from the origin to a given point in the image plane.

This difficult integral can be simplified by a number of approximations. In the **paraxial approximation**, only small deflection angles are considered. Thus, one can apply the simplifications

$$\cos(\mathbf{n}, \mathbf{r}) \approx 1 \qquad \text{and} \qquad r \approx z. \tag{C.2}$$

For the exponential term $\exp(ikr)$, this approximation for r is too coarse. Nevertheless, one can further simplify by expanding r into a power series

$$\begin{aligned} r &= \sqrt{z^2 + (x-x_0)^2 + (y-y_0)^2} \\ &= z\left[1 + \frac{(x-x_0)^2}{z^2} + \frac{(y-y_0)^2}{z^2}\right]^{1/2} \\ &= z\left[1 + \frac{1}{2}\frac{(x-x_0)^2}{z^2} + \frac{1}{2}\frac{(y-y_0)^2}{z^2} + O(x^4, y^4, z^{-4})\right]. \end{aligned} \tag{C.3}$$

The restriction to terms of order two is called **Fresnel approximation**. It is valid as long as the higher order terms are negligible, i.e. when

$$kz\frac{\left[(x-x_0)^2 + (y-y_0)^2\right]^2}{8z^4} \ll 1, \tag{C.4}$$

or in other words

$$\frac{\pi}{4\lambda}\left[(x-x_0)^2 + (y-y_0)^2\right]^2 \ll z^3. \tag{C.5}$$

By the Fresnle approximation, the diffraction integral described by Eq. (C.1) can be reduced to

$$u(x,y,z) = \frac{e^{ikz}}{i\lambda z}\iint u(x_0, y_0, 0)\exp\left(i\frac{\pi}{\lambda z}\left[(x-x_0)^2 + (y-y_0)^2\right]\right)dx_0 dy_0. \tag{C.6}$$

This integral can be interpreted as the convolution of the incoming wavefront $u(x_0, y_0)$ with the **Fresnel-Propagator** p_z

$$u(x,y,z) = u(x,y,0) \otimes p_z(x,y), \tag{C.7}$$

given by

$$p_z(x,y) := \frac{e^{ikz}}{i\lambda z}\exp\left[i\frac{\pi}{\lambda z}(x^2 + y^2)\right]. \tag{C.8}$$

In the language of linear system theory (see appendix A), the Fresnel propagator is the impulse response of a free undisturbed system.

Propagation in reciprocal space

If the transfer function of a free and undisturbed system is of interest, the process of propagation has to be studied in reciprocal space. Let $U_0(f,g) = \mathscr{F}\{u_0(x,y)\}$ be the Fourier transform of the incoming wave $u_0(x,y)$, the incoming wave can be described as a superposition of plane waves

$$u_0(x,y) = \int_{-\infty}^{\infty} U_0(f,g) e^{2\pi i(fx+gy)} df dg \tag{C.9}$$

with amplitudes $U_0(f,g)$ and wave vectors $\mathbf{k} = (k_x, k_y, k_z)$, with

$$k_x = 2\pi f \quad k_y = 2\pi g \quad k_z = \sqrt{k^2 - k_x^2 - k_y^2} = k\sqrt{1-(\lambda f)^2 - (\lambda g)^2}. \tag{C.10}$$

Propagation by a distance of z corresponds to the multiplication of each plane wave with a phase factor $\exp(ik_z z)$

$$u_1(x,y) = \int_{-\infty}^{\infty} U_0(f,g) e^{ikz\sqrt{1-(\lambda f)^2-(\lambda g)^2}} e^{2\pi i(fx+gy)} df dg. \tag{C.11}$$

If the propagated wave $u_1(x,y)$ is transformed into reciprocal space by a Fourier transform, the second phase term cancels out and we obtain

$$U_1(f,g) = U_0(f,g) e^{ikz\sqrt{1-(\lambda f)^2-(\lambda g)^2}}. \tag{C.12}$$

The Fresnel approximation in the frequency domain corresponds to the approximation of the square root in the exponential by a power series of order two

$$\begin{aligned} \sqrt{1-(\lambda f)^2-(\lambda g)^2} &= 1 - \frac{1}{2}(\lambda f)^2 - \frac{1}{2}(\lambda g)^2 + O(f^4,\ g^4) \\ &\approx 1 - \frac{\lambda^2}{2}(f^2+g^2). \end{aligned} \tag{C.13}$$

This approximation is valid, if

$$\begin{aligned} (\lambda f)^2 - (\lambda g)^2 &= \lambda\sqrt{f^2+g^2} \\ &= |\sin\vartheta| \\ &\ll 1, \end{aligned} \tag{C.14}$$

or in other words, if the angle ϑ between the wave vector and the direction of propagation is small. This is valid, because the wavelength λ of x-rays is small relative to the propagation distances. If formula (C.13) is combined with Eq. (C.12), we obtain the representation of the Fresnel propagator in reciprocal space

$$U_1(f,g) = U_0(f,g) \cdot P_z(f,g) \tag{C.15}$$

with

$$P_z(f,g) := e^{ikz} \exp\left[-i\pi\lambda z\left(f^2+g^2\right)\right]. \tag{C.16}$$

The phase factor $\exp(ikz)$ imposes a uniform phase shift onto all points of the wavefront and can thus be omitted without loss of generality.

The Talbot self-imaging effect:

An interesting phenomenon can be derived from the properties of the Fresnel propagator, if the diffraction of periodic structures like optical gratings is investigated. Let the periodic structure be described by a one dimensional transmission function T

$$T(x) = t(x) \otimes \sum_{k=-\infty}^{\infty} \delta(x - kp). \tag{C.17}$$

Here, $t(x)$ is the transmission function of a single period of the grating, extended to infinity by a convolution with a Dirac comb. If the intensity distribution downstream of the grating is of interest, the transmission function of the grating has to be convolved with the Fresnel propagator at distance z

$$u(x,z) = T(x) \otimes p_z(x). \tag{C.18}$$

In reciprocal space, the convolution becomes a simple multiplication. As the transmission function T is periodic, the frequency spectrum of the grating is discrete. Therefore, only spatial frequencies which are a multiple of the reciprocal period length p contribute to the propagator

$$f = \frac{m}{p} \qquad m \in \mathbb{N}. \tag{C.19}$$

Using this property, the propagator from Eq. (C.16) can be written

$$P_z\left(\frac{m}{p}\right) = \exp\left[2\pi i m \frac{\lambda z}{2p^2}\right]. \tag{C.20}$$

It can be seen that for distances

$$d_T := m \cdot \frac{2p^2}{\lambda} \qquad m \in \mathbb{N}, \tag{C.21}$$

the propagator is unity and thus a perfect replica of the transmission function of the illuminated grating is created at a propagation distance d_T. This effect is called the **Talbot-self-imaging effect** [Talbot36]. The first correct explanation and description using Fresnel diffraction theory is attributed to Rayleigh [Rayleigh81]. Today, the effect is studied and applied in a variety of research fields, ranging from imaging, quantum mechanics to optoelectronics and communication [Guigay71, Arrizon94, Nowak97, Vrakking96].

Following [Arrizon94], the wavefield behind a diffraction grating at a distance corresponding to a fraction of the Talbot distance $z = m/n \cdot d_T$, can be described by

$$\Psi(x, z = \frac{m}{n} d_T) = \sum_{k=0}^{n-1} C(m,n,k)\ T(x - kp/n). \tag{C.22}$$

The coefficients $C(m,n,k)$ are called Talbot coefficients and can be calculated by

$$C(m,n,k) = \frac{1}{n} \sum_{j=0}^{n-1} \exp\left[i \frac{2\pi}{n} j(k - mj)\right]. \tag{C.23}$$

At a distance corresponding to a fractional Talbot distance $m/n \cdot d_T$, the wavefield is thus given by an n-fold superposition of the transmission function of the grating, shifted by a distance kp/n and weighted with the corresponding Talbot coefficients. In Ref. [Guigay71], it is shown that for fractional Talbot distances with $m = 1$, this relation can be further simplified to

$$C(1,n,k) = \left(1 + (-1)^k i^n\right) \exp(i \frac{\pi k^2}{2n}). \tag{C.24}$$

Various authors have shown that a variety of gratings are capable of transforming an incoming wavefront into an intensity modulation. A convenient listing can be found in Ref. [Suleski97].

D Temporal and spatial coherence

Interference phenomena are based on the superposition of waves. To characterize the ability of two separate waves to create an interference pattern, in this section, the concept of coherence will be discussed. It serves as a measure of the spatial and temporal correlation between the given waves. The derivations are based on Ref. [Born99].

Let $u(x,t)$ be an incoming wave. As the integration time of common detectors is long in comparison to the oscillations of the incoming fields, in the following, we will only consider the temporal average of the incident radiation. By the **temporal average** of a signal, denoted by $\langle u(t) \rangle$, we understand

$$\langle u(x,t) \rangle := \lim_{T \to \infty} \frac{1}{T} \int_{-T/2}^{T/2} u(x,t) dt. \tag{D.1}$$

Consider a wave $u(x,t)$ at different points x_1 and x_2 and at different times t_1 and t_2. Let $u(P,t)$ be a point at a detector, where the influence of those two points $u_1(t) := u(x_1,t)$ and $u_2(t) := u(x_2,t)$ is studied

$$u(P,t) = u_1(t-t_1) + u_2(t-t_2). \tag{D.2}$$

The intensity $I(P)$ at the detector is then given by the temporal average of the squared magnitude of the incoming wave:

$$\begin{aligned} I(P) &= \left\langle |u(P,t)|^2 \right\rangle \\ &= \langle u_1(t-t_1) \cdot u_1^*(t-t_1) \rangle + \langle u_2(t-t_2) \cdot u_2^*(t-t_2) \rangle \\ &\quad + \langle u_1(t-t_1) \cdot u_2^*(t-t_2) \rangle + \langle u_2(t-t_2) \cdot u_1^*(t-t_1) \rangle \\ &= I_1 + I_2 + 2\Gamma_{12}(t_2 - t_1), \end{aligned} \tag{D.3}$$

where u^* denotes the complex conjugate of u. The intensity is thus given by the sum of the intensity of the single waves, plus an interference term proportional to Γ. The function Γ is called **mutual coherence function** (MCF) and is given by

$$\begin{aligned} \Gamma_{12}(\tau) &:= \langle u_2^*(t) u_1(t+\tau) \rangle \\ &= \lim_{T \to \infty} \frac{1}{T} \int_{-T/2}^{T/2} u_2^*(t) u_1(t+\tau) \cdot dt. \end{aligned} \tag{D.4}$$

This function can be used for the definition of the coherence of two waves. Following Eq. (D.4), the mutual coherence can be understood as the time averaged cross correlation between a wave evaluated at different positions x_1 and x_2 and times t_1 and t_2. For $x_1 = x_2$, the mutual coherence Γ simplifies to

$$\Gamma_{11}(\tau) = \langle u_1(t+\tau) u_1^*(t) \rangle . \tag{D.5}$$

In this case, the MCF is said to describe the temporal or **transversal coherence** of two waves. If we set $t_1 = t_2$ instead, the MCF

$$\Gamma_{12}(0) = \langle u_1(t) u_2^*(t) \rangle \tag{D.6}$$

is said to describe the spatial or **lateral coherence** of two waves. If we set both $x_1 = x_2$ and $t_1 = t_2$, the MCF is identical to the intensity at the plane of detection

$$\Gamma_{11}(0) = I_1 \quad \text{and} \quad \Gamma_{22}(0) = I_2. \tag{D.7}$$

By normalizing to MCF by the square root of the intensity, we obtain the **complex degree of coherence** (CDC)

$$\gamma_{12}(\tau) := \frac{\Gamma_{12}(\tau)}{\sqrt{\Gamma_{11}(0)\cdot\Gamma_{22}(0)}} = \frac{\Gamma_{12}(\tau)}{\sqrt{I_1 \cdot I_2}}. \tag{D.8}$$

With this relation, the intensity at the plane of detection as described in Eq. (D.3) can be expressed by the degree of coherence

$$I(P) = I_1(P) + I_2(P) + 2\sqrt{I_1(P)\cdot I_2(P)} \cdot \mathrm{Re}\left(\gamma_{12}(t_2 - t_1)\right). \tag{D.9}$$

Thus, if the intensity of an interference pattern at a certain point P at the detector is of interest, the complex degree of coherence has to be evaluated.

The quality of an interference pattern can be characterized by the definition of the **contrast** or **visibility**. It is defined by a relation between the brightest and darkest spots of the interference pattern:

$$v := \frac{I_{max} - I_{min}}{I_{max} + I_{min}} = \frac{2\sqrt{I_1(P)\cdot I_2(P)}}{I_1(P) + I_2(P)} \left|\gamma_{12}(\tau)\right|. \tag{D.10}$$

Thus the contrast of the interference pattern increases with increasing degree of coherence. If the intensity of both waves is equal ($I_1 = I_2$), the visibility is equal to the magnitude of the CDC

$$v = \left|\gamma_{12}(\tau)\right|. \tag{D.11}$$

For $t_2 = t_1$, the Van Cittert-Zernike-theorem states that the CDC is equal to the Fourier transform of the intensity distribution of the light source. For $x_2 = x_1$, the Wiener-Khintchine theorem states that the CDC is equal to the Fourier transform of the spatial frequency spectrum of the light source. Thus, reducing the spatial frequency bandwidth and the lateral size of the source will increase the visibility of a given interference pattern.

E Correlation and noise

This section gives an introduction into fundamental properties of noise. The intuitive notion of 'noise' can be understood and characterized using statistical methods. In fact, noise can be defined as an uncorrelated signal. The **cross correlation** between two signals $u(x)$ and $v(x)$ is given by

$$\begin{aligned} K_{uv}(\xi) &:= \int_{-\infty}^{\infty} u^*(x)\cdot v(x+\xi)\, dx \\ &=: u(x) * v(x). \end{aligned} \tag{E.1}$$

In Eq. (E.1), the correlation operation is denoted by $*$, while u^* denotes complex conjugation. The correlation of a signal with itself is named **autocorrelation**. It can be given by

$$K_{uu}(\xi) := u(x) * u(x). \tag{E.2}$$

The Wiener-Khintchine theorem states that the Fourier transform of the autocorrelation function is equal to the **power spectral density** $P_{uu}(f)$ of the signal

$$P_{uu}(f) = \int_{-\infty}^{\infty} K_{uu}(\xi)\cdot e^{-2\pi i f \xi}\, d\xi = \mathscr{F}\left(K_{uu}(x)\right). \tag{E.3}$$

Since the autocorrelation exhibits the property

$$\mathscr{F}\left(u(x) * u(x)\right) = U^*(f) \cdot U(f), \tag{E.4}$$

the power spectral density can also be calculated by

$$P_{uu}(f) = U^*(f) \cdot U(f) = |U(f)|^2. \tag{E.5}$$

The power spectral density is a measure of the energy of a signal in an infinitesimally small frequency band. If the signal consists of plain noise, the spectral density is called the **noise power spectrum** (NPS) or the **Wiener-spectrum**. The total power of a signal can be obtained by integrating the power spectral density over all spatial frequencies. Using Eqs. (E.2) and (E.5), one can see that the total power is equal to the value of the autocorrelation at the origin $K_{uu}(0)$:

$$P := \int_{-\infty}^{\infty} P_{uu}(f)\, df \overset{E.5}{=} \int_{-\infty}^{\infty} |U(f)|^2\, df \overset{\text{Parseval}}{=} \int_{-\infty}^{\infty} |u(x)|^2\, dx \overset{E.2}{=} K_{uu}(0). \tag{E.6}$$

The left and right hand side of Eq. (E.6) are related by Parseval's theorem, stating that the total power of the signal in real space is equal to the power in reciprocal space.

With these fundamental considerations, a few parameters for the characterization of noise in experiments can be developed. Of central importance for the evaluation of the image quality is the ratio between the power of signal and noise, summarized in the **signal-to-noise ratio** (SNR)

$$\text{SNR} = \frac{P_{\text{signal}}}{P_{\text{noise}}}. \tag{E.7}$$

The ratio between the SNR at the input of the system to the SNR at the output of the system leads to the expression of the **detective quantum efficiency** (DQE):

$$\text{DQE} = \frac{\text{SNR}_{out}}{\text{SNR}_{in}} = \frac{(P_{\text{signal}}/P_{\text{noise}})_{out}}{(P_{\text{signal}}/P_{\text{noise}})_{in}}. \tag{E.8}$$

The DQE is used to quantify the ability of a detector to convert incoming photons into a measured signal. Using the definition of Eq. (E.5), the DQE as a function of spatial frequency can be given by

$$\text{DQE}(f) = \frac{P_{uu}(f)_{out}}{P_{uu}(f)_{in}} \cdot \frac{\text{NPS}(f)_{in}}{\text{NPS}(f)_{out}}. \tag{E.9}$$

Similar to the MTF (see appendix A), the ideal DQE is equal to unity for all spatial frequencies, while it will be monotonically decreasing with increasing spatial frequency in real physical systems.

In linear and shift-invariant systems, the output function can be calculated from the input by a convolution with the impulse response h of the system, i.e. $u_{out}(x) = u_{in}(x) \otimes h(x)$, following Eq. (A.7). The absolute value of the Fourier transform of this relation is

$$|U_{out}(f)|^2 = |U_{in}(f)|^2 \cdot |MTF(f)|^2. \tag{E.10}$$

As $P_{uu} = |U|^2$, combining Eq. (E.10) with (E.9) yields

$$DQE = |MTF|^2 \cdot \frac{NPS_{in}}{NPS_{out}} \tag{E.11}$$

and thus the NPS can be written

$$NPS_{out} = \frac{|MTF|^2}{DQE} \cdot NPS_{in}. \tag{E.12}$$

Therefore, a simultaneous optimization of the MTF and the DQE is not possible.

F Data evaluation using Fourier methods

In this section, the evaluation of the harmonic phase-stepping oscillation in each pixel using the discrete Fourier transform will be highlighted. We assume that the phase-stepping was done using $N-1$ equidistant steps and that it was not necessarily performed over an integer number of periods of the interference pattern, i.e. we assume that $x_n/p = n/M$, with $M \in \mathbb{R}$. The phase-stepping oscillation can then be given by

$$S_n = a_0 + a_1 \cos\left(2\pi\frac{n}{M} - \varphi\right). \tag{F.1}$$

The zeroth Fourier coefficient of the phase-stepping scan can be calculated as:

$$\begin{aligned} c_0 &= \frac{1}{N}\sum_{n=0}^{N-1} S_n \\ &= \frac{1}{N}\sum_{n=0}^{N-1}\left[a_0 + a_1\cdot\cos\left(2\pi\frac{N}{M} - \varphi\right)\right] \\ &= \frac{a_0}{N}\underbrace{\sum_{n=0}^{N-1} 1}_{=N} + \underbrace{\frac{a_1}{N}\sum_{n=0}^{N-1}\cdot\cos\left(2\pi\frac{n}{M} - \varphi\right)}_{=0 \text{ if } \mathrm{mod}(M,N)=0} \\ &= a_0. \end{aligned} \tag{F.2}$$

Thus, the zeroth Fourier coefficient is equal to the mean value of the phase-stepping oscillation. In contrast, the first Fourier coefficient is

$$\begin{aligned} c_1 &= \frac{1}{N}\sum_{n=0}^{N-1} S_n\cdot\exp\left(2\pi i\frac{n}{N}\right) \\ &= \frac{a_0}{N}\underbrace{\sum_{n=0}^{N-1}\exp\left(2\pi i\frac{n}{N}\right)}_{=0} + \frac{a_1}{N}\sum_{n=0}^{N-1}\underbrace{\cos\left(2\pi\frac{n}{M} - \varphi\right)}_{2\cos(x)=\exp(ix)+\exp(-ix)}\cdot\exp\left(2\pi i\frac{n}{N}\right) \\ &= \frac{a_1}{2N}\sum_{n=0}^{N-1}\left[\exp\left(2\pi i\frac{n}{M} - i\varphi\right) + \exp\left(-2\pi i\frac{n}{M} + i\varphi\right)\right]\cdot\exp\left(2\pi i\frac{n}{N}\right) \\ &= \frac{a_1}{2N}\exp(-i\varphi)\underbrace{\sum_{n=0}^{N-1}\exp\left(2\pi in\left(\frac{1}{N} + \frac{1}{M}\right)\right)}_{=0 \text{ if } \mathrm{mod}(M,N)=0} + \frac{a_1}{2N}\exp(i\varphi)\underbrace{\sum_{n=0}^{N-1}\exp\left(2\pi in\left(\frac{1}{N} - \frac{1}{M}\right)\right)}_{=N \text{ if } \mathrm{mod}(M,N)=0} \\ &= \frac{a_1}{2}\exp(i\varphi). \end{aligned} \tag{F.3}$$

Thus, the phase of the first Fourier coefficient is equal to the phase of the phase-stepping oscillation

$$\arg(c_1) = \varphi, \tag{F.4}$$

while the magnitude is equal to half the amplitude a_1

$$|c_1| = \frac{a_1}{2}. \tag{F.5}$$

Note that these calculations are only correct if $M = N$, i.e. if an integer number of periods is scanned in the phase-stepping scan. If there are deviations from this assumption, the mean, phase and amplitude will not be independent of each other.

G Analysis of noise properties

This section covers calculations of the expectation values and the variance of the parameters of the phase-stepping oscillation, as well as the quantities derived from them.

G.1 Noise properties of the oscillation mean

If the measured raw data S_n are assumed to be corrupted by deviations δ_n, described by an additive zero-mean Gaussian distribution, the expectation value $E(a_0)$ of the mean a_0 of the phase-stepping oscillation can be calculated by

$$\begin{aligned} E(a_0) &= E(c_0) \\ &= E\left(\frac{1}{N}\sum_{n=0}^{N-1}(S_n+\delta_n)\right) \\ &= \frac{1}{N}\sum_{n=0}^{N-1}\underbrace{E(S_n)}_{=S_n}+\frac{1}{N}\sum_{n=0}^{N-1}\underbrace{E(\delta_n)}_{=0} \\ &= \frac{a_0}{N}\underbrace{\sum_{n=0}^{N-1}1}_{=N}+\frac{a_1}{N}\underbrace{\sum_{n=0}^{N-1}\cos\left(2\pi\frac{n}{N}-\varphi\right)}_{=0} \\ &= a_0. \end{aligned} \tag{G.1}$$

In the derivation, we have used the linearity of the expectation value operator.
The variance of the mean value of the phase-stepping oscillation can be calculated by interpreting the mean of the phase-stepping oscillation as a function of the raw data $a_0(S_n)$, with variance $V(S_n+\delta_n)=S_n$, following Poissonian statistics. If one assumes that the noise contributions in the different raw images S_n are independent of each other, the variance of the phase-stepping mean a_0 is given by

$$\begin{aligned} V(a_0) &= V(c_0) \\ &= V\left(\frac{1}{N}\sum_{n=0}^{N-1}(S_n+\delta_n)\right) \\ &= \frac{1}{N^2}\sum_{n=0}^{N-1}\underbrace{V(S_n+\delta_n)}_{=S_n} \\ &= \frac{a_0}{N^2}\underbrace{\sum_{n=0}^{N-1}1}_{=N}+\frac{a_1}{N^2}\underbrace{\sum_{n=0}^{N-1}\cos\left(2\pi\frac{n}{N}-\varphi\right)}_{=0} \\ &= \frac{a_0}{N}, \end{aligned} \tag{G.2}$$

where we have used $V(aX+bY)=a^2V(X)+b^2V(Y)$ for $\mathrm{Cov}(X,Y)=0$.

G.2 Noise properties of the first complex Fourier coefficient

For the calculation of the noise properties of the phase and amplitude the expectation value and variance of the complex Fourier coefficient c_1 have to be determined. The coefficient, interpreted as a function of the raw data $c_1(S_n)$, is given by

$$c_1 = \frac{1}{N}\sum_{n=0}^{N-1} S_n \cdot e^{-2\pi i \frac{n}{N}}. \tag{G.3}$$

Using additive Gaussian distributed deviations δ_n with zero mean, the expectation value of the first Fourier coefficient is

$$\begin{aligned} E(c_1) &= E\left(\frac{1}{N}\sum_{n=0}^{N-1}(S_n+\delta_n)\cdot\exp\left(2\pi i\frac{n}{N}\right)\right) \\ &= \frac{1}{N}\sum_{n=0}^{N-1}\underbrace{E(S_n)}_{=S_n}\cdot\exp\left(2\pi i\frac{n}{N}\right)+\frac{1}{N}\sum_{n=0}^{N-1}\underbrace{E(\delta_n)}_{=0}\cdot\exp\left(2\pi i\frac{n}{N}\right) \\ &= c_1. \end{aligned} \tag{G.4}$$

Using Euler's identity $\exp(i\phi)=\cos(\phi)+i\sin(\phi)$, the complex coefficient c_1 can be split into its real and imaginary part

$$\begin{aligned} \mathrm{Re}(c_1) &= \frac{1}{N}\sum_{n=0}^{N-1} S_n\cos\left(2\pi\frac{n}{N}\right) \\ \mathrm{Im}(c_1) &= \frac{1}{N}\sum_{n=0}^{N-1} S_n\sin\left(2\pi\frac{n}{N}\right). \end{aligned} \tag{G.5}$$

For the sake of readability, we will abbreviate $\mathrm{Re}(c_1)=\mathrm{Re}$ und $\mathrm{Im}(c_1)=\mathrm{Im}$. The variance of Re is

$$\begin{aligned} V(\mathrm{Re}) &= V\left(\frac{1}{N}\sum_{n=0}^{N-1}(S_n+\delta)\cdot\cos\left(2\pi\frac{n}{N}\right)\right) \\ &= \frac{1}{N^2}\sum_{n=0}^{N-1}\underbrace{V(S_n+\delta)}_{=S_n}\cdot\cos^2\left(2\pi\frac{n}{N}\right) \\ &= \underbrace{\frac{a_0}{N^2}\sum_{n=0}^{N-1}\cos^2\left(2\pi\frac{n}{N}\right)}_{=N/2} \quad + \quad \underbrace{\frac{a_1}{N^2}\sum_{n=0}^{N-1}\cos^2\left(2\pi\frac{n}{N}\right)\cos\left(2\pi\frac{n}{N}-\varphi\right)}_{=0} \\ &= \frac{a_0}{2N} \\ &\overset{\underline{\text{G.2}}}{=} \frac{V(a_0)}{2} \\ &\overset{\underline{5.8}}{=} \frac{a_0^2}{2}\cdot\tilde{\sigma}^2. \end{aligned} \tag{G.6}$$

The variance of the imaginary part is calculated analogously and leads to the same result:

$$V(\mathrm{Im}) = \frac{a_0^2}{2}\cdot\tilde{\sigma}^2. \tag{G.7}$$

G.3 Noise properties of the oscillation amplitude

The amplitude of the phase-stepping oscillation can be calculated from the first complex Fourier coefficient by

$$a_1 = 2|c_1| = 2\sqrt{\mathrm{Re}^2 + \mathrm{Im}^2}. \tag{G.8}$$

If the amplitude is interpreted as a function of the real and imaginary part of c_1, i.e. $a_1(\mathrm{Re}, \mathrm{Im})$, with standard deviations σ_{Re} and σ_{Im}, respectively, the variance $V(a_1)$ of the amplitude σ_{a_1} can be calculated by

$$\begin{aligned}
V(a_1) &= \left(\frac{\partial a_1}{\partial \,\mathrm{Re}}\right)^2 \sigma_{\mathrm{Re}}^2 + \left(\frac{\partial a_1}{\partial \,\mathrm{Im}}\right)^2 \sigma_{\mathrm{Im}}^2 \\
&\overset{\sigma_{\mathrm{Re}}=\sigma_{\mathrm{Im}}}{=} \sigma_{\mathrm{Re}}^2 \cdot \left[\left(\frac{4\,\mathrm{Re}}{2\sqrt{\mathrm{Re}^2+\mathrm{Im}^2}}\right)^2 + \left(\frac{4\,\mathrm{Im}}{2\sqrt{\mathrm{Re}^2+\mathrm{Im}^2}}\right)^2\right] \\
&\overset{G.8}{=} \sigma_{\mathrm{Re}}^2 \cdot \frac{16}{a_1^2}\left[\mathrm{Re}^2 + \mathrm{Im}^2\right] \\
&\overset{G.8}{=} \sigma_{\mathrm{Re}}^2 \cdot 4 \\
&\overset{G.6}{=} 2 \cdot V(a_0) \\
&\overset{5.8}{=} 2 \cdot a_0^2 \cdot \tilde{\sigma}^2.
\end{aligned} \tag{G.9}$$

G.4 Noise properties of the oscillation phase

The phase φ of the phase-stepping oscillation is calculated by

$$\varphi = \arg(c_1) = \operatorname{atan}\left(\frac{\mathrm{Im}}{\mathrm{Re}}\right). \tag{G.10}$$

If the phase is interpreted as a function of the real and imaginary part of c_1 with the standard deviations σ_{Re} and σ_{Im}, respectively, the variance $V(\varphi)$ of the phase φ can be calculated as

$$\begin{aligned}
V(\varphi) &= \left(\frac{\partial \varphi}{\partial \,\mathrm{Im}}\right)^2 \sigma_{\mathrm{Im}}^2 + \left(\frac{\partial \varphi}{\partial \,\mathrm{Re}}\right)^2 \sigma_{\mathrm{Re}}^2 \\
&= \left(\frac{1}{1+\left(\frac{\mathrm{Im}}{\mathrm{Re}}\right)^2}\frac{1}{\mathrm{Re}}\right)^2 \sigma_{\mathrm{Im}}^2 + \left(\frac{1}{1+\left(\frac{\mathrm{Im}}{\mathrm{Re}}\right)^2}\frac{\mathrm{Im}}{\mathrm{Re}^2}\right)^2 \sigma_{\mathrm{Re}}^2 \\
&\overset{\sigma_{\mathrm{Re}}=\sigma_{\mathrm{Im}}}{=} \sigma_{\mathrm{Re}}^2 \left[\left(\frac{\mathrm{Re}^2}{\mathrm{Re}^2+\mathrm{Im}^2}\frac{1}{\mathrm{Re}}\right)^2 + \left(\frac{\mathrm{Re}^2}{\mathrm{Re}^2+\mathrm{Im}^2}\frac{\mathrm{Im}}{\mathrm{Re}^2}\right)^2\right] \\
&\overset{G.8}{=} \sigma_{\mathrm{Re}}^2 \left[\left(\frac{4\mathrm{Re}}{a_1^2}\right)^2 + \left(\frac{4\mathrm{Im}}{a_1^2}\right)^2\right] \\
&\overset{G.8}{=} \sigma_{\mathrm{Re}}^2 \cdot \frac{4}{a_1^2} \\
&\overset{G.6+2.73}{=} \frac{2}{v^2}\tilde{\sigma}^2
\end{aligned} \tag{G.11}$$

G.5 Statistical moments of a ratio distribution

In this section, we will derive an approximate expression for the expectation value $E(x/y)$ of the ratio of two random variables x and y, using a Taylor expansion around the expectation values $E(x)$ and $E(y)$ of the two variables. This derivation will allow the calculation of the statistical moments of the visibility, transmission and dark-field signal of a measurement, as all these parameters are defined by ratios of random variables. We assume that the moments of the two distributions exist and $y \neq 0$. The expectation value $E(x/y)$ of the ratio of x and y may be rewritten

$$\begin{aligned} E\left[\frac{x}{y}\right] &= E\left[\frac{E(x)+(x-E(x))}{E(y)+(y-E(y))}\right] \\ &= E\left[\left(\frac{E(x)}{E(y)}+\frac{(x-E(x))}{E(y)}\right)\cdot\left(\frac{1}{1+\frac{y-E(y)}{E(y)}}\right)\right]. \end{aligned} \tag{G.12}$$

If we expand the expression on the right-hand side by

$$\begin{aligned} \frac{1}{1+\frac{y-E(y)}{E(y)}} &= 1-\frac{y-E(y)}{E(y)}+\left(\frac{y-E(y)}{E(y)}\right)^2-\left(\frac{y-E(y)}{E(y)}\right)^3+\ldots \\ &= \sum_{n=0}^{\infty}(-1)^n\left(\frac{y-E(y)}{E(y)}\right)^n \end{aligned} \tag{G.13}$$

and make use of the linearity of the expectation value operator, we obtain

$$\begin{aligned} E\left[\frac{x}{y}\right] &= E\left[\frac{E(x)}{E(y)}\cdot\sum_{n=0}^{\infty}(-1)^n\left(\frac{y-E(y)}{E(y)}\right)^n\right]+E\left[\frac{x-E(x)}{E(y)}\cdot\sum_{n=0}^{\infty}(-1)^n\left(\frac{y-E(y)}{E(y)}\right)^n\right] \\ &= \frac{E(x)}{E(y)}\cdot\sum_{n=0}^{\infty}(-1)^n\left(\frac{M_n(y)}{E(y)^n}+\frac{C_{1n}(y)}{E(x)\cdot E(y)^n}\right), \end{aligned} \tag{G.14}$$

where we have introduced

$$M_n(y)=E\left[(y-E(y))^n\right], \tag{G.15}$$

being the n-th central moment of the distribution of y, and

$$C_{1n}(x,y)=E\left[(x-E(x))\,(y-E(y))^n\right], \tag{G.16}$$

being the n-th central co-moment of the distributions of x and y with respect to y. With

$$\begin{aligned} M_0(y) &= 1 \\ M_1(y) &= 0 \\ M_2(y) &= V(y) \\ C_{10}(x,y) &= 0 \\ C_{11}(x,y) &= \mathrm{Cov}(x,y) \\ C_{12}(x,y) &= \mathrm{Csk}_y(x,y), \end{aligned} \tag{G.17}$$

where $\mathrm{Csk}_y(x,y)$ is the co-skewness of x and y with respect to y, we can approximate the expectation value of $E(x/y)$ by

$$E\left(\frac{x}{y}\right)=\frac{E(x)}{E(y)}\cdot\left(1-\frac{\mathrm{Cov}(x,y)}{E(x)E(y)}+\frac{V(y)}{E(y)^2}-\frac{\mathrm{Csk}_y(x,y)}{E(x)E(y)^2}+\ldots\right). \tag{G.18}$$

The variance $V(x/y)$ of the ratio distribution may be approximated in a similar way, yielding

$$V\left[\frac{x}{y}\right] = V\left[\frac{E(x)}{E(y)} \cdot \sum_{n=0}^{\infty} (-1)^n \left[\left(\frac{y-E(y)}{E(y)}\right)^n + \frac{x-E(x)}{E(x)} \cdot \left(\frac{y-E(y)}{E(y)}\right)^n\right]\right]. \quad \text{(G.19)}$$

As the variance operator is non-linear, $V(ax+by) = a^2V(x) + b^2V(y) + 2ab\mathrm{Cov}(x,y)$, the variance of the two sums cannot be evaluated without calculating the mutual covariances of all terms in the sum, greatly complicating further analysis. If we assume that $\mathrm{Cov}(x^n, y^m) = 0$ $\forall m,n$, we may write

$$V\left[\frac{x}{y}\right] = \frac{E(x)^2}{E(y)^2} \cdot \sum_{n=0}^{\infty} \left(\frac{F_n(y)}{E(y)^{2n}} + \frac{G_{1n}(y)}{E(x)^2 \cdot E(y)^{2n}}\right), \quad \text{(G.20)}$$

where we have introduced the functions

$$F_n(y) = V\left((y-E(y))^n\right) \quad \text{(G.21)}$$

$$G_{1n}(y) = V\left((x-E(x))\,(y-E(y))^n\right). \quad \text{(G.22)}$$

With

$$\begin{aligned} F_0(y) &= 0 \\ F_1(y) &= V(y) \\ G_{10}(x,y) &= V(x) \\ G_{11}(x,y) &= 0, \end{aligned} \quad \text{(G.23)}$$

we may thus approximate the variance of the ratio $V(x/y)$ up to first order by

$$V\left(\frac{x}{y}\right) = \frac{E(x)^2}{E(y)^2} \cdot \left(\frac{V(x)}{E(x)^2} + \frac{V(y)}{E(y)^2} + \ldots\right). \quad \text{(G.24)}$$

If we explicitly calculate the zeroth and first order expansion of Eq. (G.19), we obtain an additional term, depending on $\mathrm{Cov}(x,y)$

$$V\left(\frac{x}{y}\right) = \frac{E(x)^2}{E(y)^2} \cdot \left(\frac{V(x)}{E(x)^2} + \frac{V(y)}{E(y)^2} - \frac{2\mathrm{Cov}(x,y)}{E(x)E(y)} + \ldots\right). \quad \text{(G.25)}$$

Thus, in first order approximation and in the absence of correlations between x and y, Eq. (G.25) is equal to the well known formula of Gaussian error propagation.

G.6 Summary of noise properties

parameter	high SNR limit	low SNR limit
$E(a_0)$	a_0	a_0
$E(a_1)$	a_1	$\tilde{\sigma} \cdot a_0 \cdot \sqrt{\pi}$
$E(\nu)$	ν	$\tilde{\sigma}\sqrt{\pi}$
$E(\varphi$	φ	$1/(2\pi)$
$\frac{\sigma(a_0)}{E(a_0)}$	$\tilde{\sigma}$	$\tilde{\sigma}$
$\frac{\sigma(a_1)}{E(a_1)}$	$\tilde{\sigma} \cdot \frac{\sqrt{2}}{\nu}$	$\sqrt{\frac{4-\pi}{\pi}}$
$\frac{\sigma(\nu)}{E(\nu)}$	$\tilde{\sigma}\sqrt{\frac{2}{\nu^2}+1}$	$\sqrt{\frac{4-\pi}{\pi}+\tilde{\sigma}^2}$
$\sigma(\varphi)$	$\tilde{\sigma} \cdot \frac{\sqrt{2}}{\nu}$	$\frac{\pi}{\sqrt{3}}$

Table 1: *Overview over the noise properties of the parameters of the phase-stepping oscillation*

parameter	high SNR limit	low SNR limit
$E(T) \approx \frac{E(a_{0,s})}{E(a_{0,r})}$	T	T
$E(A) \approx \frac{E(a_{1,s})}{E(a_{1,r})}$	A	$\sqrt{T}$
$E(D) \approx \frac{E(\nu_s)}{E(\nu_r)}$	D	$\frac{1}{\sqrt{T}}$
$E(\Delta\varphi) = E\left(\arg\left(\frac{c_{1,s}}{c_{1,r}}\right)\right)$	$\Delta\varphi$	$\Delta\varphi$
$\frac{\sigma(T)}{E(T)}$	$\tilde{\sigma}\sqrt{1+\frac{1}{T}}$	$\tilde{\sigma}\sqrt{1+\frac{1}{T}}$
$\frac{\sigma(A)}{E(A)}$	$\tilde{\sigma} \cdot \sqrt{\frac{2}{\nu_r^2} \cdot \left(1+\frac{1}{TD^2}\right)}$	$\sqrt{\frac{8-2\pi}{\pi}}$
$\frac{\sigma(D)}{E(D)}$	$\tilde{\sigma} \cdot \sqrt{\frac{2}{\nu_r^2} \cdot \left(1+\frac{1}{TD^2}\right) + \left(1+\frac{1}{T}\right)}$	$\sqrt{\frac{8-2\pi}{\pi} + \left(1+\frac{1}{T}\right)}$
$\sigma(\Delta\varphi)$	$\tilde{\sigma} \cdot \sqrt{\frac{2}{\nu_r^2} \cdot \left(1+\frac{1}{TD^2}\right)}$	$\frac{\pi}{\sqrt{3}}$

Table 2: *Table summarizing the parameters calculated when using a reference image.*

References

[Arrizon94] V. Arrizón, J. Ojeda-Castañeda, "Multilevel phase gratings for array illuminators", Appl. Optics, **33**, 5925-5931 (1994).

[Barret96] H.H. Barrett, W. Swindell, "Radiological Imaging. The Theory of Image Formation, Detection and Processing", Academic Press Inc., 2nd edition (1996).

[Bech09] M. Bech, "X-ray imaging with a grating interferometer", Ph. D. Thesis, Faculty of Science, University of Copenhagen (2009).

[Bech10] M. Bech, O. Bunk, T. Donath, R. Feidenhans'l, C. David, and F. Pfeiffer, "Quantitative x-ray dark-field computed tomography," Phys. Med. Biol. **55**, 5529-5539 (2010).

[Bennet10] E.E. Bennett, R. Kopace, A.F. Stein, and H. Wen "A grating-based single-shot X-ray phase contrast and diffraction method for in vivo imaging," Med. Phys. **37**, 6047-6054 (2010).

[Bonny96] J.-M. Bonny, J.-P. Renou, and M. Zanca, "Optimal measurement of magnitude and phase from MR data," J. Mag. Res. **113**, 136-144 (1996).

[Bonse65] U. Bonse and M. Hart, "An x-ray interferometer," Appl. Phys. Lett. **6**, 155-157 (1965).

[Booklet09] A.C. Thompson, et al., "X-ray data booklet" (2009).

[Born99] M. Born and E. Wolf, "Principles of Optics. Electromagnetic Theory of Propagation, Interference and Diffraction of Light," Cambridge University Press, 7th edition (1999).

[Borsdorf06] A. Borsdorf, R. Raupach, and J. Hornegger, "Wavelet based noise reduction by identification of correlation", Pattern Recognition (DAGM 2006), Lecture notes in Computer science, K. Franke, K. Müller, B. Nickolay, and R. Schäfer (Eds.), Springer, Berlin **4174**, 21-30 (2006).

[Borsdorf08] A. Borsdorf, R. Raupach, T. Flohr, and J. Hornegger, "Wavelet based noise reduction in CT-images using correlation analysis," IEEE Trans. Med. Im. **27**, 1685-1703 (2008).

[Chabior11A] M. Chabior, M. Schuster, C. Schroer, and F. Pfeiffer, "Grating-based phase-contrast computed tomography of thick samples," Phys. Med. Biol. submitted (2011).

[Chabior11B] M. Chabior and M. Schuster, "Abbildung der effektiven Kernladungszahl mittels gitterbasierter Radiographie bzw. Tomographie," Technik Up2date 2011 #3, p.14, Prior Art Publishing, (2011).

[Chabior11C] M. Chabior, T. Donath, C. David, M. Schuster, C. Schroer, and F. Pfeiffer, "Signal-to-noise ratio in grating-based x-ray dark-field imaging," J. Appl. Phys. accepted (2011).

[Chabior11D] M. Chabior, T. Donath, C. David, M. Schuster, C. Schroer, and F. Pfeiffer, "Beam hardening effects in grating-based x-ray phase-contrast imaging," Med. Phys. **38**, 1189-1195 (2011).

[Chabior11E] M. Chabior, M. Schuster, C. Schroer, and F. Pfeiffer, "Analytical evaluation of grating-based x-ray imaging using imperfect gratings," in preparation (2011).

[Chapman97] L.D. Chapman, W.C. Thomlinson, R.E. Johnston, D. Washburn, E. Pisano, N. Gmuer, Z. Zhong, R. Menk, F. Arfelli, and D. Sayers, "Diffraction enhanced x-ray imaging," Phys. Med. Biol. **42**, 2015-2025 (1997).

[Clauser98] J. Clauser, "Ultrahigh resolution interferometric x-ray imaging," US patent 5,812,629 (1998).

[Cloetens97] P. Cloetens, M. Pateyron-Salomé, J.-Y. Buffiere, G. Peix, J.Baruchel, F. Peyrin, and M. Schlenker, “Observation of microstructure and damage in materials by phase radiography and tomography,” J. Appl. Phys **81**, 5878-5886 (1997).

[Coan10] P. Coan, F. Bamberg, P.C. Diemoz, A. Bravin, K. Timpert, E. Mützel, J.G. Raya, S. Adam-Neumair, M.F. Reiser, and C. Glaser, “Characterization of osteoarthritic and normal human patella cartilage by computed tomography X-ray phase-contrast imaging,” Invest. Radiol. **45**, 437-444 (2010).

[Crystallography04] E. Prince, “International Tables for Crystallography, Volume C, Mathematical, Physical and Chemical Tables,” 3rd edition (2004).

[David02] C. David, B. Nöhammer, H.H. Solak, and E. Ziegler, “Differential x-ray phase contrast imaging using a shearing interferometer,” Appl. Phys. Lett. **81**, 3287-3290 (2002).

[David07] C. David, J. Bruder, T. Rohbeck, C. Grünzweig, C. Kottler, A. Diaz, O. Bunk, and F. Pfeiffer, “Fabrication of diffraction gratings for hard X-ray phase contrast imaging,” Microelectron. Eng. **84**, 1172-1177 (2007).

[Davis95] T.J. Davis, D. Gao, T.E. Gureyev, A.W. Stevenson, and S.W. Wilkins, “Phase-contrast imaging of weakly absorbing materials using hard x-rays,” Nature **373**, 595-598 (1995).

[Donath10A] T. Donath, M. Chabior, F. Pfeiffer, O. Bunk, E. Reznikova, J. Mohr, E. Hempel, S. Popescu, M. Hoheisel, M. Schuster, J. Baumann, and C. David, “Inverse geometry for grating-based x-ray phase-contrast imaging,” J. Appl. Phys. **106**, 054703 (2009).

[Donath10B] T. Donath, F. Pfeiffer, O. Bunk, C. Grünzweig, E. Hempel, S. Popescu, P. Vock, and C. David, “Toward clinical x-ray phase-contrast-CT: demonstration of enhanced soft-tissue contrast in human specimen,” Invest. Radiol. **45**, 445-452 (2010).

[Engeler90] P. Engeler and W.D. Friedman, “Review of dual-energy computed tomography techniques,” Materials Evaluation **48**, 623-629 (1990).

[Engelhardt07] M. Engelhardt, J. Baumann, M. Schuster, C. Kottler, F. Pfeiffer, O. Bunk, and C. David, “High-resolution differential phase contrast imaging using a magnifying projection geometry with a microfocus x-ray source,” Appl. Phys. Lett. **90**, 224101 (2007).

[Engelhardt08] M. Engelhardt, C. Kottler, O. Bunk, C. David, C. Schroer, J. Baumann, and M. Schuster, “The fractional Talbot effect in differential X-ray phase-contrast imaging for extended and polychromatic X-ray sources,” J. Microsc. **232**, 145-157 (2008).

[Evans55] R.D. Evans, “The atomic nucleus,” McGraw-Hill, 1st edition (1955).

[Fisher93] N.I. Fisher, “Statistical analysis of circular data,” Cambridge University Press, 1st edition, (1993).

[Ghiglia98] D.C. Ghiglia, “Two-Dimensional Phase Unwrapping: Theory, Algorithms, and Software,” John Wiley & Sons, 1st edition (1998).

[Goodman05] J.W. Goodman, “Introduction to Fourier Optics”, Roberts&Company, 3rd edition (2005).

[Guigay71] J.P. Guigay, “On Fresnel diffraction by one-dimensional periodic objects, with application to structure determination of phase objects”, Optics Acta, **18**, 677-682 (1971).

[Ham11] retrieved from Hamamatsu Homepage http://sames.hamamatsu.com/de/produkte/solid-state-division/x-ray-flat-panel-sensor/for-non-destructive-inspection.php (2011).

[Ingal95] V.N. Ingal and E.A. Beliaevskaya, “X-ray plane wave topography observation of the phase contrast from a non-crystalline object,” J. Phys. D: Appl. Phys. **28**, 2314-2317 (1995).

[Jensen10] T.H. Jensen, M. Bech, O. Bunk, T. Donath, C. David, R. Feidenhans’l, and F. Pfeiffer, “Directional x-ray dark-field imaging,” Phys. Med. Biol. **55**, 3317-3323 (2010).

[Kak88] A.C. Kak and M. Slaney, “Principles of computerized tomographic imaging”, IEEE Press, 1st edition (1988).

[Keyriläinen02] J. Keyriläinen, M. Fernanez, and P. Suortti, “Refraction contrast in x-ray imaging,” Nucl. Inst. Meth. A, **488**, 419-427 (2002).

[Keyriläinen08] J. Keyriläinen, M. Fernandez, M.L. Karjalainen-Lindsberg, P. Virkkunen, M. Leidenius, K. Smitten, P. Sipilä, S. Fiedler, H. Suhonen, P. Suortti, and A. Bravin, “Toward high-contrast breast CT at low radiation dose,” J. Radiology **249**, 321-327 (2008).

[Kottler07] C. Kottler and C. David, “A two-directional approach for grating-based differential phase-contrast imaging using hard X-rays,” Opt. Express **15**, 1175-1181 (2007).

[Lindsey64] W.C. Lindsey, “Error probabilities for rician fading multichannel reception of binary and N-ary signals,” IEEE Trans. Informa. Theory **10**, 339-350 (1964).

[Lohmann88] A. W. Lohmann, “An array illuminator based on the Talbot-effect”, Optik **79**, 41-45 (1988).

[Momose02] T. Takeda, A. Momose, J. Wu, W. Yu, T. Zeniya, T.T. Lywin, A. Yoneymama, and Y. Itai, “Vessel imaging by interferometric phase-contrast X-ray technique”, Circulation **105**, 1708-1712 (2002).

[Momose03] A. Momose, “Phase-sensitive imaging and phase tomography using x-ray interferometers,” Opt. Express **11**, 2303-2314 (2003).

[Muehlman10] C. Muehlman, D. Fogarty, B. Reinhart, T. Tzvetkov, J. Li, and I. Nesch, “In-laboratory diffraction enhanced X-ray imaging for articular cartilage,” Clinical Anatomy **23**, 530-538 (2010).

[Mucal93] B.L. Henke, E.M. Gullikson, and J.C. Davis, “X-ray interactions: photoabsorption, scattering, transmission, and reflection at E=50-30000 eV, Z=1-92,” At. Data Nucl. Data Tables **54**, 181-342 (1993).

[Nesch09] I. Nesch, D.P. Fogarty, T. Tzvetkov, B. Teinhart, A.C. Walus, G. Khelashvili, C. Muehlman, and D. Chapman, “The design and application of an in-laboratory diffraction enhanced x-ray imaging instrument,” Rev. Sci. Instrum. **80** 093702-6 (2009).

[Nesterets08] Ya.I. Nesterets, “On the origins of decoherence and extinction contrast in phase-contrast imaging,” Opt. Comm. **281**, 533-542 (2008).

[Nielsen00] J. Als-Nielsen and D. McMorrow, “Elements of modern x-ray physics”, John Wiley & Sons, 1st edition (2000).

[NIST95] National Institute of Standard and Technology, C.T. Chantler et.al. “X-Ray Form Factors, Attenuation and Scattering Tables”, J. Phys. Chem. Ref. Data **24**, 71-643 (1995).

[NIST09] National Institute of Standard and Technology, M.E. Weiser and M. Berglund, “Atomic weights of the elements 2009”, Pure Appl. Chem. **83**, 359-396 (2011).

[Nowak97] S. Nowak, Ch. Kurtsiefer, T. Pfau, and C. David “Higher order Talbot fringes for atomic waves,“ Opt. Lett. **22**, 1430-1432 (1997).

[Pfeiffer06] F. Pfeiffer, T. Weitkamp, O. Bunk, and C. David, “Phase retrieval and differential phase-contrast imaging with low-brilliance x-ray sources,” Nature Phys. **2**, 258-261 (2006).

[Pfeiffer07] F. Pfeiffer, C. Kottler, O. Bunk, and C. David, “Hard X-Ray Phase Tomography with Low-Brilliance Sources,” Phys. Rev. Lett. **98**, 108105 (2007).

[Pfeiffer08] F. Pfeiffer, M. Bech, O. Bunk, P. Kraft, E.F. Eikenberry, Ch. Brönnimann, C. Grünzweig and C. David, “Hard-X-ray dark-field imaging using a grating interferometer,” Nature Materials **7**, 134-137 (2008).

[Pisano00] E.D. Pisano, et al., “Human breast cancer specimens: diffraction-enhanced imaging with histologic correlation-improved conspicuity of lesion detail compared with digital radiography,“ Radiology **214**, 895-901 (2000).

[Qi08] Z. Qi and G.-H. Chen, “Direct fan-beam reconstruction algorithm via filtered backprojection for differential phase-contrast computed tomography” X-ray optics and instrumentation, **2008**, 1-8 (2008).

[Qi10] Z. Qi, J. Z., N. Bevins and G.H. Chen, “Quantitative imaging of electron density and effective atomic number using phase contrast CT”, Phys. Med. Biol. **55**, 2669-2677 (2010).

[Raupach11] R. Raupach and T.G. Flohr, “Analytical evaluation of the signal and noise propagation in x-ray differential phase-contrast computed tomography,” Phys. Med. Biol. **56**, 2219-2244 (2011).

[Rayleigh81] Lord Rayleigh, “On copying diffraction gratings, and on some phenomenon connected therewith,” Phil. Mag. **11**, 196-205 (1881).

[Reznikova08] E. Reznikova, J. Mohr, M. Boerner, V. Nazmov, and P. Jakobs, “Soft X-ray lithography of high aspect ratio SU8 submicron structures,” Microsyst. Technol. **14**, 1683-1688 (2008).

[Röntgen96] A. Stanton, “W.C. Röntgen, On a new kind of rays, Translation of a paper read before the Wuerzburg Physical and Medical Society,” Nature **53**, 274-276 (1896).

[Rice45] S.O. Rice, “Mathematical analysis of random noise,” Bell S. Techn. J. **24**, 46-156 (1945).

[Sijbers99] J.O. Sijbers, A.J. den Dekker, E. Raman, and D. Van Dyck, “Parameter estimation from magnitude MR images,” Int. J. Imaging Syst. Technol. **10**, 109-114 (1999).

[Siemens11] Siemens Healthcare http://www.medical.siemens.com/webapp/wcs/stores/servlet/ (2011).

[Snigirev96] A. Snigirev, V. Kohn, I. Snigireva, and B. Lengeler, “A compound refractive lens,” Nature **384**, 49-51 (1996).

[Snigirev95] A. Snigirev, I. Snigireva, V. Kohn, S. Kuznetsov, and I. Schelokov, “On the possibility of X-ray phase contrast microimaging by coherent high-energy synchrotron radiation,” Rev. Sci. Inst. **66**, 5486-5492 (1995).

[Spanne99] P. Spanne, C. Raven, I. Snigireva, and A. Snigirev, “In-line holography and phase-contrast microtomography with high energy x-rays,” Phys. Med. Biol. **44**, 741-749 (1999).

[Suleski97] T.J. Suleski, “Generation of Lohmann images from binary-phase Talbot array illuminators”, Appl. Opt. **36** 4686-4691 (1997).

[Talbot36] W.H.F. Talbot, “Facts relating to optical science No. IV”, Philos. Mag. **9**, 401-407 (1836).

[Talukdar91] K.K. Talukdar and W.D. Lawing "Estimation of the parameters of the Rice distribution," J. Acoust. Soc. Am. **83**, 1193-1197 (1991).

[Vrakking96] M.J.J. Vrakking, D.M. Villeneuve, and A. Stolow "Observations of fractional revivals of a molecular wavepacket" Phys. Rev. A **54**, R37-R40 (1996).

[Wang09] Z.-T. Wang, K.-J. Kang, Z.-F. Huang, and Z.-Q. Chen, "Quantitative grating-based x-ray dark-field computed tomography," Appl. Phys. Lett. **95**, 094105 (2009).

[Wen08] H. Wen, E.E. Bennett, M. Hegedus, and S. Caroll, "Spatial harmonic imaging of X-ray scattering", IEEE Trans. Med. Imaging **27**, 997-1002 (2008).

[Weitkamp05] T. Weitkamp, A. Diaz, C. David, F. Pfeiffer, M. Stampanoni, P. Cloetens, and E. Ziegler, "x-ray phase imaging with a grating interferometer," Opt. Express **13**, 6296-6304 (2005).

[Wilkins96] S.W. Wilkins, T.E. Gureyev, D. Gao, A. Pogany, and A.W. Stevenson, "Phase-contrast imaging using polychromatic hard x-rays," Nature **384**, 335-338 (1996).

[Winthorp65] J.T. Winthorp, C.R. Worthington, "Theory of Fresnel images. I. Plane Periodic Objects in Monochromatic Light", J. Opt. Soc. Am. **55**, 373-381 (1965).

[Yashiro10] W. Yashiro, Y. Terui, K. Kawabata, and A. Momose, "On the origin of visibility contrast in x-ray Talbot interferometry," Opt. Express **18**, 16890-16901 (2010).

[Zanette10] I. Zanette, C. David, S. Ruitshausser and T. Weitkamp, "2D grating simulation for X-ray phase-contrast and dark-field imaging with a Talbot interferometer," AIP Conf. Proc. **1221**, 73-79 (2010).

[Zernike34] F. Zernike, "Phase-contrast, a new method for microscopic observation of transparent objects," Physica **9**, 974-986 (1942).

[Zhang08] L. Zhang, Q. Fang, and Z. Huang, "3D reconstruction algorithm for cone-beam differential phase contrast tomography," IEEE Nucl. Sci. Symp. **2008**, 4193-4197 (2008).

[Zhou94] C. Zhou and L. Liu, "Simple equations for the calculation of a multilevel phase grating for Talbot array illumination," Opt. Comm. **115**, 40-44 (1994).

[Zhu10] P. Zhu, K. Zhang, Z. Wang, Y. Liu, X. Liu, Z. Wu, S. McDonald, F. Marone, and M. Stampanoni "Low-dose, simple, and fast grating-based X-ray phase-contrast imaging," PNAS **107**, 13576-13581 (2010).

Versicherung

Hiermit versichere ich, dass ich die vorliegende Arbeit ohne unzulässige Hilfe Dritter und ohne Benutzung anderer als der angegebenen Hilfsmittel angefertigt habe; die aus fremden Quellen direkt oder indirekt übernommenen Gedanken sind als solche kenntlich gemacht. Die Arbeit wurde bisher weder im Inland noch im Ausland in gleicher oder ähnlicher Form einer anderen Prüfungsbehörde vorgelegt.

Datum, Unterschrift

Erklärung

Die vorliegende Arbeit wurde von Sep. 2008 bis Aug. 2011 in München angefertigt. Als wissenschaftlicher Betreuer agiert Prof. Dr. Schroer, Fakultät Mathematik und Naturwissenschaften, Technische Universität Dresden.

Datum, Unterschrift